UNIVERSIDAD COMPLUTENSE DE MADRID

FACULTAD DE CIENCIAS FÍSICAS
Departamento de Física Atómica, Molecular y Nuclear

C-BAND LINAC FOR A RACE TRACK MICROTRON.

MEMORIA PARA OPTAR AL GRADO DE DOCTOR

PRESENTADA POR

David Carrillo Barrera

Bajo la dirección del doctor

Vasily Ivanovicht Shvedunov

Madrid, 2010

ISBN: 978-84-693-8239-4

CIEMAT

Unidad de Aceleradores

UNIVERSIDAD COMPLUTENSE DE MADRID

Departamento de Física Atómica, Molecular y Nuclear

TESIS DOCTORAL

LINAC EN BANDA C PARA UN MICROTRON DE PISTA

C-BAND LINAC FOR A RACE TRACK MICROTRON

Memoria realizada por

David Carrillo Barrera

para optar al grado de Doctor

Director de Tesis: **Dr. Vasiliy Ivanovich Shvedunov**

Madrid - 2010

CONTENTS

ACKNOWLEDGMENTS

It is a pleasure to thank those who have contributed to the successful completion of this project. My foremost thank goes to my thesis advisor Vasiliy I. Shvedunov (SINP Moscow) without his help, guidance and wisdom it would have been next to impossible to write this thesis.

I had the pleasure of working with all members of Accelerators Unit at CIEMAT. I am heartily thankful to my supervisor Fernando Toral for his constant support and helpful suggestions through my research. Special thanks goes to Iker Rodríguez for his motivation, encouragement and fruitful discussions helped me very much. I must acknowledge the effort of Enrique Rodríguez for his brilliant technical drawings and his helpful contributions during RTM mechanical design. I appreciate all the help provided by Álvaro Lara with the thermo-mechanical calculations. I must also thank Laura Sanchez for her splendid collaboration in the study of brazing of the RTM linac. Finally, I am thankful for the collaboration of Pablo Oriol, Eduardo Molina and Luís Miguel Martínez for their help with the programming and electronics needed in the bead pull test bench.

I would like to express my gratitude to Igor Syratchev (CERN) and A.S.Alimov (SINP Moscow), for whom I have learned a lot about the design and testing of RF cavities.

I also thank Yuri Koubychine (UPC) and Luís García-Tabarés (CIEMAT) for their support and for keeping the project alive finding financial support. Also, I am aware of this research would not have been possible without the financial assistance of CIEMAT.

ACRONYMS AND ABBREVIATIONS

AGS (Alternating Gradient Synchrotron)

BBU (Beam Blow-Up)

BW (Bandwidth)

CERN (European Organization for Nuclear Research)

CIEMAT (Centro de Investigaciones Energéticas Medioambientales y Tecnológicas)

CNC (Computer Numerical Control)

CW (Continuous Wave)

DUT (Device under test)

EBW (Electron-Beam Welding)

FEL (Free- Electron Laser)

Frequency bands:

- S - Band (2 - 4 GHz)
- C - Band (4 - 8 GHz)
- X - Band (8 - 12 GHz)

GSI (Helmholtz Centre for Heavy Ion Research)

HOM (Higher Order Modes)

IORT (Intra Operative Radiation Therapy)

LEP (Large Electron-Positron collider)

LHC (Large Hadron Collider)

LINAC (Linear Accelerator)

MUSL (Microtron Using Superconducting Linac)

NC (Normal Conducting)

OFE (Oxygen Free Electronic grade)

OFHC (Oxygen Free High Conductivity)

PET (Positron Emission Tomography)

PIXE (Particle Induced Xray Emission)

REPM (Rare Earth Permanent Magnet)

RF (Radiofrequency)

RTM (Race Track Microtron)

SASE (Self- Amplified Spontaneous Emission)

SC (Super Conducting)

SINP (Skobeltsyn Institute of Nuclear Physics)

TE (Transverse Electric mode)

TEM (Transverse Electro-Magnetic mode)

TM (Transverse Magnetic mode)

UPC (Universidad Politécnica de Cataluña)

VNA (Vector Network Analyzer)

VSWR (Voltage Standing Wave Ratio)

CHAPTER 1

Introduction

The main function of a particle accelerator is to supply energy to charged particles, and this energy is provided in most of the cases, except direct current and induction accelerators, by means of resonant cavities. These accelerating cavities or accelerating structures consist basically of one or more accelerating cells where electromagnetic fields are able to transmit energy to charged particles.

Particle accelerators are the main tools to study the basic structure of matter. In high energy physics experiments, particles such as protons or electrons are accelerated to tens and hundreds of GeV and collide with each other or into fixed targets. New particles are created from the high energy collisions, and their interactions and properties are studied using sophisticated detectors. High energy accelerators such as the Fermilab Tevatron (1 TeV proton and antiproton collider), the CERN LEP (101 GeV electron and positron collider) and the SLAC SLC (50 GeV electron and positron linear collider) have discovered many fundamental particles and advanced our knowledge of the basic forces of nature. The highest energy so far has been reached recently in the LHC (CERN Large Hadron Collider which is a proton-proton collider with 14 TeV centre of mass energy).

While the frontiers of nuclear physics are going to higher and higher energies, an increasing number of small accelerators are being used for other purposes like radiation therapy, medical isotope production e.g. for PET (Positron Emission Tomography), p-therapy, radiation technologies in industry or food irradiation among others.

The RTM (Race Track Microtron), for which C-band linac described in this thesis has been developed, is dedicated to IORT (Intra Operative Radiation Therapy). IORT is a rapidly developing technique consisting in the administration, during a surgical intervention, of a single and high radiation dose directly to the tumour bed/environment in a surgically defined area and thus avoiding damage of healthy tissues.

1.1 State of the art

Nowadays C-band linacs are rapidly progressing devices. An important advantage is their potential use in compact accelerators due to the smaller lengths needed compared to those of S-band linacs, like one producing 4 MeV for a compact X-ray source [1], or a dedicated source machine for Self- Amplified Spontaneous Emission (SASE) Free- Electron Laser (FEL) [2].

RTM has many advantages (section 1.4.2) over the classical microtron because a single accelerating cavity has been changed for a linac. While there have been only two RTMs using superconducting linacs (MUSL-I&II) which were built in the University of Illinois [3] there are several tens of RTM around the world using normal conducting linacs, usually in S-band.

The highest energy normal conducting RTM is located in the University of Mainz (Germany) and includes four stages CW RTM in cascade [4] producing a 1,5 GeV and 100 μA beam in the final stage, where they have had to place four magnets instead of two, reaching each one a mass of 250 tons.

At SINP (Skobeltsyn Institute of Nuclear Physics, Moscow State University), a mobile 70 MeV RTM with permanent end magnets and S-band linac has been constructed [5].

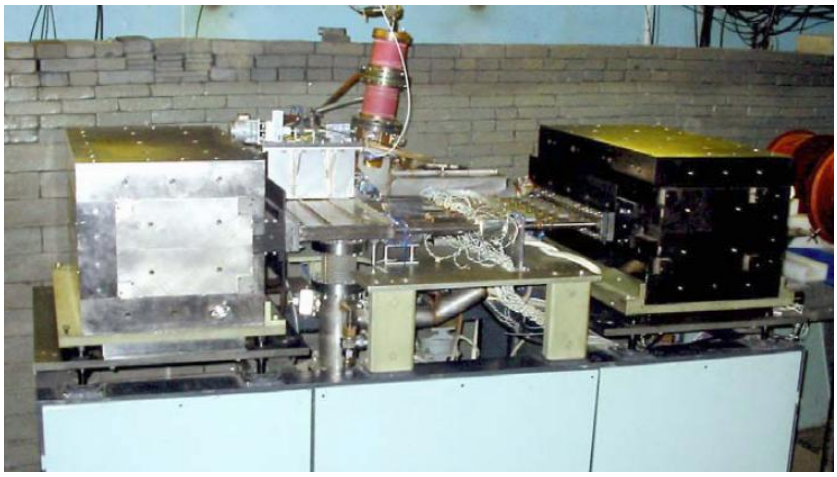

Figure 1-1. 70 MeV Race Track Microtron in SINP

An initial design of an unprecedentedly compact, light and economical RTM with output beam energies of 6,8,10 and 12 MeV [6] is the basis for an ongoing joint project led by the UPC

(Universidad Politécnica de Cataluña), where some companies and research institutes (SINP and CIEMAT- Centro de Investigaciones Energéticas Medioambientales y Tecnológicas- among others) are working to create a compact 12 MeV RTM [7] (see Figure 1-2) with medical purposes (IORT) and within its framework the main topics for this thesis have been developed.

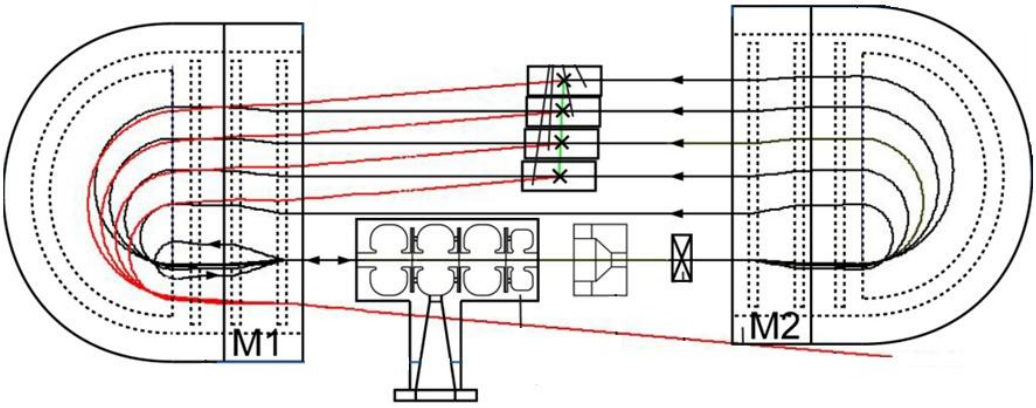

Figure 1-2. General layout RTM for IORT

Presently, the only IORT dedicated accelerators are specially designed X-band (3 cm wavelength) and S-band (10 cm wavelength) linacs, for example Mobetron (Intraop Medical Corporation, USA) [8], Novac-7 (Hitesys, Italy) [9], LIAC (Infotech, Italy)[10] and betatron (Tomsk Institute of Intrascopy, Russia) [11]. The total number of such accelerators does not exceed 30 units as compared with more than 5000 electron accelerators used for the external radiation therapy. Market size for dedicated IORT accelerators was estimated by Intraop Medical Corporation. Keeping in mind the application of their Mobetron [12] they estimate the total world market for advanced disease to be approximately 1320 units.

As the Mobetron has proven to make IORT application much simpler and less costly, applications of IORT to earlier stage disease may be expected to develop. This is because IORT during surgery for earlier stage disease can reduce the amount of following therapy by at least two weeks, resulting in a lower cost of cancer treatment.

Furthermore, because IORT delivers some of the radiation treatment at the time of surgery, higher utilization or decreased need for conventional equipment can be achieved because of the reduced number of radiation treatments per patient required.

The main requirements for the accelerators to be used in IORT are [13]: beam energy variable in the range of 6-12 MeV, maximum dose rate delivered to the tumour by electron beam of

10-20 Gy/min with minimal uncontrollable dark current contribution, accelerator head with radiation shielding must have minimal weight and dimensions to be easy and precisely positioned against tumour with a robotic arm, the overall installation weight and dimensions must be also minimized to use it in ordinary operating room. If in addition the cost of such machine would be lower as compared with present medical accelerators, then it also could be used for external radiation therapy in small hospitals. An excellent choice could be a compact RTM, machine which combines advantages of the linear and cyclic accelerators and permits to get electron beam with high intensity, narrow spectrum and precisely fixed energies using less power and in more compact and less weight installation.

1.2 Objectives and thesis structure

The general aim of this thesis is to do the radiofrequency (RF) design of a 2 MeV C-Band linac for a RTM, the mechanical design and thermo mechanical calculations and to follow the machining procedure. Afterwards, a test bench has to be designed so the RF cold measurements may be carried out. In addition, the process of brazing of accelerating cavities will be studied.

The novelty of this thesis arises from the fact that C-band linac was never used before in RTM. Specific of linac operation in RTM is defined by necessity (i) to accelerate simultaneously in the same linac low energy non relativistic beam from the electron gun and several different energy relativistic beams from the orbits; (ii) to accelerate beams moving in opposite directions; (iii) transverse dimensions are important to provide beam bypass at 1st orbit; (iv) to have sufficiently large aperture to decrease beam losses; (v) to pay attention to parasitic modes, especially to TM_{11} -like modes, which may cause transverse BBU (Beam Blow Up).

Due to this specific of RTM linac, its design for C-band cannot be just scaled from the known designs for S-band. A full scale study, including beam dynamics and RF properties simulation and optimization, engineering design, test and final measurements must be done within this thesis.

We can take a look at the specific purposes of the thesis through the structure described below. The thesis is divided into five chapters and the conclusions.

The **first chapter** includes the thesis introduction, the state of the art, the general objectives of this thesis, a review of particle accelerators and the description of microtron accelerators in order to understand afterwards the requirements for the 12 MeV RTM accelerator.

The **second chapter** gives a theoretical background to understand the methods and calculations needed to study and optimize accelerating structures.

The **third chapter** describes the steps followed to do the RF design (specifications, 2D optimization and 3D calculation). Calculation of tolerances is done for the mechanical design purposes. The analysis of multipole fields produced by structure asymmetry is performed with 3D codes. As well the parasitic modes calculations are done including estimate of the beam blow-up threshold current. In addition, the thermo mechanical behaviour of the structure is

studied in order to find out how the RF properties of the structure are changed under high level RF power.

The **fourth chapter** explains the different methods and devices needed to do the RF experimental measurements on accelerating structures. It includes a detailed description of the test bench developed and the procedure to measure the different RF parameters is explained.

The **fifth chapter** presents the design, machining, brazing and RF measurement of some test accelerating cavities to check the different procedures. Afterwards the mechanical design and RF measurements for the final LINAC are detailed.

1.3 Introduction to Particle Accelerators

1.3.1 The purpose of particle accelerators

There are many applications of the accelerators besides particle physics. These applications can be divided in three areas taking into account the type of beams used [14]:

1. Beams of particles employed as probes in the analysis of physical, chemical and biological properties of samples, where Particle Induced Xray Emission (PIXE) is a notable example.
2. Beams of particles used for the modification of the physical, chemical and biological properties of matter. Sterilisation can be quoted here.
3. The most energetic beams of particles are today the main instruments for research in basic subatomic physics.

The time tree (Figure 1-3) shows the progress of accelerators in parallel with some of their applications. It is observed that particle accelerators are very important in our society, because they provide unique contributions to human life in many knowledge areas.

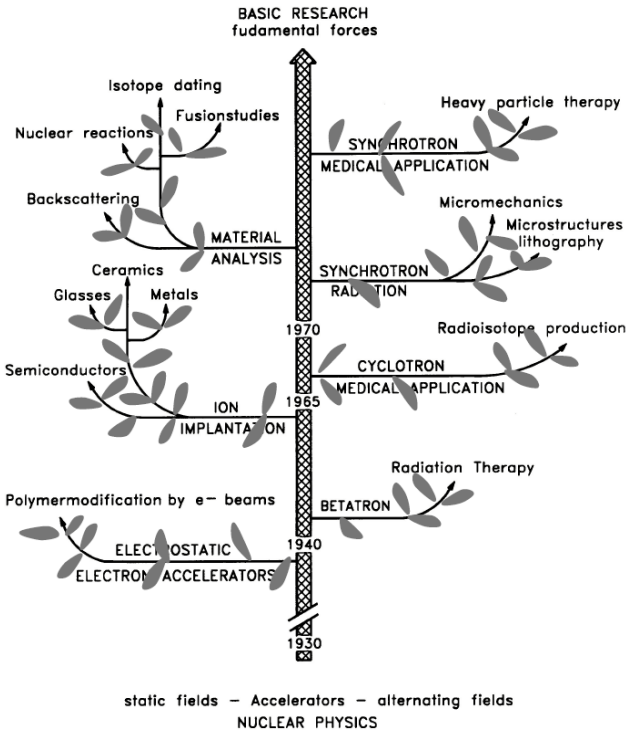

Figure 1-3. Time tree for accelerators applications [14] (Original picture from [15])

For example, research with heavy ions has led to diverse applications and technological innovations in the past. In 1998 the carbon ion therapy pilot project was completed at Helmholtz Centre for Heavy Ion Research (GSI), where about 50 patients had been irradiated. In addition, radioactive atoms are being used very successfully as probes to study processes and properties of materials. They can also be used for evaluating radiobiological risk for manned space missions, testing the materials of the spacecrafts.

In the area of femtochemistry, researchers are dealing with minuscule fractions of a second in order to trace the process of chemical reactions. Ultrafast lasers function as "cameras" taking instantaneous "snapshots" of chemical reactions with femtosecond (thousand million millionths of a second) exposure times. The principle is that an initial laser pulse triggers a photochemical reaction and a second pulse illuminates it immediately afterwards. The second flash must be precisely adjustable in order to trigger the "snapshot" at a well-defined instant. A series of such instantaneous snapshots taken with varying intervals between the first and second beams produces a film of the reaction process (Figure 1-4). The X-ray laser (obtained from synchrotron radiation) can make such films of the microcosm with up till now unique detail and time resolution. It generates an extremely intense X-ray beam and can be excellently focused. The duration of the flashes from the X-ray laser is about 100 femtoseconds. The X-ray laser flashes make possible to trace and comprehend the precise mechanisms of chemical reactions, reactions that might find applications in optoelectronics, photovoltaic and fuel or solar cells, for example.

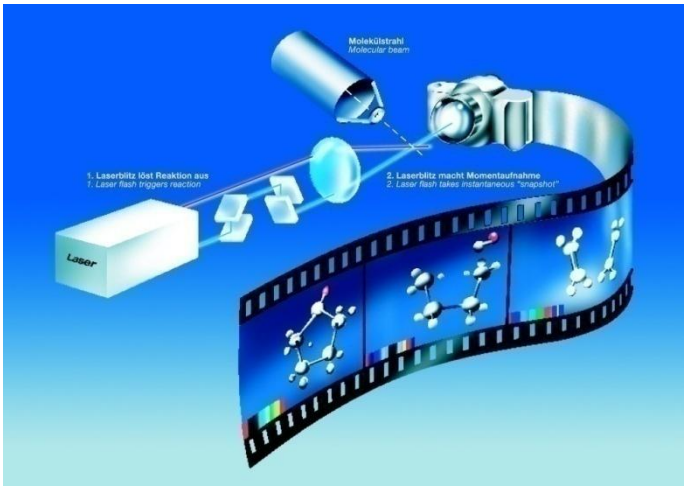

Figure 1-4. Film of a chemical reaction using a X-ray laser (© DESY**)**

Using the intense X-rays from particle accelerators, it is now possible to analyze the structure of bio molecules in detail. The X-ray laser opens up completely new opportunities to decipher

biological molecules with atomic resolution without the need for the extra step of growing crystals. The X-ray laser flashes are so intense that they can be used to create a high-resolution image of a single molecular complex. The flash duration is even shorter than 100 femtoseconds and is thus short enough to produce an image before the sample is destroyed by the intense X-rays.

Finishing this brief description of accelerator applications, we cannot forget to mention fusion power. In the long term there are only three possible ways to satisfy the energy needs of mankind: solar energy, proton driven reactors and fusion. New fission reactors and future fusion power are being developed based on technologies of existing accelerators.

The number of accelerators in the world has grown rapidly in the past years. Nowadays there are a great number of accelerators being used for many purposes (Table 1-1), and only a few of them are used for high energy particle physics, which means that accelerator science is becoming more and more common in our lives.

Table 1-1. Number of accelerators in the world (W. Maciszewski and W. Scharf, 2004)

CATEGORY	NUMBER IN USE
High Energy accelerators (E >1GeV)	~120
Synchrotron radiation sources	>100
Medical radioisotope production	~200
Radiotherapy accelerators	>7500
Research acc. included biomedical research	~1000
Acc. for industrial processing and research	~1500
Ion implanters, surface modification	>7000
TOTAL	>17500

1.3.2 History of accelerators

Not long time ago the simplest version of a particle acceleration could be found in the cathode ray tube of every conventional television. This ancestor of the modern particles accelerators was developed by J.Thomson in 1897 in order to measure the relation charge/mass of the electron.

At the beginning of the 20th century a few steady electric field accelerators were developed. Briefly, the easiest way of accelerating a charged particle is by putting it in a steady electric field. The particle will start moving along the electric field following the Lorentz force (1.1). Static magnetic fields are unable to accelerate particles, as the Lorentz force is perpendicular to the particle speed.

$$\vec{F} = q\,(\vec{E} + \vec{v} \times \vec{B}) \tag{1.1}$$

The ***Cockcroft-Walton*** accelerator was built in 1930 (Figure 1-5) by John Cockcroft and Ernest Walton. They managed to increase protons energy up to several hundreds of keV in order to explore the nuclei structure by producing the collision of these accelerated protons against a lithium target.

Figure 1-5. Example of Cockcroft-Walton accelerator at CERN

The Cockroft-Walton accelerator worked with a series of stages of diodes and capacitors fed by an alternating voltage which charged the capacitors until a multiplication of voltage was obtained in the final stage. These accelerators are sometimes still used as the starting point of present day accelerators, as they can deliver high current beams.

The voltage of the electrostatic accelerators was shortly increased by ***Van de Graaff*** (Figure 1-6) as a result of charging a metallic sphere using electrostatic principles (Figure 1-7).

Figure 1-6. Van de Graaf accelerator (© Museum of Science, Boston)

He used a rolling dielectric belt charged by brushing a metallic comb connected to a small DC voltage source. The charge was displaced to a big metallic sphere by the belt and collected by another metallic comb. The maximum charge of the sphere depends on its dimension, and so depends the maximum voltage to ground. This generator could reach several MV if immersed in a dielectric pressurized gas to improve breakdown behaviour.

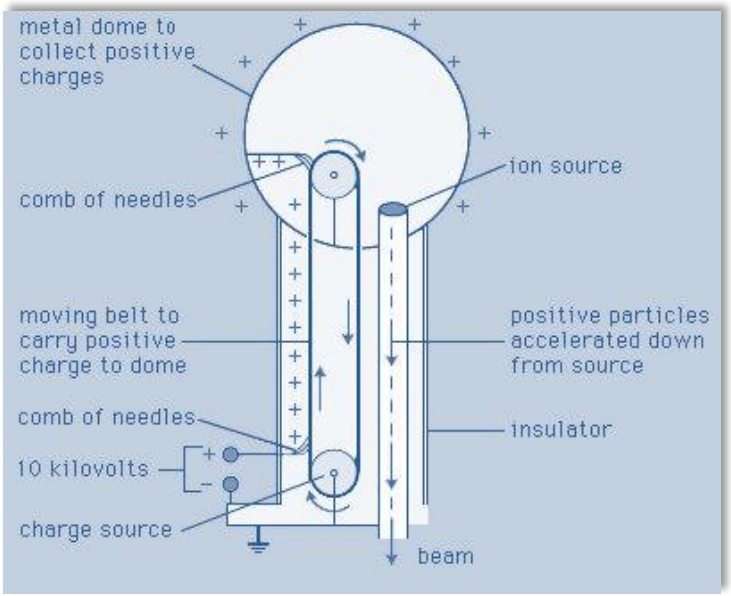

Figure 1-7. Van de Graaff electrostatic accelerator (© Encyclopaedia Britannica)

The voltage limitation of electrostatic generators pushed the scientists to develop new methods for accelerating particles. A straightforward way of increasing the particle energy can be achieved by passing several times by the accelerating structure. But this is theoretically impossible by using DC fields (conservative), as the particles must lose the same energy when re-entering the structure as they gain when exiting it. In 1924, Gustav Ising proposed the first accelerator that used time-dependent fields. This new idea used the Faraday's Law for acceleration, which basically says that a time varying magnetic field creates an electric field rotating perpendicularly around the original magnetic field (1.2).

$$\vec{\nabla} \times \vec{E} = -\frac{\partial \vec{B}}{\partial t} \tag{1.2}$$

It can also be said that an azimuthally time varying magnetic field induces an electric field in the axis of rotation of the magnetic field (Figure 1-8). Those fields encapsulated in a cylindrical cavity can resonate and this is the basis of the acceleration method with time-dependant fields.

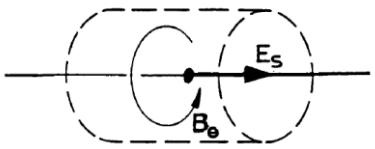

Figure 1-8. Faraday's law

The first RF linear accelerator [16] was conceived and demonstrated experimentally by Rolf Wideröe in 1927 following the concept proposed by Ising. In his experiment, an RF voltage of 25 kV from a 1 MHz oscillator was applied to a single drift tube between two grounded electrodes, and a beam of 50 keV potassium and sodium ions was measured, which is twice that obtainable from a single application of the applied voltage.

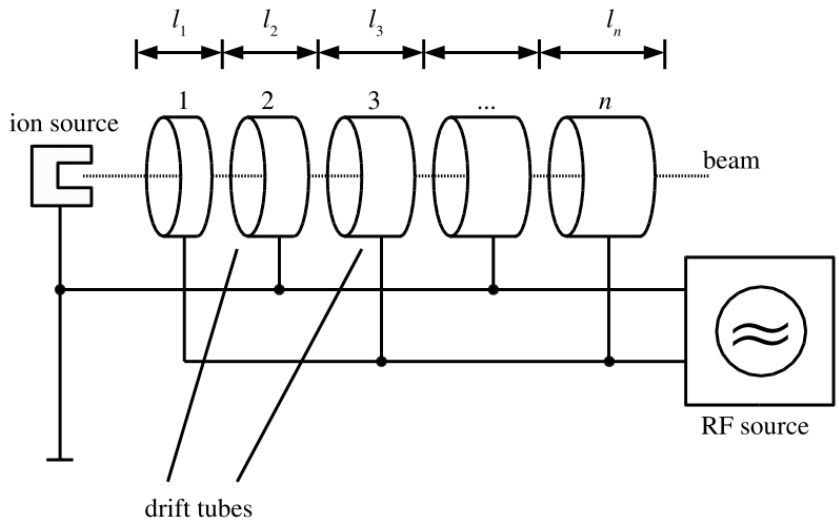

Figure 1-9. Acceleration scheme proposed by Wideröe (Drawn by Florian Nolz)

The original Wideröe linac concept was not suitable for acceleration to high energies of beams of lighter protons and electrons, which was of greater interest for fundamental physics research. These beam velocities *v* are much larger, approaching the speed of light, and the drift-tube lengths and distances between accelerating gaps L_{AB} (1.3) would be impractically large, unless the frequency *f* could be increased to near 1GHz. In this frequency range the wavelengths are comparable to the ac circuit dimensions, and electromagnetic-wave propagation and electromagnetic radiation effects must be included for a practical accelerator system.

$$L_{AB} = \frac{v}{2f} \tag{1.3}$$

Thus, linac development required higher-power microwave generators, and accelerating structures better adapted for high frequencies and for acceleration requirements of high-velocity beams. High-frequency power generators, developed for radar applications, became available after World War II.

In parallel with these events other application of the radiofrequency acceleration was conceived by Ernest Lawrence in 1929, but using a totally different approach. He thought about using the RF power several times by spinning particles and passing them repeatedly through the RF structures. He had been invented the ***cyclotron*** (Figure 1-10).

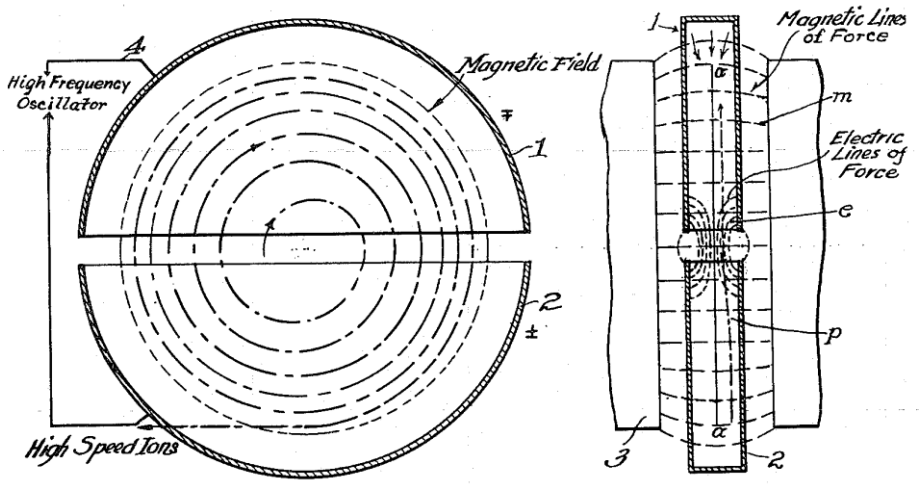

Figure 1-10. Lawrence's cyclotron layout from his 1934 patent

The cyclotron is a metallic cylindrical pill-box split in two parts ("dees") with a gap between them. The source of particles is in the axis centre and there is a perpendicular magnetic field through the flat sides of the pill-box. When a charged particle moves in a perpendicular magnetic field, the Lorentz force (1.1) makes it spinning around an equilibrium radius where centrifugal and Lorentz forces are equal. The particle is only accelerated in the gap where its trajectory is tangent to the electric field. Thanks to the increased velocity, the spinning radius grows after passing through the gap. Finally, the trajectory resembles a spiral and the revolution frequency is constant while the particles mass remains almost constant (no relativistic regime). M. Livingston demonstrated this principle in 1931 by accelerating hydrogen ions to 80 keV.

However, the cyclotron was limited by relativistic effects because of the mass increase at velocities close to that of the light. The ***synchrocyclotron*** was developed to adjust the RF frequency to keep the synchronism as the mass grows.

It is also possible [17] to take advantage of Faraday's law (1.2) if the beam encircles a time varying magnetic field (Figure 1-11). This acceleration mechanism, known as ***betatron*** acceleration, was proposed by Wideröe.

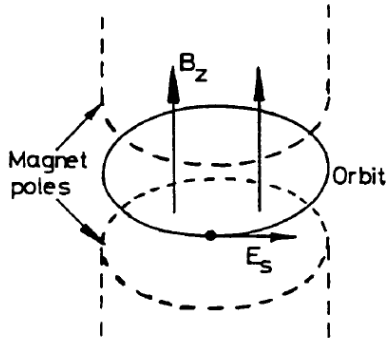

Figure 1-11. Betatron acceleration

As the magnetic field increases, the particle is accelerated by the tangential electric field created by the Faraday's law and its trajectory is curved by the own magnetic field. Evidently, if the magnetic field decreases, the particles are decelerated. The betatron, is insensitive to relativistic effects and was therefore ideal for acceleration of the electrons. It was built by D. W. Kerst many years after Wideröe's proposal, although the development of this kind of machines for high-energy physics was short, ending in 1950 when Kerst built the world's largest betatron (300 MeV).

However, the betatron was very important in the development of future accelerators. In fact, in a present synchrotron, the transverse oscillation of the particles about the equilibrium orbit is called the "betatron oscillation" due to historical reasons. This effect should be taken into account for the accurate description of particles motion.

All the acceleration mechanisms presented so far lacked one of the most important topics for fruitful acceleration: the strong focusing for beam stability. The particle beam is unstable itself due to several reasons related to its longitudinal and transverse movement: RF acceleration, natural electric repulsion between particles in the beam, gravitation effects, etc.

The ***synchrotron*** principle seems to have been originally proposed in 1943 by Mark Oliphant. But were V.I. Veksler and Edwin M. McMillan who suggested when they studied the principle of phase stability (independently), an accelerator with varying magnetic field. Phase stability

means that a bunch[1] of particles can be kept bunched during the acceleration cycle by simply injecting them at a suitable phase of the RF cycle.

The synchrotron (Figure 1-12) accelerates particles in a constant radius orbit by increasing the guiding field as in the betatron but using RF voltage gaps for acceleration. The guiding field is given by independent magnets around the orbit (Figure 1-13) and the RF acceleration is composed of several RF cavities in a small zone of the orbit.

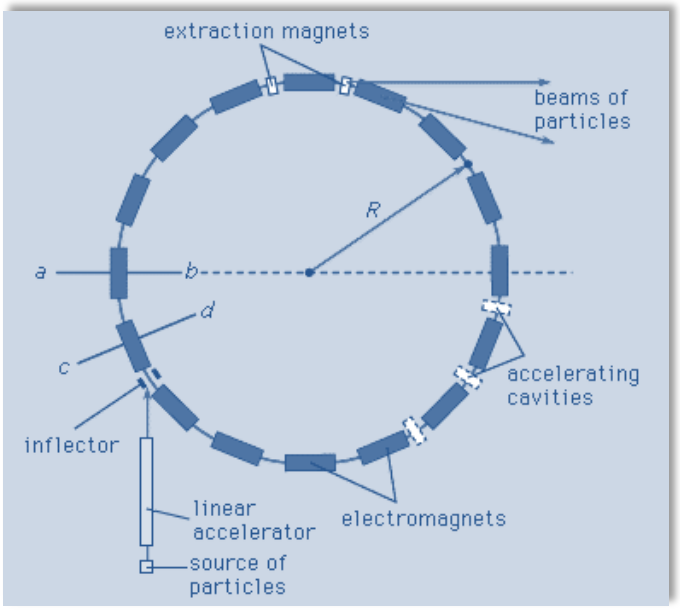

Figure 1-12 .Synchrotron schematic diagram (© Encyclopaedia Britannica)

In 1946 F. Goward and D. Barnes were the first to make a synchrotron work, and in 1947 M. Oliphant, J. Gooden and G. Hyde proposed the first proton synchrotron for 1 GeV in Birmingham.

When the synchrotron was invented, only weak focusing mechanism was known in the transverse plane. Weak (or constant-gradient focusing) is produced by the guiding magnets.

In 1952, E. Courant, M. Livingston and H. Snyder proposed strong focusing, also known as alternating-gradient focusing. This principle comes from geometrical optics, where the combined series of focusing and defocusing lenses have a net focusing effect (positive overall focal length), provided the distances between lenses are correct. Since then, the strong-focusing principle revolutionized the accelerators design. The first synchrotron to use strong focusing was the Alternating Gradient Synchrotron (AGS), built in 1957 in Brookhaven National

[1] *Particles are grouped in small discrete groups called bunches.*
This is needed for stable acceleration in RF structures.

Laboratory. The beam was focused by the pole-tips of the bending magnets (Figure 1-13). Tips with cross section *cd* focused the beam in the radial direction, while tips with cross section *ab* focused in the vertical direction.

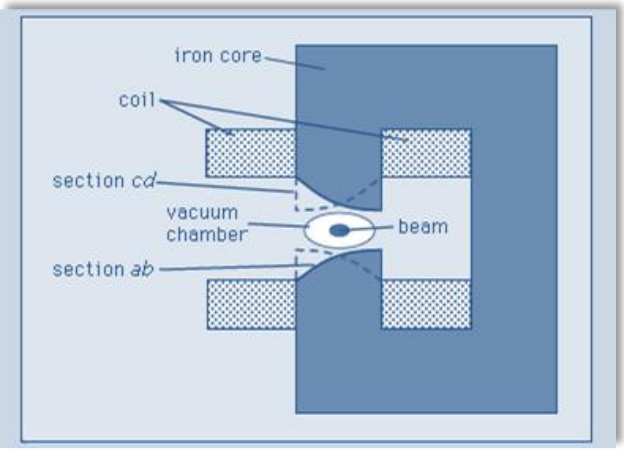

Figure 1-13. Strong or alternating-gradient focusing (© Encyclopaedia Britannica)

Present accelerators use different magnets for bending and for focusing. The alternating gradient is created by quadrupole magnets placed alternatively to focus in vertical and horizontal planes. The quadrupoles which focus in vertical also defocus in horizontal and vice versa. This pattern is called FODO (Figure 1-14), where QF focuses vertically and defocuses horizontally, QD focuses horizontally and defocuses vertically. The space between two vertically focusing quadrupoles is called a FODO cell, and a particle returns to the same position after a given number of cells (depending on the phase advance per cell). The oscillations of the particles around the equilibrium orbit are the betatron oscillations mentioned before.

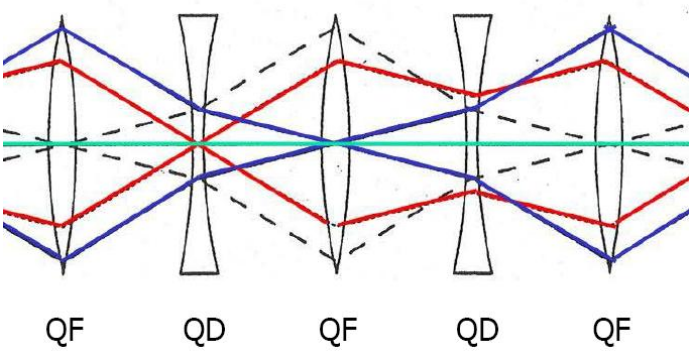

Figure 1-14. FODO pattern to align the quadrupoles (from CAS 2006. D. Brandt)

To increase the energy of the collisions even more, the synchrotron machine was the origin of the ***storage ring colliders*** (Figure 1-15). Instead of accelerating the particles in turn by turn and then colliding with a fixed target, two beams rotating clockwise and anti-clockwise were "stored" in a double synchrotron ring and then collided one against the other. A head-on collision between two particles has the combined energy of both particles, totally different as when the target is fixed, where only a fraction of the energy is liberated.

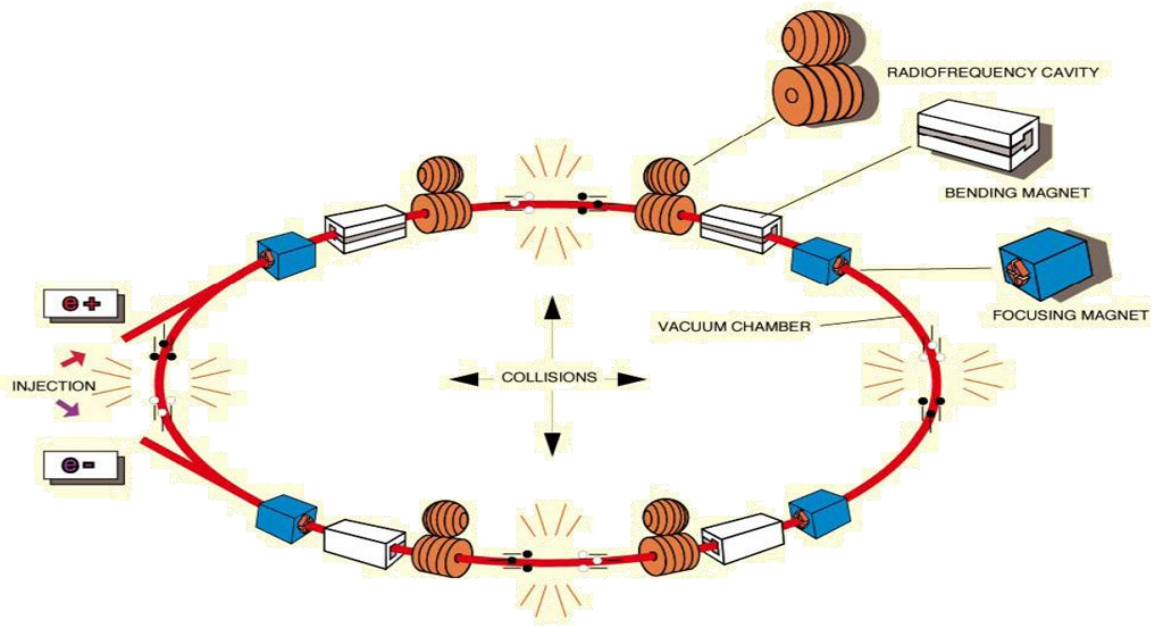

Figure 1-15. Storage ring collider (© CERN)

Storage ring colliders are presently the most used high energy physics accelerators. They are the preferred method of accelerating and colliding heavy particles as hadrons, where the synchrotron radiation lost on each turn can be easily compensated by RF accelerating structures.

On the other hand, the applied superconductivity has produced an enormous improvement in the accelerators field allowing higher energies with not very large machine sizes. The magnets have less power consumption and superconductivity allows much higher current density in their coils, which increases the bending and focusing power of these devices without increasing the size. However, the magnets become more complicated as cryogenic facilities are required in order to maintain the low temperatures needed for the coils.

There have been other improvements and acceleration mechanisms along the history. For example, the Alvarez accelerator (proposed by L. Alvarez in 1946), well known as ***Drift Tube Linac*** (DTL) (Figure 1-16) has become very popular as an injector for large proton and heavy-

ion synchrotrons all over the world with energies in the range of 50–200 MeV. It is based on a linear array of drift tubes enclosed in a high-Q cylindrical cavity.

Figure 1-16. Drift Tube Linac (Drift tubes in a prototype for Linac4. CERN)

Other example is the invention of the Radio Frequency Quadrupole (RFQ) in 1970 by I. Kapchinski and V. Teplyakov which has replaced the Cockcroft-Walton as an injector at lower energies (Figure 1-17).

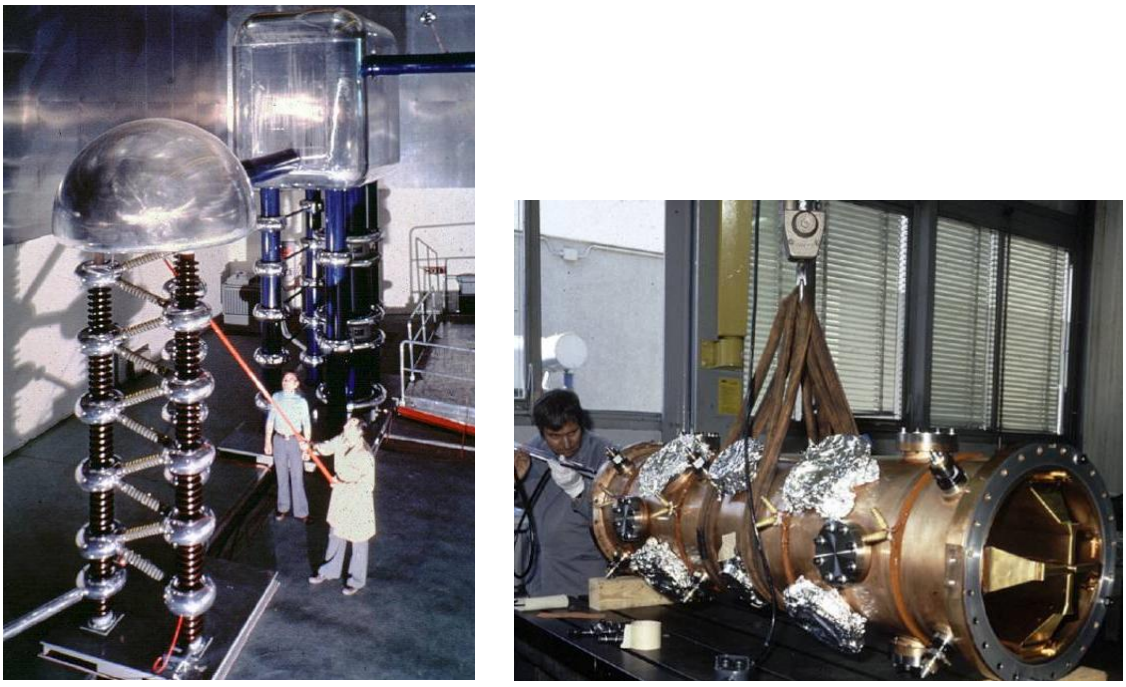

(a) (b)

Figure 1-17. Old pre-inyector 750 kV DC, CERN Linac 2 before 1990 (a). The Cockroft-Walton was substituted by this RFQ in Linac 2 after 1990 (b)

1.3.3 Typical components in a particle accelerator

This section is not intended to be a detailed report on modern accelerator components, but a brief introduction of diverse devices in an accelerator.

1.3.3.1 Particle sources

Every accelerator needs a source of charged particles to accelerate, because it is not possible to accelerate neutral particles using electric fields. Those particles can be electrons, protons or ions (or even charged antiparticles). Particle sources are basically divided in ***electron sources*** and ***ion sources*** [18].

ELECTRON SOURCES

One way of generating electrons from a material is by using the thermionic emission. When a material is heated, an electron cloud appears around the material. A simple electric field is then capable of extracting the electrons.

ION SOURCES

There are a lot of methods for extracting ions from materials. All of them require an "ion production" region (usually a plasma) and an "ion extraction" system. The main goal of an ion source is producing the required ion type and pulse parameters also maximizing reliability, beam quality and reducing material consumption.

1.3.3.2 RF cavities

There are plenty of methods to increase energy of particles in an accelerator. Several of them have already been explained in the previous section. However, in modern accelerators, RF cavities are commonly used for that purpose. They are needed not only to increase the energy of particles but also to compensate the energy losses in storage rings due to synchrotron radiation.

RF cavities (see Figure 1-18) are the preferred means of accelerating particles. Typically cavities are a few tens of centimetres in length whose frequency is set such that it gives particles an accelerating push as they pass through.

Figure 1-18 . LEP SC cavity (CERN-PHOTO-8004579X)

1.3.3.3 Beam guiding and focusing devices

To reach higher energies in linear accelerators, a high accelerating field or a long accelerator is needed, because particles run through the accelerating cavities only once. On the other hand, circular accelerators repeat the acceleration process on every turn and therefore they do not need so much acceleration power. However, circular accelerators need the particles to rotate around a closed orbit. The bending magnets which guide the particles through the orbit are dipoles and, in modern accelerators, they are independent of other focusing devices.

Dipoles create a uniform field in a volume inside their aperture (the space where particles pass through). The uniform field perpendicular to the trajectory of the particles makes them to bend around an orbit of a radius that depends on (1.4), where ρ is the radius of curvature, p is the momentum of the particle, q is the particle charge and B_0 is the dipole field.

$$\rho = \frac{p}{qB_0} \tag{1.4}$$

Nevertheless, magnets are not only necessary to bend the beam in a circular accelerator, but are also compulsory to focus the beam and to keep it stable. As shown in previous section the beam is focused using quadrupole magnets (Figure 1-19).

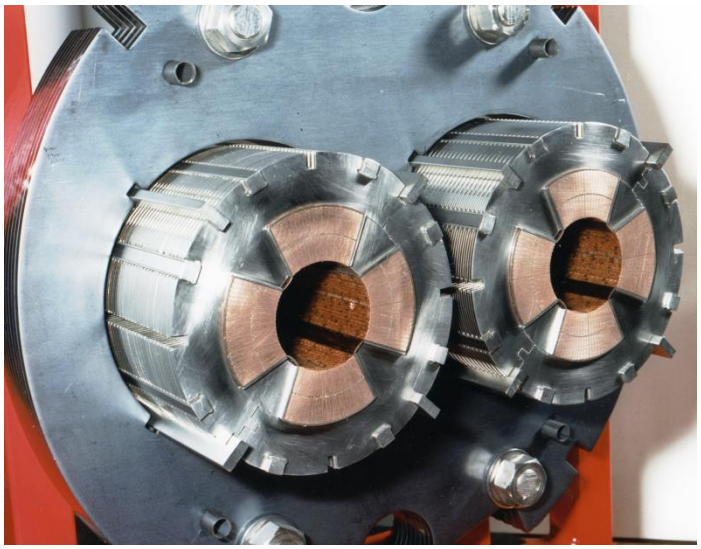

Figure 1-19. Superconducting quadrupole magnets for LHC at CERN[2]

Particles with different momentum are focused with different strength by the quadrupoles, leading to beam instability. This kind of error is described by the chromaticity, and it is corrected by higher order magnets called sextupoles, whose focusing effect is proportional to the momentum deviation of the particle. There are also even higher order magnets to fine tune the errors introduced by sextupoles (octupoles, dodecapoles, etc.).

1.3.3.4 Injection and extraction devices

Injection and extraction devices are needed to transfer the beam from its orbit (like a circular orbit in a synchrotron) to another ring or path, and vice-versa. They are installed in series with the beam pipe and they usually work by giving a fast transverse impulse to the beam (the EM field is on just during the necessary time to produce the kick), deflecting it from its original trajectory. However, special magnets called septa (septum in singular) can also be used individually for extraction.

[2] *http://irfu.cea.fr/en/Phocea/Vie_des_labos/Ast/ast_visu.php?id_ast=2411*

1.3.3.5 Diagnostics

The purpose of a beam diagnostic system is to obtain information of the behaviour of the beam in an accelerator. Beam diagnostics devices are particularly important when new machines are commissioned or at start-up after a long shutdown. However, also during routine machine operation, it is the beam measurements that tell the operator if the machine is performing correctly or not, and help to find errors in the accelerator components.

Most sensors are based on one of the following physical processes [19]:

- Interaction of the beam particles with electric or magnetic fields.
    - Coupling to the magnetic or electric field
    - Synchrotron radiation
- Coulomb interaction between the incident beam particle and electrons in the atomic shell of intercepting matter.
- Atomic excitation with consecutive light emission.

Table 1-2 shows the devices used to measure different beam properties and their effect on the beam.

Table 1-2. Diagnostic devices and measured beam properties [19]

Instrument	Physical Effect	Measured Quantity	Effect on beam
Faraday Cup	Charge collection	Intensity	Destructive
Current Transformer	Magnetic field	Intensity	Non destructive
Wall current monitor	Image Current	Intensity Longitudinal beam shape	Non destructive
Pick-up	Electric/magnetic field	Position	Non destructive
Secondary emission monitor	Secondary electron emission	Transverse size/shape, emittance	Disturbing, can be destructive at low energies
Wire Scanner	Secondary particle creation	Transverse size/shape	Slightly disturbing
Scintillator screen	Atomic excitation with light emission	Transverse size/shape (position)	Destructive
Residual Gas monitor	Ionization	Transverse size/shape	Non destructive

1.4 Circular and race-track microtrons

V.I. Veksler, in his first paper on phase stability in 1944 proposed a modification of the cyclotron for electrons, which is now called ***the microtron*** [20]. This machine has a constant and homogeneous magnetic field and a constant accelerating RF voltage usually with wavelength $\lambda \sim 10$ cm. It is the microwave band that gives the name to this machine.

Because of the subject of this thesis is strongly connected with RTM we consider below in more details peculiarities of circular and race-track microtrons.

1.4.1 Circular Microtron

The electron trajectory in a classical microtron is a system of circles, increasing in diameter, with a common tangent point where the accelerating cavity is placed (see Figure 1-20).

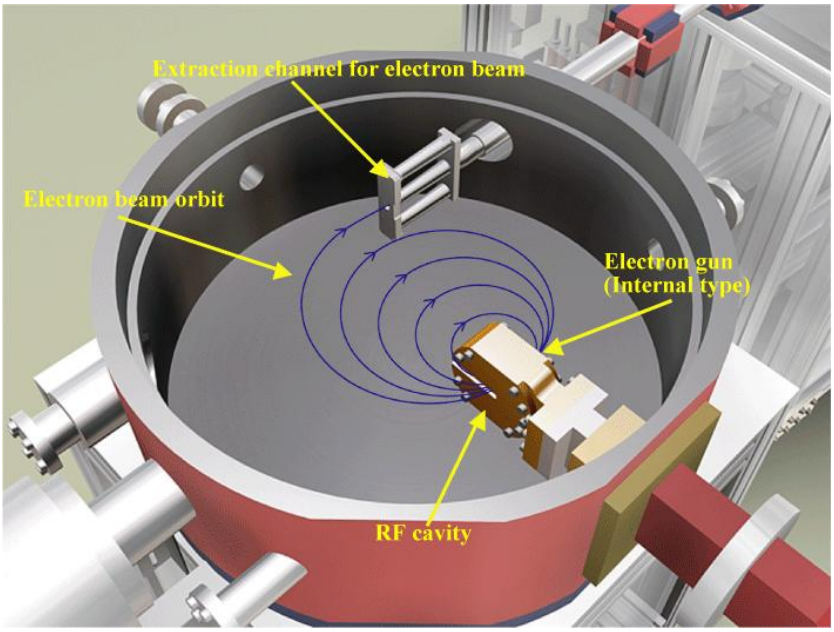

Figure 1-20. Circular Microtron from the Photon Production Laboratory, Ltd.

The revolution period of electrons in the microtron after *n* transits across the accelerating cavity is

$$T_n = \frac{2\pi E_n}{eBc^2} \tag{1.5}$$

Where E_n is the total electron energy at n_{th} revolution and *B* is the magnetic field. Thus, the time required to complete one revolution is proportional to the total energy of the particle and an increase in period from one revolution to the next ΔT is directly proportional to the energy gain ΔE as (1.6) shows.

$$\Delta T = \frac{2\pi \Delta E}{eBc^2} \tag{1.6}$$

If the energy gain per turn is adjusted to give an increase in period that is an integral multiple of the radio frequency or, in other words, if the time of revolution in each orbit is one or more periods longer than in the previous orbit, the particles will return to the accelerating cavity at the same phase for each turn. The time taken for the first turn T_1 must also be an integral number of cycles of the RF. These two conditions of synchronous motion of electrons at the microtron can be written as

$$\Delta E = \mu E_0, \qquad T_1 = \nu T_{\mathrm{RF}} \tag{1.7}$$

Where μ and *v* are integer numbers, T_{RF} is the period of accelerating voltage and $E_0=m_0c^2$ is the electron rest energy.

In modern circular microtrons the accelerating element is usually the cylindrical resonator which was proposed by S. Kapitza, V. Bykov and V. Melekhin [21]. The usage of such cavity led to a great increase in the efficiency of microtrons.

The circular microtron is usually a pulsed accelerator as it is necessary to feed the accelerating cavity with a rather high microwave power –about 300-400 kW- . Theoretically, microtron could be operated in CW regime, but the RF cavities would melt due to such high power. The classical microtron operates with a repetition rate of 100-1000 Hz and a pulse length of some microseconds. The average power of the accelerated beam is less than 1 kW and energy up to 30 MeV and average current of 20 – 30 μA can be obtained. The size and weight of the

microtron are comparatively small to other types of accelerators – the diameter of the magnet is about 1-1.5 m, and the weight ~ 1500 Kg.

1.4.2 Race-Track Microtron (RTM)

1.4.2.1 Brief history of RTM

In 1946, a few years after Veksler's original publication, the concept of a split or race-track microtron in which two uniform-field dc magnets with parallel edges are separated by a distance large compared to the magnet dimensions, and a linear accelerator placed in the common straight section, was suggested by Schwinger.

However there was a problem with a defocusing effect in crossing the fringing field of the two main bending magnets which was not solved until 1961 by the Canadian researchers Brannen and Froelich.

The development of standing wave linear accelerators (this subject will be explained in the next chapter) in the end of sixties permitted to obtain a higher final energy out of the machine.

1.4.2.2 Principles of operation

The RTM combines the linear accelerator properties with those of a circular machine. It is an optimum accelerator for electrons in applications where there is no need of high beam power but a relatively high energy of particles is required.

The RTM [20] in its more usual design (see Figure 1-21) consists of a couple of 180^{o} bending magnets facing each other and separated by a field free zone in which a linear standing wave accelerator is placed. The electrons, injected in the linac structure by means of an electron gun, are accelerated toward a magnet.

Acceleration takes place in a recirculating way, as the beam is turning around in the magnets and passing through the linac several times until the final energy is reached. This gives a compact design and a short accelerating section. Recirculating a high average power beam in

a small machine is not done without problems. If the beam, or part of it, is lost inside the accelerator, thermal drift problems or even damage may occur. Beam losses, must therefore be kept low in the accelerator structure which also must be efficiently cooled.

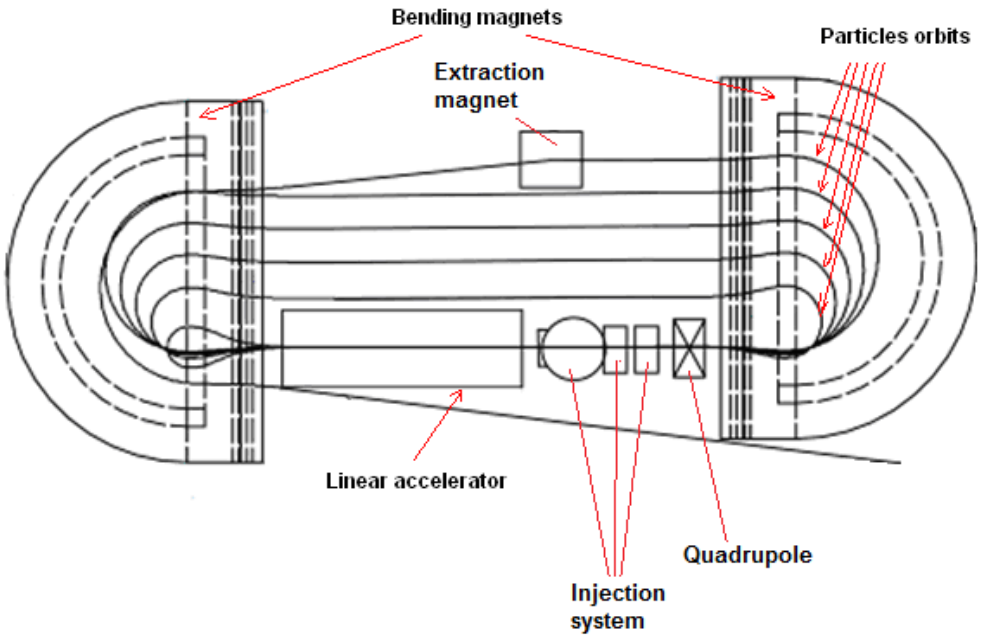

Figure 1-21. RTM layout

Let us assume electrons are injected into the linac with a total energy of

$$E_{inj} = mc^2 + eV_{inj} \tag{1.8}$$

Where eV_{inj} is the kinetic energy. On each pass through the linac they will gain an energy ΔE. To achieve resonance acceleration the same two conditions as for the circular microtron must be fulfilled:

- The revolution time of the first orbit T_1 must be an integral multiple, μ, of the period T_{RF}
- Each revolution time must exceed the preceding one in ΔT by an integral multiple, ν, of the RF period T_{RF}

Assuming electron velocity is equal to that of the light, *c*, in all orbits:

$$T_1 = \frac{2\mathrm{l}}{\mathrm{c}} + \frac{2\pi}{eBc^2}\left(mc^2 + eV_{inj} + \Delta E\right) = \mu T_{\mathrm{RF}} \tag{1.9}$$

$$\Delta \mathrm{T} = \mathrm{T_n} - \mathrm{T_{n-1}} = \frac{2\pi}{eBc^2}\Delta E = \nu T_{\mathrm{RF}} \tag{1.10}$$

Where *l* is the field-free distance between the magnets and *B* the strength of the homogeneous magnetic field. The two equations give the energy gain per turn and the magnetic field:

$$\Delta \mathrm{E} = \frac{\nu}{\mu - \nu - 2\,{}^{l}\!/_{\lambda}}(mc^2 + eV_{inj}) = \frac{\nu}{\mu - \nu - 2\,{}^{l}\!/_{\lambda}}E_{inj} \tag{1.11}$$

$$B = \frac{2\pi f}{ec^2}\frac{\Delta E}{\nu} \tag{1.12}$$

Where f= $1/T_{RF}$, and λ=c T_{RF}

The main conclusions to notice here are that the magnetic field in an RTM is proportional to the energy gain as in the circular microtron but that the denominator of (1.11) can be chosen at will. Therefore the energy gain per orbit and thus the magnet field are in the hands of the designer because they can be chosen almost independently from the injection energy. As magnets can be made up to about 1.6 T, microtrons can be constructed with energy gain per turn of the order of 10 MeV in the fundamental mode which is ν=1.

The maximum tolerable magnetic field variation depends on the largest allowed orbit length deviation and is usually between 10^{-3} – 10^{-4}. So the requirements which the magnetic field must obey are stringent in terms of uniformity but nowadays a great degree of precision in the magnet design can be reached by computer simulation.

The phase stability conditions in an RTM are the same as in a conventional circular microtron. Maximum width of phase stability region is about 32^0, which on one hand limits attainable beam current and on the other hand provides low energy spread of accelerated beam. Because of electron beam never reaches speed of light, as it is supposed in equation (1.9), essential phase slip of the accelerated beam with respect to synchronous phase takes place at the first few RTM orbits. Additional phase slip takes place in the end magnets fringe field.

The end magnets fringe field also causes strong vertical plane defocusing - the beam is already slightly bent before passing the magnet edge, so that the fringe field region will be crossed at an oblique angle to the edge. To compensate this defocusing, an additional pole with reversed magnetic field is added at the end magnet entrance following original proposal [22].

In the radial plane there is no focusing, except in the linac electric fields unless extra focusing elements, like quadrupoles (Fig. 1-21), are inserted along the beam trajectories.

Beam is injected to RTM from the low energy electron gun (20-50 KeV) via special system of injection magnets (Fig. 1-21) and during the first linac passage acquires energy close to synchronous energy gain at subsequent orbits. A compact injection system can be built with on-linac-axis electron gun having central hole for beam passage and off-axis placed cathode [23].

Reverse magnetic field at the end magnets entrance changes beam path so that the distance between the trajectories and linac axis is decreased and beam after first acceleration cannot bypass linac. To resolve this problem beam is reflected back by specially optimized end magnet fringe field into the linac, is accelerated in opposite direction, and with doubled energy bypasses the linac as it is shown in Fig. 1-21.

In order to extract the beam in the same output position at the desired energy a magnet is placed at the proper orbit which deflects the beam by an angle so that during the reflection by the following magnet it overcomes the common axis and exits the machine (Fig. 1-21).

1.4.2.3 Summary of RTM characteristics

Some general remarks and advantages of RTM are[24] [25]:

- RTM are flexible concerning extraction energies. Beam is easy extractable from different orbits.
- CW operation is possible with long straight section.
- It is a very compact high energy accelerator in pulsed mode.
- Excellent beam quality (energy spread, emittance). Beam optics is well controllable: many variants of beam optics are possible.
- Injection is well controllable, different injection schemes can be used.
- Needs homogeneous bending magnet fields: $\Delta B/B \sim 10^{-3} - 10^{-4}$.

- RTMs in cascade are required to reach very high energies, in general:
  - $E_{Extraction}/E_{Injection} < 10$
- Optimal RTM design can be found for each energy in the range 10 –1000 MeV. Maximum energy is limited only by end magnets weight and horizontal emittance growth.

1.4.3 RTM applications

There are many potential applications for the RTM in the energy range 1-100 MeV. In the Table 1-3 a summary of possible applications can be found [22], such as intraoperative and external radiation therapy, cargo inspection and defectoscopy, production of medical isotopes via photonuclear reactions, elemental analysis of substances, nuclear physics study and generation of electromagnetic radiation via different mechanisms in a small university laboratory, injection to synchrotrons and storage rings. Not all listed applications have been realised with RTM, but their feasibility was demonstrated at laboratories with different type of accelerators (betatron, circular microtron, linac). Because of these applications require modest beam power at relatively high energy, RTM is a well suited machine for their implementation.

Table 1-3. Potential RTM applications

Application	Energy range	Average beam current
Medicine, Intraoperative RT	6 MeV – 12 MeV	~1 μA
Medicine, External RT	4 MeV – 50 MeV	~100 μA
Cargo inspection, defectoscopy	2.5 MeV – 10 MeV	~10-100 μA
Elemental analysis	15-40 MeV	~10 μA
Explosive detection	30-70 MeV	~10-100 μA
Isotopes production (PET, I^{123}, etc)	15-30 MeV	~100 μA

1.4.3.1 Low energy nuclear physics

From the end of 1940 to end of 1960 nuclear physics was the main consumer of electron beams in the energy range of 10-100 MeV. The electromagnetic interacting particles (photons, electrons) are the most effective probes of nuclear structure. Betatrons, synchrotrons and pulsed linear accelerators were used in most experiments.

The best beam for nuclear physics would be a continuous beam (duty factor of accelerator *D=1*): that would mean low loads of detectors by background radiation, short time of experiment, high statistic, high energy resolution, possibility of coincidence experiments. However, when such beams appeared, mainly due to the success in RF superconductivity development, nuclear physics went to higher energies, well above 100 MeV, leaving behind many unresolved problems such as e.g. fine structure of the photonuclear reactions in the region of giant dipole resonance. Nevertheless, pulsed RTMs with energy below 100 MeV still can be used to get new knowledge about nuclei structure. An example is the study of multineutron nuclei photo disintegration being conducted at SINP RTM [26].

1.4.3.2 Injectors

Many microtrons are used as injectors for synchrotrons which in turn are used as injectors to storage rings which produce synchrotron radiation widely used in many fields as physics, chemistry, biology, etc. An example of an RTM type injector [27] is shown in Fig. 1-22.

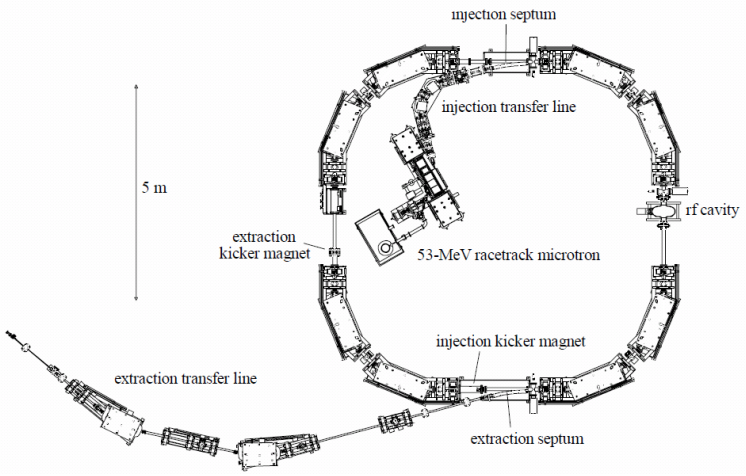

Figure 1-22. ANKA injector (from L. Praestegaard thesis. University of Aarhus, Denmark. 2001)

1.4.3.3 Radiotherapy

Radiotherapy consists of the use of ionizing radiation to kill tumour cells by destroying DNA via complicated physical, chemical and biological processes. However, together with tumour cells, normal cells on the way of radiation are also killed. Therefore, special tactics of irradiation should be implemented: irradiation from several sides, using special collimators, IORT, etc. RTM can be used for the listed below types of radiation therapy.

EXTERNAL X-RAY RADIATION THERAPY

It consists of irradiation by bremsstrahlung radiation produced by a 1-25 MeV electron beam which collides with a special target.

EXTERNAL ELECTRON RADIATION THERAPY

It consists of an irradiation by 25 – 50 MeV electron beam scattered by foil via a special applicator.

INTRAOPERATIVE RADIATION THERAPY (IORT)

This is a special radio therapeutic technique that delivers in a single session a radiation dose of the order of 10-20 Gy to a surgically exposed internal organ, tumour or tumour bed. This technique is most effective when conducted with a miniature dedicated electron accelerator with energy variable in the range 4-12 MeV, fixed at a robotic arm.

An example of an RTM specially designed and used for external photon and electron beam radiation therapy is the 50 MeV Scanditronix machine MM-50 [28]. The C-band linac described in this thesis will be used in a 12 MeV RTM dedicated to IORT [7].

1.4.3.4 Elemental analysis

The photo activation technique (Figure 1-23) is the method of elemental analysis which consists of the determination of sample elemental composition using photonuclear reactions. Nuclei level structure is unique fingerprints permitting to detect specific elements in very low quantities. The photoactivation technique consists mainly of the next steps.

1. Electron beam energy is converted to bremsstrahlung X-rays.

2. The sample is irradiated by X-rays and one or more nucleons are knocked out depending on beam energy and elements.
3. Residual nucleus can appear in isomeric state with decay time constant >> seconds and emit gamma-rays or can decay via beta decay or electron conversion with final nuclei being in excited state and emitting gamma-rays.
4. A high resolution Ge detector is used to measure sample gamma rays after irradiation.
5. To define quantitatively different elements content reference material with known composition is irradiated together with sample.

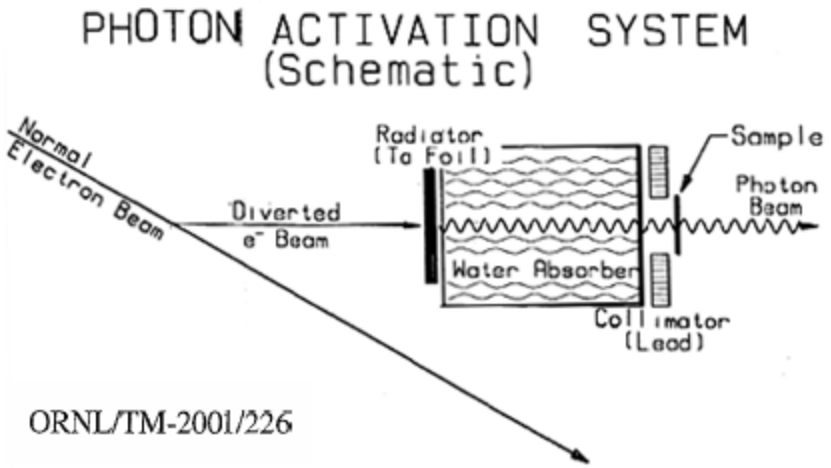

Figure 1-23. Photo activation technique (ORNL/TM 2001/226)

The use of RTM for photoactivation elemental analysis is described in [29]

1.4.3.5 Medical Isotopes Production

Accelerated particles [30], when directed onto a target material, may cause nuclear reactions that result in the formation of radionuclides in a similar manner to neutron activation in a reactor. A major difference is that the heavy particles such as proton, deuteron or helium must have high energies, typically 10-20 MeV, to penetrate the repulsive coulomb forces surrounding the nucleus, while bremsstrahlung X-rays must have maximum energy 20-30 MeV above the maximum of the nuclei photodisintegration cross section. The cyclotron is the most widely used type of particle accelerator for production of medically important radionuclides, although recent designs of compact linear accelerators also look promising.

The list of radioactive isotopes used in medicine [25] for treatment and for producing images includes more than 100 nuclei with life time from several years, e.g. ^{60}Co, to several seconds, e.g. ^{191m}Ir. An important step of isotopes production with cyclotrons is radiochemistry, which consists of the extraction of radioactive isotopes from irradiated target.

Photonuclear reactions are not widely used in medical practice for isotope production, though several remarkable examples can be found in literature, e.g. ^{123}I production at industrial scale with circular microtron [31].

In case of PET isotope [^{11}C(20.4 min), ^{13}N(10.0 min), ^{15}O(2.0 min), ^{18}F(109.8 min)] the photoneutron reaction is used, when knocking out neutron directly produces necessary isotope. Using a large volume target the total yield of isotope can be essentially higher than yield at cyclotron. But the main problem is to achieve high specific activity –required number of isotope nuclei per unit of prepared for injection pharmaceutical mass. In photoneutron reaction chemically the same element is produced, so radiochemistry cannot be applied. The way to get high specific activity is based on the collection of so called recoil nuclei. The nucleus after emission of neutron gets recoil, escapes from the target made as a fine powder, are picked-up by the gas stream and are deposited at absorbing filter. Possible application of this method with RTM as X-rays source is described at[32]

1.4.3.6 Cargo inspection

Cargo inspection goals are:

- Detection of contraband.
- Detection of fissile and radioactive materials.
- Detection of explosive and drugs.

Different approaches are necessary for each problem, but in all cases electron accelerators are used or can be used.

The cargo inspection system is composed of an electron accelerator with a bremsstrahlung target and an array of detectors. Such system, operating with electron beam energies of 3-9 MeV, permits to get container content image similar to the one shown in Figure 1-24. To discriminate materials according to atomic number (e.g. to detect fissile materials) the

container must be irradiated by two or more energies changed from pulse to pulse. The RTM offers a good possibility to change beam energy in a wide range by extracting beam from different orbits [33].

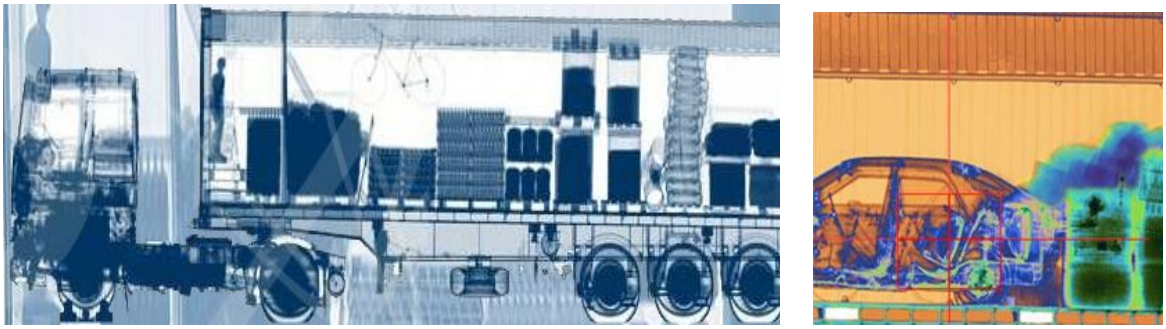

Figure 1-24. Typical images obtained during cargo inspection (from Heimann cargo vision)

RTM with beam energy switched in the range 25-70 MeV can also be used to build so called Nitrogen camera invented by Luis Alvarez [34] to detect explosives. A possible realization of this method is described in [35].

1.5 RTM parameters dependence on operating wavelength

Nearly every circular microtron and RTM built till now operates in the wavelength range 10-12 cm. A circular microtron with 5 MeV maximum energy was built in 3 cm band [36].

The choice of the operating frequency depends on many factors, including final beam energy, energy gain per turn, requirements to efficiency, to dimensions and weight, availability of RF sources and others - there is no universal solution for all cases. Let us consider the problem of the wavelength choice using as an example 12 MeV RTM for which linac described in this thesis has been developed.

Application of accelerator for IORT requires that the step with which output energy is changed at output must be about 2 MeV and accelerator must be as small and light as possible. The only way to built compact and light RTM which will be better than linac by the whole set of parameters is to use REPM (Rare Earth Permanent Magnet) material as the field source of the end magnets. Because of such end magnet field cannot be varied, the synchronous energy gain is fixed and equals ΔE_s =2 MeV, so RTM output energy is changed by beam extraction from different orbits.

The space taken by the orbits will be smaller if higher end magnet field is used. From (1.12) it follows that if ΔE_s =const, to get higher field a higher frequency (shorter wavelength) must be used. The so called "box" type design of the end magnet built with permanent magnet material [37], allows to reach as high field as B=1.8 T, which would mean operation at wavelength λ = 2.3 cm and the last orbit diameter of only 4.6 cm.

However, there are several factors which limit the choice of wavelength by longer values:

1) Magnetic field energy stored in the gap of the end magnet for fixed maximum RTM energy is nearly independent of field level if the gap height, *h*, is fixed. Really, stored energy $\sim\pi R^2 h B^2$, and pole radius $R \sim 1/B$. This means that the energy stored in the REPM material which produces the gap field, its volume and weight are also about independent of field level. On the other hand, neglecting steel saturation effects and field decay near the pole edges, the steel volume and weight should decrease at least

$\sim 1/R$ and so $\sim\lambda$ (the height of magnet must grow to accommodate constant volume of REPM material). More detailed calculations taking into account steel saturation effects and useful part of pole within which field uniformity is at acceptable level, show that below wavelength ~4.5 cm the whole magnet weight starts to grow with wavelength decrease. Thus, the wavelength ~5 cm can be considered as optimal to get minimal end magnet weight.

2) If accelerating structure dimensions are exactly scaled: When wavelength decreases, its effective shunt impedance[3] Z_{sh} increases as $\sqrt{\lambda^{-1}}$ which means a decrease of the linac length for fixed RF power or decrease of RF power for fixed length. Accelerating structure diameter decreases ~λ, so its weight decreases at least $\sim\lambda^2$. However, beam hole radius for RTM linac should be large enough to permit pass through of different orbit beams with minimal current losses. For a 4 mm beam hole radius it has been found that when λ decreases below 4 - 4.5 cm, Z_{sh} also decreases because of field penetration into the beam channel leads to transit time factor[4] decrease. Other factor which limits the choice of a shorter wavelength is that the RTM linac must provide effective capture in acceleration of non-relativistic beam after injection from the electron gun and effectively accelerate relativistic beam at subsequent orbits. For fixed accelerating gradient the shorter is wavelength, the less is particle energy gain per cell, the more cells with $\beta < 1$ are required to make particles relativistic. Linac with several $\beta < 1$ cells will non-effectively accelerate relativistic beam.

3) To extract beam from different RTM obits we must have enough space for installation of extraction magnet. Width of magnet must be approximately equal to distance between orbits, which in high energy limit approaches to value of $d = \lambda/\pi$, which is only about $d \approx 1.6$ cm at $\lambda = 5$ cm. Choosing shorter wavelength would make beam extraction problematic.

4) Lower RF power is necessary to feed the 12 MeV RTM, as compared with just 12 MeV linac, so < 1 MW RF power radar magnetron or klystron can be used, which are available in wide wavelength range. However, for other applications of this machine,

[3] *This parameter measures the acceleration efficiency of the accelerating structure. It will be explained in the next chapter*

[4] *Fraction of maximum voltage of accelerating cavity acquired by the particles when passing through the accelerating cavity. It will be explained in the next chapter as well.*

which could require higher beam current, higher RF power source will be necessary. For several C-band linac projects [38] high power magnetrons were developed at operating frequency 5712 MHz. Taking into account general tendencies of linear accelerators techniques development one would expect further appearance of RF sources at this frequency. Because of radar magnetrons and klystrons are also available at this frequency ***it has been finally chosen 5712 MHz ($\lambda \approx 5.25$ cm) as the operating frequency.***

1.6 12 MeV RTM specification

As it has been explained in section 1.2, this thesis is being developed within the framework of a 12 MeV RTM for IORT [7] which is under construction at the UPC.

The conceptual design of this IORT dedicated 12 MeV RTM is described in [39] and the accelerator schematic view is given in (Figure 1-25). The main features of this machine are:

- The use of the REPM material as the source of the bending magnetic field.
- The use of a short (~5.2 cm) wavelength compact linac fed by a radar magnetron or klystron.
- Placing the accelerator head in a single vacuum box (Figure 1-25b).

Using this approach a very compact RTM design can be obtained. Main parameters of this machine are presented in Table 1-4. The confirmation of the possibility to build an accelerator with parameters of (Table 1-4) is that there are two RTM, one goes up to 70 MeV [40] and another to 35 MeV [41]. Both have been built using REPM technology at SINP MSU (Moscow, Russia) in collaboration with World Physics Technologies Inc. (USA).

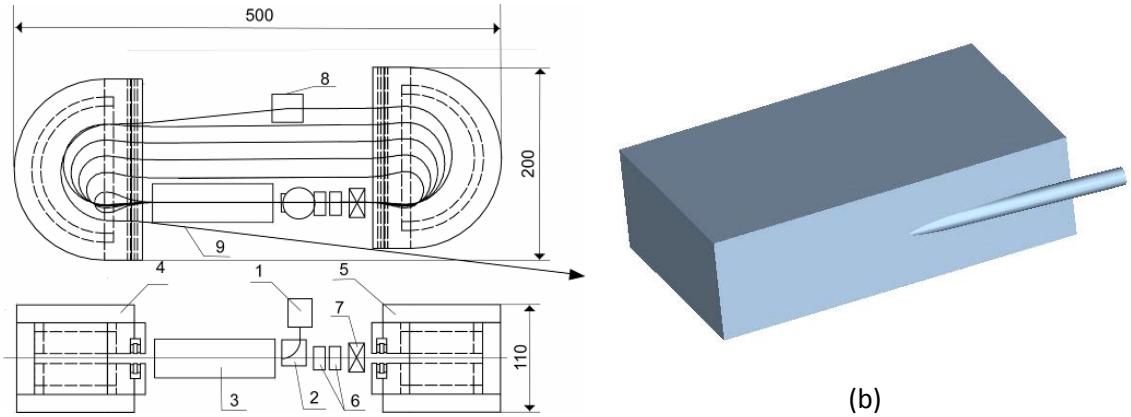

Figure 1-25. (a) RTM schematic (dimensions in mm), (1) – electron gun, (2) – injection magnet, (3) – linac, (4), (5) – end magnets, (6) – correcting dipoles, (7) – quadrupole, (8) – extraction magnet, (9) – extracted beam; (b) RTM head in the vacuum box.

Table 1-4. Main parameters of 12 MeV RTM.

Beam energies	6, 8, 10, 12 MeV
Operating wavelength	f = 5712 MHz (λ = 5.24847 cm)
End magnet field	0.8 T
Delivered dose rate	10-30 Gy/min
RTM dimensions	500x200x110 mm
RTM weight	< 40 kg
Synchronous energy gain	$\Delta E_s \approx 2$ MeV
Number of linac passages	6

A more detailed RTM scheme is shown in Figure 1-26 and choice of other parameters is explained below.

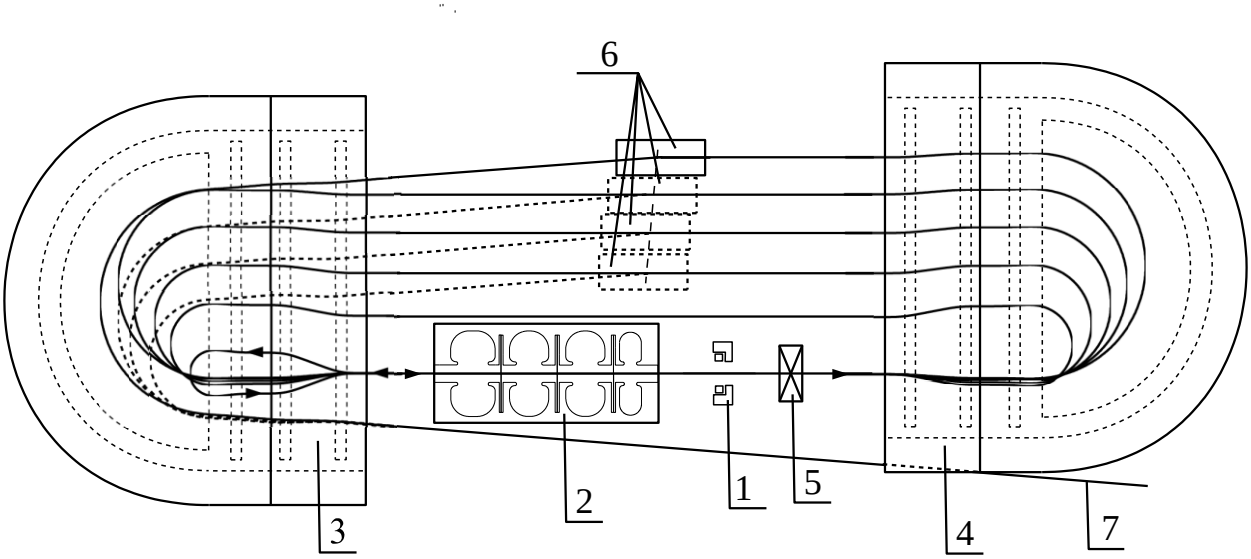

Figure 1-26. Preliminary RTM scheme. (1) – electron gun, (2) – linac, (3), (4) – end magnets M1 and M2, (5) - quadrupole lens, (6) – extraction magnets, (7) – extracted beam.

Absorbed dose about 10-20 Gy must be provided to irradiated tumour during 1-2 min by electron beam of our RTM, which means that several tens of nA average beam current is sufficient for IORT application. A typical radar magnetron or klystron has a duty factor 0.1%, which means several tens of μA of pulsed current. To have better beam current control and to widen the RTM potential applications we use the higher maximum pulsed current, up to I_{pulse}= 5 mA. To get necessary average current low duty factor (short pulse length and low repetition rate) will be used. For other applications, including external radiation therapy, by increasing

duty factor, the average beam current could be made as high as 5-10 μA or even more depending on RF source capability.

For a low final energy RTM (which is our case) the fringe field focusing exclusively can keep beam stable in vertical plane. Horizontal focusing in most simple way can be produced by quadrupole singlet placed at the common orbit ((5) at Figure 1-26).

Choice of beam injection scheme and injection energy depend on several factors. It must provide effective beam capture in acceleration and should not increase much RTM dimensions. The most compact design can be obtained with "3D" electron gun with off-axis cathode and on-axis beam hole [23], which is installed at common axis in front of linac ((1) at Figure 1-26). Since space charge does not play an essential role in our case due to low beam current, minimal injection energy for which good capture efficiency by linac can be achieved, about 25 keV, has been chosen. With this value it will be possible to feed electron gun from the same pulse modulator as the RF source.

The most suitable for IORT applications scheme of beam extraction is installation of dipole at appropriate orbit ((6) at Figure 1-26) which deflects beam for a small angle and directs it to the common for all orbits beam channel.

CHAPTER 2

Accelerating Structures: Theoretical Background

2.1 Basic microwave concepts

2.1.1 Introduction

The word *microwaves* refers to alternating current signals with frequencies between 300 MHz and 300 GHz [42], with a corresponding electrical wavelength between λ=1m to 1mm, respectively. Due to the high frequencies (and short wavelengths), standard circuit theory generally cannot be used directly to solve microwave network problems. The microwave engineering tries to reduce the complexity of the field theory solution, which gives usually much more information than we actually need for practical purposes, to a result that can be represented in terms of simpler circuit theory.

Transmission lines such as coaxial cables, cylindrical waveguides and micro strip lines are typically used for power transmission in microwave and radio frequency applications. Commonly, the coaxial cables are used in low power applications, the waveguides in high power applications, and the micro strip lines in integrated circuits. Since the lengths of the transmission lines are comparable to or longer than the wavelengths, transmission lines are considered as distributed-parameter networks, where the magnitude and the phase of the voltages and the currents vary along the lines. This admits wave propagations in transmission lines. Wave propagations in the transmission lines can be solved by equivalent circuit model.

Transmission lines and waveguides basically come in two broad types:

- Waveguides with a single closed conductor
- Transmission lines with two or more conductors

Using Maxwell's equations in a source free region filled with a homogeneous, linear and isotropic material (μ,ε), we have

$$\vec{\nabla} \times \vec{E} = -i\omega\mu\vec{H} \tag{2.1}$$

$$\vec{\nabla} \times \vec{H} = i\omega\varepsilon\vec{E} \tag{2.2}$$

where $\vec{E}$ and $\vec{H}$ are the spatial parts of the electric and the magnetic fields each with a common $e^{i\omega t}$ time dependence. Equations (2.1) and (2.2) can be combined to yield Helmholtz wave equations for the fields,

$$\vec{\nabla}^2\vec{Q} + k^2\vec{Q} = 0 \tag{2.3}$$

with $\vec{Q} = \vec{E}$ or $\vec{H}$ and $k = \omega\sqrt{\varepsilon\mu}$. Assuming the transmission lines (or waveguides) are uniform in the z-direction and the wave propagations along the z-direction ($e^{ik_z z}$) with propagation constant k_z, the fields can be expressed as the sum of the transverse (⊥) and the axial (z) field components,

$$\vec{E} = (\vec{e}_\perp + e_z\hat{z})e^{-ik_z z} \tag{2.4}$$

$$\vec{H} = (\vec{h}_\perp + h_z\hat{z})e^{-ik_z z} \tag{2.5}$$

Both the transverse and the axial fields are functions of the transverse coordinates. The transverse magnetic field is related to the transverse electric field by

$$\vec{h}_\perp = \sqrt{\frac{\varepsilon}{\mu}}\hat{z} \times \vec{e}_\perp \tag{2.6}$$

The actual forms of the electric and the magnetic field components are determined by the materials at the boundaries of the line or the guide. The boundary conditions at the interface of media 1 to media 2 are summarized as follows

$$\hat{n} \cdot (\vec{D}_2 - \vec{D}_1) = \rho_s \tag{2.7}$$

$$\hat{n} \cdot (\vec{B}_2 - \vec{B}_1) = 0 \tag{2.8}$$

$$(\vec{E}_2 - \vec{E}_1) \times \hat{n} = \vec{M}_s \tag{2.9}$$

$$(\vec{H}_2 - \vec{H}_1) \times \hat{n} = -\vec{J}_s \tag{2.10}$$

where ρ_s, $\vec{J}_S$ and $\vec{M}_S$ are the surface charge density, surface electric current and surface magnetic current, respectively, and $\hat{n}$ is the unit normal vector from medium 1 to medium 2. The quantities $\vec{D}$ and $\vec{B}$ are defined by the relations $\vec{D} = \varepsilon\vec{E}$ and $\vec{B} = \mu\vec{H}$ for linear media.

Many problems in microwave engineering involve boundaries with good conductors (e.g., metals), which can often be assumed as lossless (where the surface conductivity $\sigma_s \to \infty$). In this case of a perfect conductor, all field components must be zero inside the conducting region. If we also assume that $\vec{M}_S = 0$, which would be the case if the perfect conductor filled all the space on one side of the boundary, then

$$\hat{n} \times \vec{E} = 0 \quad \equiv \quad Electric\ wall \tag{2.11}$$

Such boundary is also known as an *electric wall*, where the tangential components of $\vec{E}$ vanish at the surface of the conductor as can be seen from (2.11).

Dual to the electric wall boundary condition is the *magnetic* wall boundary condition, where the tangential components of $\vec{H}$ must vanish. Such boundary does not really exist in practice, but may be approximated by a corrugated surface. In addition, the idealization that

$$\hat{n} \times \vec{H} = 0 \quad \equiv \quad Magnetic\ wall \tag{2.12}$$

In microwave and RF applications, the most common boundary conditions used are *electric* and *magnetic boundary conditions*. At an interface, or when some kind of symmetry exits, the use of electric or magnetic walls is often a convenient simplification that helps in accelerating structure calculations by computational procedures.

2.1.2 Waveguides and transmission lines

These are all well known devices in microwave engineering, and in the following lines just some basic results for the purpose of this thesis are included. For detail information, reference [42] should be consulted.

In accelerator applications, the *rectangular* (Figure 2-1a) and the *circular* (Figure 2-1b) *waveguides* are commonly used for high power transmissions between the power sources and the accelerating structures. This is because of their high power handling capability and low loss. On the other hand, *coaxial lines* are routinely used in low power applications as could be the probes for measuring fields in the accelerating cavities.

There are two basic types of propagating modes in the waveguides:

- TE (Transverse electric) modes
- TM (Transverse magnetic) modes

The TE modes are characterized by $e_z = 0$, while the TM modes by $h_z = 0$.

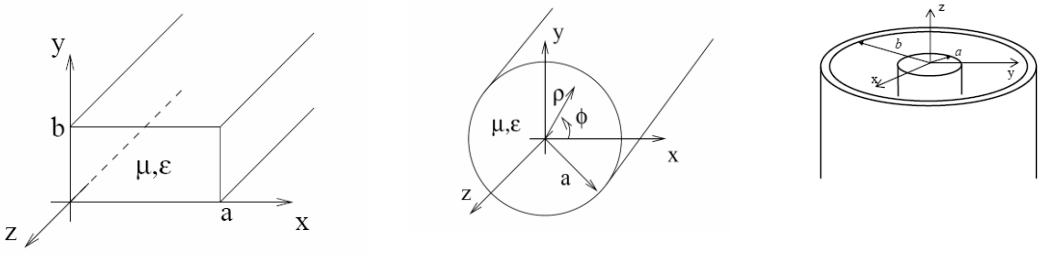

(a) (b) (c)

Figure 2-1. Rectangular waveguide (a), circular waveguide (b) and coaxial line (c)

In a waveguide, there is a *cut-off frequency* above which the propagation of an electromagnetic mode TE or TM is possible. This frequency depends on the geometry of the wave guide and on the particular mode.

- In a rectangular waveguide for $a > b$, the lowest propagating mode is TE_{10}.
- In a circular waveguide the lowest propagating mode is the TE_{11} mode, but in particle accelerators we are usually interested on the first TM mode, the TM_{01} which has the electric field along the axis [5] and is the basis of the travelling wave structures. These structures, as it will be explained later, consist of circular waveguides with a periodic array of iris inside.

[5] *In principle a circular waveguide could be used to accelerate particles, however the TM_{01} mode, which would be the ideal to accelerate particles because its E field is tangent to the beam path, has a phase velocity higher than the speed of light. A periodic array of iris is introduced in the travelling wave structures in order to reduce the phase velocity and be able to accelerate particles.*

- In a transmission line, as a coaxial line (Figure 2-1cFigure 2-1), TEM (Transverse Electro Magnetic) modes, characterized by $h_z = e_z = 0$, may exist (as well as TE and TM modes).

2.1.3 RF Cavities in accelerators

In most particle accelerators, apart from betatron and direct current machines, energy is provided by means of RF cavities (or resonant cavities). Since the beginning of accelerators, theory and technology of these devices has experienced an enormous development.

In linear accelerators, the accelerating structures typically have cylindrical symmetry. The simplest type of cavity with cylindrical symmetry is the *pill-box cavity*, which is basically a small section of a circular waveguide closed at both ends by a conductor.

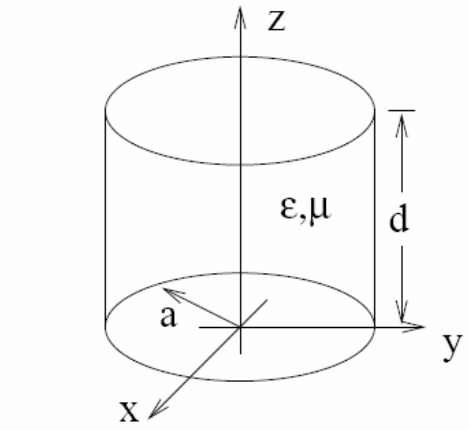

Figure 2-2. Pill-box cavity

The geometry of such a cavity is shown in Figure 2-2. The solution of the pill-box cavity is obtained from that of the circular waveguide by imposing additional boundary conditions at the closed ends [42]. The need for axial electric field (E_z) for beam acceleration means that only the TM_{nml} modes are of interest, where the indices n, m, and l are associated with the azimuthal, radial and axial degrees of freedom, respectively. The cavity modes are labelled as well as monopole (n = 0), dipole (n = 1), quadrupole (n = 2), *etc*., according to their degrees of azimuthal variation.

The first TM mode, while cavity radius a be bigger than the cavity length d, is the TM_{010} which has a resonant frequency (independent of d)

$$f_0 = 2.405\frac{c}{2\pi a} \tag{2.13}$$

Therefore, operation frequency should be chosen so this mode is the only one to appear and no other modes which could affect the particles trajectory are created in nearby frequency range. Besides TM_{010} mode has strong electric field along axis direction which is ideally suited for beam acceleration. Thus, the individual cells of accelerating structures usually operate in this mode.

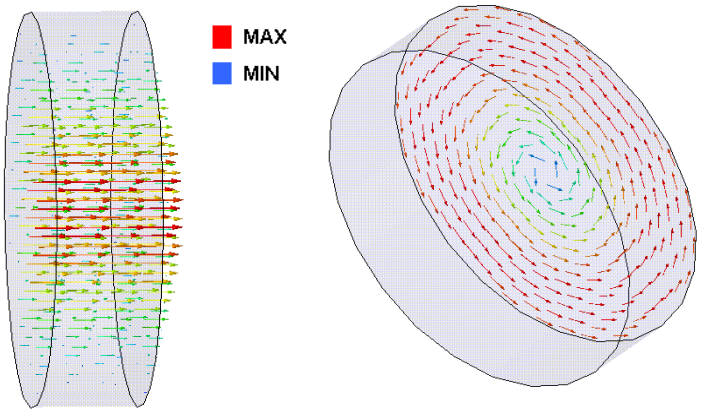

(a) (b)

Figure 2-3. (a) E field and (b) H field in pill-box cavity

In particle accelerators, pill-box cavities are no longer used because other improved cavities are used instead (Figure 2-4)

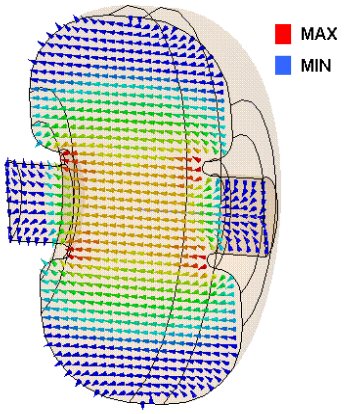

Figure 2-4. E field in a real cavity (nose cone type)

The most common and most efficient normal conducting cavities to accelerate electrons are the ones called *nose cones cavities* due to the pronounced shapes of the conductor around the beam pipe. The main differences with the pill-box cavity are summarized:

- A hole is needed along the axis in order to have a free path for the particles.
- The cones increase transit time factor and so increase the efficiency of RF power transforming into accelerating field.
- Smoother surfaces: Allow a better distribution of magnetic field and heat dissipation. Besides, the multipactor, which is a resonant avalanche discharge effect, is reduced.
- Better ratio of the cavity volume to cavity surface, thus higher quality factor which is proportional to energy stored in cavity (~volume) to RF power losses (~surface).

2.2 Travelling and standing wave accelerating structures for electron linacs

There are two basic types of linear accelerating structures:

- Travelling wave accelerating structures
- Standing wave accelerating structures

The electromagnetic wave in a *travelling wave structure* propagates down the structure and exit through an output coupler to an external load. In a *standing wave structure*, the electromagnetic wave enters the structure through an input coupler and reflects off the ends of the structure to form a standing wave pattern.

A diagram of both ways of acceleration [43] is shown in the following picture.

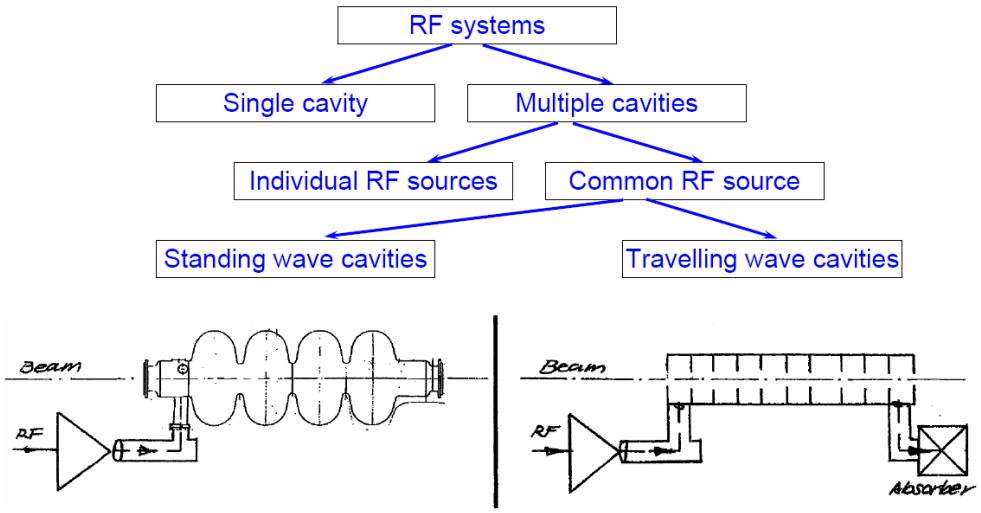

Figure 2-5. Standing and travelling wave cavities

2.2.1 Travelling wave structures

This type of structure consists of a circular waveguide into which metallic irises are inserted normal to the waveguide axis (Figure 2-6) at periodic intervals (disc loaded waveguide). The irises slow down phase velocity of the travelling wave to the velocity of electrons.

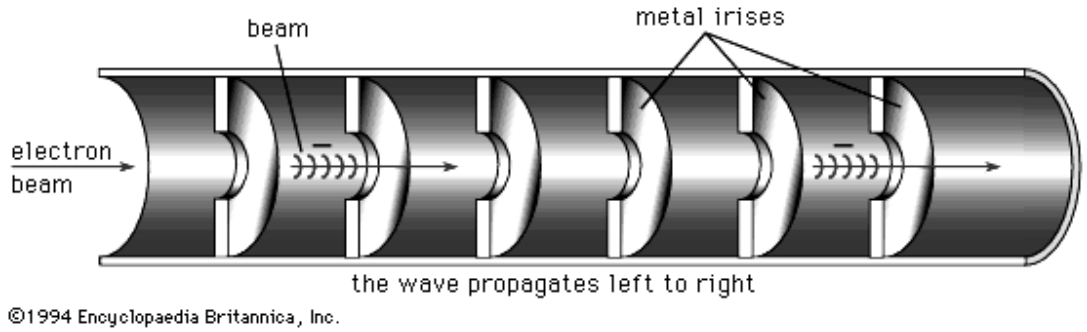

Figure 2-6. Travelling wave cavity with irises inside (© Encyclopaedia Britannica**)**

The particles travel together with the electromagnetic wave in a place where electric field is adequate for acceleration, like "a surfer" over a wave (Figure 2-7). The wave is finally absorbed by a load in the output port. Ideally no energy is wasted in the load if the beam absorbs all the power, however this would mean close to zero accelerating gradient at the end of structure, so some absorbed power is always available, which together with RF losses in waveguide walls, defines linac efficiency, which for high accelerated beam current can reach 70%.

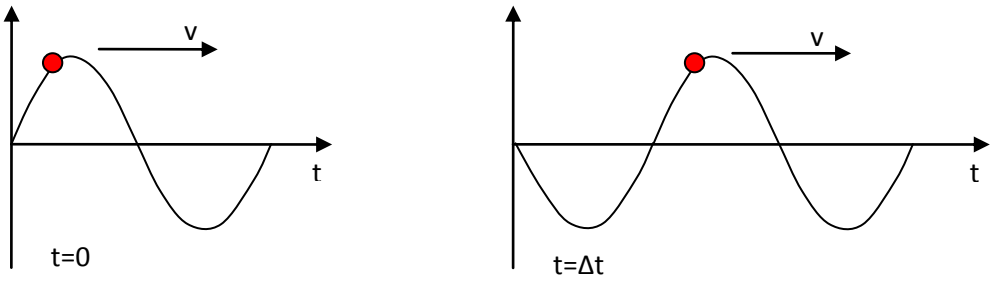

Figure 2-7. Particle travelling on the crest of a wave

Other characteristics of the travelling wave accelerating structure:

- Phase shift between cells is usually 2π/3.
- It is matched in a wide bandwidth, therefore, no circulator to protect the RF source from reflected wave is needed.
- At initial part of linac where low energy electrons from the gun are captured into acceleration, the focusing solenoid must be used to keep electrons in transverse direction, because of at the phase of optimal longitudinal beam focusing transverse defocusing by electromagnetic wave takes place.
- In general, it is preferable for high energy accelerators.

2.2.2 Standing wave structures

They are composed by various resonant cavities (cells) coupled in series and fed by a single RF source. Other way to describe these cavities is to visualize a travelling structure with metal walls at both sides to reflect the waves and create the standing wave pattern. Unlike travelling wave cavities, where the particles go with the wave, in the standing wave structures the particles "find" the E field in the right orientation to accelerate them every time they enter in a new cell or resonant cavity.

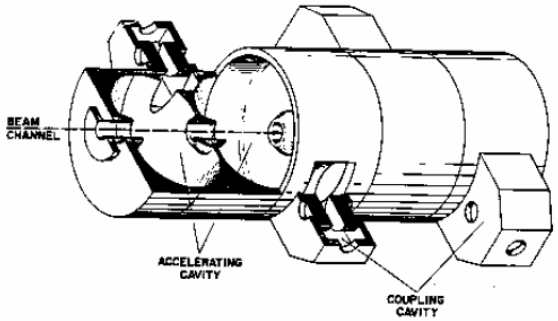

Figure 2-8. Standing Wave Structure (Sided coupled accelerating cavity from [16])

Other characteristics of the standing wave cavities:

- The most common phase shifts per cell are 0, $\pi/2$ or π.
- They have higher shunt impedance (acceleration capability) which means a shorter accelerator.
- At initial part of linac where low energy electrons from the gun are captured into acceleration beam focusing can be provided solely by electromagnetic field so focusing solenoid is unnecessary.
- High bunch charge can be accelerated using energy stored in accelerating structure.

2.3 Types of normal and superconducting standing wave accelerating structures

2.3.1 Normal Conducting Cavities

- The normal conducting cavities (NC) are usually made of copper, as this is a material which has an excellent conductivity/price ratio.
- They have extreme surfaces (as can be the cones in the nose cone structure) which are needed to minimize the power consumption given an electric field.
- Cooling is needed to keep the temperature constant, because, if temperature changes are allowed, expanding and mechanical deformations may happen which would mean a change in resonant frequency of the accelerating cavity, which in turn would produce reflection of RF power.
- Basically two types of standing wave normal conducting accelerating structures are used: side-coupled [44] and on-axis coupled [45], both operating with phase shift $\pi/2$ per cell, providing most stable accelerating field distribution along the beam path. There are a plenty of other variants of normal conducting standing wave accelerating structures, among which one should mention disk and washer structure having high shunt impedance and high coupling factor but suffering from the problem of parasitic modes [46].

2.3.2 Superconducting cavities

- The main advantage of these cavities is the reduction in power dissipation in the structure walls (up to 10^6 lower than NC cavities).
- Net gain is not as high, because of the refrigeration cost to keep the superconducting state of the material. Carnot efficiency as well as thermodynamic efficiency must be considered. Nevertheless the gain factor could be about a few hundreds [47].
- A large and rounded iris opening will increase uniformity in the field distribution from cell to cell, and will also offer smaller impedance to the beam (implying better beam quality and larger currents).

- On the other hand the shunt impedance will be lower (more refrigeration power needed) and the accelerating field will be smaller.
- The quality factor is a few orders of magnitude higher than in NC cavities (Q ~ 10^6 - 10^{10}).
- There is no need to fabricate cavities with so extreme shapes as in NC cavities, because it is not that critical to minimize power dissipation. Simpler shape and smoother cavities are used (Figure 2-9 shows a section cell of a SC cavity).

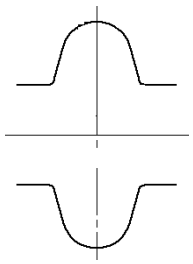

Figure 2-9. Superconducting cell section

- Due to the smoother surfaces and bigger apertures for the beam pipe, the particles trajectory is less perturbed by the *wakefields* [48] (fields created by the particles themselves -Figure 2-10- when travelling through a conductor material), so high charge bunches can be accelerated preserving low emittance.

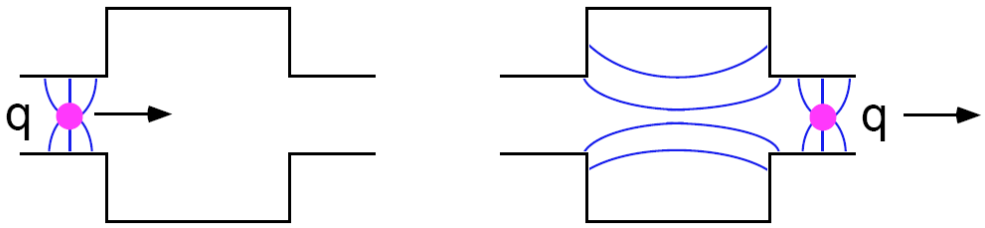

Figure 2-10. Interaction of a charged particle with a cavity (from SLAC-PUB-8026)

- Pure Nb is the most widely used material [49], supplied in sheets then shaped, cut and joined by electron-beam welding (EBW).

Both types of cavities (NC and SC) have advantages and disadvantages and the particular application will indicate the ideal choice.

2.4 Main parameters of the standing wave accelerating structure

2.4.1 Quality factor and external coupling with RF cavities

In practice, a RF cavity is coupled to some external load (or power source such as a klystron). The means of coupling could be an aperture, an electric probe, or a magnetic loop.

If the coupling is done by means of an iris (Figure 2-11) , the wave incident on the iris is at first mostly reflected [50]. However, over time, the cavity is gradually filled and, as it does, it begins to radiate. Waves diffract through the coupling hole back into the external guide. Eventually, due to losses in the cavity walls, the system reaches steady-state, and the diffracted wave may partially or totally cancel the reflected wave. If the coupling iris geometry is such that the cancellation is total, the cavity is said to be critically coupled.

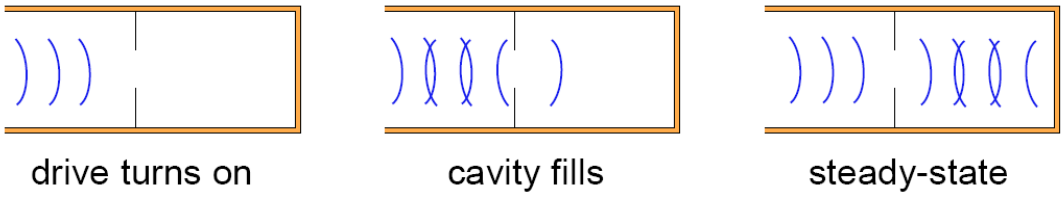

Figure 2-11. External coupling through an iris (from SLAC-PUB-8026)

To describe the consequence of loading, a parameter called the *loaded quality factor* is defined as

$$Q_{\mathrm{L}} = \omega_0 \frac{W_{stored}}{P_T} \tag{2.14}$$

Where W_{stored} is the total average stored energy in the cavity, $P_T = P_C + P_E$ represents the total power loss in the system, P_C is the ohmic loss at the cavity wall and P_E is the power flowing out of the cavity through the coupler.

Substituting the ohmic loss into (2.14), we can define the *unloaded quality factor* Q_0

$$Q_0 = \omega_0 \frac{W_{stored}}{P_C} \tag{2.15}$$

And with flowing out power the *external quality factor* Q_E

$$Q_{\mathrm{e}} = \omega_0 \frac{W_{stored}}{P_E} \tag{2.16}$$

Q_0 characterizes the intrinsic performance of the cavity, while Q_E describes its external interaction without internal loss. In the NC standing wave cavities the order of magnitude of Q_0 is 10^3- 10^4.

With these definitions (2.14) becomes

$$\frac{1}{Q_{\mathrm{L}}} = \frac{1}{Q_0} + \frac{1}{Q_{\mathrm{E}}} \tag{2.17}$$

The external coupling is quantified by the *coupling coefficient* β

$$\beta = \frac{Q_0}{Q_{\mathrm{E}}} = \frac{\mathrm{P_E}}{\mathrm{P_C}} \tag{2.18}$$

The external coupling of a cavity is characterized by the next set of β values,

- β > 1 over coupled
- β = 1 critical coupling
- β < 1 under coupled

For cavity testing in the absence of external beam, impedance matching between the cavity and the external load requires that the reflection coefficient be zero (no power reflection from the cavity). Therefore, the matching condition is that the *input power* P_{IN} to the cavity equals the power loss in the cavity P_C. However, when there is external beam loading, the cavity needs to be over coupled to account for the additional power loss to the beam. The matching condition for a beam-loaded cavity is

$$\beta = 1 + \frac{P_B}{P_C} \tag{2.19}$$

Where P_B is the power loss into the beam. The loaded quality factor can be expressed in terms of β using (2.18)

$$Q_L = \frac{Q_0}{1+\beta} \tag{2.20}$$

The effect of external loading is the reduction of the quality factor of the system.

In accelerating structures design, in order to make computational calculations easier, coupling factor β for a structure of *N* identical cells is usually obtained through the calculations of coupling factor for just one cell β_{cell}

$$\beta \approx \frac{\beta_{cell}}{N} \tag{2.21}$$

On the other hand, for an over coupled structure, which is the most common working mode in accelerating structures, β is equal to the VSWR (Voltage Standing Wave Ratio), and the reflection coefficient of the cavity, S11 parameter[6] can be expressed in terms of the coupling factor

$$S_{11} = 20log\left|\frac{\beta-1}{\beta+1}\right| \tag{2.22}$$

It can be proved [50] that the unloaded quality factor can be obtained from the magnetic field (2.23), which is an useful way to obtain the quality factor in electromagnetic simulations without the need of introducing the electrical conductivity in the model which increases computational time.

$$Q_0 = \frac{2}{\delta}\frac{\int_{Volume}\left|\vec{H}\right|^2 dv}{\int_{Surface}\left|\vec{H}_\tau\right|^2 ds} \tag{2.23}$$

[6] *Reference [30] should be consulted for more information about S parameters*

Where $\vec{H}$ is the maximum magnetic field, $\vec{H}_\tau$ is the maximum tangential magnetic field and δ is the *skin depth*, which is the distance at which the fields are damped a factor of *e* inside a conductor

$$\delta = \frac{1}{\sqrt{\mu\sigma f_0}} \tag{2.24}$$

2.4.2 Electric field, energy gain, transit time factor, shunt impedance and synchronous particle

For a standing wave structure, the time dependent electric field on axis within the cell is

$$E_Z(z, r = 0, t) = E_z(z, r = 0)\cos(\omega t + \varphi) \tag{2.25}$$

Where $E_z(z,r=0)$ are the maximums values of on-axis field, and φ is an arbitrary phase.

The average electric field E_0 at axis is defined as the integral of longitudinal coordinate of E field E_z (z, r=0) along beam direction in accelerating cavity cell of length *L*

$$E_0 = \frac{1}{L}\int_{-L/2}^{L/2} E_Z(z, r = 0)dz \tag{2.26}$$

In order to have synchronized acceleration, the particle velocity must be equal to the phase velocity of the wave[7]. The particle that fulfils such a condition is called the *synchronous particle*. The force experienced by the synchronous particle is

$$F_Z = qE_z(z, r = 0)\cos\varphi_S \tag{2.27}$$

Where φ_S is called the *synchronous phase*. The synchronous phase is defined with respect to the crest of the electric field. The energy gain of an on-axis particle in the RF field is computed by considering its passage through a gap.

[7] *Remarks. (1) For standing wave structure, in principle, it is possible to use notion of travelling accelerating wave, but for that one must first introduce standing wave decomposition in travelling waves. (2) Notion of synchronous particle is important for proton linacs, for microtron, synchrotron etc., i.e. for accelerators in which phase oscillations take place. For electron linac in which particle becomes relativistic in the initial part no phase oscillations take place. Particle is "frozen" or slightly slipping in phase with respect to acceleration field.*

$$\Delta U = q \int_{-L/2}^{L/2} E_z(z, r = 0) \cos(\omega t + \varphi_S)\, dz = q V_0 T \cos \varphi_S \tag{2.28}$$

Where V_0 is

$$V_0 = E_0 L \tag{2.29}$$

And *T* is known as the *transit time factor*

$$T = \frac{\int_{-L/2}^{L/2} E_z(z, r = 0) \cos(\omega t)\, dz}{\int_{-L/2}^{L/2} E_z(z, r = 0) dz} \tag{2.30}$$

This quantity is the fraction of the maximum energy gained by the particle due to the sinusoidal time variation of the field. For standing wave structures for relativistic electrons (above 2 MeV) , T~0.9.

The *shunt impedance* is a parameter used as a measure of the acceleration efficiency of an accelerating cavity [51]. Its dimensions of are Ω/m.

$$Z = \frac{E_0^2}{PL} \tag{2.31}$$

The higher the electric field for a given power lost in the cavity *P*, the more efficient is the cavity.

It is common to multiply shunt impedance by a factor T^2. The parameter

$$Z_{sh} = ZT^2 \tag{2.32}$$

is known as the *effective shunt impedance*

2.4.3 Coupling between cavities

In an accelerating structure made of N cavities, a coupling factor k can be defined

$$k = \frac{f_0 - f_\pi}{f_{\pi/2}} \tag{2.33}$$

Where f_0, $f_{\pi/2}$ and f_π are the frequencies of 0, π/2 and π modes (these "structural" modes will be explained in section 2.7). The coupling factor *k* gives a relative distance in frequency between these modes. The higher *k* the more frequency change can be allowed between the different cells of the cavity, which is good for the real world, because in practice there are always differences between adjacent cells (due to thermal deformations, differences in machining, etc.).

2.4.4 Pulsed and continuous mode: Duty factor

A cavity working in continuous mode is fed continuously, while if it is working in pulsed mode, the RF source (as a klystron or a magnetron) gives power only in periodic fractions of time.

The *duty factor D* is the ratio of the power pulse length T_{pulse} and the period of repetition $T_{repetition}$

$$D = \frac{T_{pulse}}{T_{repetition}} \tag{2.34}$$

The reason for using pulse mode operation falls in the fact that in an accelerating cavity a MW level power is needed in order to produce sufficiently high accelerating gradient – of the order 10-20 MeV/m. Typical duty factor for electron linac is *D* = 0.1%.

Continuous mode (*D*=1) is usually applied when high average current beams for industry or precise CW beams for nuclear physics are required. Normal conducting structure with efficient cooling in CW mode is capable to provide accelerating gradient 1-2 MeV/m.

2.5 Dependence of the standing wave accelerating structure parameters on wavelength

In most situations the choice of RF frequency in an accelerator is determined by constraints that dictate a certain frequency *f* or frequency band [52]. Frequency *f* and free-space wavelength λ are related by $\lambda=c/f$, therefore, the two quantities may be used interchangeably for the arguments in this section.

- **Cavity dimensions** $\propto \lambda$

While RF structures can be scaled over a wide frequency range, there are nevertheless limits on either side of the spectrum that determine the practical feasibility of a design.

Towards higher λ (low frequencies), the greater size of the resonating structures becomes a limiting factor (e.g., accelerating structure diameter decreases $\alpha\ \lambda$, so its weight decreases at least $\alpha\ \lambda^2$. However, beam hole linac should be large enough to permit pass through with minimal current losses.

Mechanical tolerances become generally more critical for smaller dimensions of RF resonators at very high frequencies. In particular, careful alignment of the whole structure with reference to a nominal beam axis is mandatory to avoid the excitation of transverse deflecting modes (The kick factor scales as λ^{-3} for a given ratio of aperture to wavelength).

The pumping performance is better for higher wavelengths, as the molecular conductance per unit length of vacuum pipe of diameter *d* scales as d^3, therefore providing adequate vacuum quality becomes increasingly difficult with the smaller beam pipe diameters at high frequencies.

- **Skin depth** $\propto \lambda^{1/2}$

This dependence limits the required surface finish. The skin effect limits the penetration depth of RF fields into matter. If the surface roughness is of the same order as the skin depth (2.24),

the effective path length for RF currents along the surface is increased and so are the losses. At 5.7 GHz the skin depth in copper is ~0.87μm, so surface roughness should be lower.

- **Effective shunt impedance** $Z_{SH} \propto \lambda^{-1/2}$ (If accelerating structure dimensions are exactly scaled)

The RF power loss per unit length is proportional to the product of the square of the wall current and the wall resistance *R*

$$P_l \propto i_{wall}^2 R \tag{2.35}$$

The axial electric field is proportional to the wall current divided by the radius *b* of the accelerator structure

$$E_{0z} \propto {}^{i_{wall}}/_{b} \tag{2.36}$$

and the wall resistance *R* per unit length is equal to the resistivity *ρ* of the wall material divided by the area of the surface through which the current is flowing.

Thus

$$R = {}^{\rho}/_{2\pi b\delta} \tag{2.37}$$

where δ is the skin depth (2.24) and μ is the permeability of the walls. Combining the last equations with (2.32) and noting that b ∝ λ, then

$$Z_{SH} \propto \lambda^{-1/2} \tag{2.38}$$

which means a decrease of the linac length for fixed RF power, or decrease of RF power for fixed length

- For fixed accelerating **gradient the shorter is wavelength, the less is particle energy** gain per cell, the more cells to accelerate particles with lower velocity than *c,* that is, with $\beta < 1$ are required to make particles relativistic. Linac with several $\beta < 1$ cells will accelerate relativistic beam in RTM non-effectively. Thus for application in RTM too high frequency must be avoided.

- **Voltage handling capability** $\alpha\ \lambda^{1/2}$

One of the most well known figures of merit for the voltage handling capability of vacuum is the *Kilpatrick criterion.* After some simplifications, the criterion can be expressed as

$$E \propto 25 \cdot f^{\frac{1}{2}}\ \left(E\ in \frac{MV}{m}, f\ in\ GHz\right) \tag{2.39}$$

The important fact is that the voltage handling capability in vacuum increases at high frequencies.

The practical voltage limit is influenced by many factors such as vacuum condition, surface smoothness, surface deposits, and temperature. The Kilpatrick criterion is therefore considered more as a generally accepted figure of merit than a hard limit. It can be exceeded in practical designs by a factor of 1.5.

Other important factor is the RF pulse length: Experience shows that single-pulse voltage limits decrease with longer pulse duration.

Thus, to get higher accelerating gradient one must go to higher frequencies and shorter pulses. An example is the 12 GHz operating frequency, 80 MV/m accelerating gradient and 180 ns pulse duration used in CLIC facility [53].

- $\mathbf{E_{stored}} \propto \boldsymbol{\lambda^3}$

The energy stored in accelerating cavity is proportional to cavity volume, and hence to λ^3. So, in order to accelerate bunch with high charge (of the order of 10 nC or more) low frequency cavity must be used.

- **Multipactor** [54] discharge voltage V_{mp} depends on the factor ($f.d$), where f is RF field frequency and d distance between electrodes. Because of RF cavities characteristic dimensions $d \propto 1/f$, in the first approximation discharge voltage is independent of frequency. On the other hand, electric field strength providing conditions for multipactor discharge, $E_{mp}=V_{mp}/d$, is growing proportionally to frequency.

- **RF average power handling capabilities** (acceptable average RF power dissipated per unit length) as follows from the heat conductivity equation and boundary conditions is independent on frequency [55].

2.6 Standing wave accelerating structure description in lumped circuit theory

The characteristics of RF cavities can be modelled as lumped-element resonant circuits. At a particular frequency, a RF cavity can be modelled by either a parallel or a series RLC circuit. For the following analysis, the parallel RLC circuit as shown in Figure 2-12 is used.

The inductance *L* is proportional to the magnetic stored energy and the capacitance *C* is proportional to the electric stored energy and the resistance *R* simulate the losses in resistive walls. In effect, when increasing the frequency in a standard DC or low frequency electrical circuit with L and C, the coil and the capacitor tend to become distorted and behave as the pill-box cavity [56].

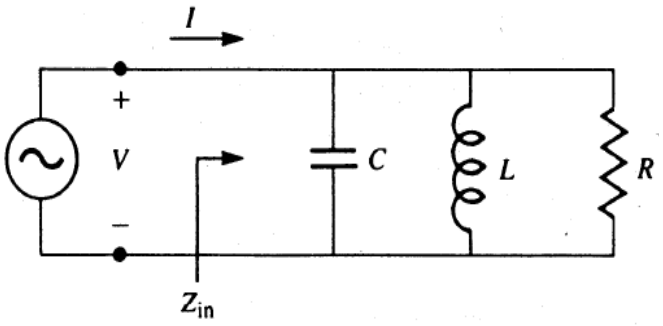

Figure 2-12. A parallel RLC circuit model of the RF cavity

For a sinusoidal excitation source ($e^{i\omega t}$), the input impedance is

$$Z_{in} = \left(\frac{1}{R} + \frac{1}{i\omega L} + i\omega C\right)^{-1} \tag{2.40}$$

The complex power delivered to the resonant circuit is

$$P_{in} = \frac{1}{2}VI^* = \frac{|V|^2}{2Z_{in}^*} = \frac{|V|^2}{2}\left(\frac{1}{R} + \frac{i}{\omega L} - i\omega C\right) \tag{2.41}$$

where V is the voltage across the terminal and I^* is the complex conjugate of the input current. The individual terms of the input power are identified as the power loss $P_{loss} = |V|^2/(2R)$, the time averaged electric stored energy $U_e = |V|^2C/4$, and the time averaged magnetic stored energy $U_m = |V|^2/(4\omega^2 L)$. Thus, the input power becomes $P_{in} = P_{loss} + 2i\omega(U_m - U_e)$. At resonance, the magnetic energy equals the electric energy, and the input impedance is purely resistive, *i.e.*, $Z_{in} = R$. The resonant frequency for the equivalent circuit is

$$\omega_0 = \frac{1}{\sqrt{LC}} \tag{2.42}$$

The parameter that characterizes the performance of the resonant circuit is the quality factor which is defined as

$$Q = \omega \frac{U_T}{P_{loss}} = \omega \frac{U_m + U_e}{P_{loss}} \tag{2.43}$$

where U_T is total average stored energy. At resonance, the quality factor becomes

$$Q_0 = \omega_0 \frac{2U_m}{P_{loss}} = \frac{R}{\omega_0 L} = \omega_0 RC \tag{2.44}$$

The behaviour of the input impedance near resonance can be studied by letting $\omega = \omega_0 + \Delta\omega$. Near the resonance, the input impedance (2.40) becomes

$$Z_{in} \approx \frac{R}{1 + i2Q_0\Delta\omega/\omega_0} \tag{2.45}$$

Equation (2.45) gives the typical resonance curve of a resonant circuit that peaks at ω_0 (Figure 2-13).

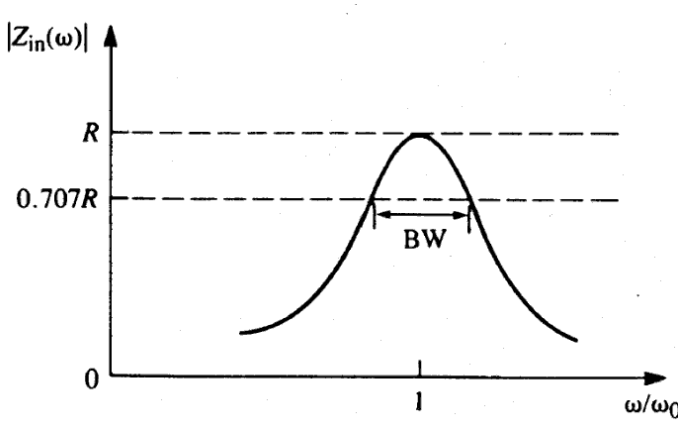

Figure 2-13. Resonant curve in a RLC parallel circuit

The higher the quality factor the better the resonator, but the bandwidth (2.46) is also smaller and therefore the circuit becomes more selective in frequencies.

$$BW = \frac{\omega_0}{Q_0} \tag{2.46}$$

2.7 Modes of accelerating structure. Dispersion characteristic

If we are to accelerate particles at high energy with single cavities, many power feeds and a lot of copper-waveguides would be needed. A more economical scheme turns out to be feasible and consists of a series of cavities placed along a common beam-tube (configuration of periodic coupled cavities [51]) and feed by a single RF source.

Given an arbitrary mode in the waveguide, the *dispersion diagram* (frequency ω vs. Waveguide number[8] $\beta = 2\pi/\lambda$ - also called *Brillouin diagram*) is an hyperbola (Figure 2-14).

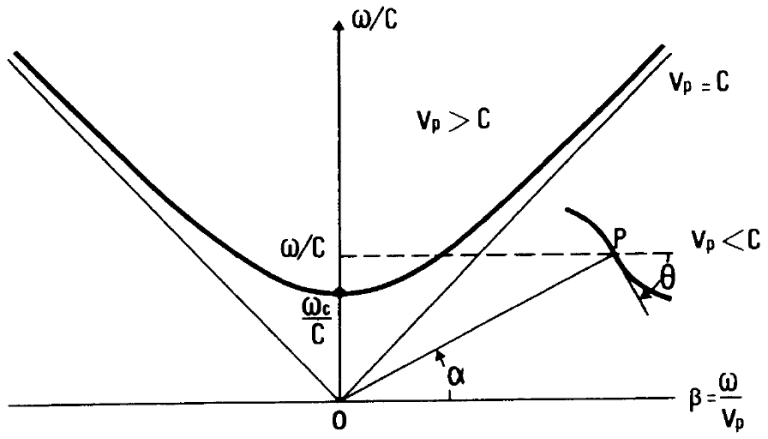

Figure 2-14. Dispersion diagram for a single mode in a waveguide (from CAS 2003. J. Le Duff lectures)

Phase velocity is the relationship ω/β and , as the previous picture shows, it is always higher than the speed of light[9].

In this diagram can also be seen that cut-off frequency from which the wave propagation begins (a waveguide is a high pass-filter)

From the point of view of RF, both travelling and standing wave structures are analogous and the transformation of the dispersion diagram is similar for an array of coupled cavities as for a circular waveguide with iris (Figure 2-6).

[8] *It should be notice that letter β has different meanings in particle acceleration.*
[9] *This fact is not affected by Relativity Theory because information is never transmitted at phase velocity.*

With these periodic structures the dispersion diagram transforms into (Figure 2-15). As can be seen in this picture, by changing the distance *d* between irises, phase velocities lower than the speed of light can be achieved. A coupled array of cavities is a “band pass filter”.

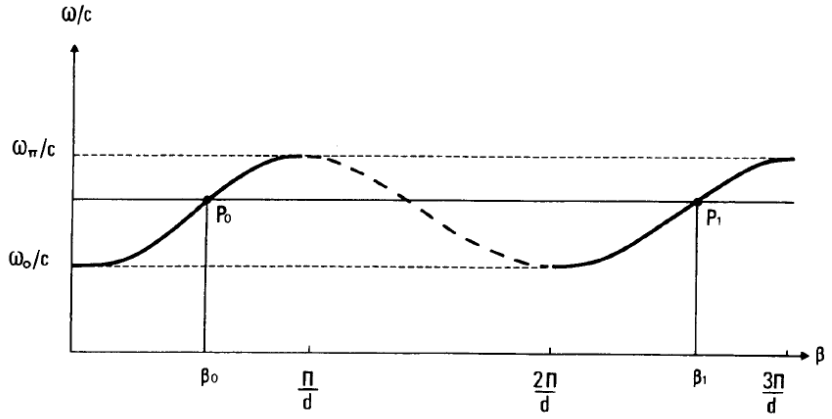

Figure 2-15. Dispersion diagram of a periodic structure (from CAS 2003. J. Le Duff lectures)

In order to accelerate electrons which have already reached the speed of light, the working operation point in the dispersion diagram must correspond to the intersection between the curve and a straight line with slope equal to 1, in other words, when the phase velocity of the wave is equal to the speed of light.

The easiest way to describe a periodic structure consists of a periodic array of coupled EM oscillators. It can be proved [16] that for an infinite number of oscillators with the same resonant frequency and electrically coupled, a dispersion diagram like the one represented in Figure 2-15 is obtained.

If the number of oscillators is not infinite but a discrete number *N*, number of N points in this diagram can be reached. Each of these points is a mode of operation of the structure in which there is a fixed phase change between one oscillator (or cavity) to the next. Given N oscillators, the phase shift between them are {0,π/(N-1), 2π/(N-1) ,…, π}.

Let’s consider the next three electrically coupled oscillators (they are coupled through the capacitor C_k).

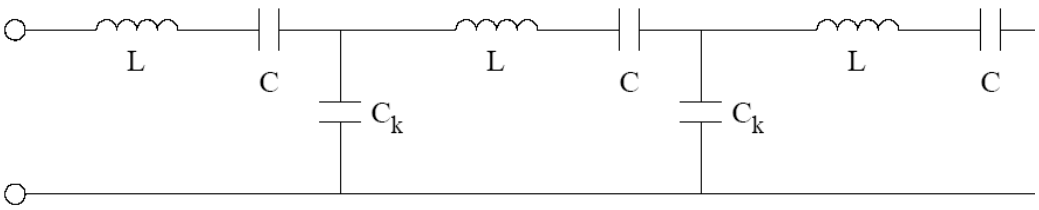

Figure 2-16. Three electrically coupled oscillators

In this particular example, three modes in the structure would be obtained (0, π/2 and π), that is, three points in the dispersion diagram.

It should be noticed that for a single frequency of one mode, an infinite number of harmonics would exist, each of them with different phase velocity. This is important for standing wave structures because just the first mode for which the structure has been designed will contribute with a net acceleration while the other harmonics will not have an average effect.

Therefore multi-cell cavities have one additional designation associated with the total number of cells (the additional longitudinal degree of freedom). As we have seen, when N number of single-cell cavities are coupled together, each mode in the single-cell cavity is split into N modes. The band of N modes is called the pass band of the corresponding single-cell cavity mode. Multi-cell accelerating cavities usually operate in one of the pass band modes of the TM monopole mode (TM_{010}).

For example, the multi-cell cavity of the Figure 2-17, is working in the (TM_{010}, π) mode.

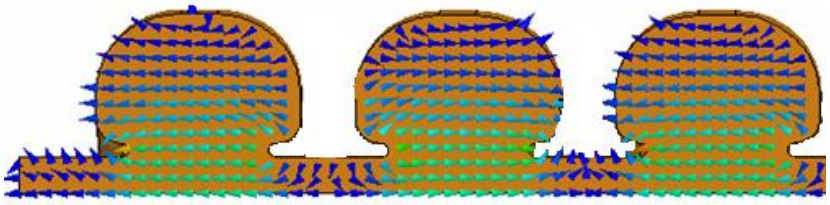

Figure 2-17. TM_{010} mode in a standing wave cavity with a phase shift π between cells

Standing wave biperiodic structures operating in the π/2 mode have the advantage of good stability and insensitivity to mechanical, temperature and assembly variations [57]. The structure consists of a chain of accelerating and coupling cavities. The latter, being much shorter than the accelerating, serve only for coupling and in the π/2 mode are not excited to the first order. The coupling cavity can be mounted either off-axis or on axis. In both cases it does not contribute practically to beam acceleration. As it has shown in section 2.4.3 the

higher the coupling between cells *k* the more stable is the structure, however, the shunt impedance and therefore the accelerating capability may be smaller.

Unless the frequency of accelerating and coupling cells have the same frequency at π/2, a discontinuity in the dispersion curve will appear. One π/2 mode corresponds to excited accelerating cavities and unexcited coupling cavities and the other mode corresponds to excited coupling cavities and unexcited accelerating cavities [16]. For a finite number of cells the latter mode is not allowed, because it would require unexcited end cells. In general there are two branches called the lower and upper pass bands. Between them is the stop band (Figure 2-18), within there are no normal-mode solutions. This stop band is not desirable and may be removed by tuning all cavities so that the frequency of accelerating and coupling cells be equal.

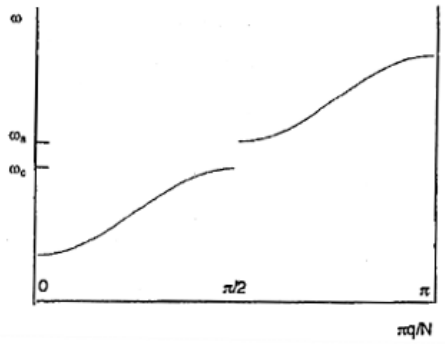

Figure 2-18. Stop band in a biperiodic structure

2.8 Numerical methods and codes for accelerating structure optimization

Optimization of accelerating structure for RTM differs from optimization of accelerating structure for standing wave linac in two aspects. First of all, RTM linac based on that accelerating structure must both effectively capture into acceleration non-relativistic beam from electron gun and effectively accelerate relativistic beams from the orbits. Second, beam current, accelerated in RTM rarely exceeds few tens mA, so space charge effects can be neglected in beam dynamics simulations.

There are many tools that are used to calculate beam dynamics and electromagnetic fields in high frequency. The ones that have been used in this thesis are described here.

2.8.1 RTM Trace

The main part of the "RTMTRACE" code was written in 1984 in the Institute of Nuclear Physics, Moscow State University by V.I. Shvedunov and M.A. Sotnikov , and later was modified with the participation of A.V. Tiunov, I.V.Surma et al.

The code is intended to investigate the beam dynamics in the race-track microtron and its main systems: chopper, buncher, capture section, linear accelerator, beam transport lines, 180 deg. end magnets, etc. It gives possibility for calculations of the space charge effects in RTM with well formed bunches.

2.8.2 Superfish

Poisson Superfish is a collection of programs for calculating static magnetic and electric fields and radio-frequency electromagnetic fields in either 2-D Cartesian coordinates or axially symmetric cylindrical coordinates. The programs generate a triangular mesh fitted to the

boundaries of different materials in the problem geometry. Plotting programs and other postprocessor codes present the results in various forms. In [58] the software can be downloaded.

2.8.3 Ansys

Multi-physics simulation from ANSYS provides engineering analysis tools that enable the accurate simulation of complex coupled-physics behaviour. The software combines: structural mechanics, heat transfer, fluid flow and electromagnetic. Therefore, thermal calculations of cavities and the subsequent RF resonant frequency change could be obtained [59]. The software allows 2D and 3D simulations.

2.8.4 Ansoft HFSS

It is a 3D code used to obtain EM fields at high frequency. Its main characteristic are:

- Calculations are performed in the frequency domain.
- Possibility to obtain resonant frequencies of resonant accelerating cavities.
- Post-processor capabilities to analyze the results in detail.
- Element finite method is implemented, getting the solutions by mean of approximation to Maxwell's equations.
- Tetrahedral mesh is used

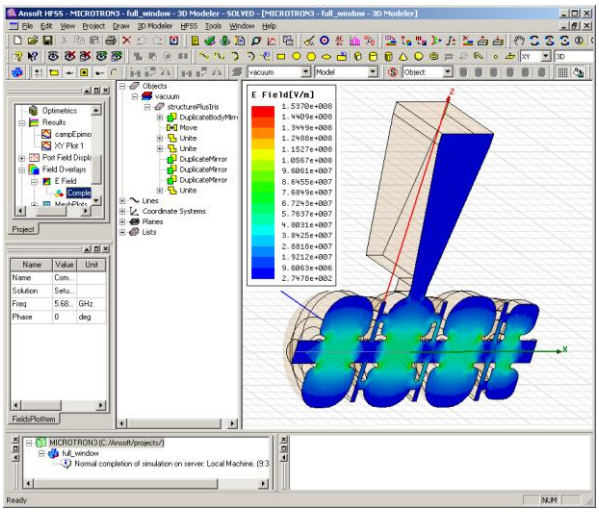

Figure 2-19. Main window of HFSS. 3D model of accelerating structure is shown

2.8.5 CST Studio

This is a code with many useful characteristics to accomplish the 3D design of an accelerating cavity. It uses the finite integration technique (FIT) that makes use of the discretization of integral form of Maxwell's equations (rather than the differential form as it is performed in the FEM). The CST Particle Studio allows to study some beam dynamics features as well as the wake fields caused by the particles when interacting with the structures.

2.9 Main steps of standing wave accelerating structure optimization

Ordinary accelerating structure optimization for RTM linac consists of several steps. First of all, following expected accelerating structure shunt impedance, required synchronous energy gain per turn, available RF power, expected beam power the number of accelerating cells is preliminary defined. Then, following simplified model of accelerating field distribution the first accelerating cell(s) length and field level and the rest regular accelerating cells number and field level are adjusted in order (i) to get as high as possible beam energy after first beam acceleration when synchronous energy gain is provided for the relativistic beam; and (ii) to get as high as possible RTM longitudinal acceptance. These calculations can be done e.g. with RTMTRACE code. After that 2D optimization of the first and regular accelerating cells is done iteratively with beam dynamics simulations with "real" field distributions from 2D RF codes.

The 2D cavity design consists of the optimization of next parameters:

- **Maximize effective shunt impedance Z_{SH}**

It is desirable that Z_{SH} (2.32) be high so that the amount of RF power required for a given energy gain will not be excessive.

- **Maximice Z/Q**

This parameter is obtained dividing the impedance (2.31) by the quality factor (2.15) and only depends on the geometry of the cavity (it does not depend on the material or on the brazing quality). It gives an idea of the accelerating field over the EM energy stored.

- **$E_{accelerating}$ vs $E_{surface}$**

The *over-strength factor* (maximum surface electric field / maximum accelerating field on axis[10]) should not be higher than 3, in order to keep the accelerating cavity operating without undesirable electric breakdowns.

[10] *Sometimes instead of maximum E field on-axis, the average E field on-axis is used (as in Superfish calculations)*

- **Maximize the transit time factor T**

T (2.30) should be maximized to provide the maximum energy possible to the particles. As T is higher when distance between noses of cavity is shorter a compromise between T, Q and Z_{SH} must be found.

- **Resonant frequency**

The resonant frequency must be accurately designed to synchronize the EM fields with the particles trajectory.

After a 2D analysis is performed, a 3D analysis must be carried out because the 2D design does not take into account:

- Coupling between cells. In the case of the magnetic coupling through coupling slots, they are not axially symmetric.
- Waveguide coupling to the structure is performed by means of a coupler. This system is not axially symmetric either.

CHAPTER 3

C-band RTM linac optimization

3.1 Peculiarities of RTM linac

Before starting to do the linac optimization, there are some peculiarities of RTM linac that must be taken into consideration:

- As a general rule linac in a RTM operates in a standing wave mode because of:
  - Standing wave linacs have a higher Z_{SH} than travelling wave linacs. Therefore for an identical RF power standing wave structures are shorter.
  - Standing wave linacs provide bunching and focusing allowing a compact design.
  - Linac in the RTM must be able to accelerate beam in opposite directions which can only be done by standing wave linacs.

- On-axis coupled or side-coupled biperiodic accelerating structures are generally used.

- Linac for RTM with low injection energy from the electron gun (15-100 keV) must be optimized in order to capture into acceleration with good efficiency non-relativistic electrons providing them energy close to synchronous energy gain, and at the same time, be able to accelerate with high efficiency relativistic beams from higher orbits.

- When optimizing the linac coupling with waveguide, the beam current loading from all orbits must be taken into account.

- The parasitic modes, especially TM_{11} like are essentially more dangerous for RTM linac than just for linac, therefore they must be studied and countermeasures used if necessary.

3.2 RTM linac parameters specification

The accelerating structure for the 12 MeV IORT RTM linac must satisfy the next requirements:

- **Frequency Input**: 5712 MHz pulsed

As it has been discussed in section 1.5, 5712-MHz in the C-band as the optimum frequency has been chosen.

- **Material**: OFE Copper

Copper has been chosen, as this is the common material used in normal conducting accelerating structures. There is no need to use a superconducting structure because the linac will work in pulsed mode with a low duty factor. The reason for this low duty factor is that a high intensity beam is not needed for the medical purposes. Therefore a superconducting structure is not required to minimize the power lost in the cavity surfaces.

- **Type of Structure**: Biperiodic standing wave

As it has already been discussed, in most RTM designs the beam must be accelerated in both directions by a standing wave linac: After the first acceleration of the particles coming from the electron gun, the electrons are forced to get into the accelerating structure again in the opposite direction by means of small bending magnets. In this way, the injection energy is increased [20] and so beam bypasses linac at the first orbit.

Besides, a biperiodic π/2 on-axis coupled accelerating structure has been chosen because it provides higher stability of accelerating field if a detuning in frequency of separate cells or beam loading happen. On the other side, with this configuration not significant lost of impedance is produced and therefore the structure has a high acceleration capability [60]. In addition machining tolerances are not very critical than for other operation modes and the transverse dimension and mass are minimal.

- **Energy gain**: 2 MeV

Energy gain of synchronous particle is 2 MeV at phase $\varphi_s = \varphi_{max}+16^0$, where φ_{max} is phase at linac entrance at which maximum energy gain is reached for relativistic particle.

- **Good capture efficiency and beam quality**

Capture into acceleration of 25 keV beam with good capture efficiency, this means a high ratio of the gun current to accelerated beam current.

Maximum possible output beam energy, at least equal to energy gain of relativistic synchronous particle, i.e. ~2 MeV. Maximum particles bunching near the maximum energy must take place.

Good transverse beam characteristics – beam radius must be essentially smaller than the beam hole radius.

- **Minimal dimensions**

Minimal accelerating structure length to produce compact RTM design and minimal accelerating structure outer radius to bypass structure by the beam at the 1^{st} orbit.

- **Minimal weight of linac**

Because of RTM will be moved by robotic arm.

- **Minimal RF power**

Minimal possible RF power spent to produce accelerating field, at least less than 1 MW.

- **Accelerating structure surface electric field**

The electric field strength produced should be found well below of the value known for RF discharge development.

- **Simplicity of manufacturing and parameters sensitivity**

Simplicity of accelerating structure manufacturing and tuning, reasonable sensitivity of accelerating structure parameters to dimension changes in order to be within attainable accuracy of manufacturing.

Part of listed above requirements are contradictory and compromise solution must be found during structure optimization.

3.3 Electrodynamics characteristics optimization

A preliminary IORT RTM linac design [39] was based on a standing wave biperiodic $\pi/2$ on-axis coupled accelerating structure operating at 5712 MHz. Field distributions used for the choice of the number of accelerating cells, their lengths and field amplitudes were obtained by scaling field distributions calculated for 2450 MHz accelerating structure designed for operation in CW mode [61]. The RF power required to produce certain field amplitude was calculated by scaling effective shunt impedance according to relation:

$$z_{sh}(f) = z_{sh}(2450\,\mathrm{MHz})\sqrt{\frac{f(\mathrm{MHz})}{2450\,\mathrm{MHz}}} \tag{3.1}$$

For the speed of light cells $\beta = 1$ $z_{sh}(2450\,\mathrm{MHz}) = 76\,\frac{\mathrm{MOhm}}{\mathrm{m}}$, so $z_{sh}(5712\,\mathrm{MHz}) = 116\,\frac{\mathrm{MOhm}}{\mathrm{m}}$.

Resulted accelerating structure consists of four $\beta = 1$ cells and one $\beta = 0.55$ cell. On-axis accelerating field distribution is shown in Figure 3-1(a) and dependence of exit particle energy on its phase at entrance in Figure 3-1a (b). Total RF power required to produce accelerating field estimated was 550 kW.

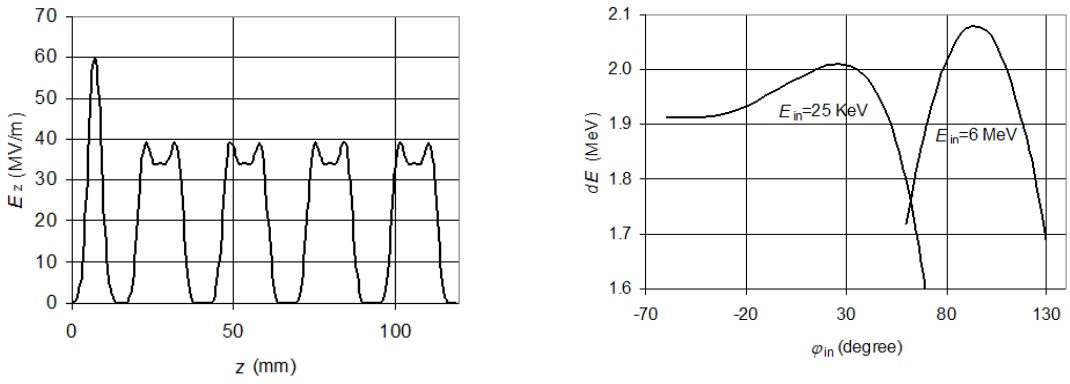

(a) (b)

Figure 3-1 (a) Linac on-axis field and (b) linac energy gain in [39]

The main conclusion following from the calculations done in [39] is the possibility to build at 5712 MHz a linac capable of effectively accelerate low energy beam from the electron gun and the high energy beams from RTM orbits. However, directly scaled accelerating structure designed for CW operation at 2450 MHz is not optimal for pulsed operation at 5712 MHz because of beam hole radius would be too small (only 2.15 mm) and surface electric field strength at noses would be too high, producing RF discharges. So a new set of accelerating structure optimization has been done to produce design optimal for application in 12 MeV RTM.

3.3.1 2D linac optimization with RF and beam dynamics codes

2D RTM linac optimization was done without taking into account coupling slots and involves the following basic steps: (1) optimization of a $\beta = 1$ cell geometry with SUPERFISH [62] and definition of the geometry of $\beta < 1$ cells with different lengths; (2) beam dynamics optimization of linac parameters with RTMTRACE (see section 2.8.1) for a 25 keV injected beam and for a relativistic beam with different number of $\beta = 1$ cells and different lengths and field amplitudes of the first $\beta < 1$ cell; (3) first $\beta < 1$ cell geometry optimization.

2.5.2.1 Regular β=1 cell optimization

Parameters, describing geometry of accelerating structure are presented in Figure 3-2. The main factors influencing on the high β standing wave accelerating structure effective shunt impedance are: (1) internal geometry of accelerating cell, defined by radii *R1*, *R2*, and *Ra*; (2) nose radius, *Rn*; (3) distance between noses, *g*; (4) coupling slots parameters – cutting radius , *Rs*, slot height, *Hs* and angular width, α_s; (5) beam hole radius, *Rb*; (6) thickness of the web between accelerating and coupling cells, *t*; (7) length of the coupling cell, *Lc*.

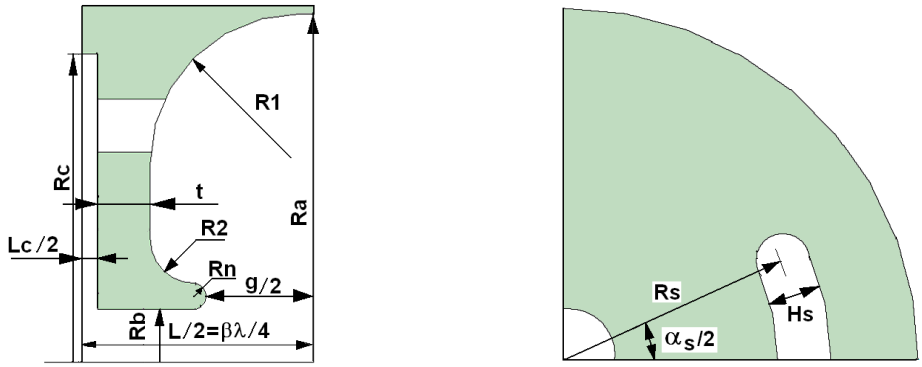

Figure 3-2. Parameters describing geometry of accelerating structure

The internal geometry of accelerating cell does not change much between variants of accelerating structure used in numerous projects and its optimization for specific set of structure parameters can produce only several percents of effective shunt impedance increase. Decrease of the nose radius could increase shunt impedance, but also increases over-strength factor (see section 2.9), and thus increases the probability of RF discharge.

The distance between noses *g* is an important parameter permitting to optimize structure effective shunt impedance for specific other parameters set and required accelerating gradient. Decrease of *g* increases the transit time factor, but simultaneously increases over-strength factor and decreases quality factor, so a special study for this parameter has been done.

Position of the coupling slots (their height and angular width) influence on the coupling factor (see section 2.4.3), which defines stability of accelerating structure field distribution (the greater coupling the less stringent requirements are to accuracy of structure manufacturing). However, in commonly accepted design of on-axis coupled structure, the increase of coupling factor, which is reached by increasing its angular width, produces a decrease of effective shunt impedance. Special version of on-axis coupled structure was suggested with high coupling factor attained without drop in effective shunt impedance [63], but some problems of this structure (bad noses cooling, high sensitivity to coupling cell dimensions change) make problematic its practical use. It has been followed the traditional approach to the coupling slots design and used empirical SUPERFISH estimations of effective shunt impedance drop with coupling factor.

Parameters which have strong influence on the effective shunt impedance (beam hole radius *Rb*, length of the coupling cell *Lc* and thickness of the web between accelerating and coupling

cells *t*) are fixed by external circumstances. The beam hole radius Rb=4 mm was chosen to decrease current losses in RTM, this is a rather large value (ratio of $2Rb/\lambda$ is about of 0.15, while commonly used value in electron linacs is about of 0.1). It has been chosen coupling cell length Lc=1.75 mm as compromise between effective shunt impedance drop and sensitivity of coupling cell frequency to geometrical parameters change. The web was taken sufficiently thick, t = 1.9 mm, to provide adequate cooling of the nose region in order to decrease temperature gradient in accelerating structure body and thus to decrease its thermal deformations and shift of resonance frequencies of accelerating and coupling cells. Ratios Lc/λ and t/λ are close to minimum values used in different variants of on-axis coupled structure. Choosing larger values of Lc and t would not only decrease effective shunt impedance, but also would make impossible to use noses in low β (small L) 1st cell into which the low energy beam is injected. The absence of noses would decrease the effective shunt impedance and also would lead to appearance of parasitic coupling of electrical type due to electric field penetration into the coupling cell.

Accelerating and coupling cells radii Ra and Rc were used to tune resonant frequencies of accelerating and coupling cells.

Electric field distribution for β=1 cell with magnetic type boundary conditions, corresponding to $\pi/2$ mode excitation, is shown in Figure 3-3 (a) within cell volume and (b) on axis.

It has been studied the effective shunt impedance dependence on the distance between noses for β=1 cell obtaining the results presented in Figure 3-4. As can be seen from Figure 3-4(a) for the beam hole radius chosen, the effective shunt impedance reaches a maximum in the range 1.2 cm < z < 1.5 cm, this maximum is reached as a compromise between transit time factor decrease (Figure 3-4(b)) and quality factor increase (Figure 3-4 (c)) when distance increases. The effective shunt impedance and quality factor are given for two values of coupling factor 0% (no coupling slots) and 4%. Taking into account behaviour of the over-strength factor (Figure 3-4 (d)) it has been chosen g = 1.42 cm for the structure.

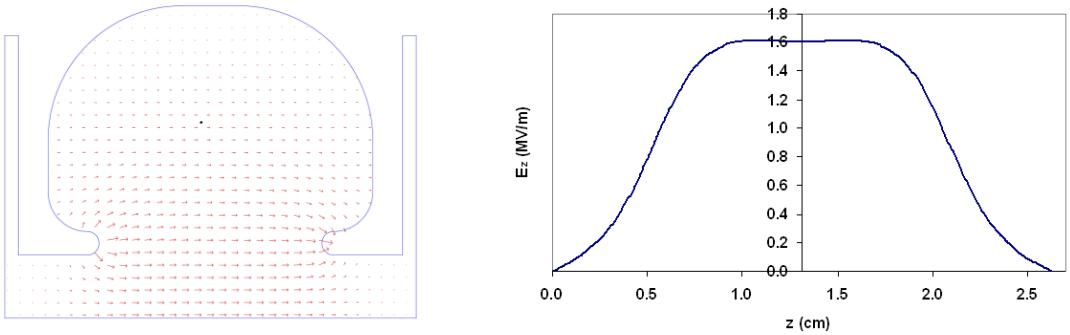

(a) (b)

Figure 3-3. Electric field distribution for β=1 cell with magnetic type boundary conditions (a) within cell volume, (b) on axis

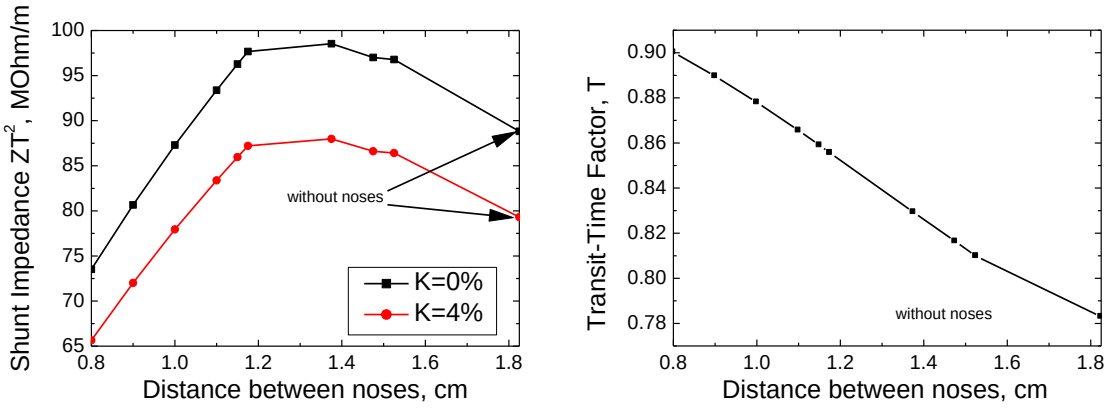

(a) (b)

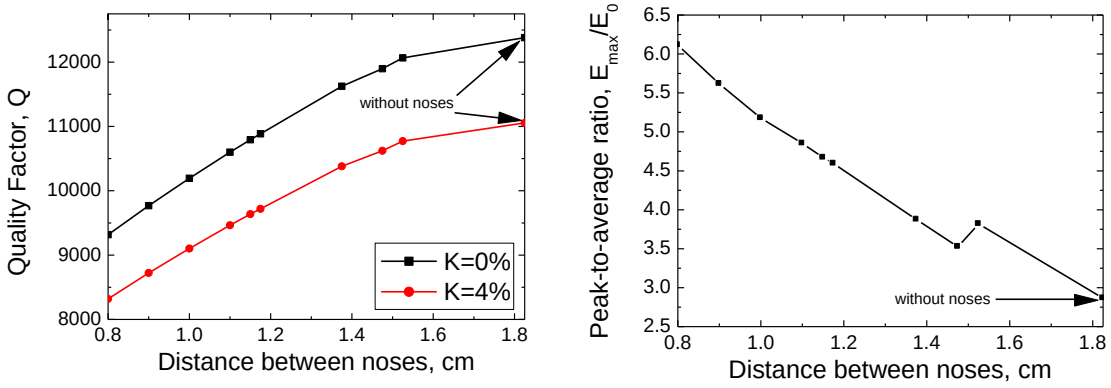

(c) (d)

Figure 3-4. Dependence on the distance between noses (a) effective shunt impedance, (b) transit time factor, (c) quality factor, (d) over-strength factor

The main properties of the β=1 cell are summarized in Table 3-1 for two coupling factor, k_{coupl}, values: 0 and 4%. Q_0 is the unloaded quality factor, ZT^2 the effective shunt impedance, K_{o-s} is the over-strength factor, E_{av} is the average on-axis field, P_w is the power dissipated in the cell walls, and E_{max} is the maximum on-axis electric field strength.

Table 3-1. The main properties of the β=1 cell

k_{coupl}	Q_0	ZT^2(MΩ/m)	K_{o-s}	E_{av}(MV/m)	P_w(W)	E_{max}(MV/m)
0	11720	108	4.0	1	162	1.61
4%	10465	96	4.0	1	182	1.61

3.3.1.1 End β=1 cell calculations

The end β=1 cell differs from regular cell in two aspects:

(1) Because of large beam hole radius electric field penetrate deeply inside beam channel. SUPERFISH code is unable to treat open space boundary conditions and therefore a long channel must be used in calculations to ensure sufficient field attenuation.

(2) There are coupling slots only at one web of end accelerating cell, so when correcting effective shunt impedance for additional RF power losses due to coupling slots this should be taken into account. With 2D SUPERFISH code, the shift of cell resonance frequency due to coupling slots cannot be calculated, so cell radius Ra and the rest parameters describing cell geometry are the same as for regular cell.

Electric field distribution for end β=1 cell with magnetic type boundary condition at right side and electric at left side, is shown in Figure 3-5(a) within cell volume and (b) - on axis. The main parameters of the end β=1 cell are summarized in Table 3-2.

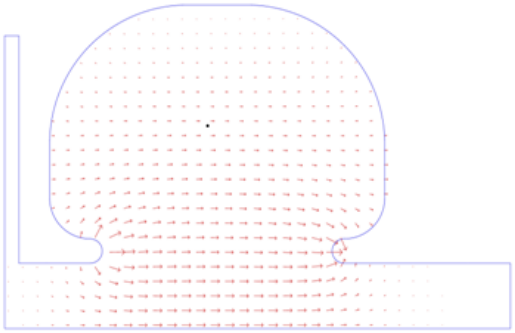

(a)

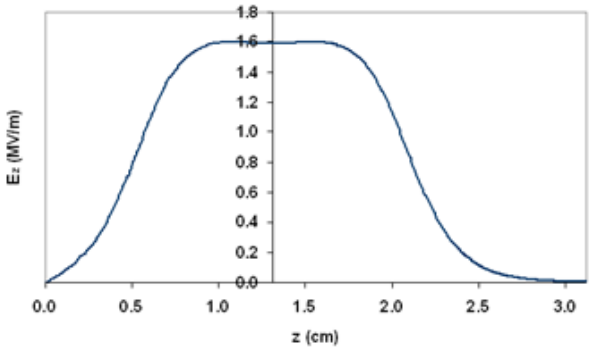

(b)

Figure 3-5. Electric field distribution for the end β=1 cell (a) within cell volume, (b) on axis

Table 3-2 .The main properties of the end β=1 cell

k_{coupl}	Q_0	ZT^2(MΩ/m)	K_{o-s}	E_{av}(MV/m)	P_w(W)	E_{max}(MV/m)
0	11720	108	4.0	1	159	1.59
4%	11090	102	4.0	1	169	1.59

3.3.1.2 First β<1 cell calculation and linac optimization

The main task of 1st β<1 cell calculations is the choice of its length and field amplitude in order to provide effective capture into acceleration of non-relativistic particles from the electron gun. From the point of view of beam dynamics the main issue is the position of the 1st cell accelerating gap centre with respect to the next accelerating cell gap centre. Because of the

1st cell is end cell it can be made asymmetric to optimize its quality factor and shunt impedance. Nevertheless, the first step was to consider a symmetric 1st cell, which length can be characterized in terms of average relative particle velocity, β.

The parameters of the 1st cell depend on the number and field amplitude of subsequent β=1 cells. The linac composed of β<1 cell and β=1 cells must accelerate a non-relativistic beam to approximately 2 MeV when its field amplitude is tuned to provide 2 MeV synchronous energy gain for relativistic beams. In order to accelerate particles with minimum phase slip in β=1 cells, their energy at exit of 1st β<1 cell must be about 0.5 MeV, which for short wavelength of C-band linac means 1st cell accelerating gradient about 30 MV/m. The parameters of the 1st cell influence essentially on linac optical properties during first beam acceleration.

Calculations were done for three values of the 1st cell length: L = 0.5λ/2, 0.6λ/2 and 0.7λ/2 (β=0.5, 0.6 and 0.7). Number of β=1 cells in one variant was taken to be 4 and in another 3. The order of calculations was the next: for a given number of β=1 cells and given 1st cell β field amplitude on axis of 1st cell was fixed at some level. Then, field amplitude of β=1 cells was varied until maximum energy gain of relativistic particle, injected from the β=1 side, reached 2.08 MeV. After that, a 25 keV beam was injected from the β<1 cell side and the dependence of the output energy and phase on input energy was calculated. For each 1st cell β<1, calculations were performed for several values of its field amplitude and for number of β=1 cells 3 and 4.

The optimal alternative was found the next: the 1st cell β=0.5, number of β=1 cells equal 3. Field amplitude in 1st cell is 43 MV/m and in the rest β=1 cells 44.8 MV/m. However, length of symmetric β=0.5 cell is so short, that for reasonable field over-strength factor and reasonable values of web thickness and coupling cell length this cell has no noses, therefore its effective shunt impedance would be very low and the RF power necessary to produce accelerating field would be too high. For these reasons the 1st cell geometry has been changed: it was made asymmetric as it is shown in Figure 3-6(a), but on-axis field distribution (Figure 3-6 (b)) was adjusted by cell geometry to reproduce the β=0.5 cell field distribution which had been found earlier. The main parameters of the 1st cell are summarized in Table 3-3.

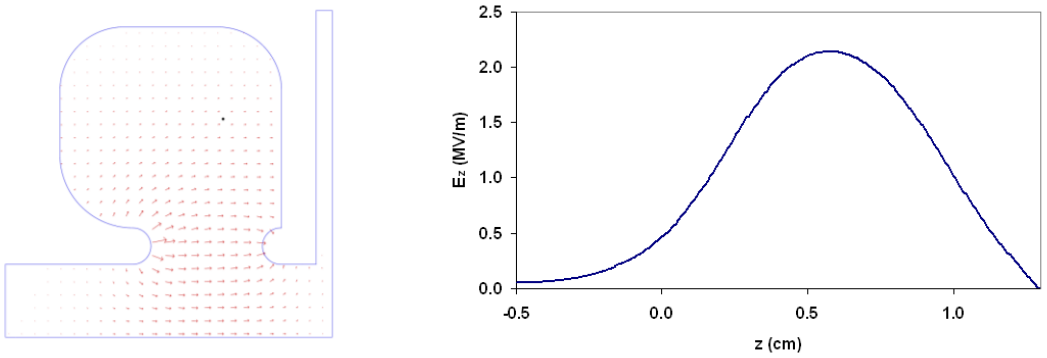

(a) (b)

Figure 3-6. Electric field distribution for the 1st cell (a) within cell volume, (b) on axis

Table 3-3. The main properties of the 1st cell.

k_{coupl}	Q_0	ZT^2(MΩ/m)	K_{o-s}	E_{av}(MV/m)	P_w(W)	E_{max}(MV/m)
0	7775	67	5.6	1	232	2.14
4%	6942	60	5.6	1	260	2.14

The Field distribution along linac for optimal variant is shown in Figure 3-7 (a). The RF power dissipated in the 1st cell is 105 kW, in two regular β=1 cells, 141 kW and in the end β=1 cell, 134 kW. Total RF power dissipated in linac walls is 521 kW.

In Figure 3-7(b) energy gain of 25 keV and 6 MeV electrons in linac depending on injection phase is given.

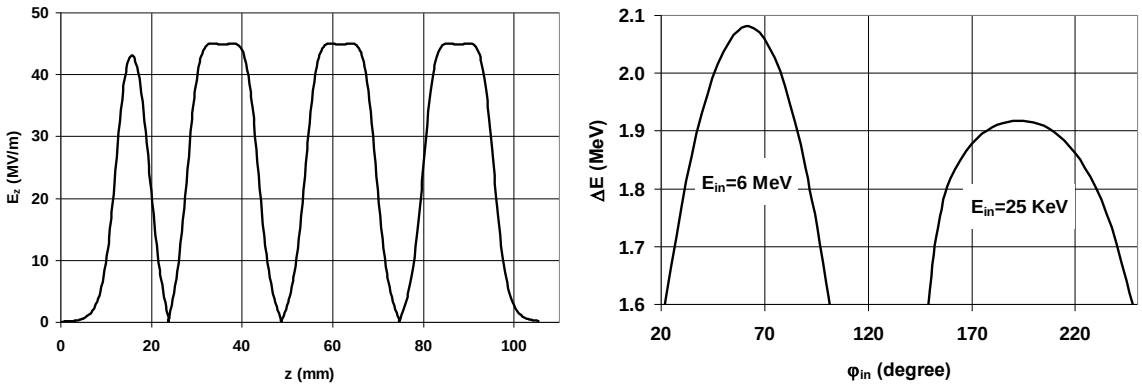

(a) (b)

Figure 3-7 : (a) Linac on-axis field and (b) linac energy gain

In Figure 3-8 it is shown the transverse and longitudinal phase space calculated at 1st cell exit and at linac exit for a continuous 25 keV beam injected with radius 0.5 mm, maximum divergence 50 mrad. Red lines are ellipses calculated with rms beam parameters. Beam energy after 1st cell is about 280 keV, and beam is quite well focused inside linac with dimensions much less than beam hole radius. At linac exit the beam is slightly divergent. About 43% of injected particles reach the linac exit, however the essential part of particles are in low energy tail (these particles will be lost at next linac entrance after beam reflection from the end magnet).

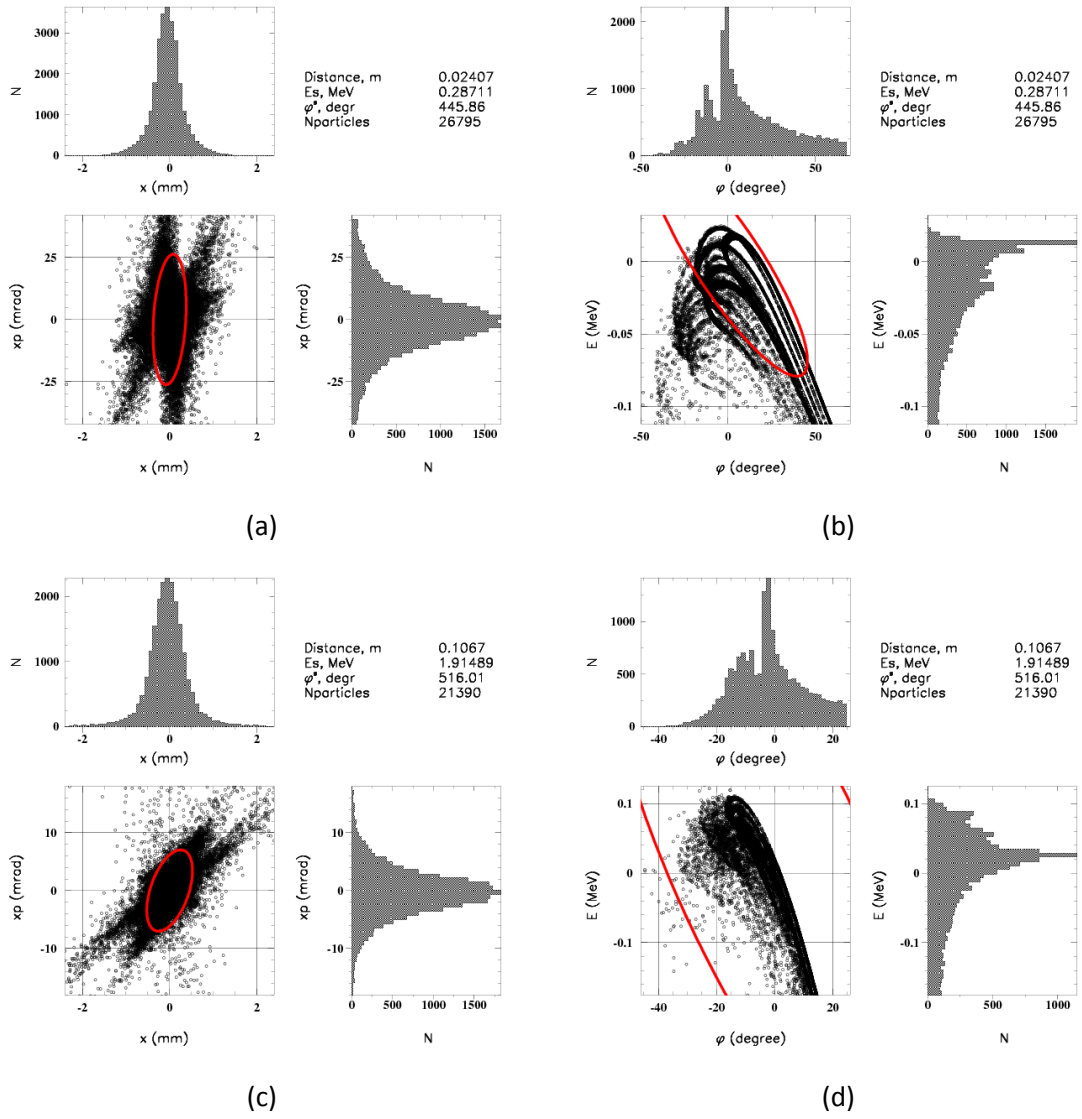

Figure 3-8. Transverse (a) and longitudinal (b) phase space at 1st cell exit and (c), (d) at linac exit

3.3.1.3 Summary of 2D linac optimization

At the first step it was conducted accelerating structure optimization with 2D code SUPERFISH [62] in iterative process including beam dynamics simulation with PARMELA [64] and RTMTRACE (see section 2.8.1). The number of cells, the length of the first cell, accelerating field amplitude in $\beta < 1$ and $\beta = 1$ cells were defined at this step. Required RF power was estimated taking into account effective shunt impedance decrease due to coupling slots cutting. 2D fields of accelerating structure synthesized in this way were used for RTM beam dynamics simulation.

3.3.2 3D linac cells calculation, coupling factor and field distribution optimization

3.3.2.1 Initial considerations

The parameters which describe geometry of IORT RTM accelerating structure are shown in Figure 3-9 and accelerating structure schematic view with geometry of coupler is given in Figure 3-10. It should be noticed that parameters designations differ slightly from those of Figure 3-2.

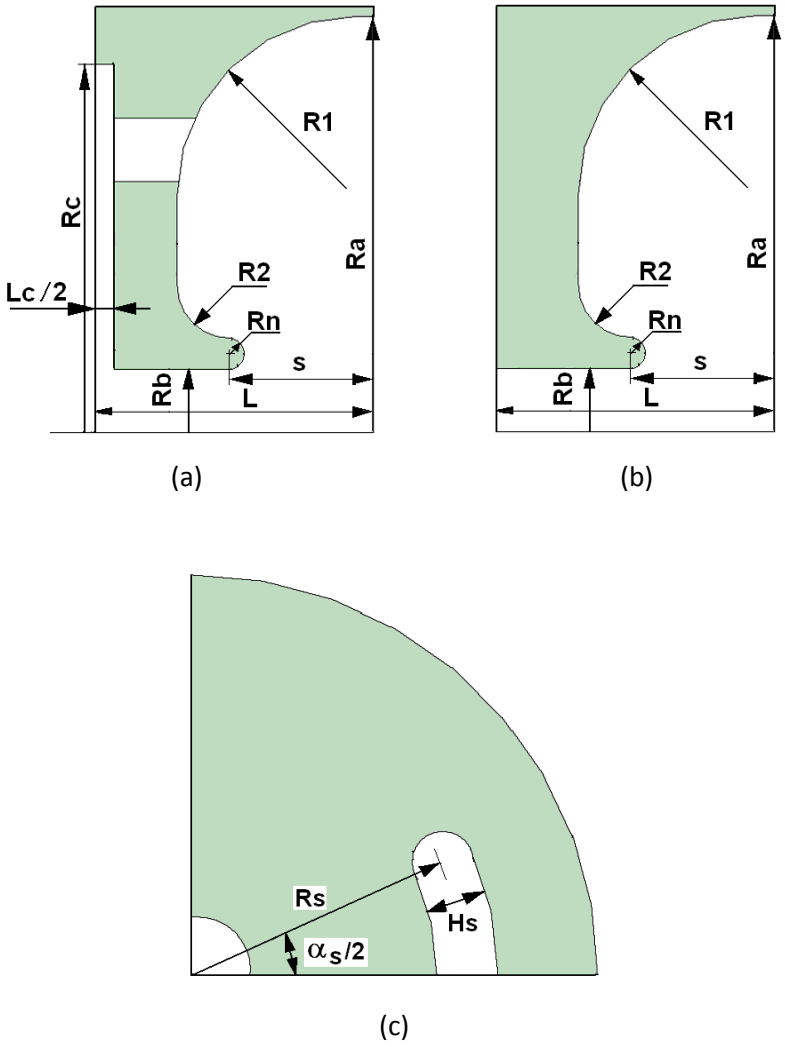

Figure 3-9. Parameters describing accelerating structure geometry. (a) for accelerating half-cell with coupling half-cell, (b) for the end half-cell, (c) coupling slots geometry

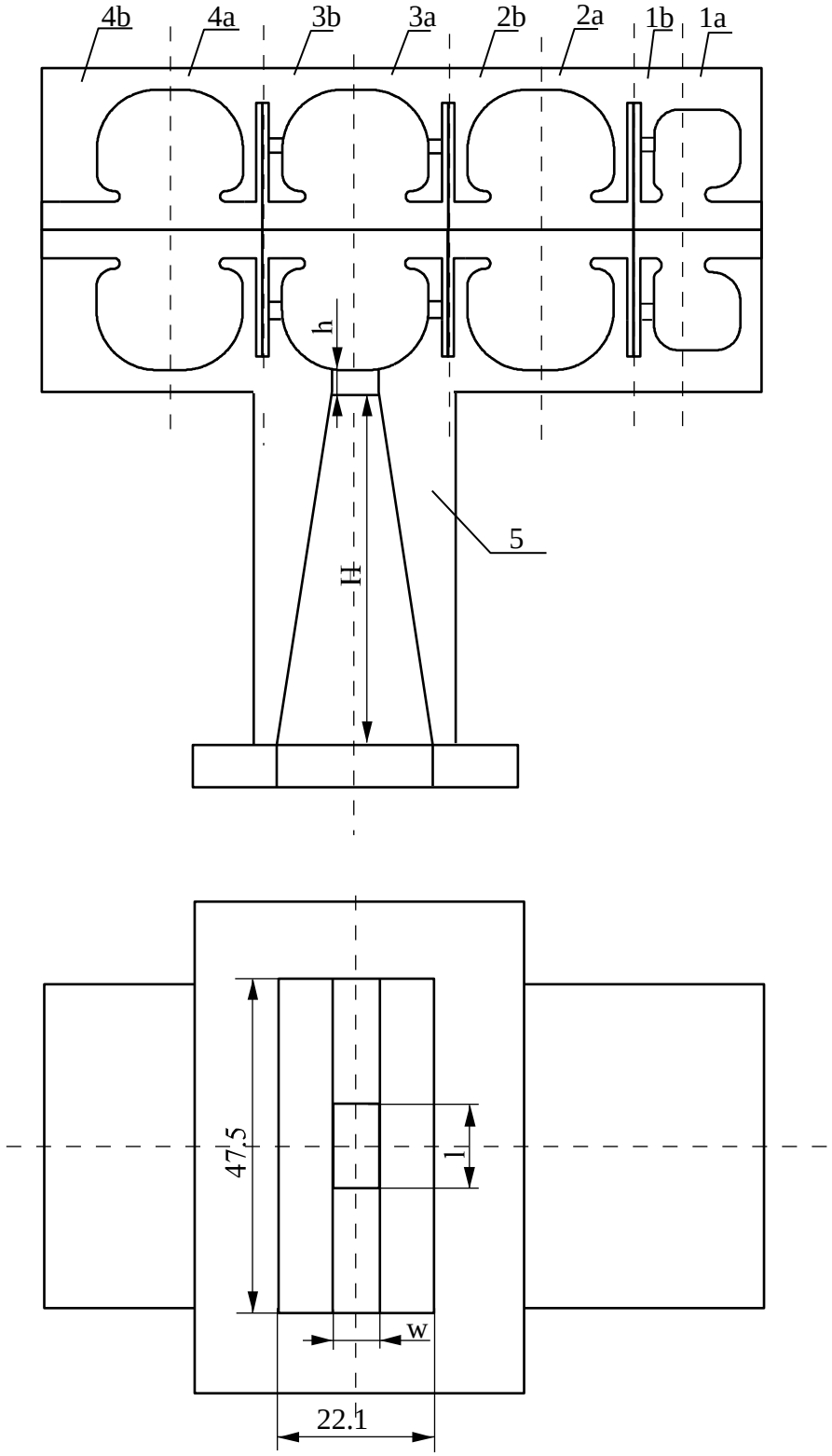

Figure 3-10. Schematic view of accelerating structure with feeding waveguide. Parameters describing geometry of coupler are shown

The accelerating structure consists of four accelerating cells and three coupling cells. The first accelerating cell (1a+1b in Figure 3-10) is essentially different from the next three cells. As it

has been explained in previous section this cell is shorter and it is asymmetric with respect to the centre of accelerating gap (which is done to provide an effective capture in acceleration of non-relativistic beam from the electron gun with minimum RF power spent). The half-cell 1a is part of the end cell and has no coupling slots at the web. Three accelerating cells (2a+2b, 3a+3b, 4a+4b) have similar, but not fully identical internal geometry: Cell 2 is coupled with two neighbouring coupling cells by coupling slots, cell 3 being also coupled with two coupling cells, but also is coupled with feeding waveguide via coupling iris. Half-cell 4b is the part of the end cell and has no coupling slots at web.

In the previous section an initial optimization of accelerating cells geometry and tuning to resonance frequency 5712 MHz were done with 2D code without taking into account coupling slots and coupler.

3.3.2.2 Order of 3D calculations: Methodology

The 3D calculations have been done according to the next sequence:

a. To calculate regular half-cell (2a=2b=3a=3b=4a) without coupling slots and compare results with 2D calculations.
b. To calculate short end cell (1a+1b) without coupling slots and compare results with 2D calculations.
c. To calculate assembly 2b+3a with coupling slots, but without coupler, adjust position and dimensions of the coupling slots, providing coupling factor 6-8%, adjust accelerating and coupling cells radii (Ra and Rc) to tune $\pi/2$ accelerating cell frequency (electric wall boundary condition at end planes) and $\pi/2$ coupling cell frequency (magnetic wall boundary condition at end planes) to 5712 MHz. Coupling slots must be rotated 90^0 in coupling cells.
d. To calculate assembly 2a+1b with coupling slots, adjust dimensions of the coupling slots of the 1b half-cell to provide field amplitude ratio according to Figure 3-7(a), adjust accelerating and coupling cells radii (Ra and Rc) of the 1b half-cell to tune $\pi/2$ accelerating cell frequency (electric wall boundary condition at end planes) and $\pi/2$ coupling cell frequency (magnetic wall boundary condition at end planes) to 5712 MHz. Coupling slots must be rotated 90^0 in coupling cell.

e. To elongate assembly - calculate assembly 2a+1b+1a with coupling slots, further adjust dimensions of the coupling slots of the 1b half-cell to provide field amplitude ratio according to Figure 3-7(a), adjust accelerating (1a and 1b) and coupling cells radii (1b) (Ra and Rc) to further tune $\pi/2$ accelerating cell frequency (electric wall boundary condition at end planes) and $\pi/2$ coupling cell frequency (magnetic wall boundary condition at end planes) to 5712 MHz .

f. To calculate assembly 4b+4a+3b with coupling slots, but without coupler, adjust accelerating (4a and 4b) cells radius (Ra) to tune $\pi/2$ accelerating cell frequency to 5712 MHz . Coupling slots must be rotated 90^0 in coupling cell.

g. To calculate full assembly: 1a+1b+2a+2b+3a+3b+4a+4b with coupling slots, but without coupler, control field distribution, value of resonance frequency, quality of tuning of coupling cell (if any field is excited in these cells), if necessary, try to tune structure, define quality factor, get 3D fields distributions in beam channel for beam dynamics simulation; coupling slots must be aligned parallel in accelerating cells and rotated 90^0 in coupling cells.

h. To calculate accelerating cell 3a+3b without coupling slots but with coupler, sending exciting signal to waveguide analyze reflected wave, estimate external quality factor, by changing coupling iris length *l* (Figure 3-10) tune coupling factor of the accelerating structure with waveguide.

3.3.2.3 Step (a). Calculation of regular cell (2a=2b=3a=3b=4a) without coupling slots.

3D calculations were done using ANSYS and HFSS codes. 2D and 3D results of the regular cell calculations are very close (see Figure 3-11). Small differences in the main RF parameters of the cell are within the accuracy of calculations (Table 3-4).

Table 3-4. Main RF parameters in regular cell

	SUPERFISH (2D)	ANSYS (3D)	HFSS (3D)
Q	11720	11820	11700
f (MHz)	5726.0	5725.0	5726.3
Z_{sh} (MΩ/m)	108	-	107

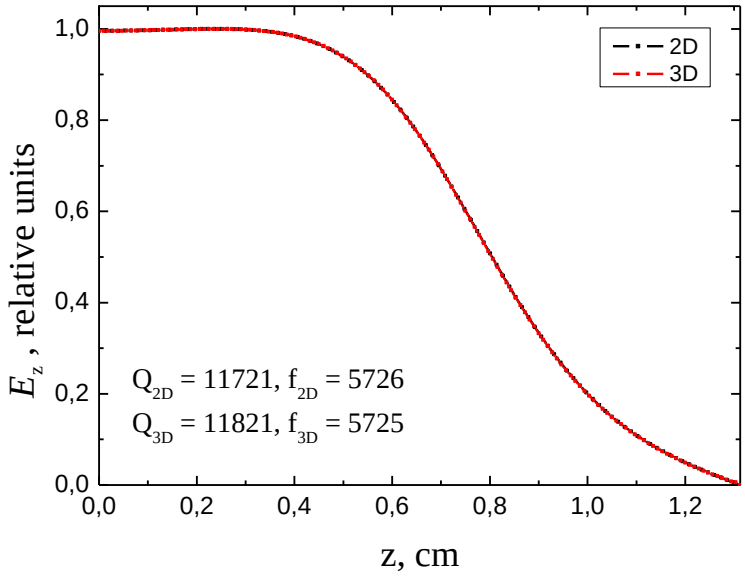

Figure 3-11. Distribution of the longitudinal field in the regular half cell produced in 2D (SUPERFISH) and 3D (ANSYS) calculations

The following pictures show the initial mesh used to calculate the regular cell (Figure 3-12a) and the E field (Figure 3-12b).

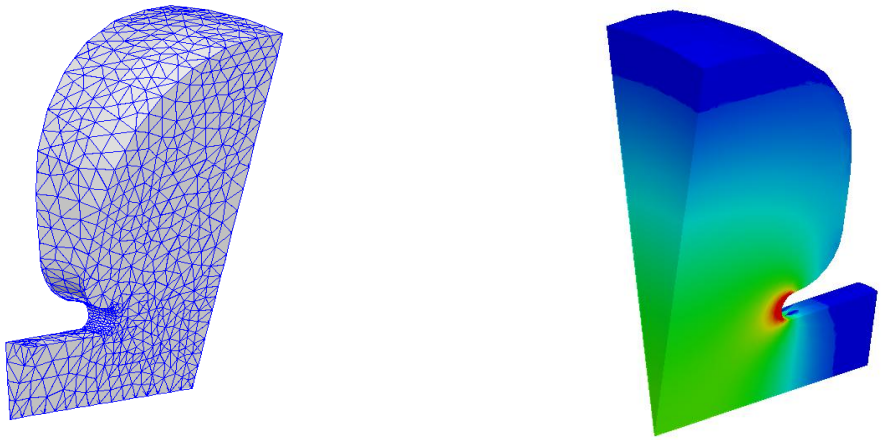

(a) (b)

Figure 3-12. HFSS mesh used to calculate the regular cell (a) and E field (b)

3.3.2.4 Step (b). Calculation of short end cell (1a+1b) without coupling slots.

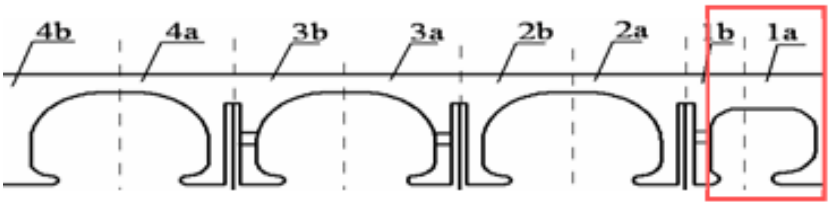

Figure 3-13. 3D optimization: Step (b)

2D and 3D results of the short end cell calculations are also very close to each other (see Figure 3-14).

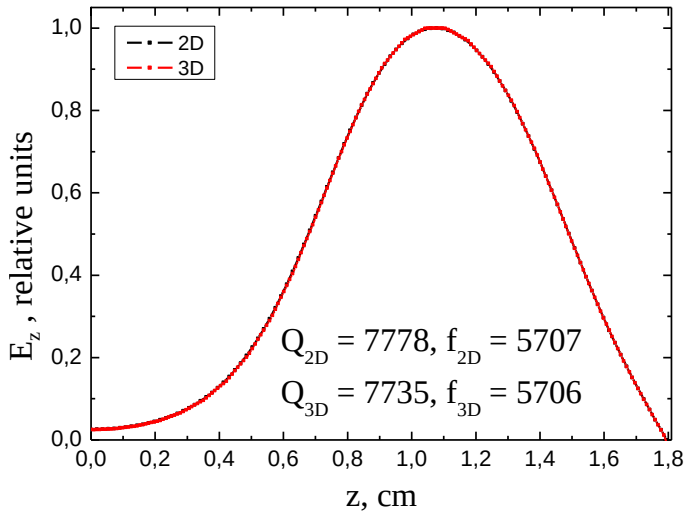

Figure 3-14. Longitudinal field distribution produced in 2D (SUPERFISH) and 3D (ANSYS) calculations of the short end cell.

The main RF parameters of the cell produced in 2D and 3D calculations are included in Table 3-5.

Table 3-5. Main RF parameters in short end cell

	SUPERFISH (2D)	ANSYS (3D)	HFSS (3D)
Q	7780	7740	7780
f (MHz)	5707.5	5706.5	5707.2
Z_{sh} (MΩ/m)	67	-	71

3.3.2.5 Step (c). Tuning 2b+3a assembly with coupling slots

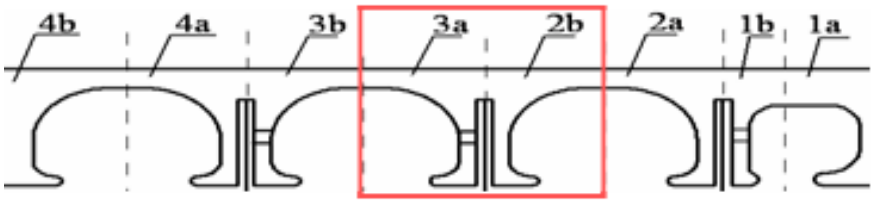

Figure 3-15. 3D optimization: Step (c)

The aim of this step is to calculate the coupling cell and coupling slot dimensions without placing yet the coupler. The model for 3D calculations consists of two regular half cells and coupling cell between them with two coupling slots rotated for 90^0 one relative to another (in order to minimize direct coupling between neighbouring accelerating cells).

Taking into account structure symmetry, all calculations in this step were carried out for quarter of the cell geometry (Figure 3-16).

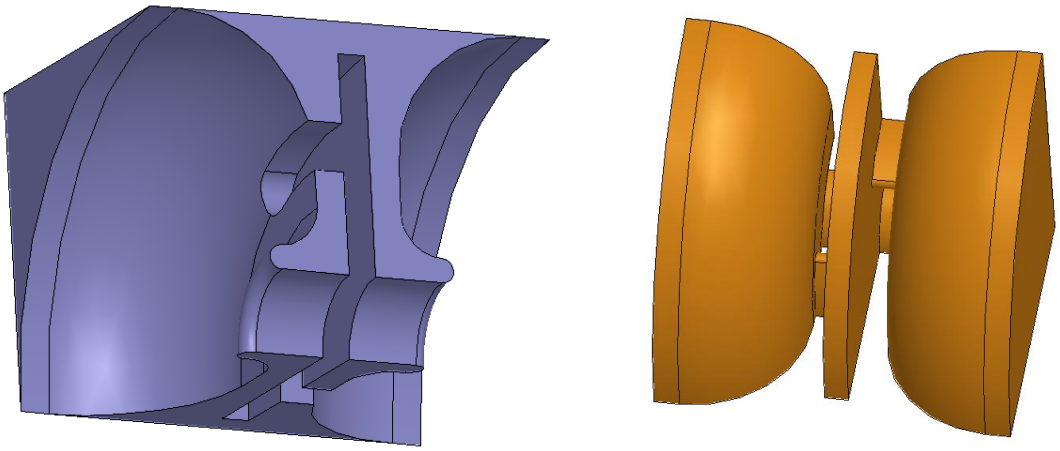

(a) (b)

Figure 3-16. 3D view of a quarter of regular and coupling cells connected through the coupling slots. (a) Solid model and (b) Vacuum model

Coupling cell tuning

The first step is to tune the coupling cell. Tuning to resonance frequency f = 5712 MHz was carried out by adjusting the inner radius of the coupling cell, Rc.

It should be noticed that an analytical value could be obtained having in mind that the coupling cell is quite similar to a pill-box cavity which has a resonant frequency (2.13) equal to 5712 MHz for the TM_{010} mode at Rc=2.01cm. This is a rough approximation because the effect of the beam pipe produces an increase in the resonant frequency due to the reduction of capacitive component and, the other way round, the coupling slots produce a decrease in the resonant frequency due to an increase in the inductive component.

The way to tune the coupling cell consists of putting magnetic boundary conditions at both end planes (see Figure 3-17) because in this case the acceleration mode is not the one we need to excite but the coupling mode, and, as the structure is biperiodic both accelerating and coupling cells must be tuned to the operation frequency (5712 MHz for the $\pi/2$ mode).

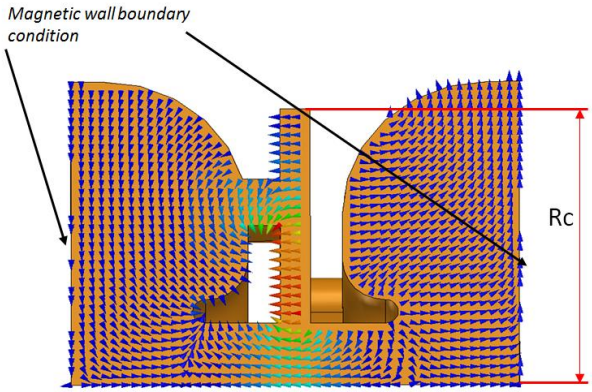

Figure 3-17. Coupling cell excited: E field vector

The following table shows the parameters of coupling cell tuned.

Table 3-6. Coupling cell tuned

f (MHz)	Q_0	Rc (mm)
f=5712.1 MHz	1840	16.17

Regular cell tuning.

To tune regular cell to π/2 –mode resonance frequency f = 5712 MHz- it has been used calculated coupling cell geometry from previous calculations and electric wall boundary conditions at both end planes have been placed (where in previous step were magnetic walls -Figure 3-17-). Frequency tuning was carried out by adjusting the regular cell inner radius, Ra. The main RF parameters of the tuned assembly are included in Table 3-7.

Table 3-7. Assembly 2b+3a tuned

0 mode0	π/2 mode	π mode
f=6059.8 MHz	f=5712.5 MHz	f=5456.3 MHz
Q_0=3330	Q_0=9730	Q_0=2950

As the assembly 2b+3a has three resonant cavities (2 accelerating cells and 1 coupling cell), three operation modes are obtained (see section 2.7) in the dispersion curve. The following picture shows the π/2 mode operation in which the structure will work.

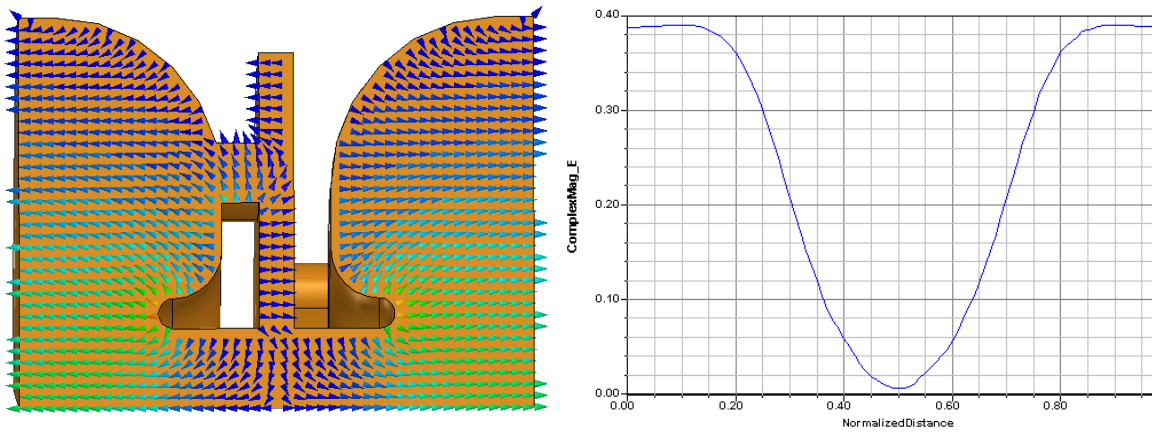

(a) (b)

Figure 3-18. Assembly 2b+3a working in π/2 mode. E field vector (a) and E field along axis(normalized to max E field on surface)

Figure 3-19 shows the two other adjacent modes to the working mode, which are the 0 and π modes.

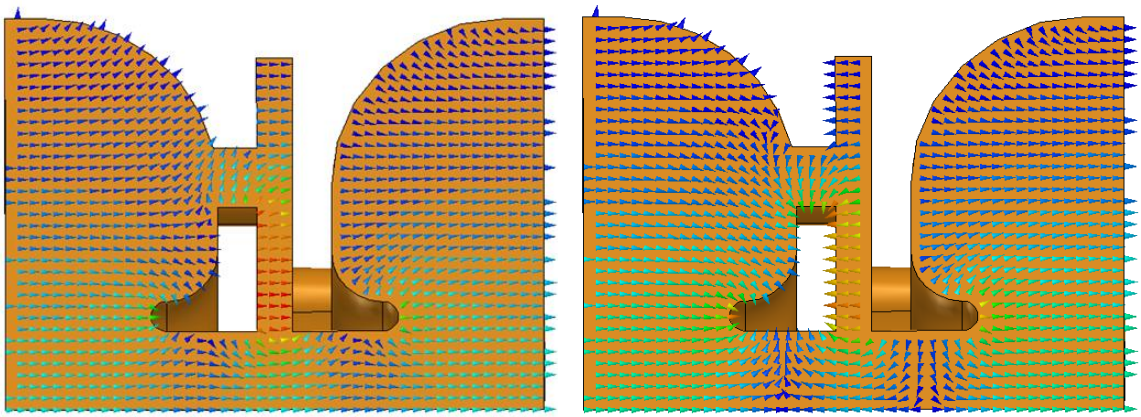

(a) (b)

Figure 3-19. 0 (a) and π (b) modes

After tuning the final data from Table 3-7 are used to calculate the coupling factor between cells, which is **k = 10.5 %**.

Values of the main geometrical parameters after the tuning of assembly 2b+3a are summarized in the Table 3-8.

Table 3-8. Geometrical parameters of the assembly 2b+3a

s(cm)	0.785		Rc(cm)	1.617
Ra(cm)	1.952		α_s	60°
Rb(cm)	0.400		Rs(cm)	1.180
Rn(cm)	0.075		Hs(cm)	0.300

3.3.2.6 Steps (d), (e). Tuning 2a+1b+1a assembly with coupling slots.

The first step consists of tuning the coupling cell (the one placed between segment 1b and 2a).

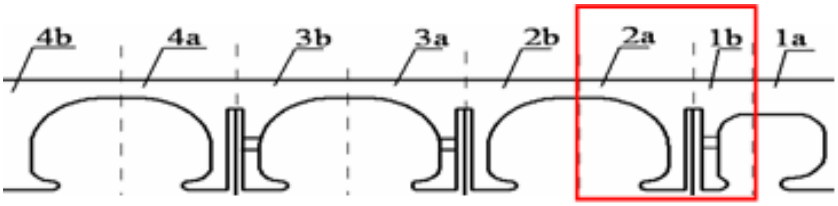

Figure 3-20. 3D optimization: Step (d)

In order to tune this cell, a simulation of the section marked in red from Figure 3-20 is needed. In this step just the resonant frequency of coupling cell can be tuned because cell 1a1b is not symmetric. Magnetic walls are placed at both sides to excite the resonant mode in the coupling cell (Figure 3-21).

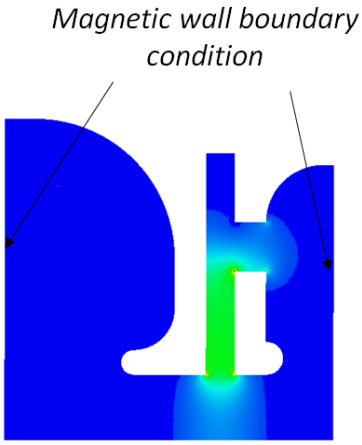

Figure 3-21. Coupling cell excited (assembly 2a+1b)

To tune the accelerating cells and to get the coupling slots dimensions the segment 1a is needed. Therefore an iterative process between step (d) and (e) is performed.

Only the final results of this iterative method are described here (Table 3-9).

Table 3-9. Final RF parameters of assembly 2a+1b

$f_{\pi/2}$ (MHz)	Q_0
5711.8	1810

The other part of this iterative method is to simulate the three segments, 2a+1b+1a, all together (Figure 3-22).

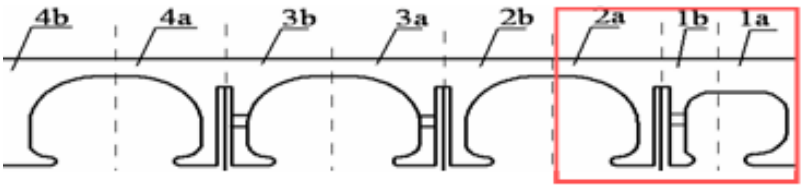

Figure 3-22. 3D optimization: Step (e)

Coupling slots in segment 1b and 2a have been modified in order to get the right electric field amplitude relation between accelerating cell 2a2b and accelerating cell 1a1b. As we have seen, in the three β =1 cells the maximum E field on axis must be equal to 44.8 MV/m and in the β=0.5 cell the maximum E field on axis must be equal to 43 MV/m (Figure 3-7). Once this requirement is fulfilled, the electric field that the following picture shows is obtained.

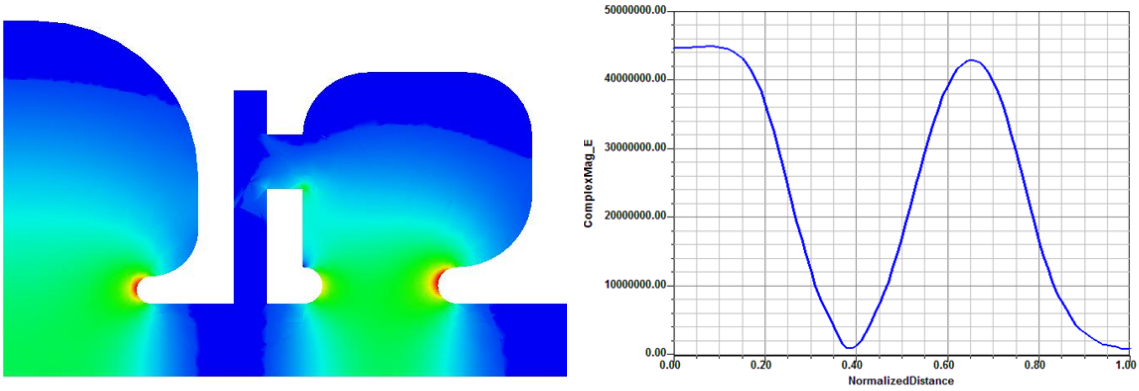

(a) (b)

Figure 3-23. E field amplitude in a cross section (a) and on-axis E field distribution at π/2 - V/m (b) in assembly 2a+1b+1a

In Table 3-10 the final results for the assembly 2a+1b+1a are shown.

Table 3-10. Final RF parameters of assembly 2a+1b+1a

0 mode0	π/2 mode	π mode	k(%)
f=6069.5 MHz	f=5714.5 MHz	f=5453.5 MHz	10.8
Q_0=3190	Q_0=8100	Q_0=2830	

In this step, the computing resources begin to be substantial: In order to get accuracy better than 1 MHz, more than 1.5 GB RAM memory is needed[11] (110000 tetrahedra, see Figure 3-24(b))

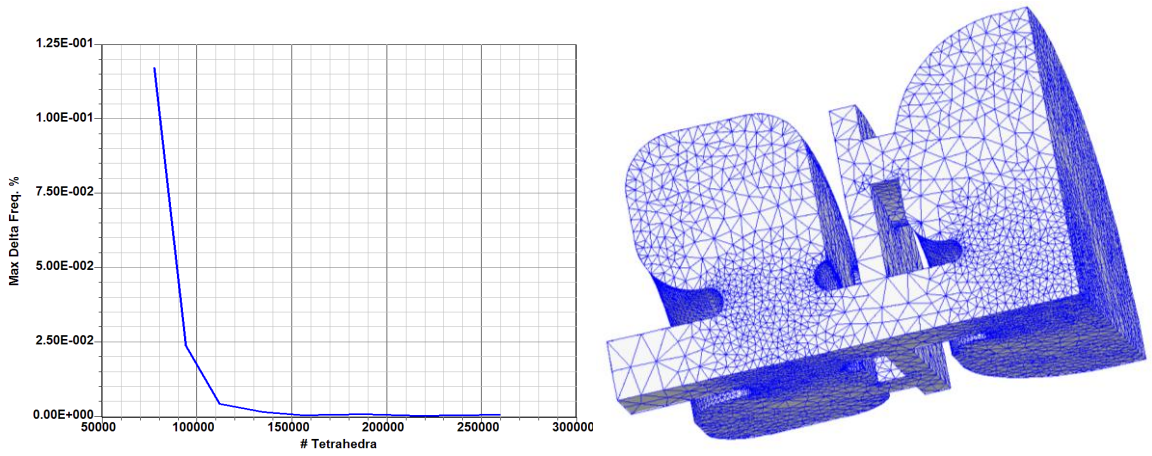

(a) (b)

Figure 3-24. 3D optimization: Step "e": Analysis convergence (a) and HFSS Mesh (b)

The main final geometrical parameters of this assembly are summarized in Table 3-11 and Table 3-12.

Table 3-11. Geometrical parameters of the 1b halfcell.

s(cm)	0.406		Rc(cm)	1.572
Ra(cm)	1.670		α_s	63°
Rb(cm)	0.4000		Rs(cm)	1.180
Rn(cm)	0.100		Hs(cm)	0.300

Table 3-12. Geometrical parameters of the 1a halfcell.

s(cm)	0.4062		Rc(cm)	-
Ra(cm)	1.6700		α_s	-
Rb(cm)	0.4000		Rs(cm)	-
Rn(cm)	0.1000		Hs(cm)	-

[11] *In a HFSS v10 simulation with infinite conductivity*

3.3.2.7 Step (f). Tuning 4b+4a+3b assembly with coupling slots

This step is meant to tune the end cell 4a+4b including the coupling slots (Figure 3-25).

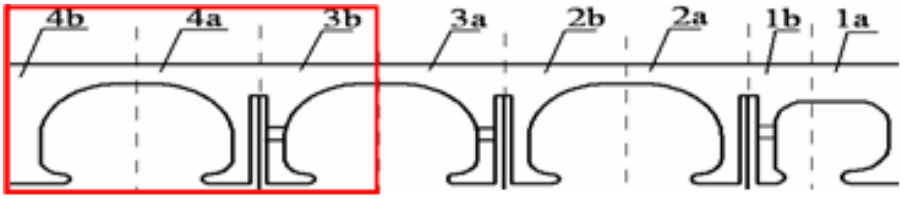

Figure 3-25. 3D optimization: Step (f)

Compared to the regular assembly, some parameters must be slightly modified. This is because the segment 4b does not have coupling slots. In order to get the same field amplitude (as obtained in cell 3a+3b and 2a+2b) in the cell 4a+4b, a reduction in angle of coupling slot in segment 4a was needed. After doing so, the coupling cell must be modified as well.

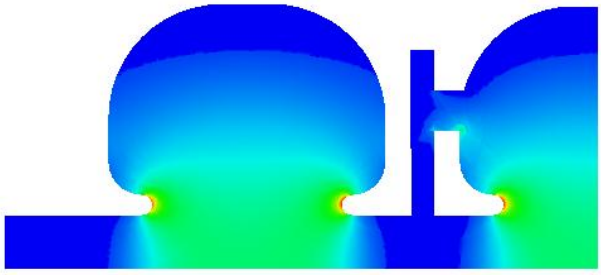

(a)

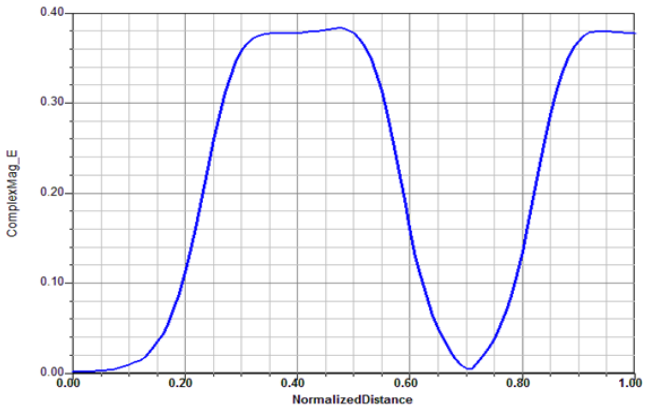

(b)

Figure 3-26. Assembly 4b+4a+3b. π/2 mode E field amplitude in a cross section (a) and on-axis distribution (normalized to max E field on surface) (b)

In Table 3-13 the final RF results for the assembly 4b+4a+3b are shown.

Table 3-13. Final RF parameters of assembly 4b+4a+3b

0 mode0	π/2 mode	π mode	k(%)
6003.8 MHz	5712.6 MHz	5488.3 MHz	9.0
3310	Q_0=10290	2980	

In this step the accelerating cells are almost the same, and there is not extreme rounding as in the 1st cell. That is why the convergence is quite good with less tetrahedral (Figure 3-27).

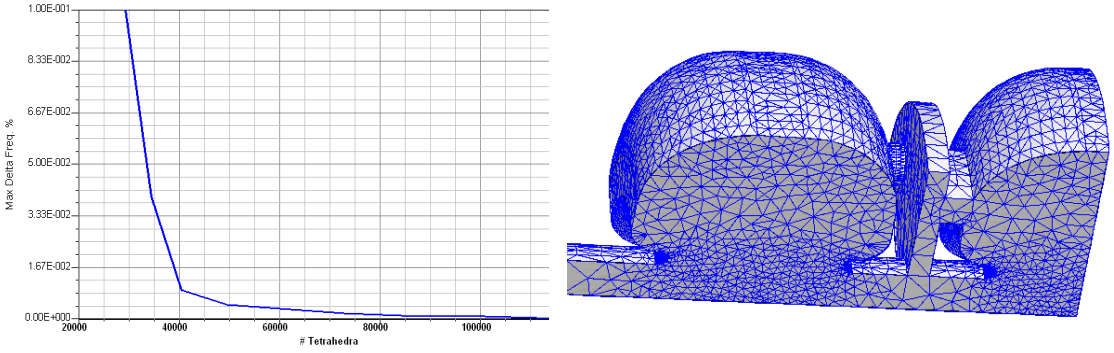

(a) (b)

Figure 3-27. 3D optimization: Step "f": Analysis convergence (a) and HFSS Mesh (b)

The main final geometrical parameters of this assembly are summarized in the following tables.

Table 3-14. Geometrical parameters of the 4a half cell.

s(cm)	0.785		Rc(cm)	1.630
Ra(cm)	1.970		α_s	59°
Rb(cm)	0.400		Rs(cm)	1.180
Rn(cm)	0.075		Hs(cm)	0.300

Table 3-15. Geometrical parameters of the 4b half cell.

s(cm)	0.785		Rc(cm)	-
Ra(cm)	1.970		α_s	-
Rb(cm)	0.400		Rs(cm)	-
Rn(cm)	0.075		Hs(cm)	-

3.3.2.8 Step (g). Calculation of the full assembly: 1a+1b+2a+2b+3a+3b +4a+4b

In this step the full assembly with coupling slots but without coupler will be analyzed. Figure 3-28 shows the vacuum HFSS model made in order to simulate the whole structure, nevertheless only a quarter of this model is needed due to the symmetries.

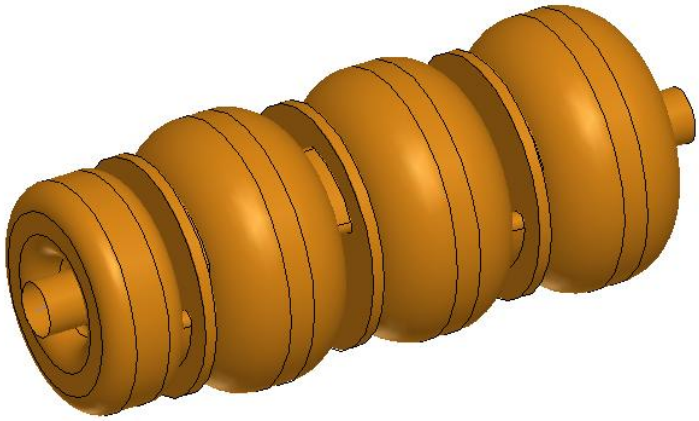

Figure 3-28. HFSS linac vacuum model without coupler

This step consists of checking out that the process followed in the previous steps has produced a well tuned structure according to the specifications. In this step, simulating the full assembly, a good accuracy as in the individual steps cannot be accomplished (the more complex is the 3D model, the more computation resources are needed). However, by doing this simulation, a global understanding of the whole structure can be acquired.

The following picture shows the results of the accelerating field (Figure 3-29(a)), the maximum E field in a cross section (Figure 3-29 (b)) and the vector electric field values at an arbitrary phase (Figure 3-29 (c)).

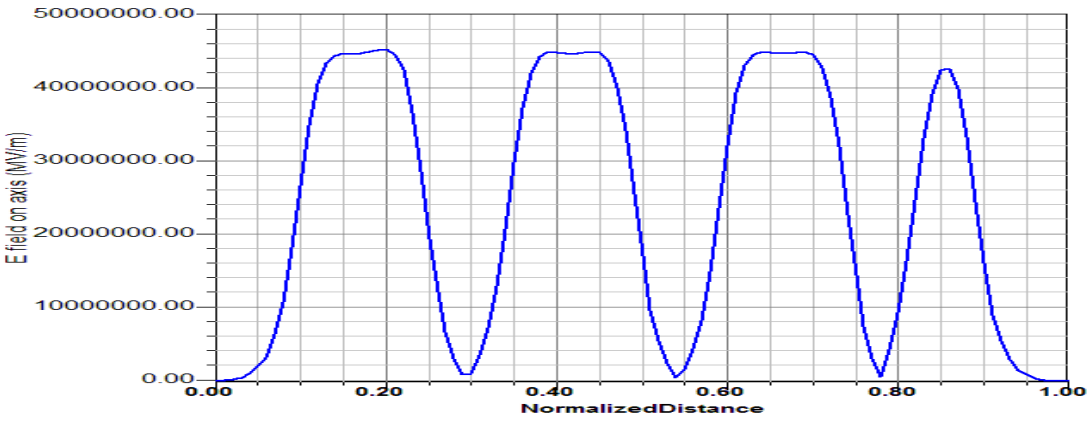

(a)

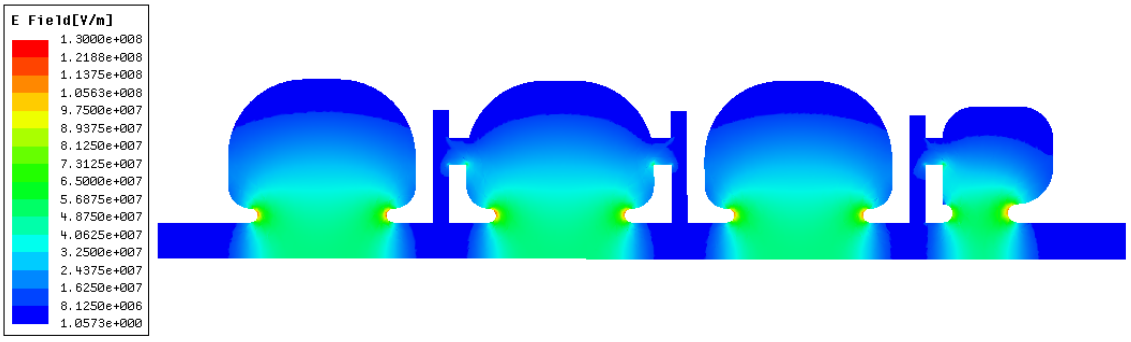

(b)

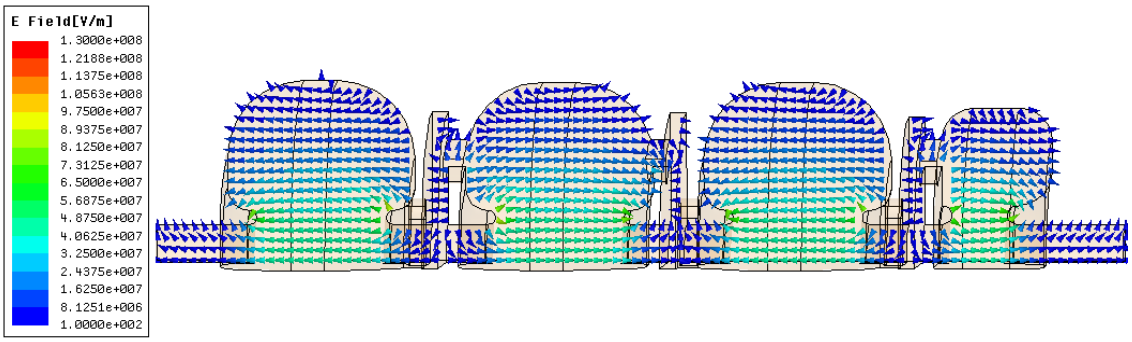

(c)

Figure 3-29. E field values of $\pi/2$ mode. On axis (a), on a cross section (b) and vector values (c)

The main RF characteristics obtained in 3D calculation of the full assembly are listed in the Table 3-16.

Table 3-16. RF characteristics of the full accelerating structure.

Unloaded quality factor Q_0 (π/2 - mode)	9500
Maximal value of electric field on the metal surface, E_{max}(MV/m)	130
Resonant frequencies (MHz)	
π - mode	5461.5
	5507.3
	5594.2
π/2 - mode	**5712.7**
	5849.5
	5975.2
0 - mode	6055.3

The full structure is made of 7 cells: 4 accelerating and 3 coupling cells. Therefore, according to section 2.7, we can expect to get 7 points in the dispersion diagram (being the π/2 mode, which is the one we are interested in, in the middle of the curve). All these resonant modes, belonging to TM_{010} -like mode, appear in Table 3-16 and are represented in the dispersion diagram in Figure 3-30.

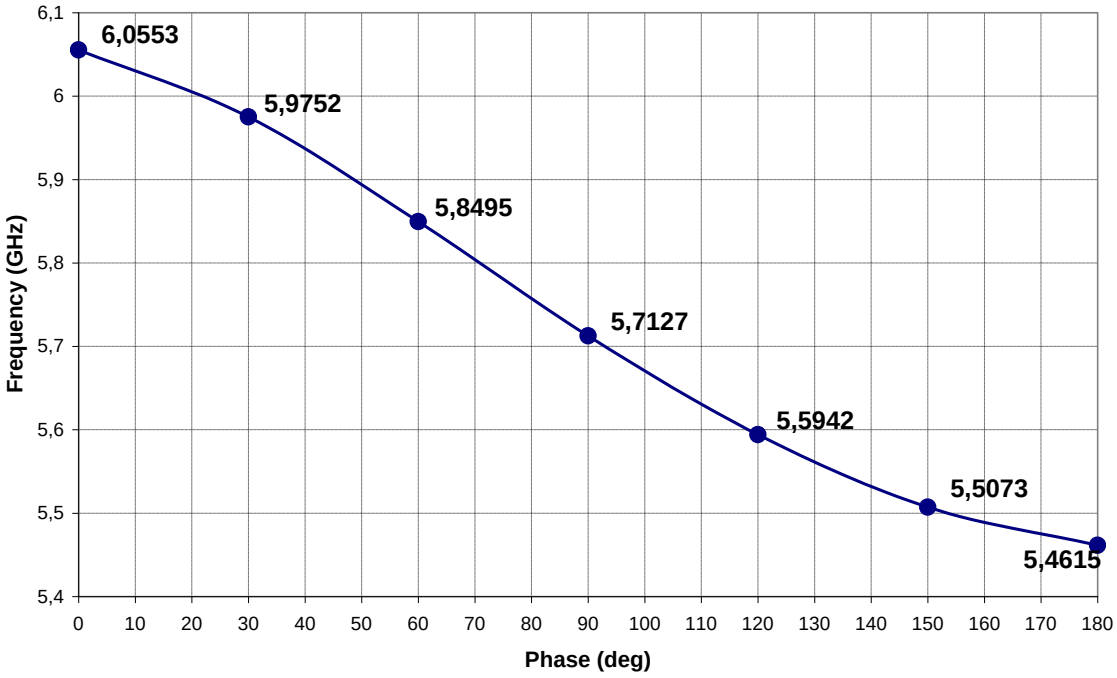

Figure 3-30. Dispersion diagram

It can be noticed that the slope of the curve is negative: it means that phase velocity and group velocity have opposite directions. This fact in a standing wave structure has no relevant meaning. It would be more important in a travelling wave cavity because it should be fed from the end of the structure. The reason for this negative slope falls in the type of coupling between cells: which is of the magnetic kind. If the coupling was electric, that is, with the electromagnetic energy propagating through the beam tube, the slope would be positive.

There could be more resonant modes, besides TM_{010}, that may appear in the accelerating structure disturbing the particles trajectory. These modes will be studied in the following sections.

Looking at the convergence in Figure 3-31(a) and the final mesh Figure 3-31(b) it can be seen that the accuracy of the simulation falls within the order of 0.5 MHz which is enough for the analysis. It must be said that the results depend perceptibly on the mesh used. For this accelerating structure, the mesh has been manually refined in the more delicate surfaces and high fields (as the nose cones). After consecutive iterations, the software also automatically refines the places where the high electric field appears.

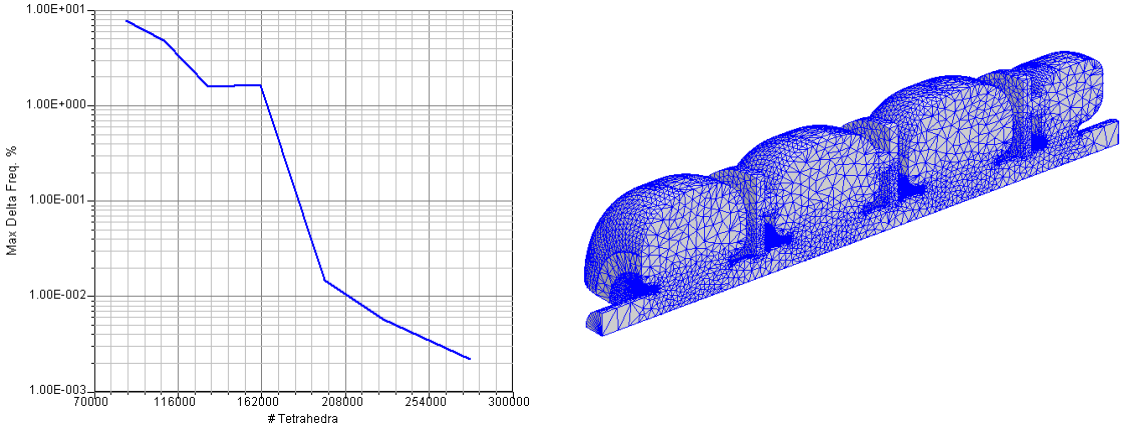

(a) (b)

Figure 3-31. Full structure analysis: Analysis convergence (a) and HFSS Mesh (b)

3.3.2.9 Step (h) Optimization of accelerating structure coupling with waveguide

In this step the accelerating structure coupling with feeding waveguide is studied. It should be noticed that the choice of the coupling with waveguide is defined by two circumstances: by beam loading and by amplitude of the reflected wave necessary for magnetron frequency pulling. For our design pulsed current I_p=5 mA, maximum pulsed beam power is $P_b \approx 60$ kW, while pulsed RF power dissipated in the structure walls is $P_C \approx 600$ kW, so coupling factor to have zero reflected power at steady state in resonance must be (2.19): β=1.1. This would be the coupling factor chosen in a linac fed by a klystron. In that case about zero reflected power comes out from linac under nominal beam loading. However, when operating with magnetron (which is a generator in contrast to klystron, which is an amplifier) one method to provide magnetron operation in resonance with linac is to send back part of RF power from linac (the so called frequency pulling technique). In this case the linac must be over coupled (see section 2.4.1) under nominal beam loading. The exact amount of power, which must be sent back from linac to magnetron to provide frequency pulling with definite accuracy, depends on many parameters, including magnetron parameters and ferrite isolator parameters. Basing on different data over literature it has been chosen a coupling factor 2 to 2.5 as sufficient. Of course, in this case RTM efficiency is decreased, as more power must be produced by the magnetron.

3.3.2.9.1 Method 1: Simulating coupler with single cell

To calculate the coupling, a WR187 waveguide will be connected to an accelerating cell only. Afterwards the coupling factor of the full assembly with the feeding waveguide can be approximately expressed through the external coupling factor β_{cell} of the single cell. According to (2.21) the coupling factor for the whole structure would be:

$$\beta \approx \frac{\beta_{cell}}{4} \tag{3.2}$$

Which means that the coupling is calculated considering that the power dissipated in the whole structure was lost in one single cell.

The main reason to do the calculations with just one single cell is because the computational resources are considerably higher when all the structure plus coupler is included in the model. Besides, as the simulation needed in this step is a sweep in frequency and includes finite conductivity boundary condition (this was optional in previous steps), the resources are even higher than in the previous steps where resonant analyses were performed.

The 3D model made for this step, including finite conductivity boundary condition is shown in Figure 3-32(a). An electric (Figure 3-32(b)) and a magnetic wall (Figure 3-32(c)) are used to take advantage of the symmetry and they simplify the model.

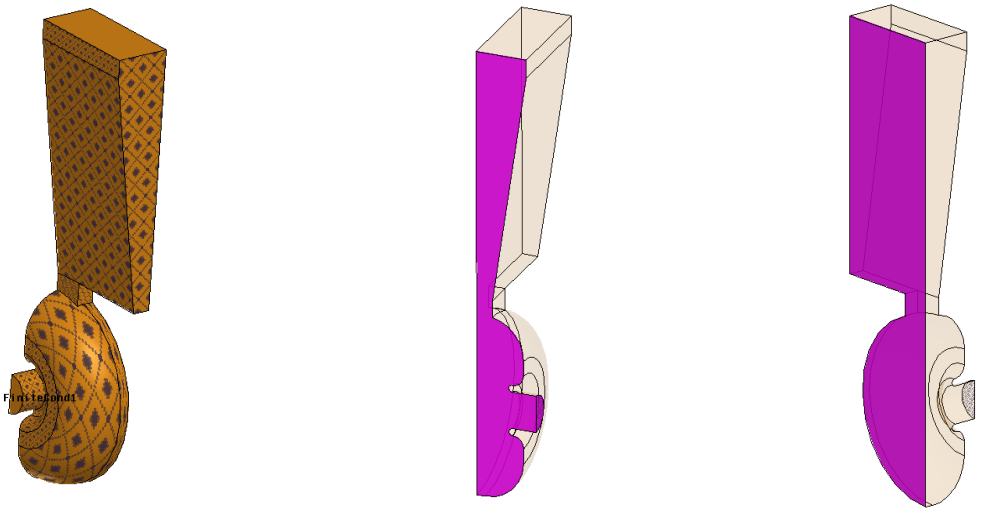

(a) (b) (c)

Figure 3-32. Model for coupler. Finite conductivity (a), magnetic wall (b) and electric wall (c) boundary conditions

As a coupling factor between coupler and structure needed is β=2- 2.5, then the coupling to the single cell β_{cell}=8- 10. Taking into account (2.22), the iris of the structure should be designed to have a minimum reflection at: S11= (-2.18dB to -1.74dB)

By changing the iris parameters *l, w* and *h* (Figure 3-10) when performing various sweep analyses, the minimum S11 is adjusted. According to the simulations the coupling looks more sensitive to the *l* parameter variation.

If the iris dimensions change, the inductive component of the accelerating cell changes as well. Therefore its resonant frequency is not longer tuned and needs to be tuned again modifying its geometrical dimensions.

Figure 3-33 illustrates how *l* parameter modifies the coupling (S11 magnitude) and alters the frequency. This picture is just to make clear the effect of iris dimensions, but analyses have been performed with finer steps.

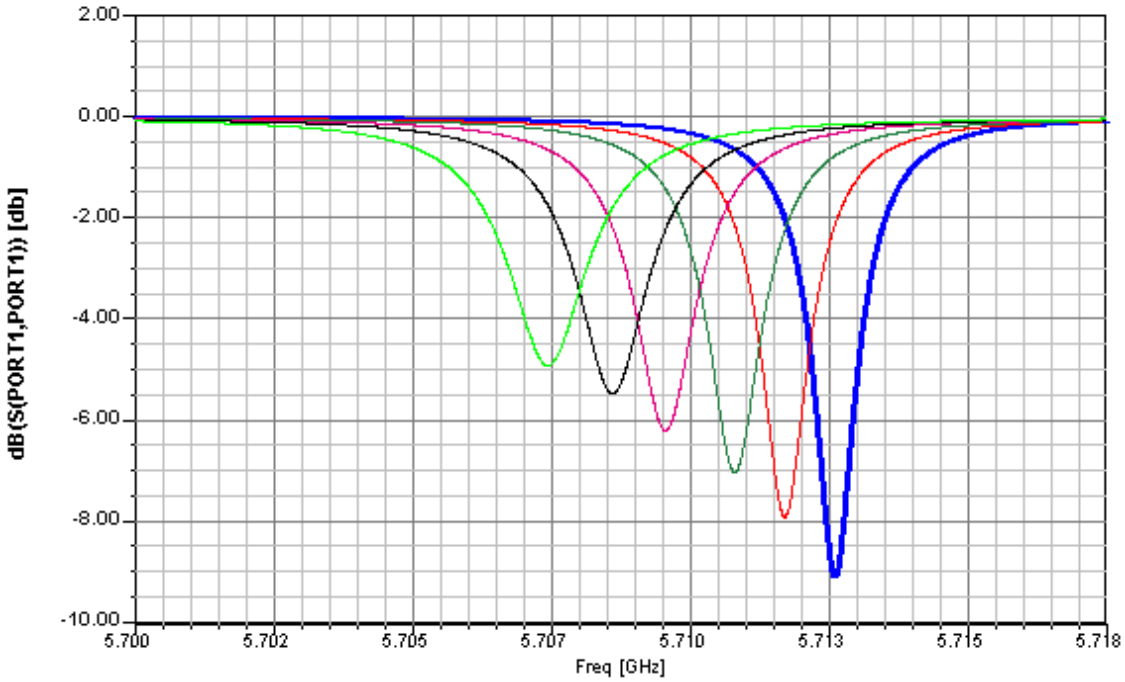

Figure 3-33. S11 variations when *l* changes (*l* blue < *l* green)

When cutting coupling hole in the accelerating cell we decrease cell resonance frequency. To tune the cell to proper frequency we must take into account difference in resonance frequencies of the assembly 3a+3b with coupling slots and without them. From the

calculations with and without coupling slots (Figure 3-34) it can be concluded that the difference is equal to 102 MHz. Therefore the 3a+3b+waveguide assembly without coupling slots must be tuned to the frequency f = 5712+102=5814 MHz by adjusting cell radius Ra (Figure 3-35).

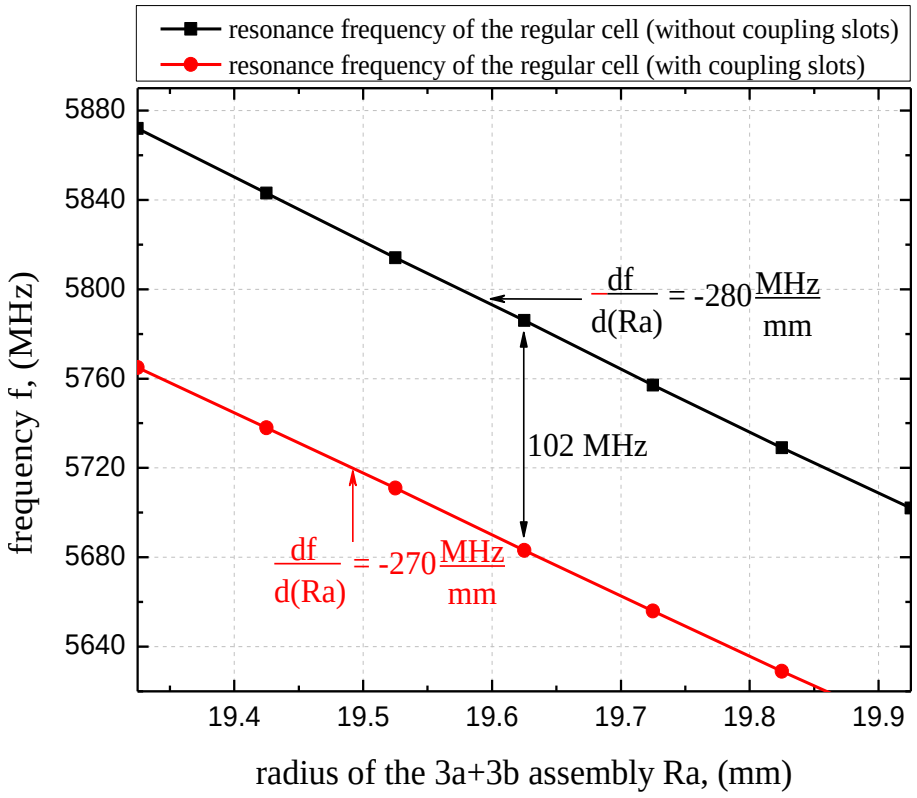

Figure 3-34. Resonance frequency of the 3a+3b assembly versus the assembly radius Ra.

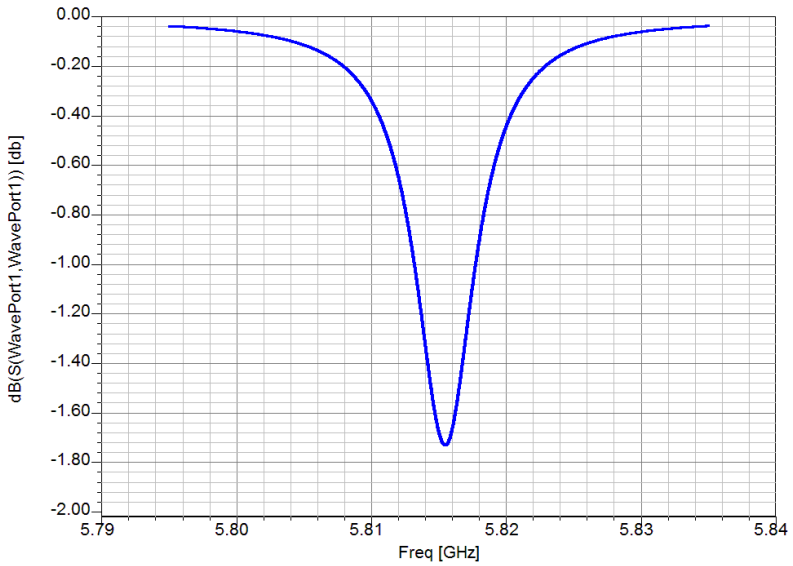

Figure 3-35. Frequency sweep for 3a+3b+waveguide assembly

To provide required coupling with waveguide the length of the coupling hole has been adjusted. The reflection is S11=-1.74dB which, according to (2.22) means a coupling factor β=10. Then, according to (3.2), the coupling factor for the full assembly would be β = 2.5.

However, it should be noticed that coupling with waveguide for real accelerating structure depends on the unloaded quality factor Q_0 (2.15) which, in turn, depends on the surface roughness. The lower Q_0, the longer coupling slot must be to provide the same coupling factor. So, ordinary practice is to produce final adjustment of the coupling iris length during measurements and tuning of the brazed structure. That is why in calculations it has been considered a coupling factor in the range 2 – 2.5 as satisfactory. Optimal geometrical parameters and corresponding RF characteristics of the tuned assembly 3a+3b+waveguide are listed in Table 3-17.

Table 3-17. Geometrical parameters and RF characteristics of the tuned assembly 3a+3b+waveguide.

Assembly radius, Ra (cm)	1.940
Coupling iris width, w (cm)	0.700
Coupling iris length, l (cm)	1.440
Coupling iris height, h (cm)	0.350
Coupler height, H (cm)	5.00
Coupler length, L (cm)	4.750
Coupler width, W (cm)	2.210
Coupling factor, β	2.5

The advantage of this first method used is, as it has been said before, the less computational resources needed. In Figure 3-36 the convergence and final mesh are shown. In this case the iterations are referred to the maximum variations of S parameters because a driven modal analysis is used[12]. With this method the convergence is quite good and with less than 80000 tetrahedra an accuracy better than 1 MHz is obtained.

[12] *Type of HFSS analysis in which RF ports are used (instead of eigenmode analysis in which resonant frequencies are computed)*

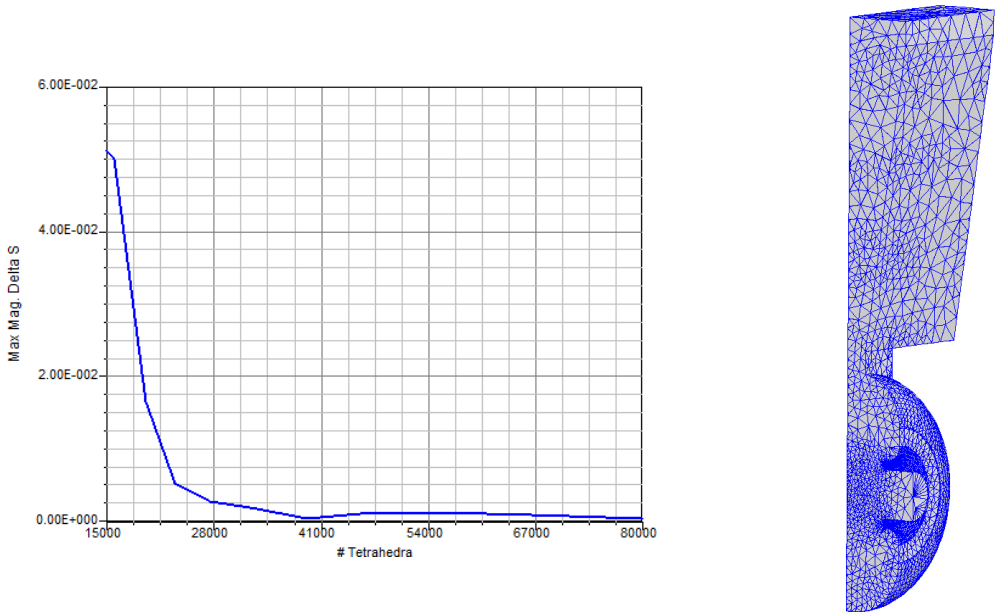

(a) (b)

Figure 3-36. Step h. Method1. Convergence (a) and final mesh (b)

3.3.2.9.2 Method 2: Coupler and full assembly

The main error of the previous method is due to the lack of symmetry of the accelerating structure (the β=0.5 initial cell is smaller). That is why the calculation of the coupling factor in the first method is just an approximation: all the accelerating cells do not dissipate the same power in their walls. Nevertheless, the accuracy to obtain a coupling factor within the range 2 to 2.5 is enough. Besides, the accuracy of geometrical calculations for the cell 3 is quite good.

The second method, which consists of simulating the whole structure plus the coupler, is just available with new modern computer and codes capabilities. They permit to make this step by modelling behaviour of the full assembly 1a+1b+2a+2b+3a+3b+4a+4b with coupler. 3D model of the full assembly for coupling factor tuning is represented in the Figure 3-37.

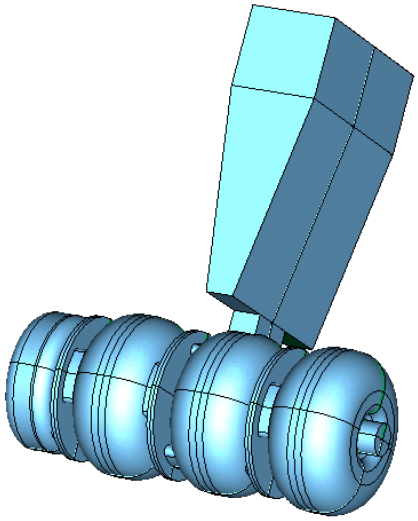

Figure 3-37. The geometry of the full assembly for coupling factor tuning

The resonance frequency of the full assembly, obtained during the calculation with the geometrical parameters of the feeding waveguide, is equal to 5712.5 MHz (Figure 3-38).

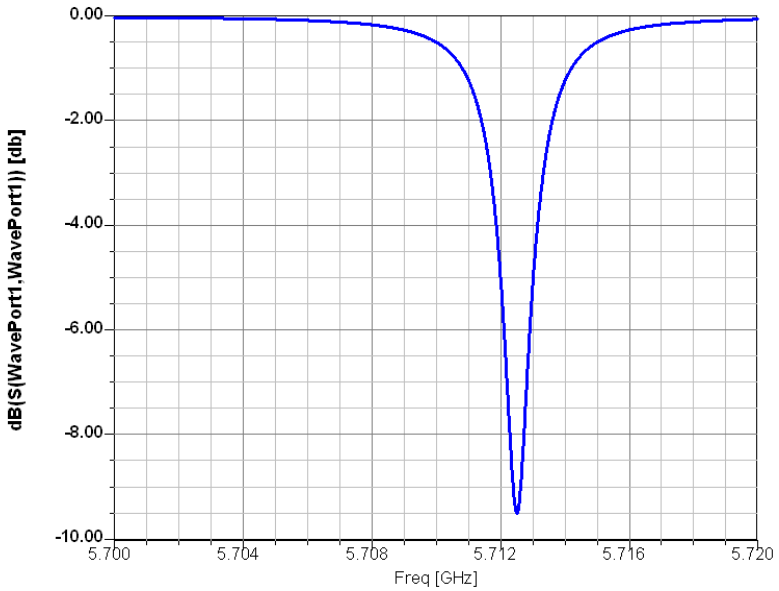

Figure 3-38. S11 parameter in full assembly with coupler[13]

And, from the reflection S11= -9.50 dB, the coupling factor is calculated with (2.22)=>β= 2.0. Looking at the convergence Figure 3-39(a) and checking that the mesh is good Figure 3-39(b), it can be concluded that the accuracy falls within the order of 0.01 for S parameters and so according to (2.22) the error in β is lower than 0.1. This enough for the design of the

[13] *Iris coupling dimensions are equal in both methods*

accelerating structure as both the mechanical errors and surface roughness will be much more decisive in the final coupling.

Pass Number	# Tetrahedra	Max Mag. Delta S
1	353250	N/A
2	396207	0.048289
3	436644	0.018574
4	487008	0.010342

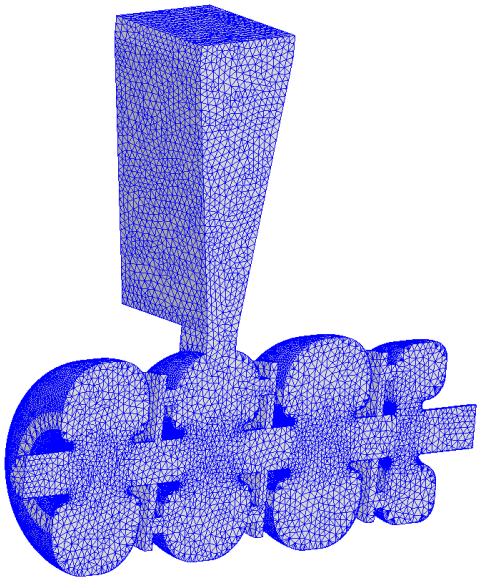

(a) (b)

Figure 3-39. Convergence of the full analysis (a) and final mesh used (b)

This result, obtained with a 24 GB RAM computer, is excellent and confirms that the structure is well tuned. However, as it has been anticipated before, the iris dimensions differ from the one obtained in the first method. In spite of this difference, the two different coupling factor values fall within the range desired for this coupling.

3.3.2.10 Summary of 3D linac optimization

The main goal of 3D structure simulation step was preparing data for engineering design of accelerating structure: choice of the coupling slots position and dimensions to provide necessary field distribution with maximum structure efficiency and field stability, tuning of the accelerating and coupling cells resonance frequency after cutting coupling slots, calculation of coupler cell geometry providing RF power input in accelerating structure with designed value of coupling between feeding waveguide and linac.

3.3.3 Calculations of the tolerances for basic cell dimensions

In order to obtain the basic tolerances of the structure, a sensitivity analysis must be performed. A 2D analysis is enough to study the sensitivity. In fact, this kind of analysis provides tighter tolerances than a 3D analysis because the fact of including the coupling slots makes these tolerances to be more relaxed. This 2D analysis can be done with either a 2D code (like SUPERFISH) or a 3D code (like HFSS or ANSYS). Finally the study has been performed with HFSS software.

To study the sensitivity the geometrical dimensions of regular β=1, β=0.5 and coupling cell are modified and their change in frequency is observed. Even though we are interested in small changes in the dimensions, for the study, the change of the geometrical dimensions should be relevant so the accuracy of the numerical mesh does not ruin the results. So, steps from 20 to 50 microns along an interval of 100 – 500 microns have been used as reasonable values.

In the following figures, the sensitivity analysis in 2D (without coupling slots) is shown.

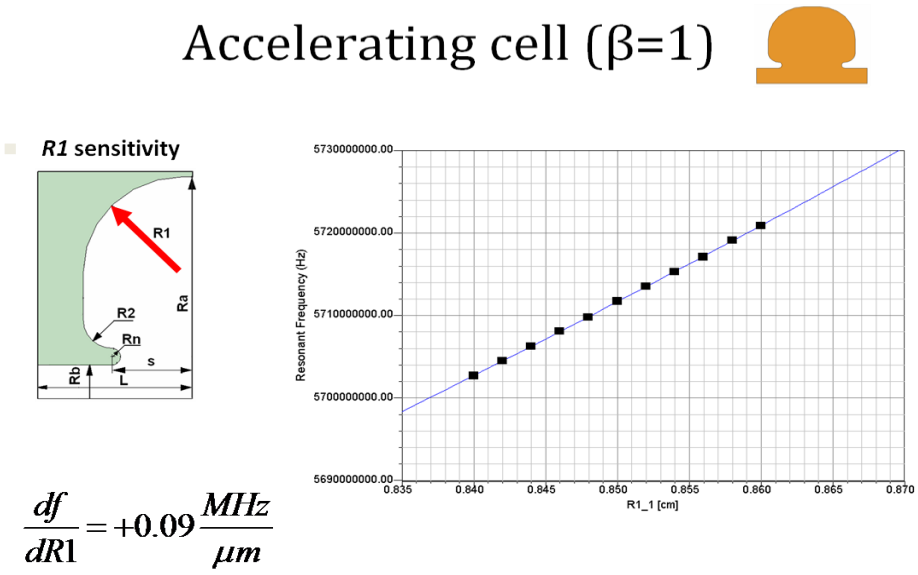

Figure 3-40. R1 parameter sensitivity for β=1 cell

R2 sensitivity

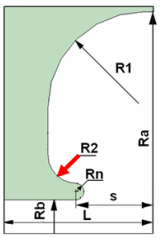

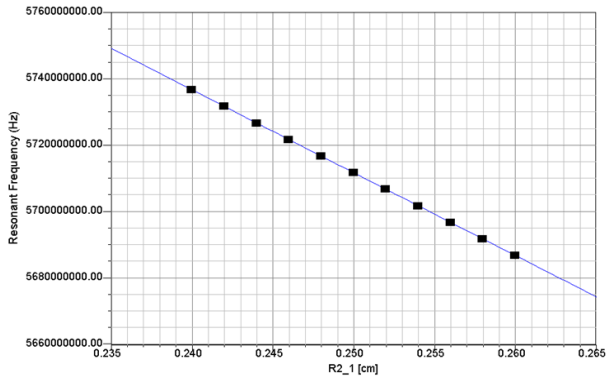

$$\frac{df}{dR2} = -0.25\frac{MHz}{\mu m}$$

Figure 3-41. R2 parameter sensitivity for β=1 cell

Ra sensitivity

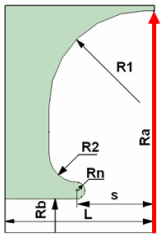

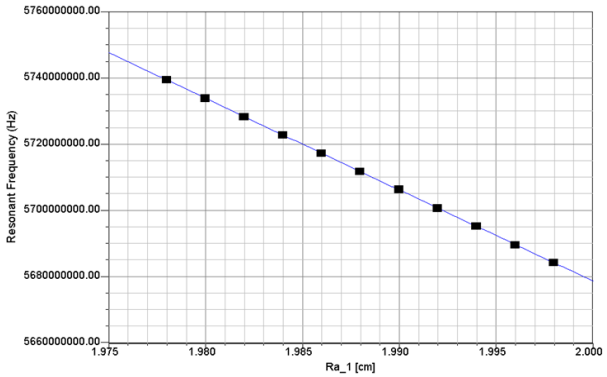

$$\frac{df}{dRa} = -0.28\frac{MHz}{\mu m}$$

Figure 3-42. Ra parameter sensitivity for β=1 cell

Rb sensitivity

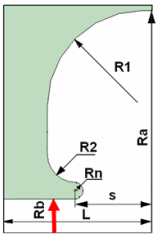

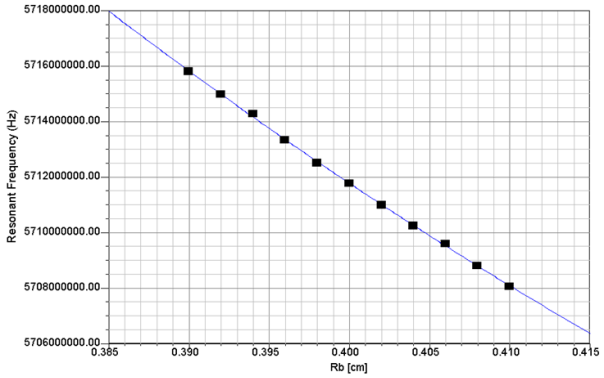

$$\frac{df}{dRb} = -0.04\frac{MHz}{\mu m}$$

Figure 3-43. Rb parameter sensitivity for β=1 cell

Rn sensitivity

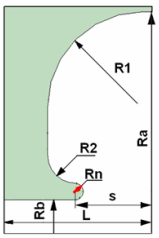

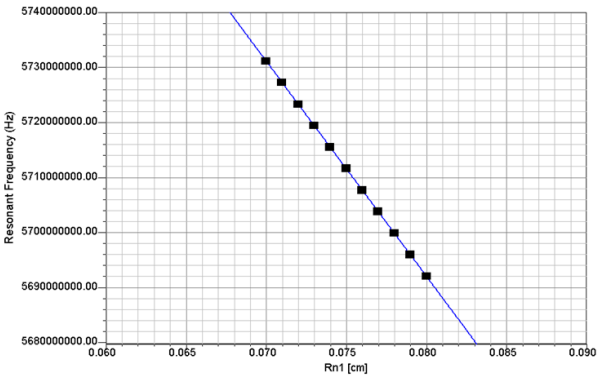

$$\frac{df}{dRn} = -0.39 \frac{MHz}{\mu m}$$

Figure 3-44. Rn parameter sensitivity for β=1 cell

q sensitivity

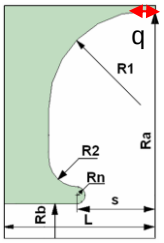

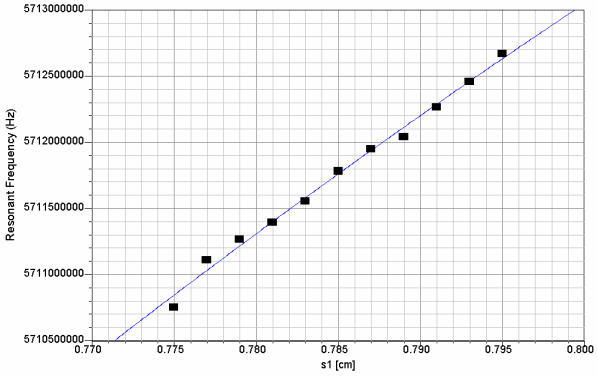

$$\frac{df}{dq} = +0.01 \frac{MHz}{\mu m}$$

Figure 3-45. q parameter sensitivity for β=1 cell

s sensitivity

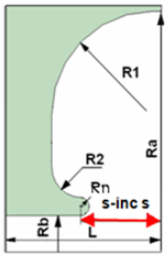

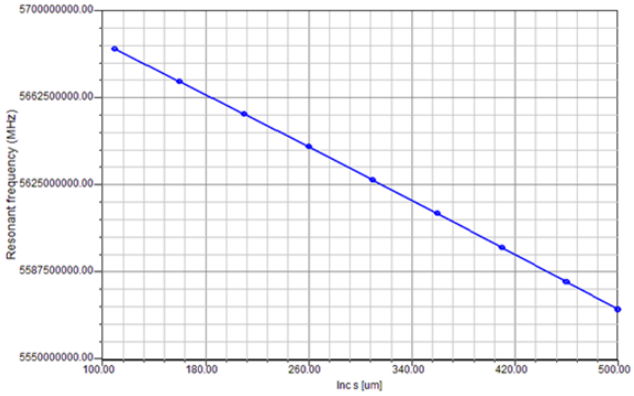

$$\frac{df}{ds} = +0.28 \frac{MHz}{\mu m}$$

Figure 3-46. s-Δs parameter sensitivity for β=1 cell

- *R1* sensitivity

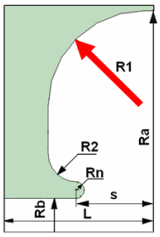

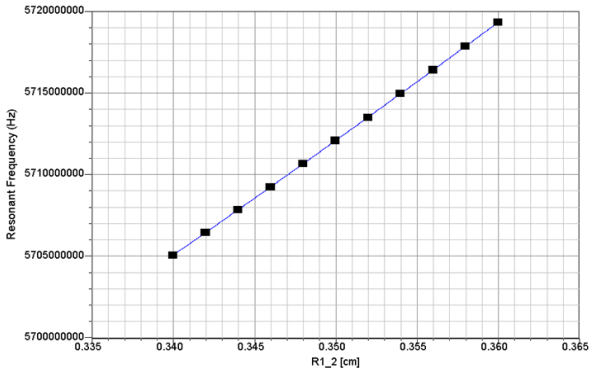

$$\frac{df}{dR1} = +0.07 \frac{MHz}{\mu m}$$

Figure 3-47. R1 parameter sensitivity for β=0.5 cell

- *R2* (1a) sensitivity

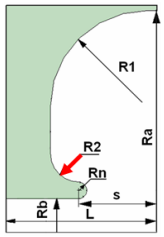

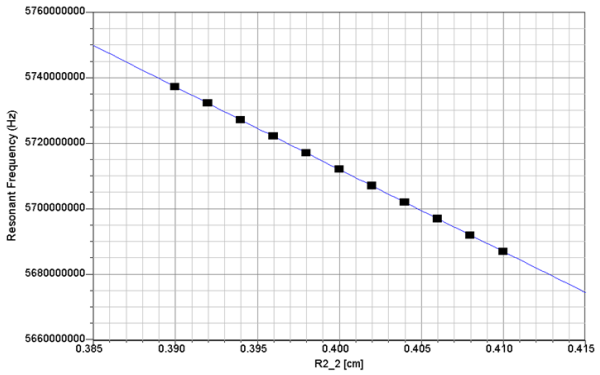

$$\frac{df}{dR2} = -0.25 \frac{MHz}{\mu m}$$

Figure 3-48. R2 parameter sensitivity for β=0.5 cell

- *Ra* sensitivity

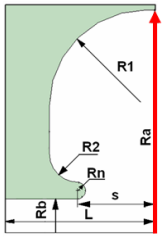

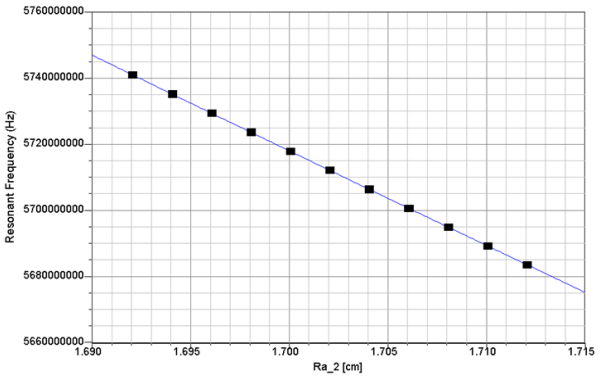

$$\frac{df}{dRa} = -0.29 \frac{MHz}{\mu m}$$

Figure 3-49. Ra parameter sensitivity for β=0.5 cell

Rb sensitivity

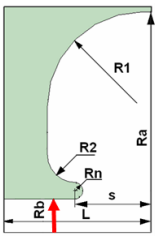

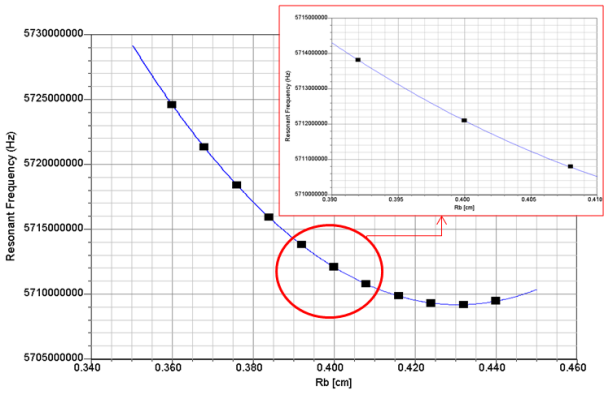

$$\frac{df}{dRb} = -0.02 \frac{MHz}{\mu m}$$

Figure 3-50. Rb parameter sensitivity for β=0.5 cell

Rn sensitivity

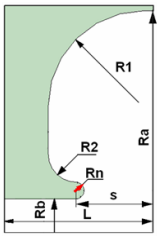

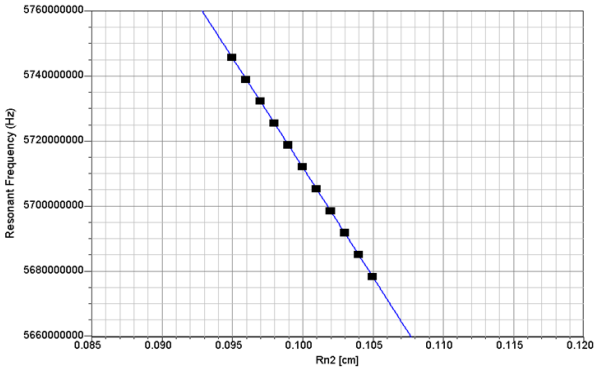

$$\frac{df}{dRn} = -0.67 \frac{MHz}{\mu m}$$

Figure 3-51. Rn parameter sensitivity for β=0.5 cell

q sensitivity

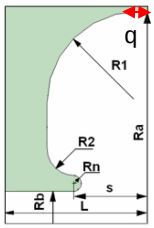

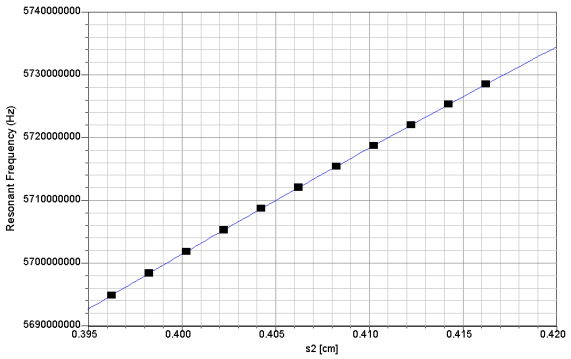

$$\frac{df}{dq} = +0.17 \frac{MHz}{\mu m}$$

Figure 3-52. q parameter sensitivity for β=0.5 cell

Coupling cell

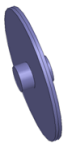

Rc sensitivity

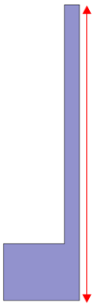

$$\frac{df}{dRc} = -0.29 \frac{MHz}{\mu m}$$

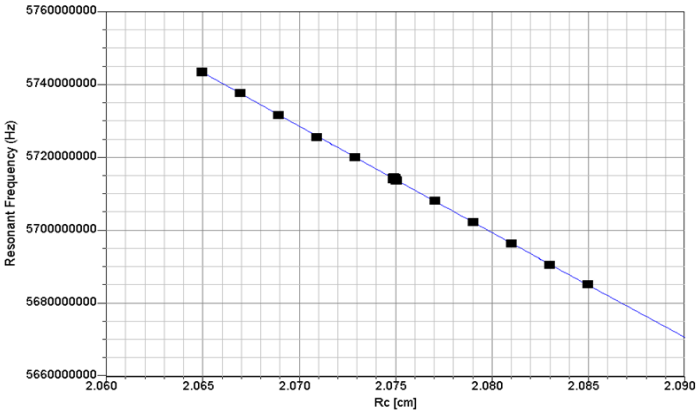

Figure 3-53. Rc parameter sensitivity coupling cell

Rb sensitivity

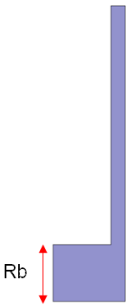

$$\frac{df}{dRb} = +0.11 \frac{MHz}{\mu m}$$

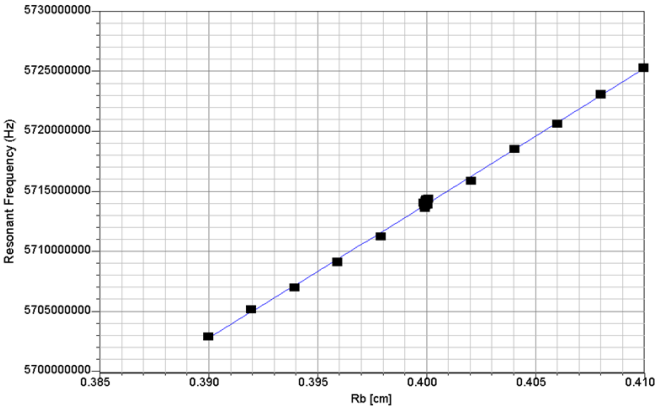

Figure 3-54. Rb parameter sensitivity for coupling cell

Lc sensitivity

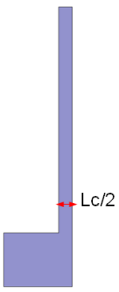

$$\frac{df}{d\,Lc/2} = -0.01 \frac{MHz}{\mu m}$$

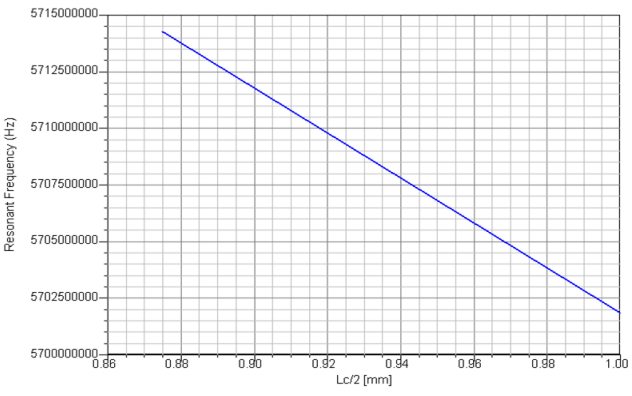

Figure 3-55. Lc parameter sensitivity coupling cell

The study has shown that the resonant frequency is quite sensitive to certain parameters. The most important parameter is the radius of the nose cones *Rn* (for both accelerating β=1 and β=0.5 cells), reaching a maximum value of -0.67 MHz/μm in the β=0.5 cell: That means that with just an error of 2 μm, the change in resonant frequency is more than 1 MHz. The other two relevant parameters are the external radii *Ra* (and *Rc*), distance between nose cones *s* and *R2*, with a bit less effect on the resonant frequency than Rn.

Concerning the tolerances for the machining of the accelerating structure: this high resonant frequency dependence on geometrical dimensions makes mandatory to ask for the best tolerances available for the more delicate parameters. As it is not reasonable to ask for machining tolerances of ±1 μm, a sensible value for the better tolerance could be ±10 μm. We will deal with this problem in more detail in chapter 5.

3.3.4 Analysis of multipole fields caused by the coupling slots and waveguide

If a cavity has axial asymmetry geometrically, the asymmetry mixes the otherwise symmetric accelerating mode with multipole modes [65] therefore, the possibility of these fields producing a deflecting force on the particles must be studied. These calculations may be of extreme importance when e.g. very small emittance beam generation with RF gun will be studied.

At early stages of standing wave accelerating structures development no special attentions were paid to the number and position of coupling slots. Typically for biperiodic on-axis coupled structure the coupling slots both in accelerating and coupling cells were rotated for 90^0 to decrease direct coupling over one cell. Later on with improvement of beam emittance and development of beam diagnostic effect of coupling slots on beam dynamics was discovered and methods to suppress coupling slot effects were elaborated [66][67]. Specifically, placing coupling slots parallel in ACs provide partial cancellation (depending on particle phase) of their influence on the beam. The slots in short CC must be rotated for 90^0 to avoid direct coupling between ACs and so produces quadrupole focusing. But two coupling CCs partially compensate each other acting as quadrupole doublet.

Nevertheless. (1) Compensation in AC and for CCs is not 100%. (2) The number of CCs in linac can be odd so one CC can be uncompensated. (3) The AC placed at linac end contains slots at only one web, which are uncompensated. Finally, coupler cell contains coupling iris which can introduce essential field asymmetry near the axis. That is why numerical simulation must be conducted to study mentioned effects. In the RTM linac there are various kind of asymmetries:

- Coupling cell asymmetry caused by the coupling slots.
- First accelerating cell with coupling slots at one web.
- β=1 accelerating cell with coupling slots at both webs and with coupling loop hole.
- β=1 accelerating cell with coupling slots at both webs and with waveguide coupling hole.
- β=1 accelerating cell with coupling slots at one web.

3.3.4.1 Effect of coupling slots

The main effect of coupling slots on the transverse beam dynamics for on-axis coupled accelerator structure is quadrupole beam focusing in one plane and defocusing in the other, which is explained by quadrupole field asymmetry in accelerating cells introduced by coupling slots [66]. To compensate this effect coupling slots in accelerating cells are aligned with the pair of slots at one accelerating cell web exactly against the pair at the other web.

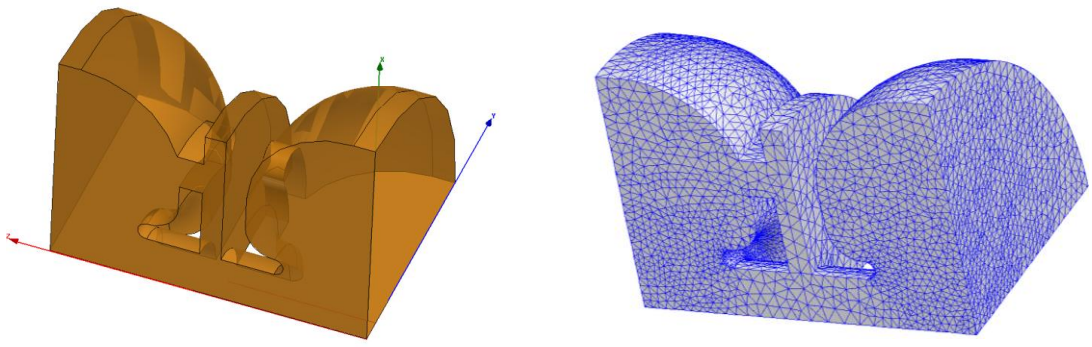

(a) (b)

Figure 3-56. Model used (a) and mesh (b) for the multipole field effect caused by coupling slots

For this study, a model made of two half accelerating cells and one coupling cell with coupling slots has been used (Figure 3-56). Inter cell coupling is provided by the strong asymmetric

fields excited in the coupling cells. In Figure 3-57 the quadrupole shape of the H field in the coupling cell middle plane is shown. This picture shows clearly the quadrupole effect of the coupling slots in the coupling cell, however, the field near the axis which is the one that could affect the particles motion is much lower. The amplitudes of the quadrupole disturbance fields are small-scale comparing to axial-symmetric accelerating fields, therefore the calculation of asymmetrical components in the system with small perturbation of symmetry is very delicate question.

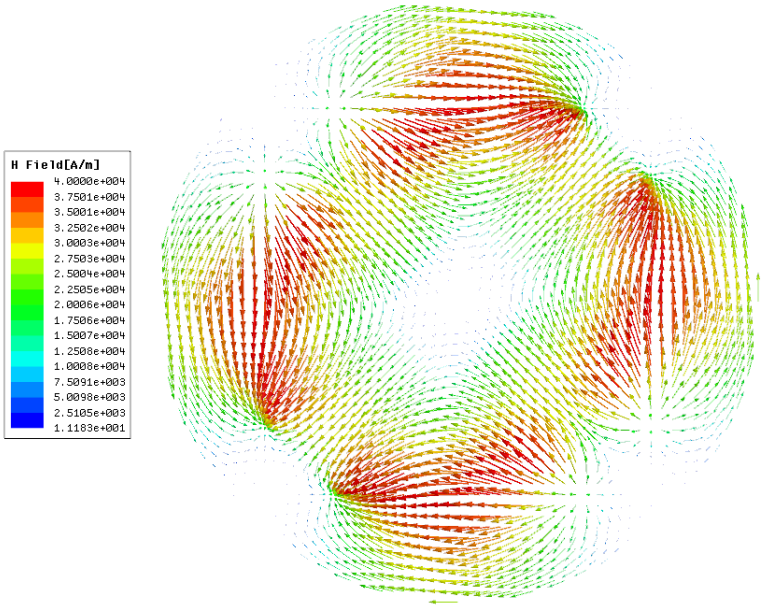

Figure 3-57. H field vector in coupling cell middle plane

The following picture has been obtained scaling the minimum H azimuthal field to 0 and the maximum to 1. This way, one of the four lobes of the quadrupole field may be represented near the axis (at 2mm off axis). The accuracy of the HFSS simulation performed is the highest possible with a 24 GB RAM computer.

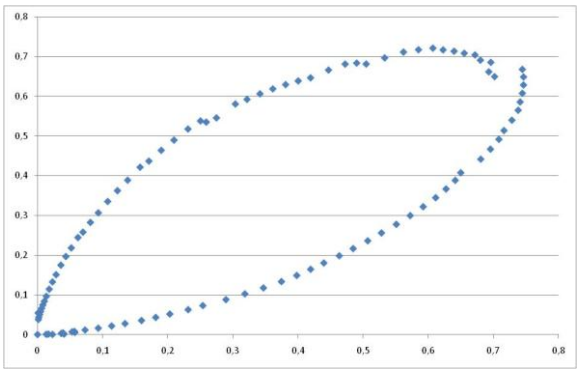

Figure 3-58. Scaled H field to [0-1] at 2mm off axis showing one lobe of the quadrupole

To look into the transverse momentum kick [67] on particles off-axis, calculations have been performed in which the x and y components of net force integral are

$$U_x = e\int_{z1}^{z2}\left[-vB_y\sin\left(\frac{\omega z}{v}\right)+E_x\cos\left(\frac{\omega z}{v}\right)\right]dz \tag{3.3}$$

$$U_y = e\int_{z1}^{z2}\left[vB_x\sin\left(\frac{\omega z}{v}\right)+E_y\cos\left(\frac{\omega z}{v}\right)\right]dz \tag{3.4}$$

These integrals must be understood as an energy transfer from the longitudinal direction to the transverse one by magnetic field (the magnetic force does not increase particles energy) and transverse acceleration by transverse component of electric field.

The signs in the previous integrals have been chosen according to the fields of the accelerating mode from Figure 3-59.

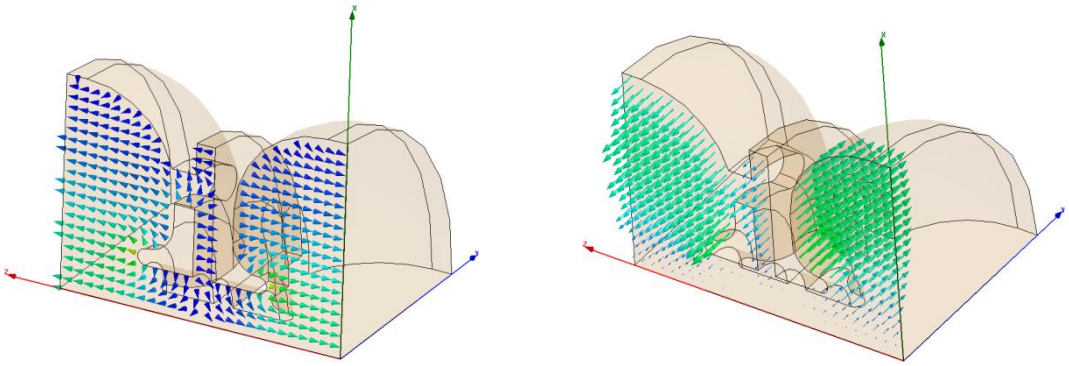

(a) (b)

Figure 3-59. E field at RF phase = -10 deg (a) and H field at RF phase=-10deg

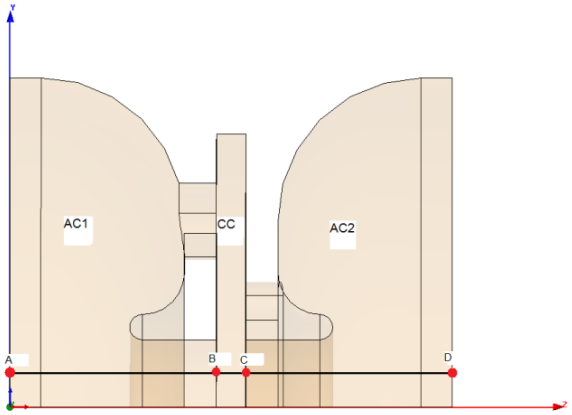

Figure 3-60. Integration path

The results of the integrals calculated along the lines at 2mm off axis in different planes (ZX, ZY and ZY-ZX 45deg) are represented in Table 3-18[14]. In Figure 3-60 the integration paths(ZY plane in the picture) are shown. The maximum E accelerating field on axis has been scaled to 44.8 MV/m.

Table 3-18. Coupling and accelerating cell contribution to transverse momentum kick (eV)

	AC1 (A-B)	**CC (B-C)**	**AC2 (C-D)**
ZY Plane	**Ux=-4.5** Uya=-21111 Uyb=-23502 **Uy=-44613**	**Ux=+11** Uya=-2410 Uyb=-4.4 **Uy=-2414**	**Ux=+36** Uya=+19306 Uyb=+23757 **Uy=+43063**
ZY/ZX 45deg Plane	Uxa=-13765 Uxb=-16846 **Ux=-30611** Uya= -14868 Uyb=-16655 **Uy=-31523**	Uxa=+1878 Uxb=2.62 **Ux=1880** Uya=-1870 Uyb=-0.7 **Uy=-1871**	Uxa=+14872 Uxb= +16654 **Ux=+31426** Uya=13744 Uyb=16867 **Uy=+30611**
ZX Plane	Uxa=-19347 Uxb= -23679 **Ux=-43026** **Uy=+1**	Uxa=+2410 Uxb= 7.7 **Ux=+2418** **Uy=+7**	Uxa=+21118 Uxb=+23559 **Ux=+44677** **Uy=+3**

It can be shown with Panofsky-Wenzel theorem [68] that for axially symmetric cavity and axially symmetric fields which values go to zero at both ends of the beam pipe, U_x and U_y must be equal to zero. This means that for ultra relativistic particle moving parallel to the axis the net focusing power is zero independently of initial phase. Nevertheless, if one takes into account particle displacement and change of its velocity within the cavity, then cavity acts as a weak focusing lens with focal power decreasing inversely with the square of particle momentum.

The values of U_x and U_y given in Table 3-18 for halves of accelerating cells are mainly due to axially symmetric radial electric and azimuthal magnetic fields. For the cavity with axial symmetry within accuracy of calculations U_x for ZY plane and U_y for ZX plane must be equal to zero for both accelerating cell halves and U_y for ZY plane and U_x for ZX plane must be equal to each other. The difference between U_x and U_y in separate accelerating cell and difference between U_x and U_y in AC1 and AC2 comes from the breaking of axial symmetry.

[14] *Ux=Uxa+Uxb and Uy=Uya+Uyb Being Uxa and Uya the contribution from the magnetic force and Uxb and Uyb the contribution from the electric force*

Looking at the data from Table 3-18 we can see that the accelerating half, besides the main azimuthally uniform transverse energy, contains also quadrupole component. Extracting azimuthally symmetric part (calculated as average of U_y in YZ plane and U_x in XZ plane) it has been found that quadrupole fields provide transverse beam energy of 0.8 keV at 2 mm displacement in one or another plane. The focal length *f* is

$$f \cong \frac{h}{\varphi} \tag{3.5}$$

where *h* is the distance from axis, and φ is the deviation angle of particles found at *h* off axis

$$\varphi = \operatorname{atan}\left(\frac{p_x}{p_z}\right) \tag{3.6}$$

where p_x [15] and p_z are the transverse and longitudinal momentum respectively.

For 2 MeV electrons after the first acceleration through the linac this means getting of about 0.3 mrad inclination of the trajectory to the axis corresponding to about 6.7 m focal length. This focal length grows proportionally to particle momentum. When two halves of accelerating cell are connected together focusing of one half is compensated by defocusing of the second half.

For coupling cell, the transverse energy distribution along the azimuth is dominated by quadrupole component, and corresponding focal length for a single coupling cell is about 2 m at 2 MeV.

3.3.4.2 Effect of coupling iris

The structure with the coupling iris does not have cylindrical symmetry. This asymmetric configuration generates asymmetric fields at their adjacent regions so the deflecting fields on the axis are no longer zero.

[15] *$p_x = U_x/c$. If kinetic energy = 2 MeV, then p_z=2.458 MeV/c*

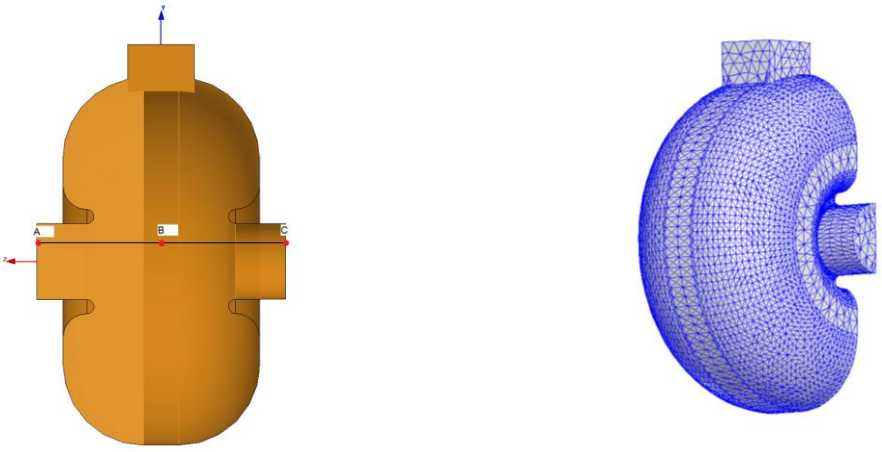

(a) (b)

Figure 3-61. Model used, integration path (a) and mesh (b) for the multipole field effect caused by the coupling hole

For this study, a model made of an accelerating cell without coupling slots and with coupling hole has been used (Figure 3-61).

Table 3-19. Coupling iris contribution to transverse momentum kick (eV)

	A-B	**A-C**
ZY Plane	**Uy=-40028** (Uya=-16400 Uyb=-23628) **Ux= -35**	**Uy=-105.4** **Ux= -37**
ZX Plane	**Uy=2775** (Uya=2962 Uyb=-187) **Ux=43038** (Uxa=+20165 Uxb=+22873)	**Uy=44.6** **Ux= -221**

These results show that the asymmetry produced by the coupling hole has a little effect on the transverse momentum compared to the effect caused by the coupling slots. The maximum net effect is found in the ZX plane with px=0.2 KeV/c. Therefore deviation angle for electrons at kinetic energy of 2MeV is approximately 0.08 mrad and the focal length is equal to 25 m.

3.3.4.3 Effect of asymmetry in segment 1a+1b

As it has seen, when two halves of accelerating cell are connected together focusing of one half is compensated by defocusing of the second half. Therefore analysis of asymmetries may be quite important in the first accelerating cell as in the first segment (1b) having no coupling slots, the multipole fields will not be compensated. Besides, geometry of accelerating cell is not symmetric.

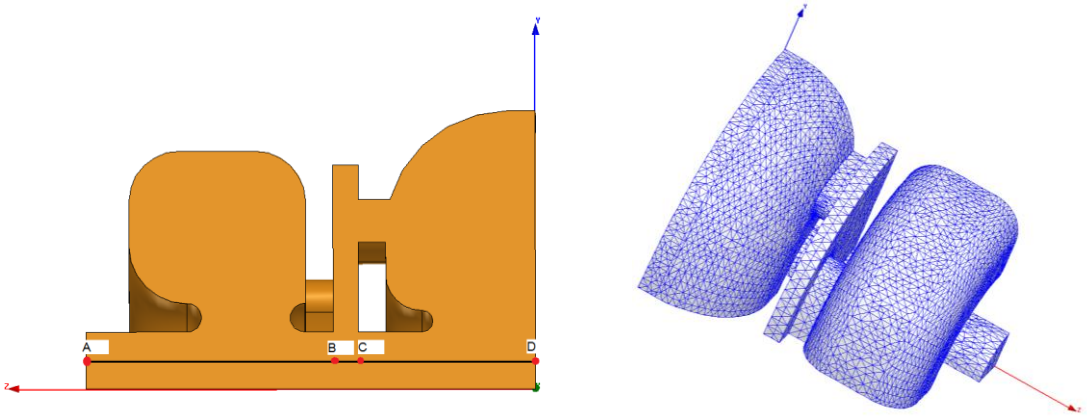

(a) (b)

Figure 3-62. Model used (a) and mesh (b) for the multipole field calculations in the 1a+1b+2a segments

Table 3-20. 1a+1b+2a segments contribution to transverse momentum kick (eV)

	B-A	**C-B**	**D-C**
Plane ZY	**Ux=-12.5** **Uy=-883** (Uya=25317 Uyb=-26200)	**Ux=-9** **Uy=-1659** (Uya=-1711 Uyb=52)	**Ux=6** **Uy=-44284** (Uya=-20567 Uyb=-23717)

Table 3-20 shows that 1st accelerating cell along integration path A-B has multipole fields not compensated, with a net effect of py=0.8 keV/c, therefore having a deviation angle for 2 MeV kinetic energy electrons at 2mm off axis of 0.3 mrad and a focal length equals to 6.7 m. The coupling cell (py=1.6 keV/c would produce a deviation of 0.65 mrad and its focal length is 3 m. Accelerating cell (path C-D) shows same results as previous analysis.

3.3.4.4 Effect of asymmetry in segment 4b+4a

In the segments 4b+4a there is a lack of symmetry produced by the absence of coupling slots

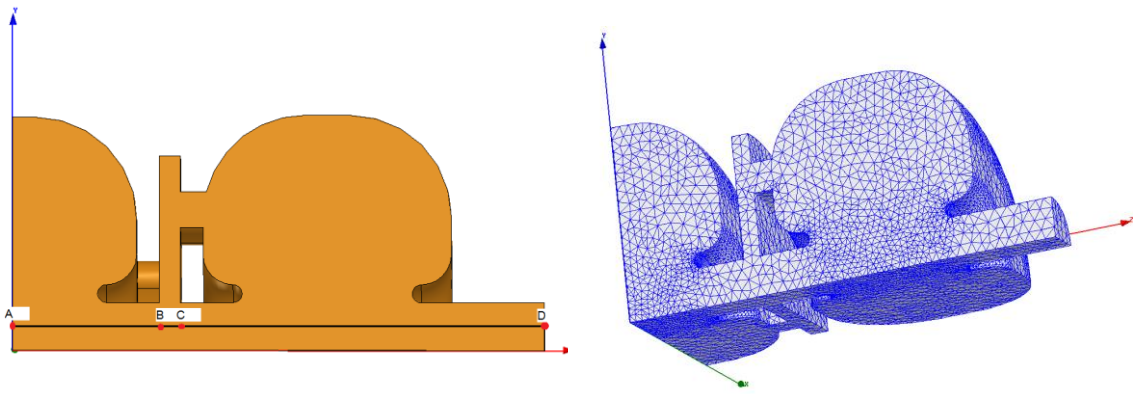

(a) (b)

Figure 3-63. Model used (a) and mesh (b) for the multipole field calculations in the segments 4b+4a+3b

Table 3-21. 4b+4a+3a linac segments contribution to transverse momentum kick (eV)

	A-B	**B-C**	**C-D**
Plane ZY	**Ux=11** **Uy=-44726** (Uya=-20113 Uyb=-24613)	**Ux=1** **Uy=2499** (Uya= 2491 Uyb=8)	**Ux=28** **Uy=559** (Uya=1402 Uyb=-843)

According to the results from Table 3-21 there are some fields not compensated in segment 4b+4a(path C-D) with py=0.5 keV/c, therefore the deviation angle would be 0.2 mrad and focal length equals to 9.8 m.

As it happens with the previous calculations the coupling cell would produce the maximum deviation with py=2.5 keV/c and a deviation of 1 mrad (focal length 2 m). Accelerating cell (path A-B) shows same results as previous analysis i.e. high field effect caused by symmetric fields which will be compensated by the adjacent accelerating half cell (3a).

3.3.4.5 Summary and conclusions for multipole fields calculations

According to the previous results it can be concluded that the main effect on the transverse momentum of the electrons will be the quadrupole field in coupling cells due to the coupling slots and to a lesser extent the effect of coupling slots in the accelerating cells. Depending on the plane we are dealing with, the different lenses will act as focusing or defocusing. In Figure 3-64 the lenses along the RTM horizontal plane are shown. In this plane it can be considered there are two focusing lenses followed by one defocusing lens and another two more focusing lenses. The effect of coupling iris and probe hole is neglected as it was too small and within accuracy of calculations.

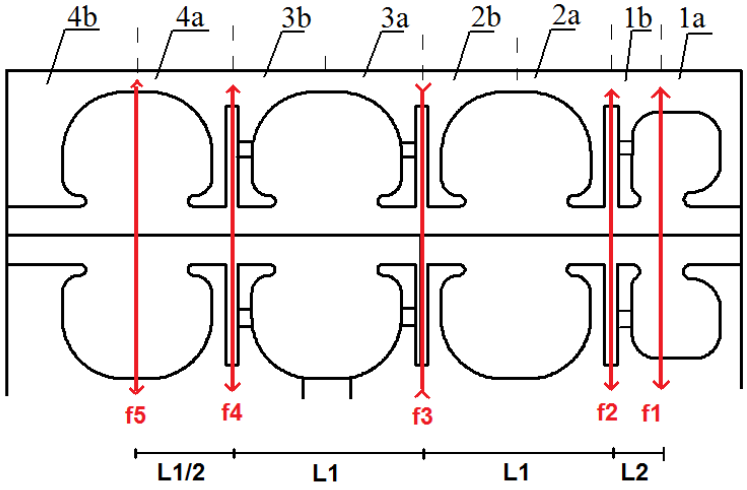

Figure 3-64. Lenses in horizontal plane

As the focal lengths of the different lenses are much bigger than the lengths of the elements, the thin lens approximation can be done, therefore the matrix elements [69] for a focusing lens is [16]

$$m_{QF\,i} = \begin{pmatrix} 1 & 0 \\ -1/f_{QF\,i} & 1 \end{pmatrix} \tag{3.7}$$

and for defocusing lenses

$$m_{QD\,i} = \begin{pmatrix} 1 & 0 \\ 1/f_{QD\,i} & 1 \end{pmatrix} \tag{3.8}$$

[16] *This is a estimation, as dispersion is not included in the matrix*

and the matrix form for the drift spaces is

$$d_i = \begin{pmatrix} 1 & l_i \\ 0 & 1 \end{pmatrix} \tag{3.9}$$

To get the total matrix for the system

$$M_{Total} = m_{QFn} * d_n * m_{QDn} * d_{n-1} * \dots \tag{3.10}$$

In previous sections the focal lengths for these lenses were obtained for 2 MeV electrons. The values are summarized in the following table.

Table 3-22. Focal length obtained for electrons 2mm off axis at 2MeV

f1 (m)	f2 (m)	f3 (m)	f4 (m)	f5 (m)
6.7	3	2	2	9.8

The most essential effect of quadrupole fields will take place during first acceleration up to 2 MeV when beam relative energy is essentially changed from cell to cell. Besides, the focal length is proportional to γ of electrons. This is why the total matrix for the linac must be obtained for the first pass of particles after the injection at 25 keV where the quadrupole field will have more influence on the transverse dynamic of the electrons. The focal length for every lens can be obtained, knowing the kinetic energy of the particles along the first pass, with:

$$f(Ei) = f(2MeV)\frac{p(Ei)}{p(2MeV)} \tag{3.11}$$

Table 3-23 shows the focal lengths values and the kinetic energy and momentum during the first pass of electrons through the linac

Table 3-23. Focal length values after injection

f1(m) Ek1= 0.114 MeV p1=0.231 MeV/c	f2(m) Ek2= 0.310 MeV p2=0.504 MeV/c	f3(m) Ek3=0.876 MeV p3=1.102 MeV/c	f4(m) Ek4= 1.445MeV p4=1.681 MeV/c	f5(m) Ek5= 1.732 MeV p5=1.971 MeV/c
0.41	0.61	0.89	1.36	7.85

It should be noticed that f1(p1) has not been obtained directly with (3.11). As electrons passing through the first cell after injection are not ultra relativistic (in the middle of accelerating cell

β=0.63) the electric field is able to deflect the particles in a greater extent. Therefore, taking into account the lower velocity of particles (3.4) is recalculated giving: Uya =2554 eV and Uyb=-1236 eV . Therefore the new fields contribution to transverse momentum, py = 1.3 keV/c is obtained (deviation angle = 4.86 mrad).

Now the total matrix may be obtained:

$$M_{Total} = \begin{pmatrix} 1 & 0 \\ -1/f5 & 1 \end{pmatrix} \begin{pmatrix} 1 & L1/2 \\ 0 & 1 \end{pmatrix} \begin{pmatrix} 1 & 0 \\ -1/f4 & 1 \end{pmatrix} \dots \begin{pmatrix} 1 & 0 \\ -1/f1 & 1 \end{pmatrix} = \begin{pmatrix} 0.9 & 0.04 \\ -3.8 & 1.0 \end{pmatrix} \quad (3.12)$$

If focal length describing the asymmetrical fields was much greater than RTM orbit circumference, then it could be ignored in consideration of RTM optics. If it was much less than the orbit circumference, then this would be a real problem.

Looking at the elements of the matrix we see $M_{21\ total}$ =-3.8 m^{-1} so it can be concluded that in the horizontal plane the whole linac will behave as a focusing lens with focal length equal to 26.3 cm. If the same procedure is applied to the vertical plane we obtain $M_{21\ total}$ =+3.9 m^{-1} and therefore focal (defocusing lens) is equal to 25.6 cm.

According to these results, the focal length of linac due to coupling slots during the first pass of electrons is smaller than the RTM orbit circumference, which is about 1 m, so effect of coupling slots must be taken into account in RTM optics analysis

3.3.5 Parasitic modes calculations and beam blow-up current estimation for RTM

In section 2.1.3 we have seen that the fundamental TM_{010} -like mode is used for particle acceleration. All other *higher order modes* (HOM) are unwanted, but may be excited by the beam itself if the resonant frequency of any HOM f_{HOM} is an integer multiple *n* of the bunch repetition frequency f_b [70].

$$f_{HOM} = nf_b \quad (3.13)$$

Each deflecting mode is characterized by the quality factor and the beam-coupling impedance. HOM effects can be reduced in several ways, e.g. optimizing the cavity shape or absorbing HOM power (with special coupling antennas).

RTM BBU (Beam Blow-up) is an effect that may limit the beam current which can be accelerated in RTM and is caused by the excitation of parasitic modes with on-axis transverse magnetic fields and off-axis longitudinal electric fields (e.g., cylindrical cavity TM_{110} mode). Beam blow-up was first predicted and was real reason of current limitation for Illinois superconducting continuous wave race-track microtron MUSL [71].

An off-axis RTM beam transfers energy to parasitic modes by interacting with the longitudinal electric field and gains transverse momentum by interacting with the transverse magnetic field. On the next pass through the structure the beam has a different displacement and phase with respect to the parasitic mode field and depending on the beam optics and return path length, the beam can transfer additional energy to the parasitic mode and get an additional transverse displacement. If the energy transfer rate of beams from all orbits exceeds the rate of parasitic mode energy dissipation in the structure walls and external loads, then the energy stored in the parasitic mode and the beam displacement grow exponentially and the beam will touch an aperture and disappear. BBU takes place at a threshold beam current (I_t).

The potentially most troublesome modes, are TM_{11}-like modes with high Q and large transverse shunt impedance,

$$r_{\perp} = \frac{U^2}{P} \tag{3.14}$$

where *U* is the energy gained by an optimally phased particle passing at distance $x = \lambda_r/2\pi$ off the cavity axis,

$$U = \int_{-l/2}^{l/2} Ez(x = \lambda r/2\pi)dz \tag{3.15}$$

and *P* is the parasitic mode power dissipated in the cavity walls, and λ_r is the parasitic mode wavelength.

A worst case estimation for a single cell structure for the threshold current [72] is

$$I_t = \frac{4Ez\lambda_r}{\pi r'_{\perp}\beta N \ln\frac{W_e}{W_i}} \tag{3.16}$$

where E_z is accelerating gradient of the linac, β function is taken at the structure centre, and W_i and W_e are injection and extraction energies, $r'_{\perp} = r_{\perp}/L$ is the transverse shunt impedance of parasitic mode per unit length, L is the cavity length, λ_r is the parasitic mode wavelength and N is the number of turns.

The previous equation assumes a constant phase slip with respect to the parasitic mode field for all orbits, a worst case which we can approach only for $\lambda_r = \lambda_{RF}/n$, where n is integer, and ignores all details of RTM optics. Further, it describes a steady state, which probably cannot be reached during an RTM pulse. To take into account our RTM optics and real phase slips on different orbits, computer codes are needed [73].

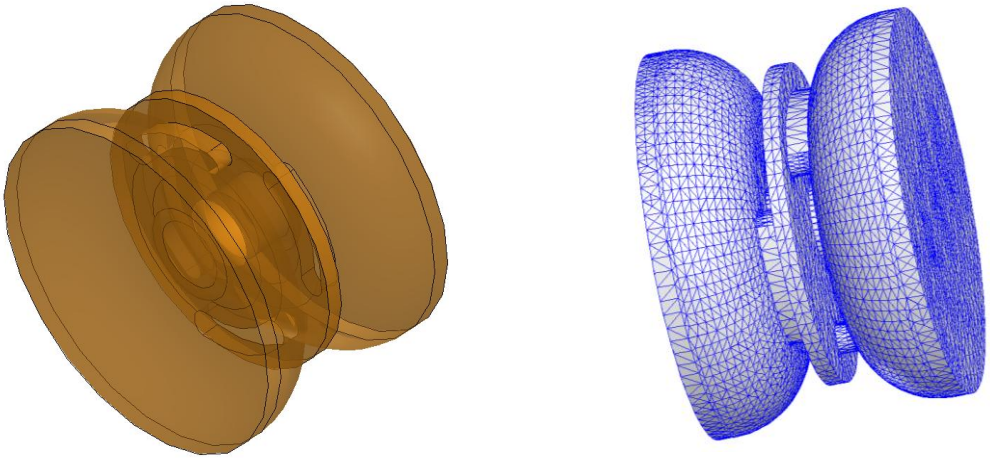

(a) (b)

Figure 3-65. Solid model used to obtain HOM (a) and mesh(b)

In order to calculate the threshold current for BBU, 3D calculations have been performed on the model consisting of two half accelerating cells and one coupling cell (Figure 3-65). E walls have been placed at both accelerating cells middle planes and no azimuthal symmetries have been used in order not to overlook some HOM.

Table 3-24. HOM

Frequency (MHz)	Q
5712 (accelerating mode TM_{010}-like)	9750
6059 (TM_{010}-like)	3340
8954 (TM_{110}-like, degenerated)	2580
9925 (TM_{110}-like, degenerated)	14100
9982 (TM_{110}-like, degenerated)	10690
11484	3520
12567	6130
13166 (degenerated)	4550
13250 (degenerated)	15500

Table 3-24 shows the first modes obtained. In principle, according to [74], in biperiodic structures, the most dangerous mode is a TM_{110} like blow-up mode that is found approximately at 1.7 times the accelerating frequency (9925 MHz or 9982Mhz mode).

TM_{110}-like modes for rotational symmetry cavities are doubly degenerated. However in practice in single cavity degeneration is removed by imperfections, two modes appear instead of one with difference in frequencies and field pattern orientation defined by imperfections. For multi cavity structure additional complication takes place. The simulation performed for system from Figure 3-65 has shown e. g. for the TM_{110}-like at 9925 MHz (Figure 3-66) that the axes of the modes are oriented perpendicularly to the coupling slots in the cavity webs, so degeneration is removed by coupling slots.

Nevertheless we have two modes at the same frequency 9925 MHz, one mode with field concentrated in one accelerating cell and second mode in another. The reason is that, because of low coupling between cells at this two modes, they do not interact with each other and because of these cells are identical they have the same frequency.

(a) (b)

Figure 3-66. TM_{110} like at 9925. Two modes with different polarization

In more details field distribution of this mode is shown in Figure 3-67. In Figure 3-68 the partner of this mode with frequency 9982 MHz is shown. Without coupling slots these two modes would be single degenerated mode with frequency about 9953 MHz. Coupling slots split this mode to two having difference in frequency 57 MHz, and field patterns oriented perpendicular to each other.

One more TM_{110} -like mode with frequency 8955 MHz and with field concentrating in coupling cell is shown in Figure 3-69.

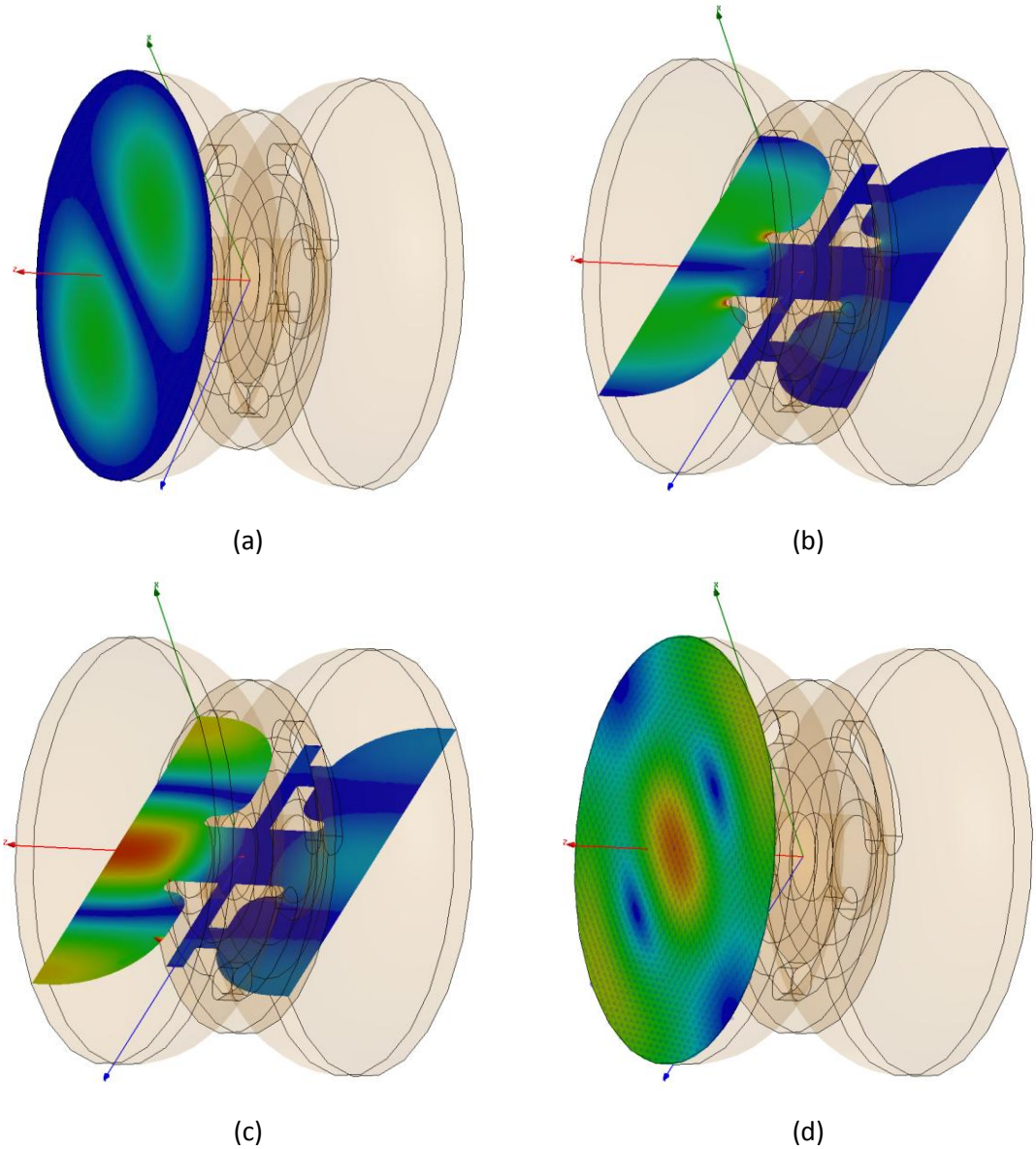

Figure 3-67. Mode TM_{110} like at 9925 MHz: E field magnitude on accelerating cell (a), E field magnitude along longitudinal plane (b), H field magnitude (c) and H field vector in central plane of accelerating cell (d)

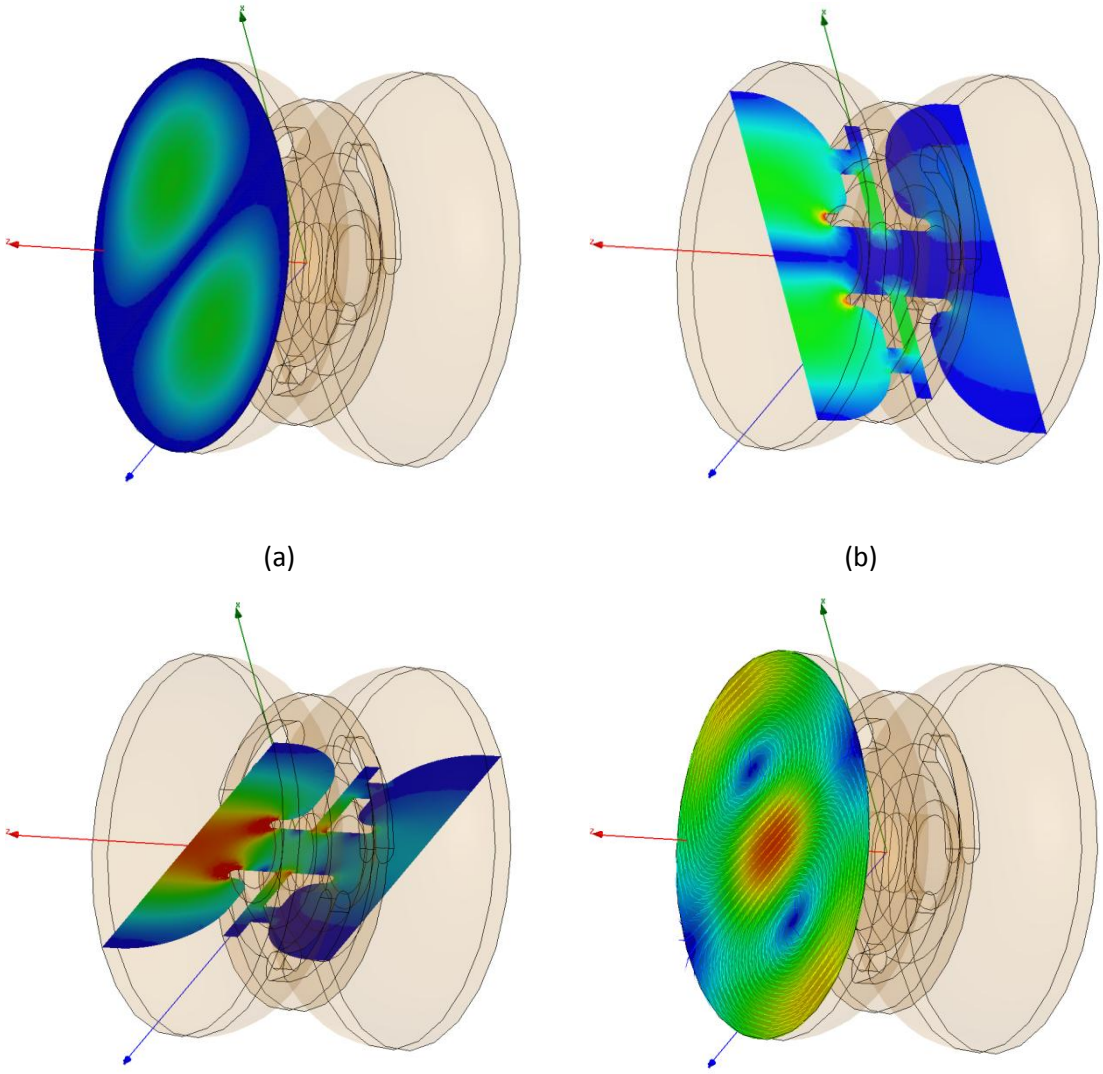

(a) (b)

(c) (d)

Figure 3-68. Mode TM_{110} like at 9982 MHz: E field magnitude on accelerating cell (a), E field magnitude along longitudinal plane (b), H field magnitude (c) and H field vector in central plane of accelerating cell (d)

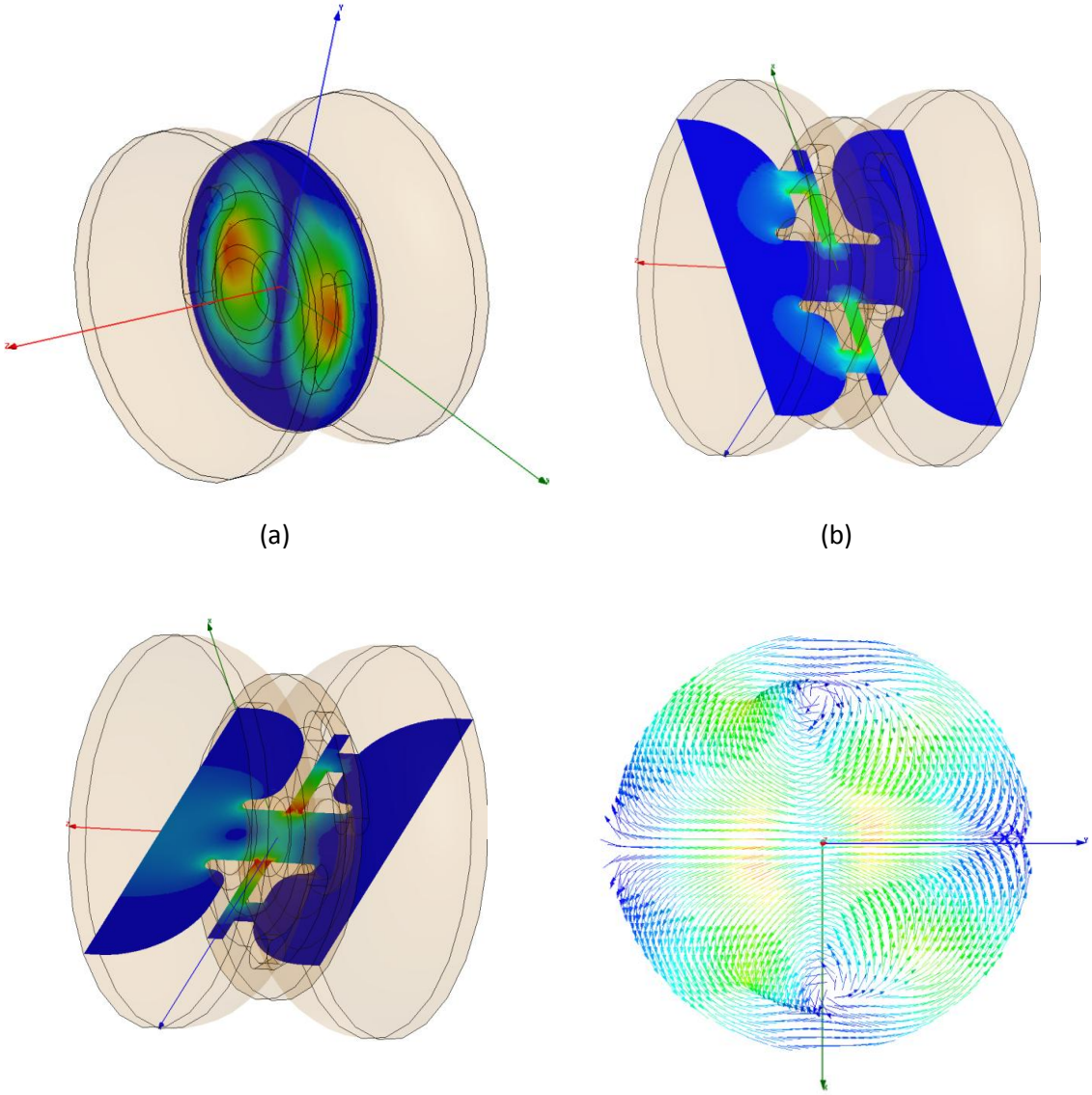

Figure 3-69. Mode TM_{110} like at 8955 MHz: E field magnitude on coupling cell (a), E field magnitude along longitudinal plane (b), H field magnitude (c) and H field vector in central plane of coupling cell (d)

Figure 3-70 shows some of the modes different from TM_{110} -like. E.g. Figure 3-70 (a) a TM_{210}-like can be observed (with quadrupole field) where just the coupling cell is excited. It should be noticed that for this analysis just TM modes have been studied (only E walls at both sides have been placed).

An estimation of the threshold current for the BBU has been performed for the three TM_{110} like modes using (3.16). According to (3.14) and the transverse impedance must be obtained

at $x = \lambda_r/2\pi$ off the cavity axis, but as this distance for the TM_{110} modes falls out of the beam pipe, an approximate expression for the energy gained for the particles will be used:

$$U(\frac{\lambda r}{2\pi}) \approx U(x)\frac{\frac{\lambda r}{2\pi}}{x} \tag{3.17}$$

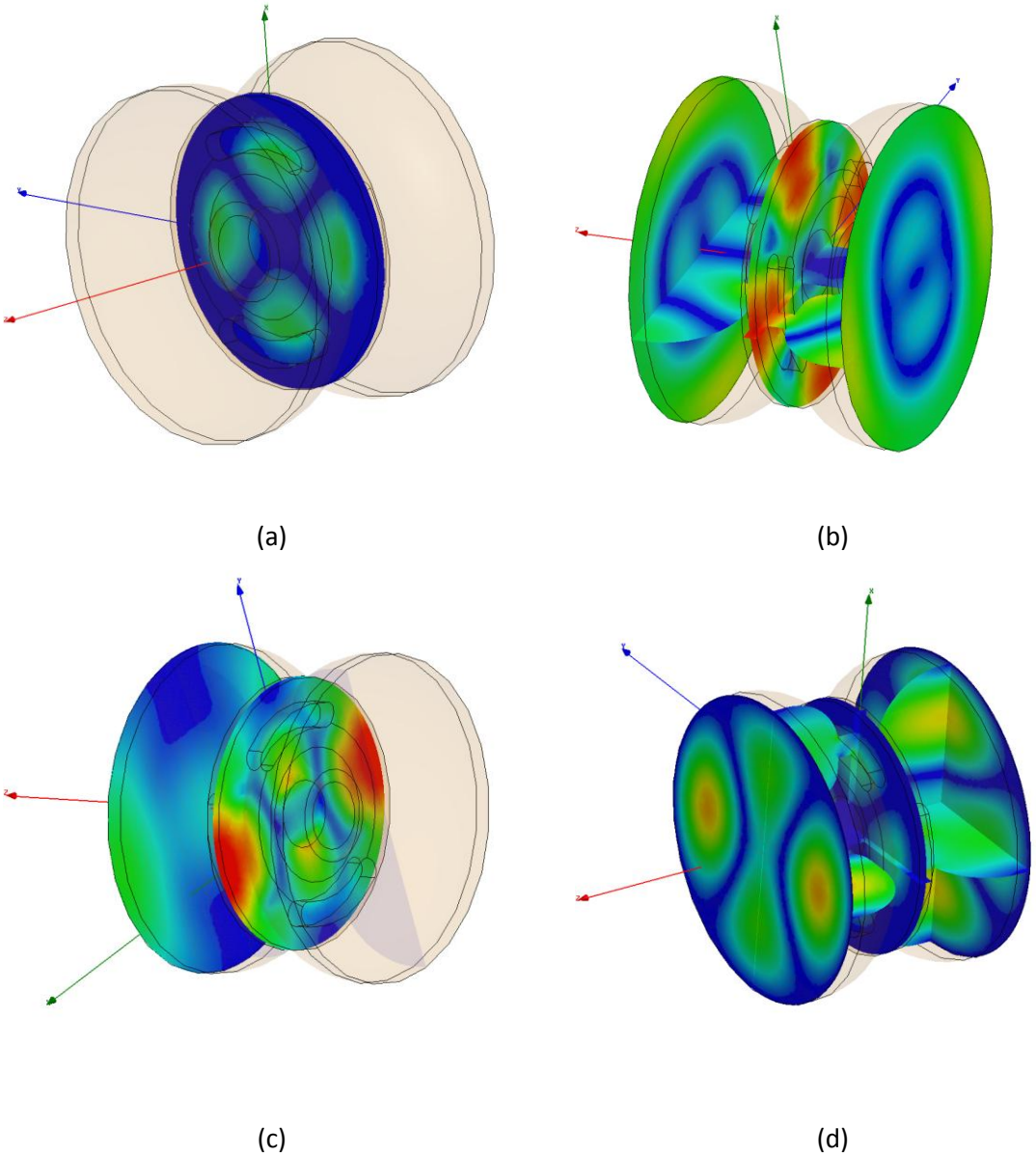

(a) (b)

(c) (d)

Figure 3-70. E field in coupling cell. TM Mode at 11484 MHz (a), H field in different sections for the mode at 12567 MHz (b), H field in different sections for the mode at 13166 MHz (c) and E field in different sections for the mode at 13250 MHz (d)

For the analysis x has been chosen equal to 3.5mm off axis (choosing the direction in order to have the maximum energy gained by the particle). The gradient Ez for the RTM linac is equal to 2 MeV/(linac length) which gives Ez=18.9 MeV/m. The beta function is of the order of the orbit length for our RTM optics, i.e. approximately 1m in our case. As we are doing just order of magnitude estimations, this accuracy is sufficient. This value of the beta function, depending on RTM optics, can be different: It may be decreased by installing many quadrupoles along the orbit. The less is beta the stronger is focusing and higher current can be accelerated.

Table 3-25 summarize the main parameters of the BBU current estimation for the TM_{110} like modes studied.

Table 3-25. BBU estimations for TM_{110} modes

Mode frequency (MHz)	**λ_r (m)**	**$r'_\perp$ (MΩ/m)**	**BBU I_t estimation (mA)**
8954 (TM_{110}-like, degenerated)	0,0335	0.2	385
9925 (TM_{110}-like, degenerated)	0,0302	27.4	2.5
9982 (TM_{110}-like, degenerated)	0,0300	64.5	1.0

The first TM_{110}-like mode at 8954 MHz having a high threshold current is not dangerous at all compared to the other modes. The lowest threshold current is found for the TM_{110}-like mode at 9982 MHz (Figure 3-68) with It= 1 mA. Experimental results in [74] showed what has been obtained with the 3D calculations, that the most dangerous mode is found at 1.7 times the frequency of the accelerating mode (In our case it is found at 1.74 times the accelerating mode frequency).

Nevertheless, the BBU current has been estimated for some other modes to check out that worst case corresponds to the TM_{110} -like mode.

Table 3-26 shows the results obtained. The most dangerous from these modes is found at 12567 MHz with a I_t = 3.5 mA. In principle, the mode at 11484 MHz could be quite dangerous being a harmonic of the accelerating mode (*n*= 2.01), but the threshold current is by far higher than the worst case of 1mA.

Table 3-26. BBU estimations for other modes

Mode frequency (MHz)	λ_r (m)	$r'_\perp$ (MΩ/m)	BBU I_t estimation (mA)
11484	0,0261	0.04	1380
12567	0,0239	14.8	3.5
13166	0,0228	3.3	150
13250	0,0226	3.8	130

The 1mA predicted for the threshold current is lower than the real value for our RTM linac because of:

- the estimation is performed for steady state, as time is required for development of this phenomena (it is potentially more dangerous for continuous operation).

- and the orbit length is chosen to be equal to integer number of parasitic mode wavelength (worst case).

With a 3 μs pulse and with parasitic mode frequency not being harmonic of operating one, the real threshold current will be much higher. However, these calculations are being performed in order to characterize the accelerating structure in all details. So, in the future, if higher currents are needed, results presented here of calculations of the shunt impedance for these modes will be quite useful for beam blow-up simulation with more sophisticated models.

3.4 Study of thermo mechanical behaviour of accelerating structure

In the three β =1 cells the maximum E field on axis must be equal to 44.8 MV/m and in the β=0.5 cell the maximum E field on axis must be equal to 43 MV/m (Figure 3-7). In order to provide the precise electric field, a certain quantity of power must be dissipated in the linac walls. This power, as well as the power that might be deposited by the electron beam itself, will heat the copper structure. Therefore a special study of thermo mechanical behaviour of the accelerating structure has been performed.

3.4.1 RF power losses distribution along the cavity surface

In order to calculate the dissipated power in the linac surface, a quarter of the geometry has been used (Figure 3-71). No coupler has been included so the simulation could be performed with reasonable accuracy.

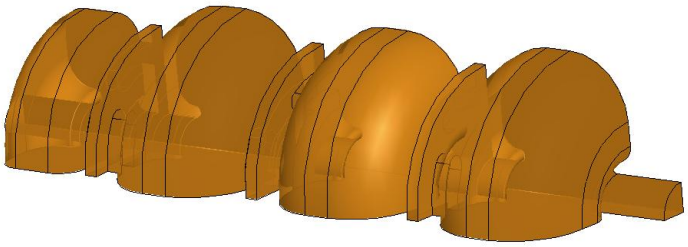

Figure 3-71. HFSS solid model to calculate the power lost on the surface

For a good conductor, the power dissipated in the cavity walls [42], can be obtained from

$$P = \frac{R_S}{2} \int_S \left| \overline{H}_t \right|^2 ds \qquad (3.18)$$

where H_t is the tangential magnetic field on the surface, and Rs is the surface resistivity of the conductor

$$Rs = \frac{1}{\sigma \delta_S} = \sqrt{\frac{\omega \mu}{2\sigma}} \qquad (3.19)$$

with σ being the conductivity and δ the skin depth.

The following table summarizes the results obtained with HFSS for the power dissipation (3.18) in the copper walls due to the accelerating mode.

Table 3-27. Pulsed power dissipated in the structure

Total pulsed RF power dissipated in the structure, P_{RF} (kW)	**529**
Pulsed RF power dissipated in 1st accelerating cell included in 1a+1b (coupling slots included) (kW)	**95**
Pulsed RF power dissipated in regular accelerating cell included in 2a+2b (coupling slots included) (kW)	**137**
Pulsed RF power dissipated in regular accelerating cell included in 3a+3b (coupling slots included) (kW)	**137**
Pulsed RF power dissipated in regular accelerating cell included in 4a+4b (coupling slot included) (kW)	**132**
Pulsed RF power dissipated in all the coupling cells (kW)	**28**

In Figure 3-72 the H field on the linac surface is represented, therefore showing the places where the heating of the structure is expected. The maximum heat flux (at maximum duty factor) is 8.5 W/cm^2 located in the small rounding of the coupling slots

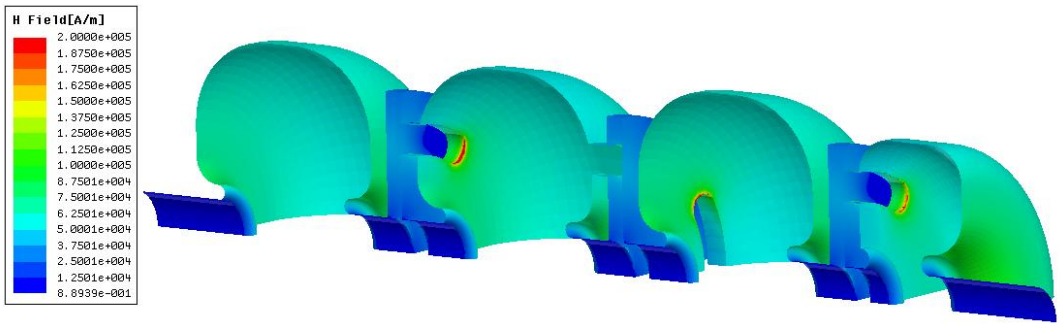

Figure 3-72. H field on linac surface

The maximum exit beam current which can be obtained with our microtron is expected to be 5 mA pulsed and 3.75µA average (max duty factor of the modulator is 0.075%).

That means that the maximum average beam power at 12 MeV will be 45 W. On the other hand the maximum average RF power dissipated in the linac walls considering maximum duty factor will be 529 kWx0.00075= 397 W and some influence on resonance frequency could take place.

3.4.2 3D calculations of the cell thermo mechanical behaviour[17]

The cooling in our RTM will consist of four longitudinal cooling pipes in a similar way as the cooling design of the MAMI-C 4.9 GHz structure. The number of cooling pipes and diameter have been chosen according to the space available in the structure[18] and to guarantee a turbulent regime of the water flow.

For this study ANSYS has been used [75]. Due to the difficulty of getting the 3D models with this software, they have been created with Solid Works and imported into ANSYS. Due to the extremely high computational resources needed, just a quarter of two halves accelerating cells and one coupling cell were used for the analysis (Figure 3-73).

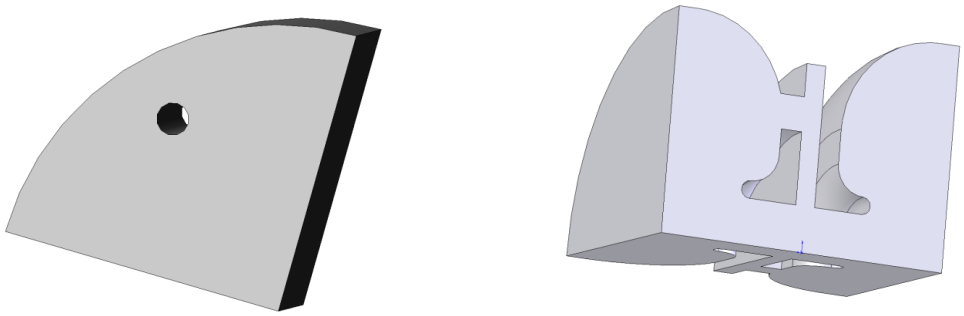

(a) (b)

Figure 3-73. 3D solid model for the copper bar including a cooling pipe (a) and 3D solid model for the vacuum in which RF fields are created

The meshed geometry for resonating vacuum model used is shown in Figure 3-74(a). The copper model is obtained subtracting Figure 3-73(b) to Figure 3-73 (a), therefore Figure 3-74(b) is obtained. For the analysis it must shared its inner boundary surface with the outer boundary surface of the vacuum model in order to communicate the heat flux results as a load for the thermal calculations.

[17] *All calculations in this section are performed taking into account maximum duty factor = 0.075%*
[18] *Details of mechanical design will be shown in Chapter 5*

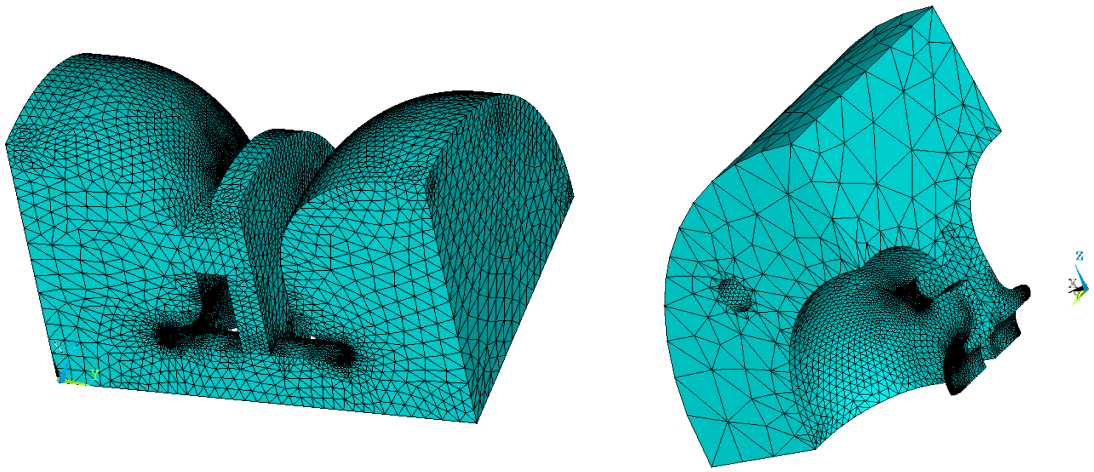

(a) (b)

Figure 3-74. Vacuum meshed with 3D HF119 electromagnetic elements (a) and copper meshed with SOLID 87 thermal elements

To consider the desired power loss distribution it is necessary additionally to mesh the cavity boundary surface with surface effect elements resembling the electromagnetic elements.

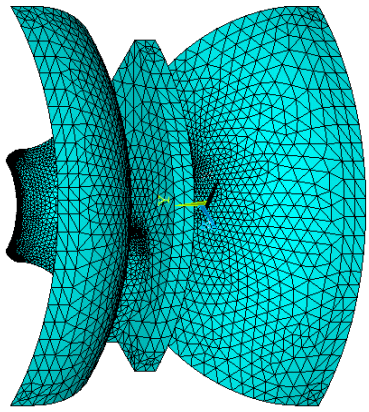

Figure 3-75. Surface elements SURF152 to transfer heat fluxes from RF to thermal analysis

The surface effect elements work as a mediator to transfer the heat fluxes directly to the thermal elements producing a realistic RF induced heat source. The flux distribution of the outer faces for the elements in the RF analysis is transferred face by face to the inner faces for the thermal analysis. The water flow along the cooling pipes is simulated by means of the heat transfer coefficient, characterizing the efficiency of the heat convection at the interface between the cavity body and the cooling area. To determine α the definition

$$\alpha = k\frac{Nu}{D} \tag{3.20}$$

has been used, where *k* is the thermal conductivity of the water (0.606 $W \cdot m^{-1} \cdot K^{-1}$ at 295 K), Nu is the dimensionless Nusselt number and *D* the hydraulic pipe diameter. The Nusselt number principally relates the heat transferred between two surfaces at different temperatures for a flowing coolant (convection) to the coolant at rest (conduction). Thus it depends mostly on the flow state. Since the heat transfer coefficient in a meander is improved due to water turbulences, flow rates should be high enough to produce a turbulent flow. A criterion for turbulent water flow(Re ≥ 10000) in a water tube is given by the Reynolds number:

$$Re = \frac{v_m D}{\nu} \qquad (\nu = \frac{\mu}{\rho}) \tag{3.21}$$

Where ν is the kinematic viscosity (in $m^2 \cdot s^{-1}$) obtained from the dynamic viscosity μ (0.000959 $kg \cdot s^{-1} \cdot m^{-1}$ at 295K) and the water density ρ (998.8 Kg/m^3 at 295 K), and v_m is the water velocity which is imposed to be 4m/s for technical reasons in our RTM accelerator. This gives a Reynolds number equal to 16660 proving that the cooling flow is in turbulent regime (Re>10000).

The Nusselt number that appears in (3.20) is a complex measure of the Reynolds number Re, the given geometry and the material-dependent Prandtl number which mainly describes the relation of the heat in a viscous fluid generated by friction related to the conducted heat (Pr=6.6 for water at 295 K). The Nusselt number Nu can only be determined accurately by experiments. Different approximations can be found in literature. For turbulent flow the following empirical formula has been used

$$Nu = \frac{f}{8} \frac{Re\ Pr}{1.07 + 12.7\sqrt{\frac{f}{8}}(Pr^{2/3} - 1)} \quad 0.5 < Pr < 2000 \quad 10^4 < Re < 5.10^6 \tag{3.22}$$

Where the friction factor f of the tube generally depends on the surface condition. It is minimal for smooth surfaces and increases with surface roughness. For smooth pipes f can be expressed - depending on the flow situation

$$f = \frac{1}{(0.79Ln(Re) - 1.64)^2} \quad 3000 \leq Re \leq 5.10^6 \tag{3.23}$$

Finally the transfer coefficient α=19430 $W \cdot m^{-2} \cdot K^{-1}$ has been evaluated with the help of previous equations for the cooling pipe allowing. Having defined the transfer coefficients and the thermal conductivity of the cavity material (k = 400 $W \cdot m^{-1} \cdot K^{-1}$ for OFE copper - Oxygen Free Electronic grade- which is the oxygen free copper with the highest possible electronic and thermal conductivity) the steady-state temperature distribution can be calculated in ANSYS. Figure 3-76 shows the temperature distribution in the linac segment assuming an average temperature of water = 293 K and a power dissipated of 27.75 W[19]. The distribution shows the maximum temperature is located at the coupling slot centre (304.9 K) and that about 12 K difference from maximum temperature in the copper to the average temperature of water.

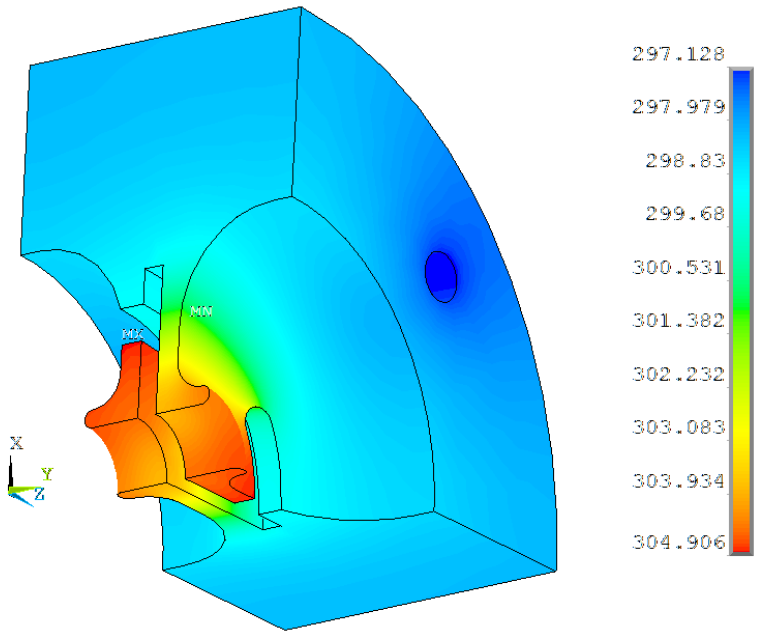

Figure 3-76. Temperature distribution

There will be four cooling pipes in the linac structure having the entrance and exit in the same segment: therefore water will get through the linac four times. This means a change of water temperature from one cooling pipe to another so the outlet temperature T_{out} could be significantly higher than the inlet water temperature T_{in} which could alter the temperature distribution from the quarter of the segment where water has just been introduced to the quarter where the water is about to get out. If the heat is removed by convection (neglecting

[19] *Power dissipated for a quarter of segment (111 W for the whole segment and 397 W for the whole linac- see previous section-)*

air convection -structure is in vacuum- and heat radiation effects) the heat rate dQ/dt extracted by the water equals the dissipated mean power. Then the maximum possible temperature rise ΔT can be obtained by the following calorimetric formula where the water volume flow rate is dV/dt:

$$\Delta T = \frac{dQ/dt}{\rho C_p \frac{dV}{dt}} \qquad \left(\frac{dV}{dt} = A_{pipe} v_m\right) \tag{3.24}$$

An increment of temperature per kW of 4.759 K/kW is obtained. The water temperature increment is

$$\Delta T = 4.759 \frac{K}{kW} * \ 0.396 kW = 1.88\ K \tag{3.25}$$

This increment in the water temperature is negligible for the temperature distribution and for deformations in the cavity (maximum temperature will just rise to 306.8 K).

Having the temperature distribution, a structural analysis can be carried out. Structural analyses give information about the thermal deformation of the cavity, producing frequency resonant shifts and intrinsic stresses. Material properties, boundary constraints and forces acting on the geometry as caused by temperature loads have to be set before the analysis is performed. First the mesh thermal elements must be switched into structural mass elements. The previous thermal solution is imported as a load for the structural analysis. The resulting cavity distortion depends on the fixation of the cavity so realistic structural constraints must be applied. The fixation scheme can be emulated in ANSYS assigning symmetries constraining the expansion in specified cavity regions. In the quarter of segments, symmetry planes must be obviously placed at XY and ZY to get the whole (360deg) disk (where Y is the longitudinal axis). The structure may expand along Y axis and radial direction freely. A reference has been assigned in the middle of the structure so the deformations do not get mixed with possible displacements along longitudinal direction.

The structural material properties to be defined for the OFE copper are the thermal expansion factor at a reference temperature T=293K ($1.67.10^{-5}$), the Young's modulus (ratio of stress to strain = $1.26.10^{11}$ Pa) and the Poisson's ratio (the ratio of the transverse strain -perpendicular to the applied- load to the axial strain -in the direction of the applied load- = 0.31).

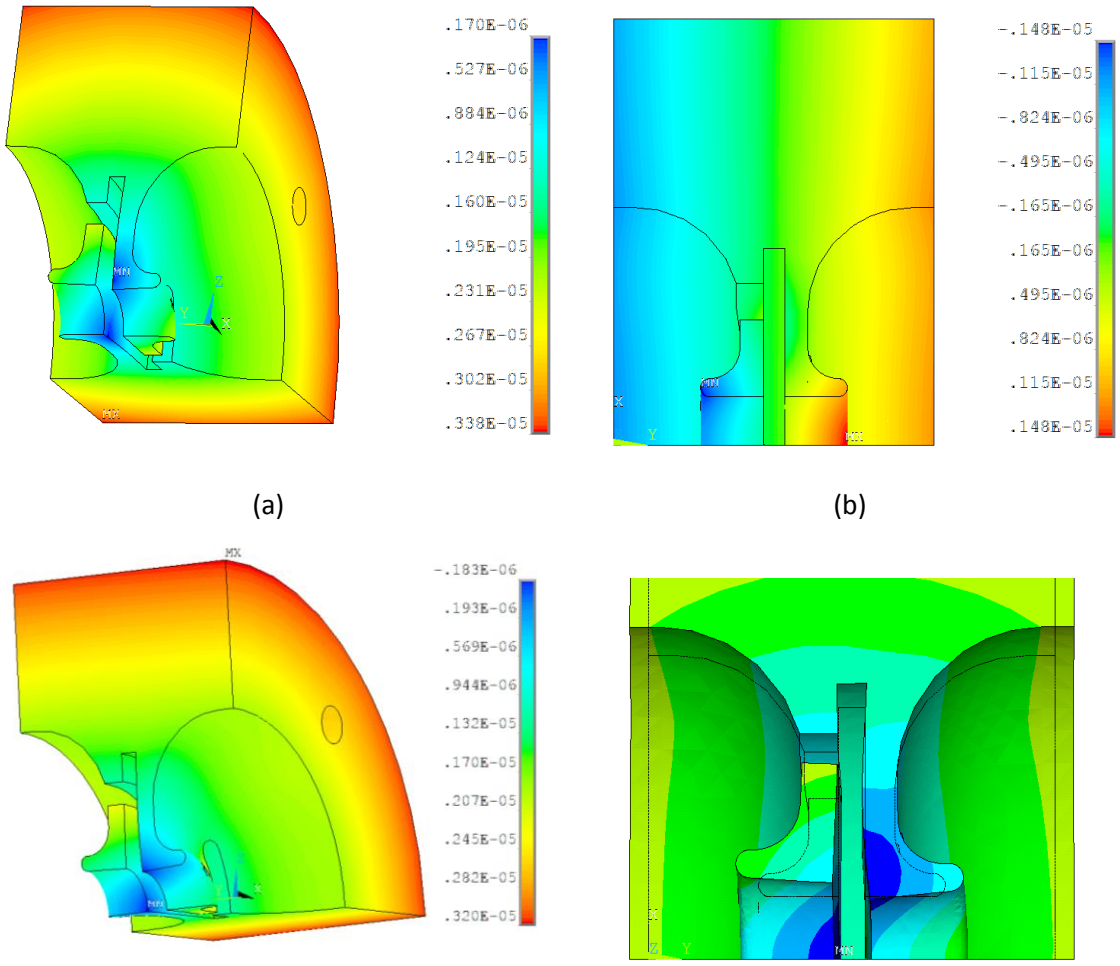

Figure 3-77. Deformations in the structure. Sum (a), axial (b) and radial deformations (c). Comparison magnified (1000 times) of deformed to original structure (d)

In Figure 3-77 (a) the sum of deformations in the structure are shown. In the inner profile, which is the part that may have some influence on the RF properties, the maximum deformation is approximately 2 µm.

On that surface we can obtain some conclusions of what will happen in the real structure by looking at the sensitivity analysis carried out in 3.3.3 for the tolerances of the basic cell dimensions:

- Looking at **axial deformations** (Figure 3-77 (b)) at the cones and at both sides of the cavity we notice a maximum axial deformation of about 1 µm which according to the sensitivity obtained for parameter *q* (df/dq=+0.01 MHz/µm) this would translate into a resonant frequency change of just -0.01 MHz. Besides, we can consider that only the cones are

displaced towards the centre of accelerating cell about 0.5 μm, therefore, the parameter *s* must be taken into account (df/ds=-0.28 MHz/ μm) making the resonant frequency to decrease -0.14 MHz. Concerning the coupling cell, it can be considered that the width Lc is incremented by 0.32 μm, and as sensitivity for this parameter is $df/dLc_{/2}$ = -0.01 MHz/μm the change in frequency is negligible.

- Figure 3-77 (c) shows the **radial deformations**. Here the main place affected is the accelerating cell radius Ra, the coupling cell radius Rc and the cone radius Rn. A resonant frequency change in accelerating cell of -0.48 MHz could be expected (df/dRa=-0.28 MHz/μm) and -0.38 MHz for the resonant frequency of coupling cell (df/dRc=-0.29 MHz/ μm). The shape of the nose is quite important, and according to the radial deformations we could expect up to 1 μm increase in the nose cone diameter. This would translate in a accelerating resonant frequency change of -0.33 MHz (df/dRn=-0.67 MHz/ μm).

Considering accelerating cell and coupling cells separately, in accordance to these calculations, a resonant frequency reduction of 1 MHz and 0.4 MHz in accelerating cells and coupling cells respectively is expected.

This change must be understood as the frequency shift produced from the beginning of operation to the moment when the steady state has been reached, so, even if it seems a small effect, it must be taken into account during operation of the machine. The reason is that a method based on frequency pulling will be used so the magnetron may provide a RF power at stable frequency and no significant frequency changes should happen in order to work properly. Acceptable value of frequency drift during the structure heating (which takes place for our linac mass with time constant about 10 s) depends on the amount of RF power sent back to the magnetron to force it to generate power at the linac frequency. For about 10% of magnetron RF power returned back to its input a few MHz frequency drift is acceptable, while for ~1% several hundred kHz are the limit.

CHAPTER 4

Methods and stand for cold measurements of accelerating structure

4.1 Methods of the accelerating structure electrodynamics characteristics measurements

4.1.1 Introduction

Experimental studies of electrodynamics characteristics of accelerating structures are an important phase in the development of accelerator of charged particles. The need for such studies lies in the many errors that could produce deviations of the parameters of manufactured structure from the expected one. These errors could come from:

- Insufficient accuracy of analytical and numerical techniques used to design the cavities.

- Errors during machining process and/or insufficient accuracy to machine the cavities.

- Change of the cavity dimensions when internal stresses of material are released e.g. after brazing process if a proper thermal treatment has not been carried out.

- Change of cavity dimensions and of the surface quality due to alloy penetration inside the cell during brazing procedure.

Also, it is important to perform measurements to examine the characteristics of different resonant modes that could exist in the structure besides the accelerating one.

4.1.2 RF instrumentation and measuring probes

The main device needed for measuring electrodynamics properties such as Q factors, resonant frequencies, electric field profile, etc. is the network analyzer. Along this work, the device employed is a Vector Network Analyzer (VNA) HP8720 Figure 4-1 (a). This model is a two port device which measures both amplitude and phase properties (specially s -scattering- parameters of a device under test - DUT-see Figure 4-1 (b)) and has a range from 50 MHz to 20 GHz.

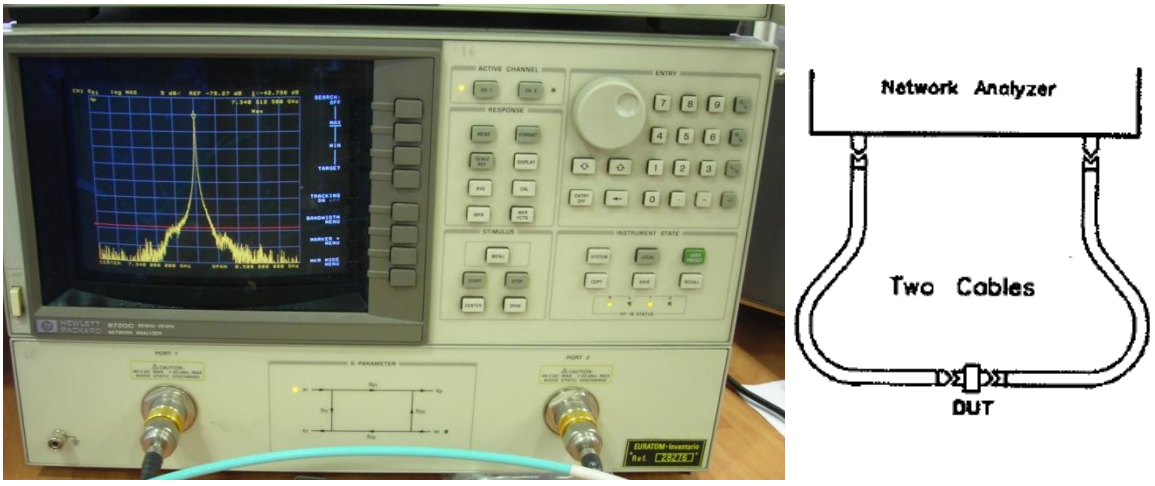

(a) (b)

Figure 4-1. Network Analyzer employed for measuring the RF properties of RTM cavities (a) and schematic representation of measurements of a DUT (b)

Different cables have been used to perform the measurements:

- Semi-rigid SMA coaxial cables -50 Ω- (Figure 4-2(a)) EPIRSA - MICROCOAX

- Special flexible 3.5 mm cables -50 Ω- (Figure 4-2(b)) with low attenuation and high phase stability when bending - Rosenberger -. Where the latter have been used when accuracy in phase measurements were needed, e.g. when measuring E field profile along axis.

(a) (b)

Figure 4-2. Semi-rigid coaxial cables (a) and special flexible cables (b)

A calibration process has been performed at t

he beginning of every set of measurements. It is important to carry out the calibration because when time passes or when measurement cables change, the VNA is not longer adjusted. It should be noticed that a calibration is only valid for a range of frequencies specified so calibration is gone if we want to analyse some other RF properties outside this range. The (mechanical) calibration is done by placing known microwave devices (short, open and load) at both ports[20] and also by measuring transmission between them. Figure 4-3 shows the calibration kit used.

Figure 4-3. Calibration kit

In order to measure linac RF properties, some RF components were needed:

- A transition from SMA to N connector - Ordered to Rosenberger- (Figure 4-4(a))

[20] *There are VNA with more than two ports*

- A transition from N connector to WR187 - Ordered to ATM- (Figure 4-4(b))
- A section of waveguide WR187 - Ordered to ATM- (Figure 4-4(c)). In order to stabilize the RF input mode and exclude interaction of the higher modes of coaxial-waveguide adapter and object under the study.
- A N panel connector that will be used as magnetic probe in the linac - Rosenberger- A copper wire has been welded in order to make the loop. (Figure 4-4(d)).
- Electric and magnetic probes connected to a transition from SMP to SMA connector 50 Ω. The electric probe consists of a coaxial probe whose inner conductor tip will be used to excite (or to pick up) the E field in the resonant structure (Figure 4-5(a)). The magnetic probe is created when the inner tip of the coaxial is forced to make a loop. This loop will be placed in some region of the resonant structures to excite (or to pick up) the magnetic field (Figure 4-5(b)). The probes were ordered to EPIRSA–MICROCOAX with two different outer diameters (UT-047 1.1 mm and UT-085 2.2 mm).

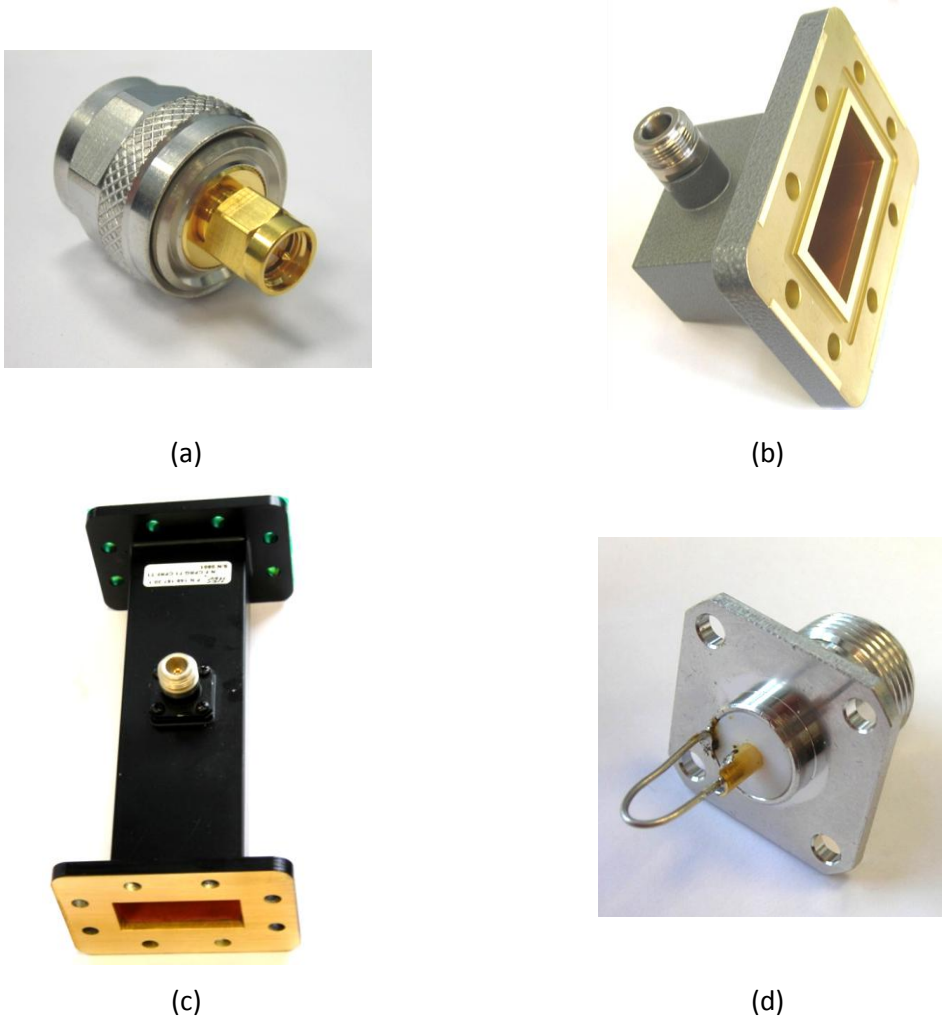

(a) (b)

(c) (d)

Figure 4-4. Some RF components used for testing purposes

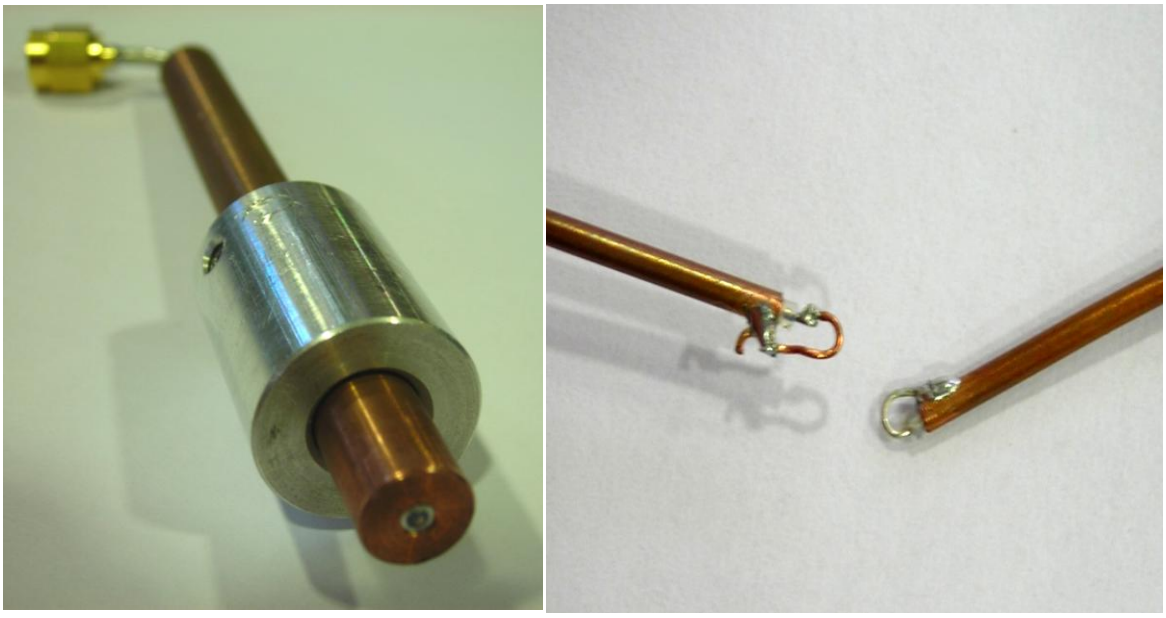

(a) (b)

Figure 4-5. Electric (a) and magnetic (b) probes

The electric probe UT-085 is inserted into a cylinder of copper (Figure 4-5(a)). This cylinder is 8 mm diameter in order to fit to the beam pipe. The purpose of transverse aluminium disc surrounding the copper cylinder is to fix the length of probe inserted in the structure.

4.1.3 EM modes measurements

The method used for measuring the mode spectrum and the quality factor in the different resonant cavities manufactured and linac (see Chapter 5) will be the measurement of transmission S21 or reflection S11 parameters using the electric and magnetic probes (and coupler in the linac case) . Depending on the place where the probes are inserted, the excitation of the resonant modes is caused by an electric Figure 4-6(a) or by a magnetic field Figure 4-6(b).

Experimentally the frequency at which extremes of S21 or S11 are found correspond to the different resonant frequencies of the EM modes. The experimental Q factor of each mode is calculated with

$$Q_{exp_i} = \frac{fr_i}{BW} \tag{4.1}$$

where fr_i is the resonant frequency of an EM mode and BW is the bandwidth. The value measured in this way is the loaded quality factor Q_L (2.14).

When measuring the S21 parameter in a cavity with two probes, the BW is measured at -3dB below the maximum of S21. Under a very weak coupling condition, the unloaded Q_0 factor (2.15) may be approximated by the Q_L factor ($Q_L \approx Q_0$).

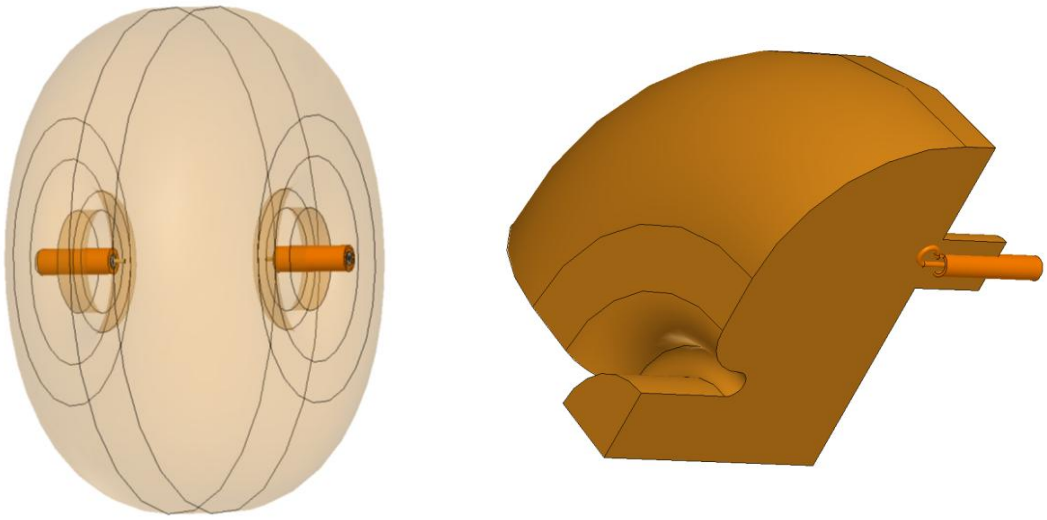

(a) (b)

Figure 4-6. Excitation of an EM mode by an E field (a) or by a H field (b)

In order to measure the quality factor of the whole linac, it must be taken into account that the coupler will load the cavity so via the S21 BW at -3 dB one measures loaded quality factor.

The coupling factor β may be obtained from the peak value of S11 using (2.22). It should be mentioned that the BW function of the VNA may be also used to find the value of the Q_L knowing that the value of S11 at both frequencies which define the BW is[21]

$$\left|S_{11}\left(f = f_0 \pm \Delta f/2\right)\right|^{NA} = 20\log\frac{\sqrt{\beta^2+1}}{\beta+1} \tag{4.2}$$

[21] *For overcoupled structures*

Once the QL has been acquired the unloaded quality factor may be obtained using (2.20). Another reflection-type measurement method to get Q_0 and Q_L may be found in [76] using the Smith Chart (Figure 4-7).

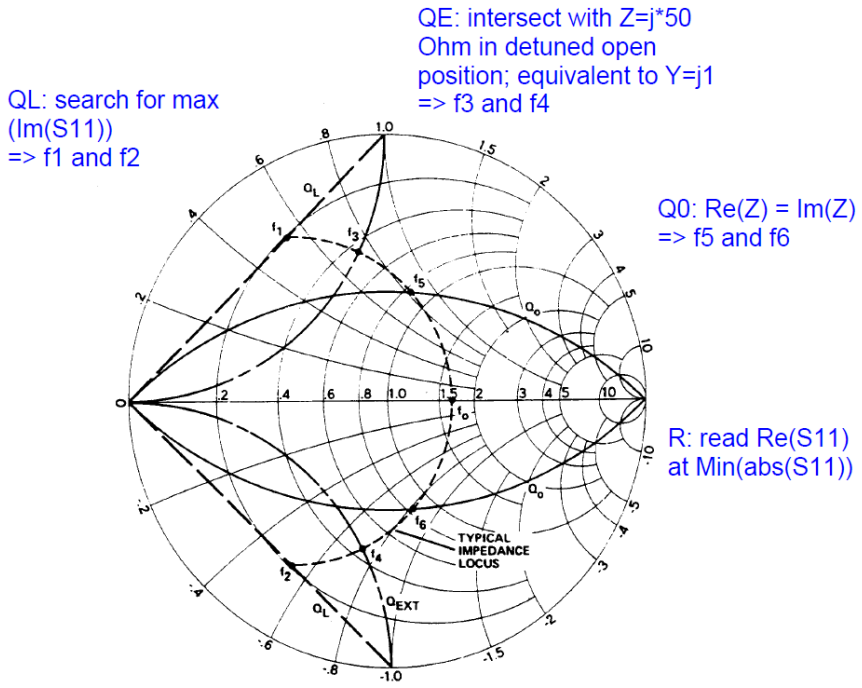

Figure 4-7. Loci of Q0, QL and QEXT of a cavity (from CAS 1992. F. Caspers lectures)

When measuring individually the linac cavities (or test cavities) the presence of the probes inevitably will perturb the quantities that we are trying to measure. Therefore, for accurate results, the probes should be inserted into the cavities just enough to excite the modes.

Before proceeding to the experimental measurements simulations have been performed in order to find out what the actual effect of electric and magnetic probes will be.

Figure 4-8(a) shows the model used to obtain the optimum distance to place the electric probe on axis (parameter *d* is the distance from the centre of the nose cones to the probe). The bigger is d (probe less introduced into the cell) the more accurate is the measurement of the resonant frequency (but in practice measurements become more difficult because less power is transmitted from one probe to the other and signal may get mixed with noise).

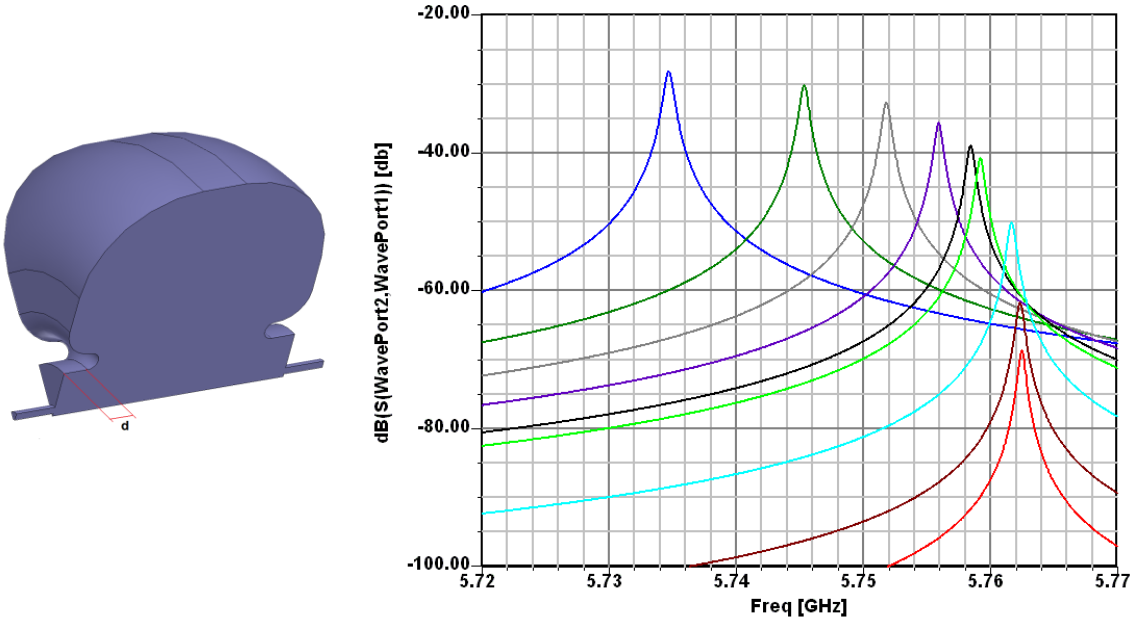

(a) (b)

Figure 4-8. Simulation model for electric probes on axis (a) and resonant frequency response to the probe insertion (b)

In order to know the effect of the probes we must know the theoretical resonant frequency for this model in absence of probes which is 5763.5 MHz. Figure 4-8(b) shows the transmission from one probe to the other as a function of the parameter d. In this picture the blue line corresponds to maximum penetration of the electric probes (d≈0) where the change in resonant frequency is quite noticeable (a 0.5% lower than theoretical value). As we remove the probes the resonant frequency tends to approach the theoretical value. The pale blue curve (d=3mm) has a maximum at 5762 is 1.5 MHz below theoretical value (0.026 % lower) where the red curve (d=5mm) has the maximum at 5763.2 MHz. With these results we can get a good idea of the optimum positions of the probes. It could be possible to take far away the probe, but signal will be mixed with noise so in practice according to these results measured resonance frequency will be a few hundredths of kHz lower than real frequency.

As it is expected to measure the properties of half accelerating cavity as well, a simulation with magnetic probes have been performed over the HFSS model in Figure 4-9(a) . The probes are introduced into the middle plane of an accelerating cell a distance *d* and they are away from the axis where the coupling with magnetic field is maximal. In order to optimize this coupling the loop plane is oriented perpendicular to the magnetic field lines.

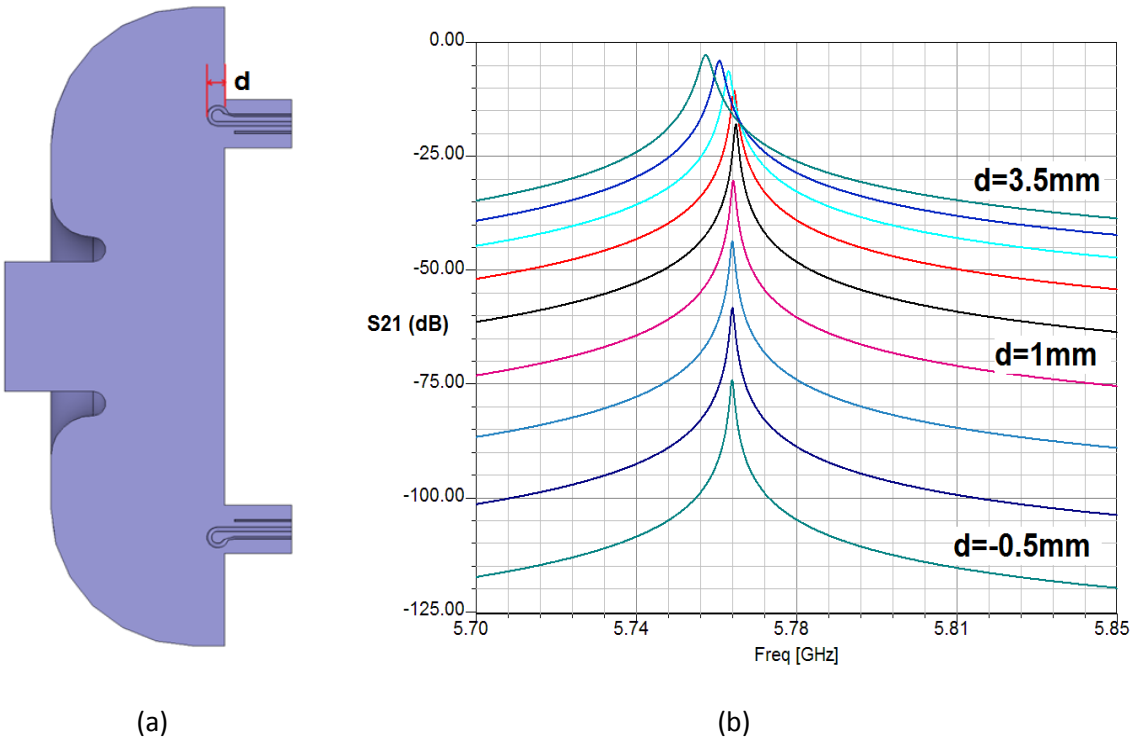

(a) (b)

Figure 4-9. Simulation model for magnetic probes on axis (a) and resonant frequency response to the probe insertion (b)

Making two holes where the probes are introduced gives a new theoretical resonant frequency of 5762.0 MHz. Figure 4-9(b) shows the transmission from one magnetic probe to the other for different values of the penetration d. Looking at these results it can be noticed that the probe has influence on the resonant frequency when it is introduced more than 2mm. Compared to the electric probe the magnetic probes seem to have a lower effect in the resonant frequency. Of course the lower volume of the magnetic probes produces a small perturbation in the resonance.

Real data will slightly differ from these simulations because of the probe geometry used in the model does not correspond to the real one. The main difference is due to the shape of the coupling loop (compare to Figure 4-5(a)).

On the other hand, when measuring RF properties of whole linac, if something wrong is found (differences with theoretical coupling factor, resonant frequency, E field profile, etc.), the separate cavities must be tested. In order to do that the electric probes must be introduced into the beam pipe. As doing so, the adjacent cells (from the cell we want to measure) are short circuited by the bars carrying the antennas, which significantly detune them. Due to this

detuning electromagnetic field is not excited in neighbouring to measured cell and in this way situations equivalent to conditions for π/2 mode exist. This gives the possibility to measure separately π/2 accelerating cells frequency (Figure 4-10(a)) and π/2 coupling cell frequency (Figure 4-10(b)).

Obtaining the differences between accelerating and coupling cells π/2 frequencies the stop band may be found (see section 2.7) and if necessary, removed.

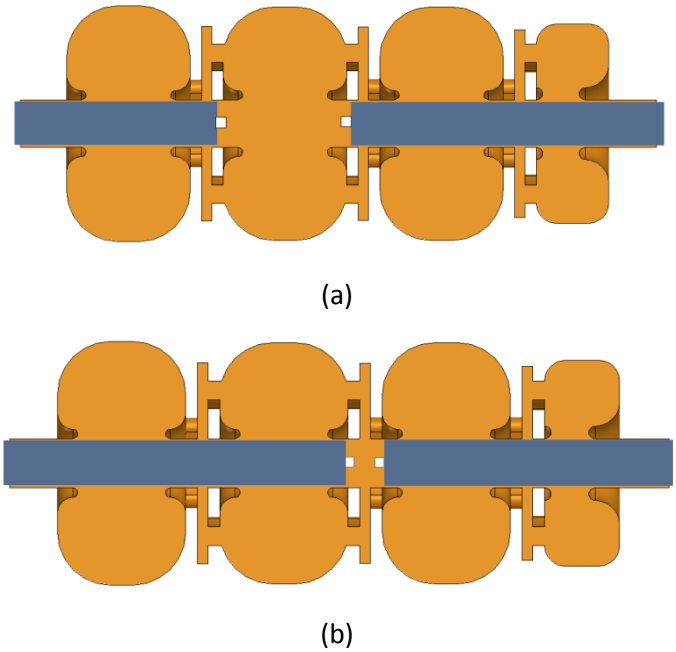

(a)

(b)

Figure 4-10. Measuring method to get resonant π/2 mode frequency of separate cells of accelerating structure

4.1.4 Axial field measurements

There is another important RF measurement that must be done after the accelerating cavities have been manufactured: the measurement of the on axis electric field distribution. This will give us a hint of whether the structure has some error or it is behaving as we expected.

Introducing an ideally conducting object into a metallic cavity will perturb the resonant frequency by an amount depending on the local electric and magnetic fields. This fact is expressed in the Slater perturbation theorem [77]

$$\frac{f-f_0}{f_0}=\frac{-1}{4W}\left[\varepsilon_0\iiint_{v_\tau}|E|^2dV-\mu_0\iiint_{v_\tau}|H|^2dV\right] \tag{4.3}$$

where f is the perturbed frequency, f_0 is the unperturbed frequency, H and E are the magnetic and electric fields in the unperturbed cavity, W is the total energy stored in the cavity and the volume integrals are over the volume V_t, occupied by the object.

Experimentally the probe is moved along the axis and change of resonance frequency is measured with VNA using two probes as shown in Figure 4-11 via S21 parameter or with one probe via S11 parameter dependence on frequency.

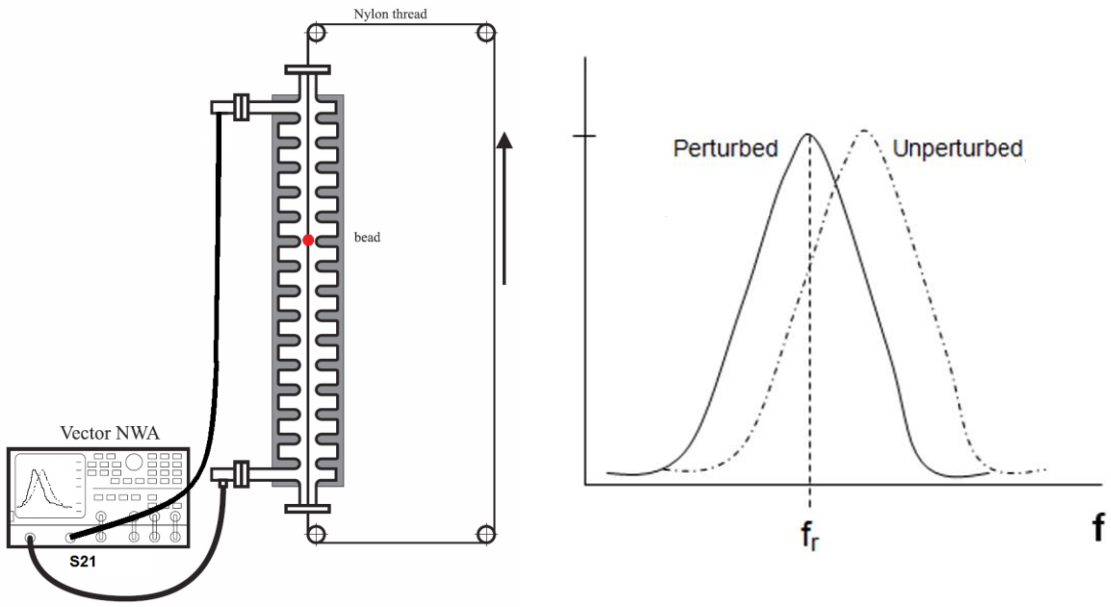

Figure 4-11. Scheme of VNA measuring S21 when bead passes through an accelerating cavity (a) and qualitative S21 change when bead is being introduced (b)

When measuring field distribution on-axis, where there are no magnetic field and no transverse electric field, the measured frequency shift when metallic bead is moving along axis *z*, the electric field strength on-axis and the stored energy are connected [78] by:

$$\frac{\Delta f(z)}{f_0}\approx-\frac{k_z E_z^2(z)}{W} \tag{4.4}$$

where k_z is a constant, the so called ***form-factor of the probe***, which

(1) can be calculated analytically in sophisticated models,

(2) can be determined in measurements with cavity with known analytically field distribution, e.g. pill-box cavity with TM_{010} field

(3) or could be calculated with a 3D code if accuracy of simulation is sufficiently good. In calculations with HFSS of the frequency shift, absolute value of electric field strength and stored energy are known, so form-factor can be obtained. In literature attempts to find form-factor in this way have not been found.

When form factor is known, value of effective shunt impedance can be obtained: using definition of quality factor (2.15) and combining with (4.4) we get:

$$E_z(z) \approx \sqrt{\frac{\Delta f(z)}{f_0}\frac{PQ_0}{2\pi f_0 k_z}} \tag{4.5}$$

Therefore effective shunt impedance is:

$$Z_{eff} = \frac{\left[\int_{-L/2}^{L/2} E_Z(z)\cos\left(\frac{2\pi z}{\beta\lambda}\right)dz\right]^2}{PL} \approx \frac{Q_0}{2\pi f_0 k_z L}\left[\int_{-L/2}^{L/2}\sqrt{\frac{\Delta f(z)}{f_0}}\cos\left(\frac{2\pi z}{\beta\lambda}\right)dz\right]^2 \tag{4.6}$$

The perturbation technique is an approximation and is usually valid [78] for changes in resonant frequency lower than 5 % (280 MHz). However in order to obtain a good accuracy in places where E field is very low (as could be the coupling cells) a maximum perturbation of 0.1% should be applied. This means that for the linac these changes must be below 6 MHz.

A set of simulations have been performed on the single accelerating cell taking into account different available objects that could be used for real measurements and that nylon thread can be threaded through them.

A first study has consisted of comparing the effect of a 3mm and 1mm diameter spherical beads when moving along a single accelerating cell (Figure 4-12). The simulation is meant to check the validity of Slater theorem for the bigger ball (being its size comparable to the beam pipe diameter).

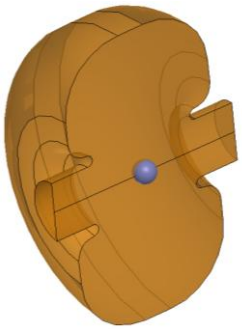

Figure 4-12. Metallic spherical bead moving along axis

In Figure 4-13 E field calculated for a single accelerating cell without slots is compared with field restored according to (4.4) in calculations with two spherical bead placed at different positions along z axis.. The 3mm and 1mm diameter metallic ball produce a maximum frequency shift equal to 26.3 MHz and 1.0 MHz respectively.

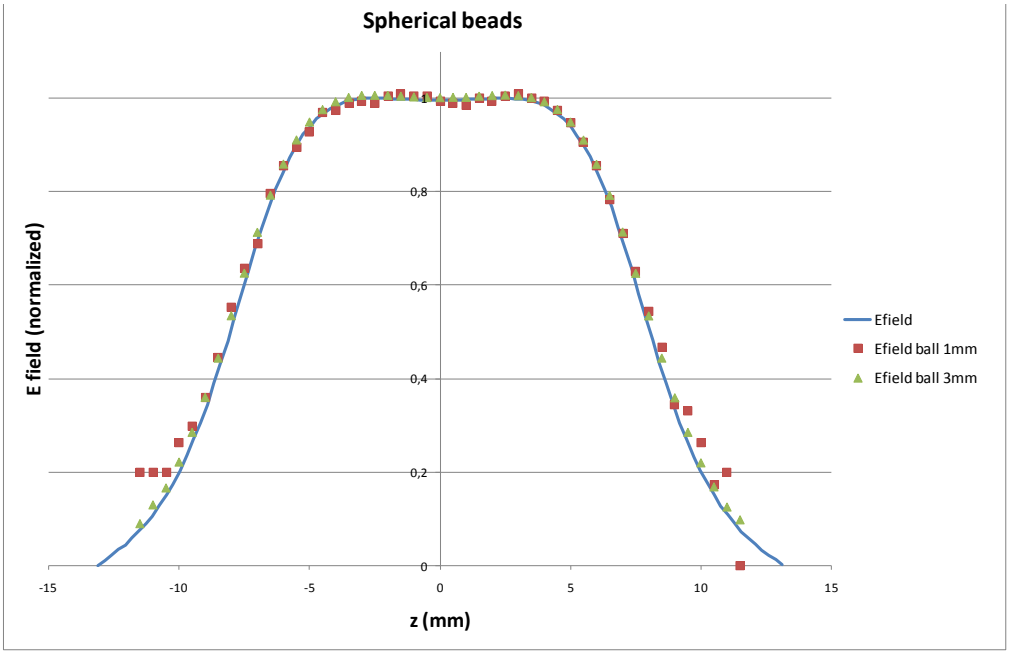

Figure 4-13. E field comparison with perturbation method: spherical beads

According to these results the bigger bead follows quite accurately the Slater formula, however it should be noticed that the 3 mm ball is larger than the width of the coupling cell and is comparable with beam hole diameter so it will smear out coupling cell field if such is available and radial electric field components will influence on the results of shunt impedance measurements. The small bead does not behave so well which in principle is due to accuracy of calculations as the maximum change produced by the smaller bead is only 1 MHz.

For real measurements, to get metallic cylinders, a needle from a syringe (0.8 mm outer diameter, 0.6 inner diameter) has been cut in pieces of different length. A set of simulations has been performed for three of these pieces cylindrical (length equal to 0.56 mm, 2.3 mm and 4.45 mm). Figure 4-14 shows the cylinder moving along axis.

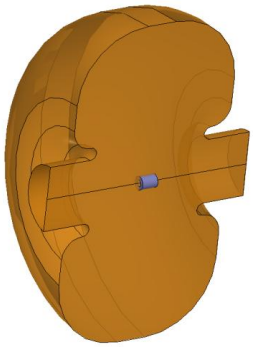

Figure 4-14. Metallic cylinder moving along axis

In this case, just results for half accelerating cell are shown (as it is symmetric). Figure 4-15 shows the result of fitting the resonant frequency changes (4.4) with E field for the three cylinders.

Knowing that the simulations are more accurate for the bigger objects and looking at fit of the curves it can be noticed that bigger cylinder (4.45mm) fits worse than the medium cylinder (2.3mm) which likely means perturbation method begins to be less precise. The fit curve for the smaller cylinder shows again the effect of poor accuracy of simulating a low perturbing bead. This lack of accuracy when changes of resonant frequency are smaller is an effect quite similar to what is expected in experiment in which the signal/noise ratio would get worse when beads are smaller. This issue will be checked out when performing real measurements in the following chapter.

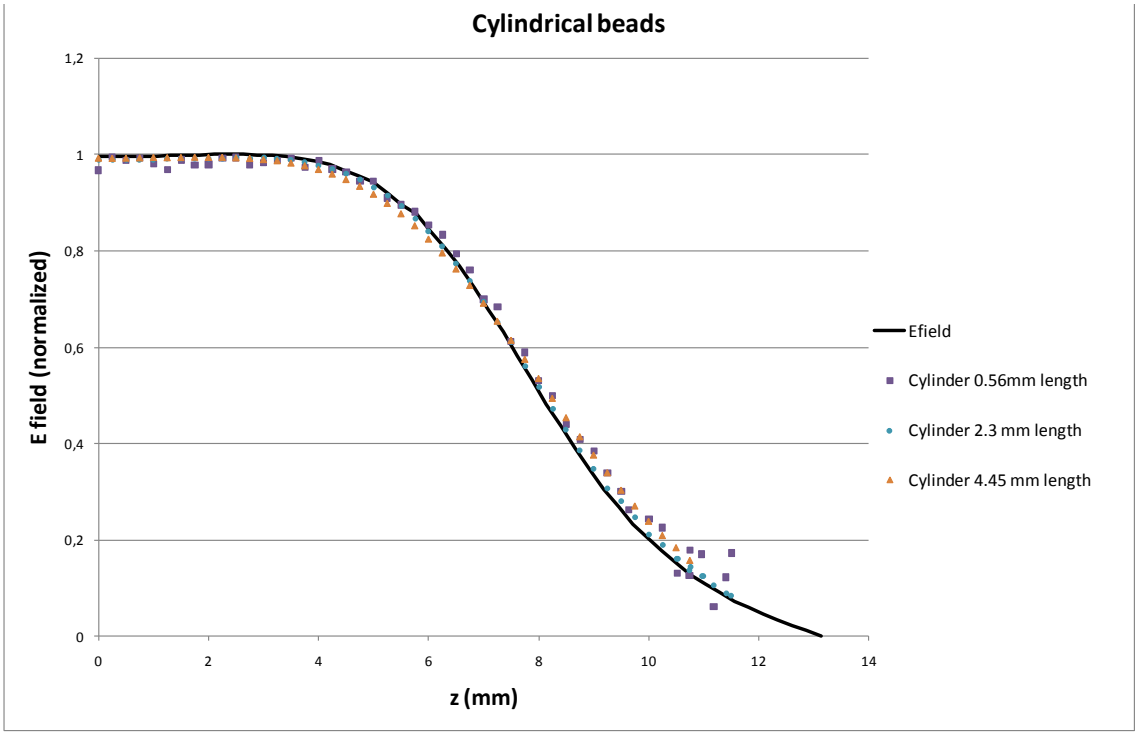

Figure 4-15. E field comparison with perturbation method: cylindrical beads

From the fit of the curves the form factor for the different beads can be obtained. With these values the effective shunt impedance of the cavity can be calculated if the following approximation of (4.6) is done

$$Z_{eff} \approx \frac{Q_0}{2\pi f_0 k_z L}\left[\sum_i \sqrt{\frac{\Delta f(z_i)}{f_0}}\cos\left(\frac{2\pi z_i}{\beta\lambda}\right)\Delta z_{i+1}\right]^2 \qquad (4.7)$$

Maximum frequency shift when introducing the beads, the beads form factors, effective shunt impedance of single accelerating cavity and relative difference from theoretical shunt impedance and calculations are shown in Table 4-1.

As a short conclusion, taking into account all the beads simulated, the 2.3 mm cylinder gives the best results for the accelerating cell. Besides, the values of effective shunt impedance are closer to the theoretical value (105.1 MΩ/m) for cylindrical beads. Nevertheless, smaller beads must be checked out during real measurements for the field which changes essentially at short distance i.e. coupling cell field while the signal/noise ratio allows performing the measurement. In section 4.2 the experimental test bench to carry out these measurements will be described.

Table 4-1. Main parameters for the metallic calculated with different beads

Type of metallic bead		Maximum frequency shift	Form factor	Zeff AC cavity and (difference from theoretical)
Spherical (3mm diameter)		0.456 %	$1.03\ 10^{-8}\ \varepsilon_0$	110.7 MΩ/m (+5.3 %)
Spherical (1mm diameter)		0.018 %	$4.0\ 10^{-10}\ \varepsilon_0$	110.9 MΩ/m (+5.5 %)
Cylinder R_{out}/R_{in}=0.8 / 0.6mm Length = 0.56mm		0.023%	$5.2\ 10^{-10}\ \varepsilon_0$	103.3 MΩ/m (-1.7 %)
Cylinder R_{out}/R_{in}=0.8 / 0.6mm Length = 2.3mm		0.257 %	$5.9\ 10^{-9}\ \varepsilon_0$	102.6 MΩ/m (-2.3 %)
Cylinder R_{out}/R_{in}=0.8 / 0.6mm Length = 4.45mm	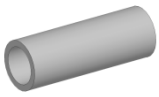	0.987 %	$2.29\ 10^{-8}\ \varepsilon_0$	102.6 MΩ/m (-2.3 %)

4.1.5 Possible causes for resonant frequency changes

There are a number of reasons that could cause discrepancies in experimental measurements from theoretical simulations in our RTM linac.

4.1.5.1 Accuracy of simulations

In principle with current calculation capabilities of computers small deviations are expected for single cavity if its geometry has been properly meshed and good convergence has been observed. Bigger errors could appear in the assembly of all accelerating segments plus coupler when simulating the whole linac: taking into account convergence obtained in previous chapter, the resonant frequency error is expected to be within 1 MHz.

4.1.5.2 Machining error

The resonant frequency deviation of an accelerating structure assembly [78] is connected with the machining tolerances as

$$\frac{\Delta f_0}{f_0} = \frac{1}{f_0}\sqrt{\sum_i \left(\frac{\partial f}{\partial q_i}\Delta q_i\right)^2} \tag{4.8}$$

where Δq_i are the tolerances associated with dimensions q_i and $\frac{\partial f}{\partial q_i}$ are the sensitivity of resonant frequency when q_i changes.

A rough estimation with (4.8) for manufactured linac can be obtained taking into account all cells in the linac without coupler and without coupling slots. Sensitivity values have been taken from calculations obtained in section 3.3.3 for single cells. Knowing that machining tolerances for fundamental dimensions are ± 0.02 mm we can assume (according to the machining company) the rms values of errors will below 5 µm. According to the previous values, a relative

frequency change equal to 0.1% could be expected which means that the accelerating mode could be found at 5712 ± 6 MHz.

4.1.5.3 Instrumentation errors

No significant error from our VNA is expected. However a special care to calibration, movement of cables and parameters of VNA must be paid. E.g. the option "span", "number of points" and "tracking" must be intelligently used to get resonant peaks with accuracy. As it has been discussed previously, a systematic error of a few hundred kHz may appear due to field perturbation by the probes.

4.1.5.4 Brazing

Brazing consists of the joining of metals through the use of heat and a filler metal alloy –one whose melting temperature is above 450°C but below the melting point of the metals being joined [79]. Particularly, in accelerating structures made of copper, as the optimum filler use to be an alloy based in silver and copper, the process must be done approximately at 800º C.

Vacuum brazing is the preferred brazing technique [80]. During the brazing process, as the brazing alloy becomes liquid the pieces and the brazing joint itself have to be designed such that a) the melted filler material moistens the joint surface well, in a controlled and regular fashion, that b) the pieces to be joined do not “float” out of their position while the brazing alloy is liquid, and that c) the liquid brazing alloy will not penetrate into the cavity and form drops inside.

Brazing process may affect the resonant frequency in two different ways:

- Deformations due to release of internal stresses: The copper used to built the accelerating structure may have acquired internal stresses previous to the machining of the structure. The amount of stress accumulated depends on its fabrication process. To decrease influence of this source of errors the copper segments after rough machining are annealed at temperatures above 400^{o}C to relief the stresses.

- Change of inner volume due to the spread of filler into the inner surface of cavities consequently causing a detuning in the resonant frequency.

During the thesis, plenty of effort has been put into the matter of brazing. Various tests and different designs have been used before performing the final brazing of the linac as it will be explained in the following chapter. The brazing of the different test for our RTM cavities has been performed by two different specialised groups (AIMEN and CERN).

4.1.5.5 Environmental Conditions

The mode frequencies of the cavity depend on the ambient atmospheric environment as the temperature fluctuation may expand or contract the cavity causing a frequency change. It must be taken into account that the linac operating conditions within the RTM accelerator will be vacuum and stable temperature (maintained by water cooling). Usually high accuracy for absolute value of frequency is required for multi-section accelerators in which different sections are excited by the same reference signal and must be in resonance with this signal. For our RTM hard requirements to absolute value of frequency are not applied because bandwidth of magnetron (400 MHz) is sufficiently large.

According to simulations performed with air instead of vacuum, when measuring cavities we could expect to obtain a resonant frequency reduction approximately equal to -0.7 MHz. Besides, assuming changes in room temperature of 2 or 3 K (above 20 ºC) and taking into account results from thermal calculations of previous chapter, we can expect frequency variation of about 1 MHz.

4.2 Stand for accelerating structure cold measurements

In addition to the basic RF components shown in previous section, and before proceeding to measure the RF properties of the test cavities and linac, a test bench has been designed and built.

The RF cavities are made of copper segments and, as we put them together to form the cavity it is not possible to guarantee the electrical contact along the whole surface. Indeed electrical contact is needed only a few times the skin depth (a few microns). In Figure 4-16 the places where this contact is needed are marked in red (qualitatively). If the contact is not produced, the currents will not only circulate on the inner surface but on the contact surface of segments as well. This would cause more RF losses and the quality factor of resonance would be lower.

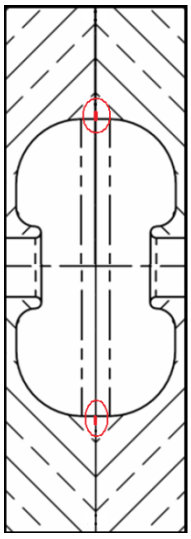

Figure 4-16. Electric contact must be provided between copper segments

This is one of the reasons for brazing the pieces, as the filler alloy when melted is supposed to spread evenly between the contact surfaces producing the electrical contact.

In order to do the measurements before brazing a hydraulic press is going to be used. In principle, as pressure is incremented between the copper segments, the RF losses can be measured with the VNA (Q factor): at the pressure at which the Q factor is saturated the best possible electrical contact has been guaranteed. However, with this proceeding one must be careful especially with large area of contact surface because of deformations can change the

resonant frequency (and especially careful not to produce plastic deformations which would spoil the structure).

Figure 4-17 (a) shows the Solid Works 3D model for the two stainless steel supports where the RTM linac segments are going to be placed. Figure 4-17 (b) shows these devices manufactured (at CIEMAT workshop) and two copper segments in between as well as the electric probes for measuring.

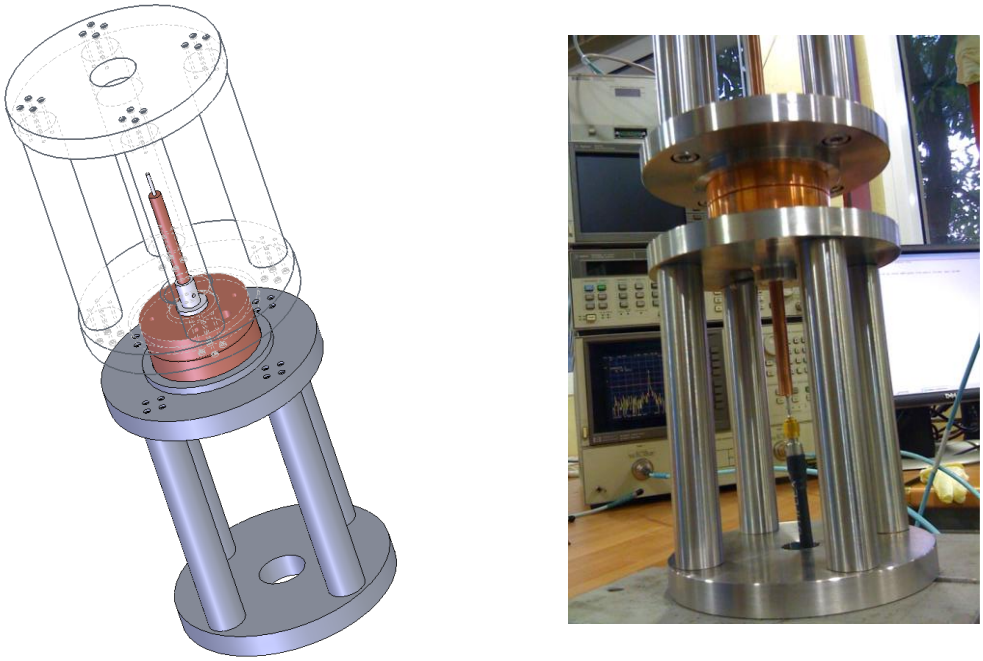

(a) (b)

Figure 4-17. Solid Works model for support device (a) and devices manufactured (b)

The previous design was valid just for measuring test cavities with electric probes at both sides and it was adapted to be able to do measurements with magnetic probes as well (Figure 4-18(a)). An structure to connect waveguide and flanges to linac and aluminium model was needed too (Figure 4-18(b)).

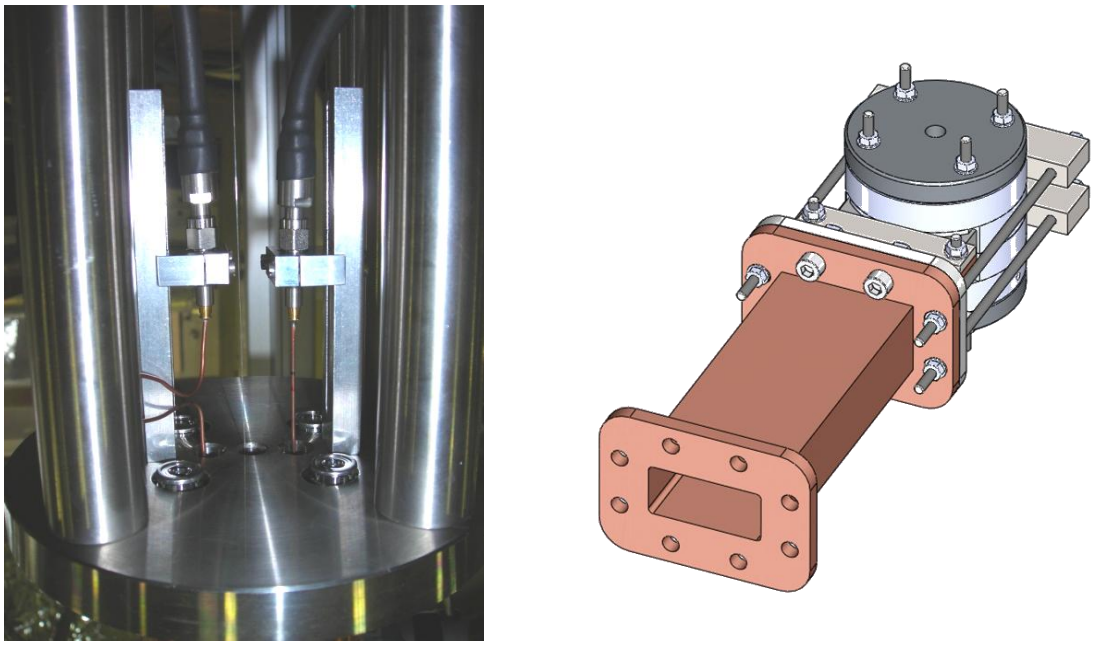

(a) (b)

Figure 4-18. Support device for magnetic probes (a) and support for linac plus coupler (b)

In order to measure E field on axis (see section 4.1.4) the idea represented in Figure 4-19 with pulleys has been carried out.

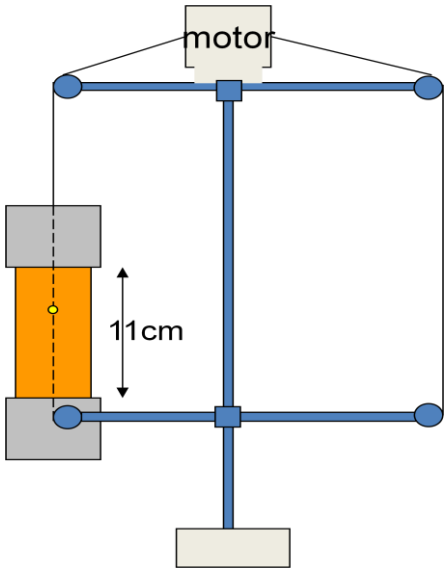

Figure 4-19. Pulleys and motor scheme to move bead along accelerating structure axis

As measurements every 0.1 - 0.3 mm are needed to represent E field with sufficient accuracy that means that for linac more than 1000 measurements have to be performed. That would mean at least one day of manual measurements every test performed with a different metallic bead moving along axis. Besides, the frequency drifts in such a long time would reduce

dramatically the accuracy of E field obtained. In order to improve the efficiency and accuracy of E field profile measurements an automatic system has been developed. A PC with LabVIEW software is used to control a step motor and the VNA. Some of the components (step motor, reduction device, acquisition device and step motor drive board) are shown in the following picture.

Figure 4-20. Step motor, reduction device, drive board and acquisition device

As it has been shown in section 4.1.4 a change in the resonant frequency (which is proportional to the square of E field on axis) is produced when the metallic bead is moving along axis, therefore the program sends signal to move the step motor and time the data (frequency of maximum of Log magS21) from the VNA is acquired.

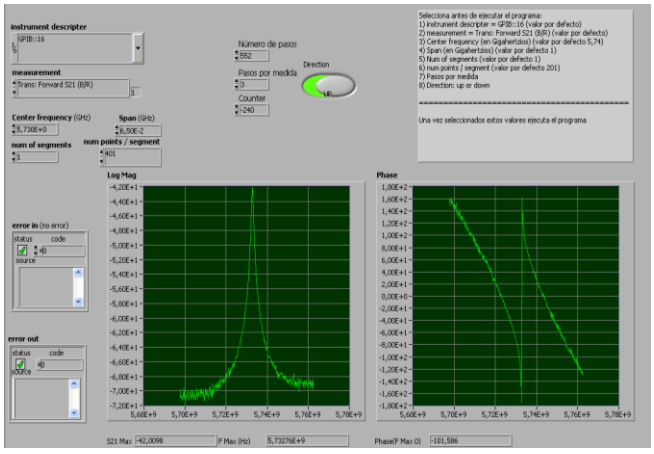

Figure 4-21. LabVIEW software to control VNA and step motor

Taking advantage of the hydraulic press structure, the design based on pulleys to make a nylon thread to pass through the cavities axis is shown in Figure 4-22.

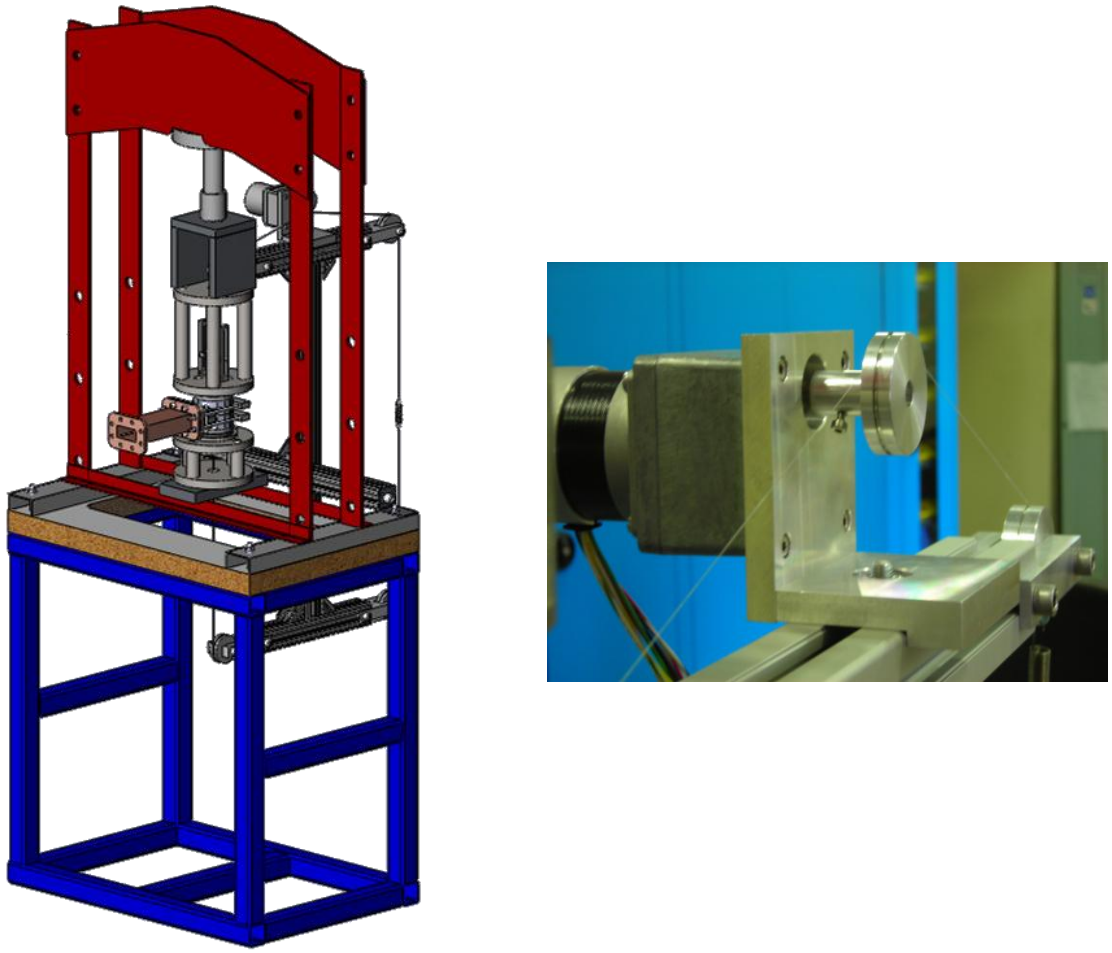

(a) (b)

Figure 4-22. Mechanical design to hold step motor and to move the thread with the bead by means of a system based on pulleys (a) and real motor moving the thread (b)

A 0.25 mm diameter fishing thread made of nylon has been used for this test bench. Knowing that every step of the motor produces a lineal displacement of the bead equal to 0.115 mm and having acquired the values of frequency shifts every step, the E field on axis can be easily obtained if the appropriate bead is used (see section 4.1.4).

CHAPTER 5

Linac engineering design, manufacturing and measurements

5.1 Test cavities

Before accomplishing the construction of the final accelerating structure, it is mandatory to perform a number of tests to check out many important steps in the process of the design, fabrication and measuring the linac. The main important issues to test out are:

- The quality of copper machining achievable (good accuracy and roughness).
- The quality of brazing.
- The performance of the design (by checking out if some specially complicated parts of the drawings can be fabricated in real life and executing individual tests to verify specific RF parameters of the design).
- If the RF probes and experimental test bench developed to measure the RF properties are working properly.
- Isolation of cooling tubes (as the operation of linac will be in vacuum no leakages should exist from the water cooling tubes).

5.1.1 Test cavity I

5.1.1.1 The goals and the parameters of the test cavity I

The first test performed, the cavity test I, is intended to prove that a chosen machining company is suited for the final machining of the linac. The quality of copper machining achievable should be good (and cheaper) enough to guarantee minimal deviations from the RF properties obtained in the optimization study of linac.

With this test, there are two RF parameters to be tested:

- Quality factor
- Resonant frequency

The quality factor tells us about the magnitude of the RF losses in the copper surface which depend on the roughness of surface machining.

The discrepancy of the measured resonant frequency and the one calculated in the simulation tells us how good is the accuracy in the machining. As well, 3D numerical control machine can be used to compare the solid model to the geometry of the machined structure.

Another important issue to verify with the help of this test is the study of pressure needed to guarantee the electrical contact in the measurements before brazing.

Also, it has been taken advantage of this test to do a first attempt in the complex matter of the brazing.

The test cavity I consists of two discs which form a single accelerating cell without coupling slots (only a regular accelerating cell). In order to get a cell very close to real one, maximum radius of accelerating cell is 1.9699 cm, which is the maximum radius in real structure (cell 4a+4b). This is done so that the brazing test will be as difficult as in real structure (if we chose the biggest radius possible, then the less surface we have left to place the alloy for brazing because the diameter of the copper structure is limited as it will be explained in section 0). A design of a simple accelerating cell has been done in HFSS. Figure 5-1 shows the solid model used for the design and the electric field for the acceleration mode. The resonant frequency is 5763 MHz and the unloaded quality factor is Q_0=11500.

(a) (b)

Figure 5-1. Solid model of vacuum (a) and E field in the test cavity I

The resonant frequency of this regular cell, which has the same dimensions as the assembly 4a+4b, is higher than the operation frequency (5712 MHz) because there are not coupling slots included (inductive component has been reduced producing an increase in the resonant frequency).

5.1.1.2 Mechanical design, machining technology and results

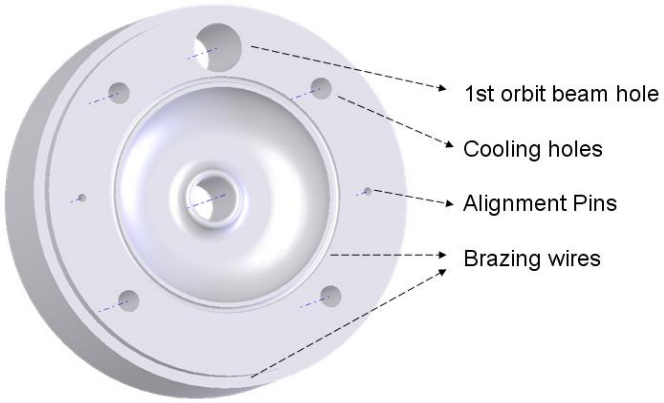

Figure 5-2. Solid Works view of one segment of the cavity test I

Figure 5-2 shows one segment of the test cavity I designed with the software Solid Works. The mechanical design includes the cooling pipes and also the hole for the 1st orbit beam in order to have test cavity as closer as possible to the real linac. Also, the segment includes alignment pins to guarantee that the axis between the two segments is aligned.

The material of the cavities is a high purity OFE copper (impurity content less than 40 ppm) which has been supplied by Luvata in form of extruded rods. The machining has been made in Utillajes HUERTA S.L.. In order to get quality factor close to the one calculated in a simulation,

the roughness must be lower than the skin depth (approximately 0.8 um) at the operation frequency. A roughness of Ra=0.3 µm has been asked. As it has been shown in section of 3.3.3, a variation of 1 to 3 µm can change the resonant frequency in 1 MHz. As a compromise solution (availability of machining companies, price and performance), 10 to 20 µm tolerance has been chosen for the most delicate parts of the cavity.

The two high precision copper segments have been made by turning, drilling and milling operations using CNC (Computer Numerical Control) machine tools. The segments have been rough machined, stress relieved in air for 1 hour at 220^{o}C with the subsequent fine machining to obtain the final dimensions. One pair of segments machined are shown in Figure 5-3

Figure 5-3. Copper segments of the test cavity I machined

5.1.1.3 Technology and results of brazing

One of the cavities built was brazed after the first set of RF measurements while the other has been kept with educational purpose. The process has been performed in the technological centre AIMEN. A vacuum furnace TAV has been used (Figure 5-4(a)) and the filler chosen is the eutectic alloy Cu28.41 % Ag 71.5%.

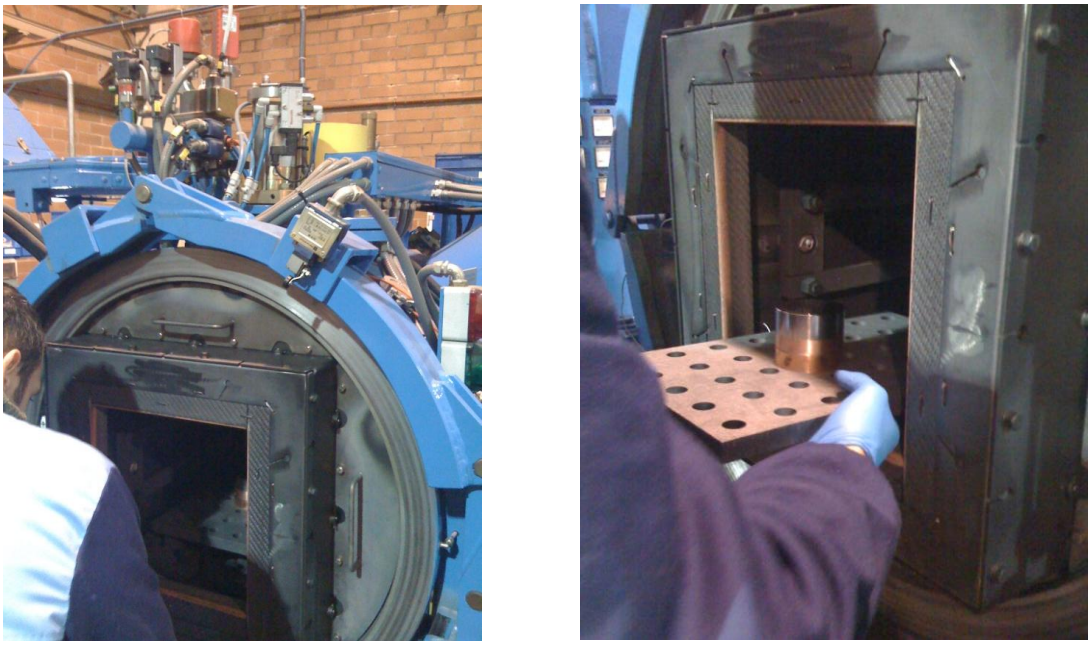

(a) (b)

Figure 5-4. Brazing furnace at AIMEN (a) and test cavity I with stainless steel mass on the top when being introduced into the furnace (b)

According to the advice from experts in brazing at CERN a pressure of 30-50 g/cm^2 must be applied. A mass of stainless steel is placed on the top of the cavity (Figure 5-4(b)).

In Figure 5-5 a cross section of the cavity is shown. The places where the filler is placed are pointed out as well (other view of these grooves for the filler can be seen in Figure 5-2). The aim, by placing the both concentric fillers, is to guarantee the electrical contact between surfaces (see Chapter 4). Both inner and outer filler would provide the vacuum tight condition to isolate the cooling channels.

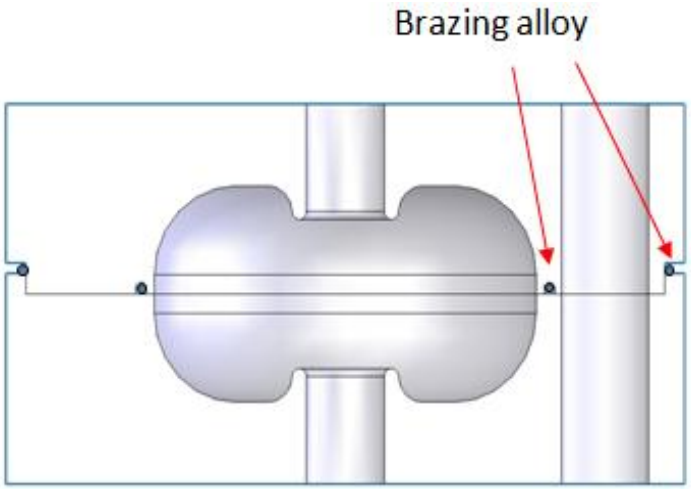

Figure 5-5. Cross section of test cavity

Concerning the contact surfaces between segments, in both of them the surface roughness has been asked to the machining company to be 0.8 μm. This value has been used by other authors in the vacuum brazing of accelerating structures [80]. Besides, sharp corners have been required in the surfaces to be brazed in order to avoid any overflow of the brazing alloy, especially into the inner surfaces of the RF cavity.

Trying to follow the thermal cycle recommended in [81] some test were performed with other copper structures before proceeding to braze the test cavity I. It was observed that the alloy was spread everywhere, and as the filler alloy is not supposed to enter into the inner surface it was decided to reduce the time the temperature of the piece was above the melting point of the filler (780 ºC). In the following figure the thermal cycle followed to braze the test cavity I is shown.

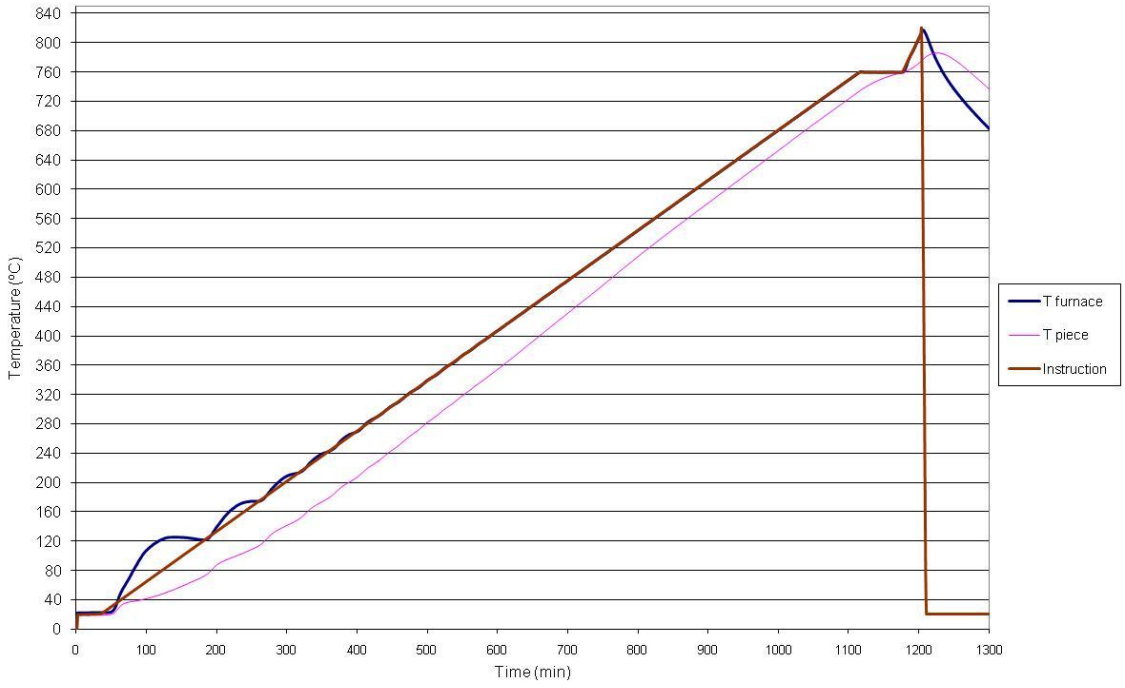

Figure 5-6. Brazing cycle for test cavity I

The temperature of the piece[22] was above the filler melting point no more than five minutes and the maximum temperature reached by the piece was 6 º C higher than the melting point.

After brazing, the RF properties of the cavity were measured again, and as it will be shown in the following section, these properties showed a significant change which likely had been produced by the penetration of the alloy into the inner surface.

[22] *Measured with a thermocouple introduced into a hole machined in the cavity*

The cavity was cut to observe what had happened (Figure 5-7(a)), showing that the alloy had indeed been spread into the inner surface (Figure 5-7(b)).

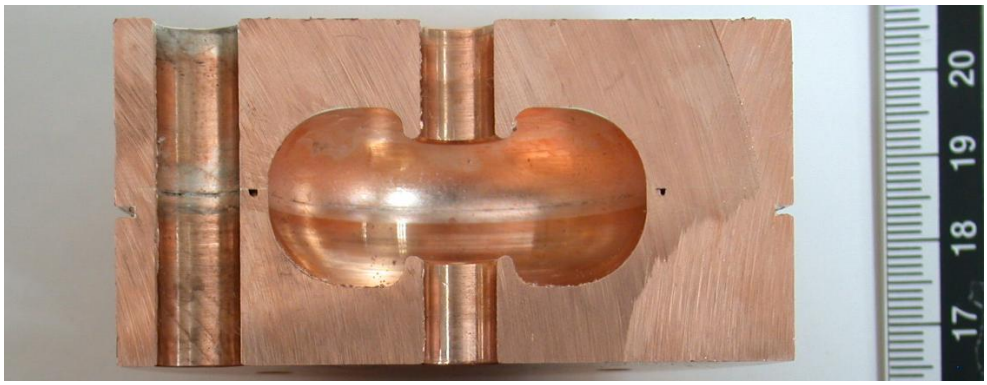

(a)

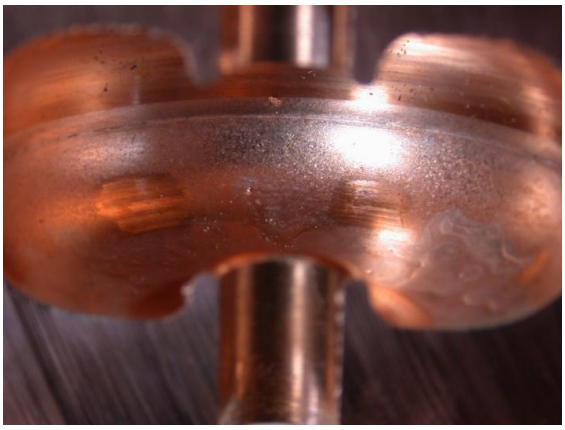

(b)

Figure 5-7. Cut of the test cavity I

5.1.1.4 Results of RF measurements

RF measurements in the test cavity I have been performed before and after brazing. The main reason for measuring before brazing was to check out the accuracy in the machining (tolerances and roughness managed in the machining process) and to find out what was the order of pressure (applied by the hydraulic press) needed to guarantee electrical contact between the copper segments.

RF measurements afterwards have been carried out in order to know if there is any stress relief in the copper that could affect to the geometry, and to find out as well if there is any problem with the brazing design or brazing procedure (e.g. the alloy does not produce electrical contact, or the alloy spreads into the inner surfaces).

5.1.1.4.1 RF measurements before brazing

Two different pairs of copper segments have been built. Let us name the pairs: number I and number II. Because of the pieces were not brazed yet, the electrical contact must be managed by applying pressure to the segments. Therefore, as discussed in previous chapter, the stainless steel support (Figure 5-8 (a)) and the hydraulic press were needed.

(a) (b)

Figure 5-8. Support device with copper segments (a) and experimental stand for measurements (b)

Figure 5-8(b) shows the hydraulic pressure and the experimental configuration used. First, measurements were performed on the copper pair I.

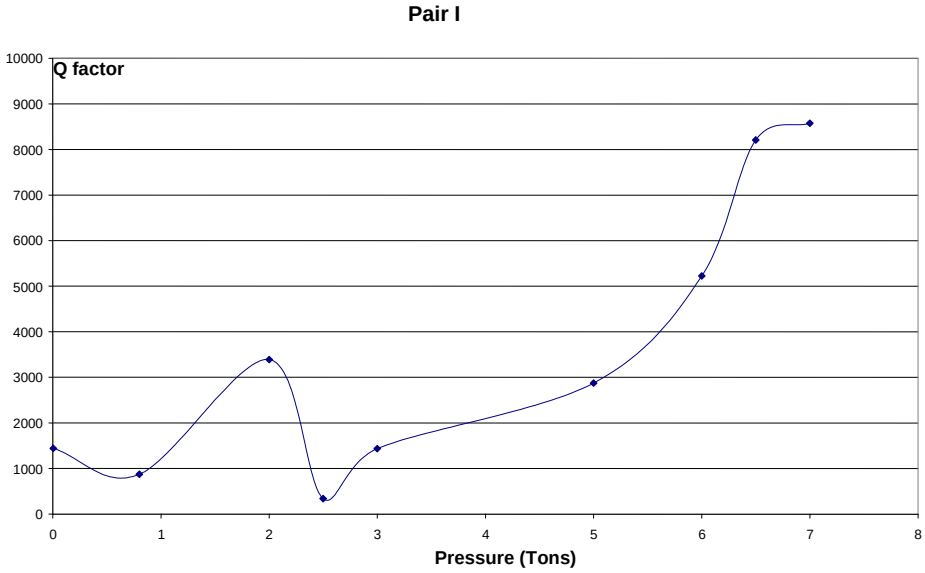

Figure 5-9. RF Measurements of copper pair I. Q factor versus pressure

Figure 5-9 shows that the Q factor stabilizes at really high pressure. Up to 7 tons are needed to provide a good electrical contact. The same happens with the frequency (Figure 5-10) which stabilizes applying more than 6-7 tons.

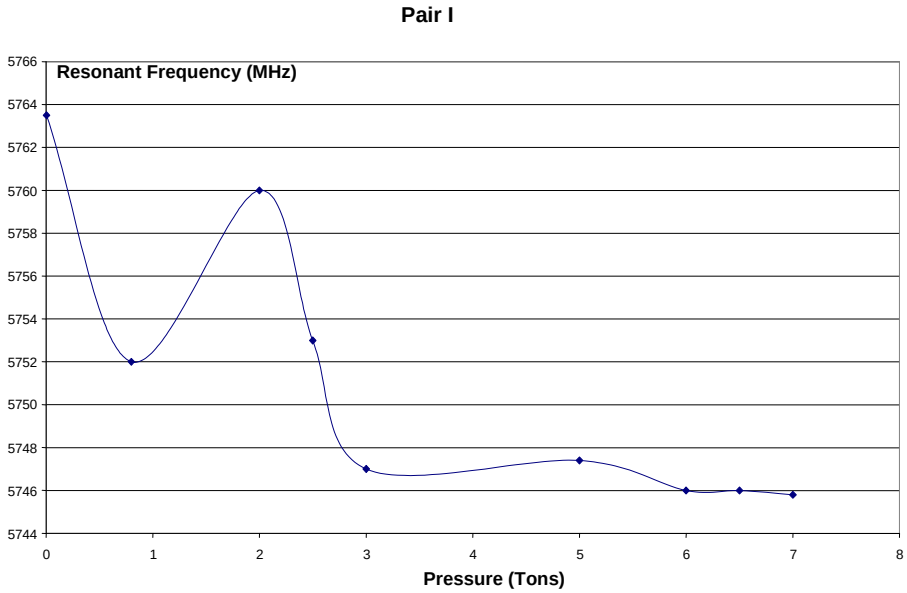

Figure 5-10. RF Measurements of copper pair I. Resonant frequency versus pressure

Q factor reaches a 74% of theoretical one and the resonant frequency stabilizes at 5746 MHz: that is 17 MHz below theoretical one. The transmission between electrical probes (S21) had a maximum of -55 dB so the probes were not influencing on the frequency change.

In principle, at a given pressure, the Q factor should be stabilized, and if from these point pressure increased the Q factor should fall. That means, that even with a mass of 7 tons we did not reach sufficient pressure or, more likely, that the pressure applied was not good to produce contact along all the circumference which defines the contact between the inner surfaces. Therefore, in order to control the places were pressure is applied, two washers have been made and placed at both sides of the copper discs (Figure 5-11). With these washers less kg are needed to produce electrical contact.

Figure 5-11. Washers made to apply pressure

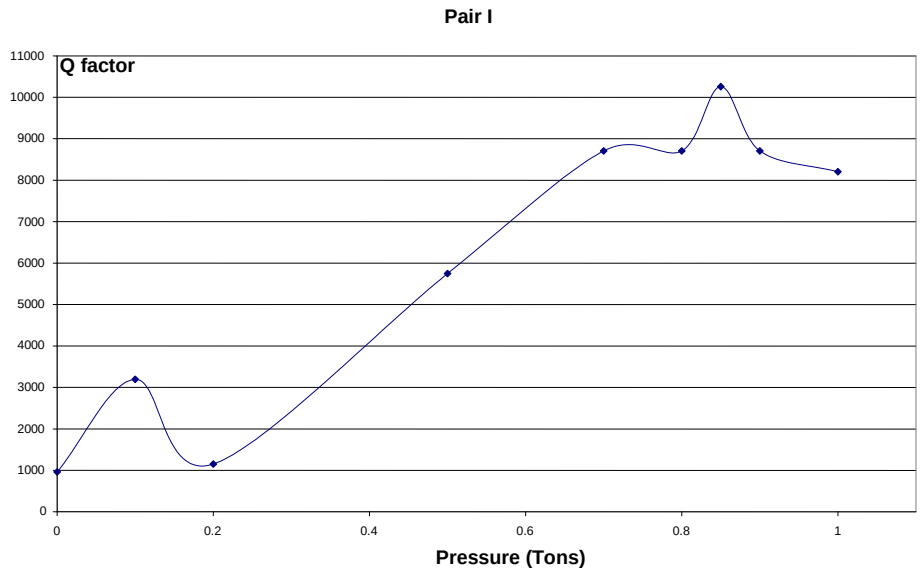

Figure 5-12. RF Measurements of copper pair I. (with washers). Q factor versus pressure

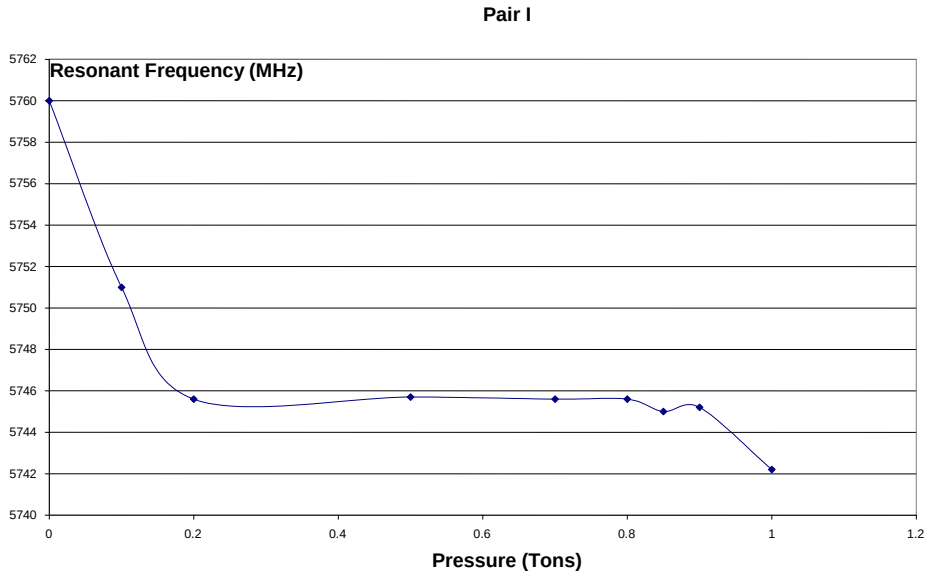

Figure 5-13. RF Measurements of copper pair I (with washers). Resonant frequency versus pressure

When pressure is applied, contact is improved but in certain places may be lost. This is the cause of the oscillations shown in the pictures before the stabilization.

From the previous analysis it is obvious that for this specific cavity test a better electrical contact is managed applying pressure with washers locally (washers are 20mm radius). Q factor obtained is better than in previous analysis (89 % of theoretical one), which is probably

due to the fact that before the pressure limit to get optimum contact had not been reached. Is interesting to notice that in this case the measurements show that at certain pressure (0.9 tons applied over the washers) Q factor goes down and so does the frequency. This is caused by the elastic deformation of cavity volume.

Similar results have been obtained with the second pair of segments (Figure 5-14 and Figure 5-15). In this case pressure needed is a little bit higher, likely because of the positioning of the washers.

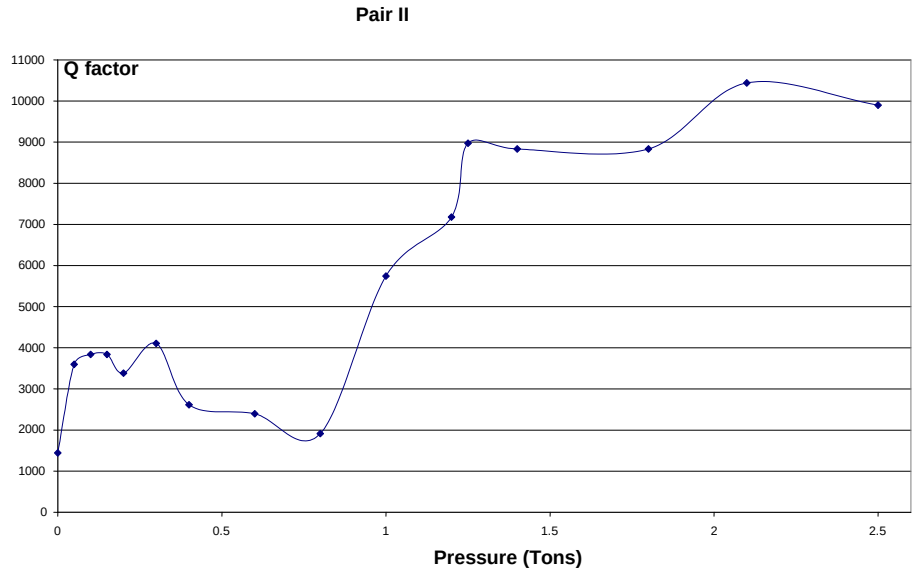

Figure 5-14. RF Measurements of copper pair II. Q factor versus pressure (with washers) .

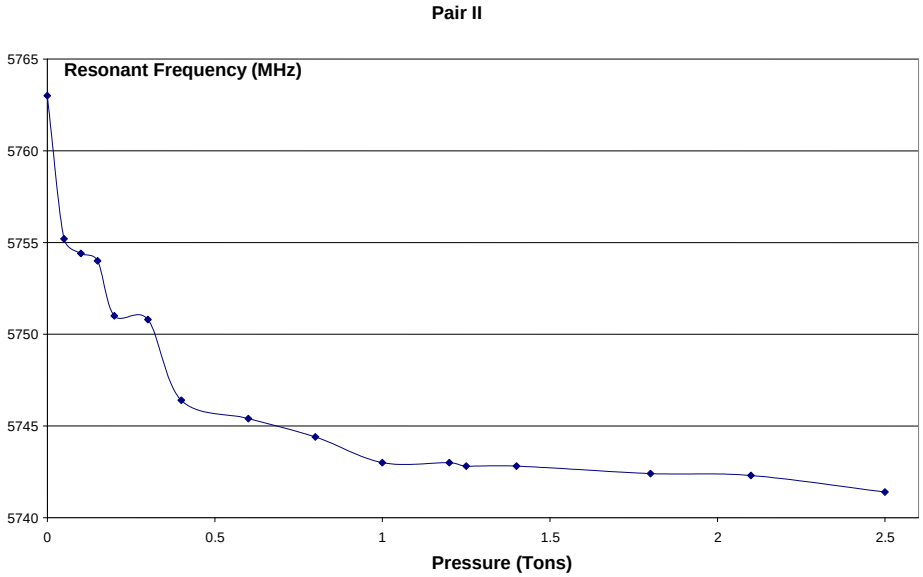

Figure 5-15. RF Measurements of copper pair II Resonant frequency versus pressure (with washers) .

It should be noticed that pressure to produce plastic deformation in copper (70 MPa) has never been reached (maximum pressure of 30 to 35 MPa with and without washers has been applied). Also it must be taken into account that an annealed piece (which is not the case of this test cavity) could have been deformed as its yield strength would be lower (33 MPa).

In view of the fact of the high quality factors measured, it can be concluded that the machining company can reach required surface roughness. However there seems to be a problem with the geometry: The resonant frequency is 17-20 MHz lower than the one obtained in simulations.

A mechanical analysis has been performed to find out the problem. However, results show that applied pressure would not produce an elastic deformation sufficient to cause the discrepancy observed in frequency. With 7 tons maximum applied (first measurements) less than 10 um increase in diameter Ra would occur (33 MPa applied in contact surface between copper discs). This deformation would reduce resonant frequency in about 3 MHz which would not explain the great discrepancy observed.

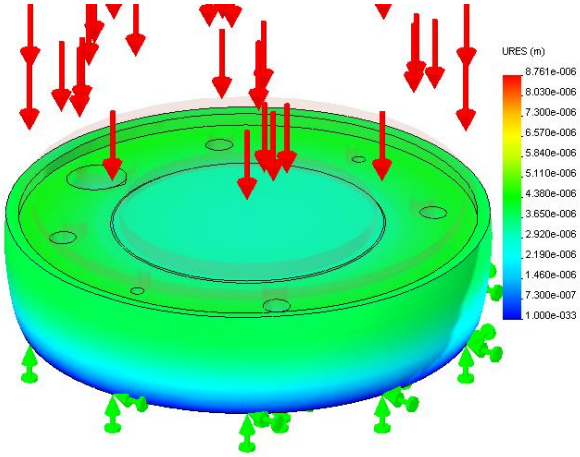

Figure 5-16. Deformation when 7 tons are applied

The company have been asked to check the discs once more and it has been found that the dimensional control was wrong. One segment in each pair of copper has a problem. The machining company did not perform the flat part showed in green in Figure 5-17. So machined segments mechanized are 1.85 mm shorter along the beam axis.

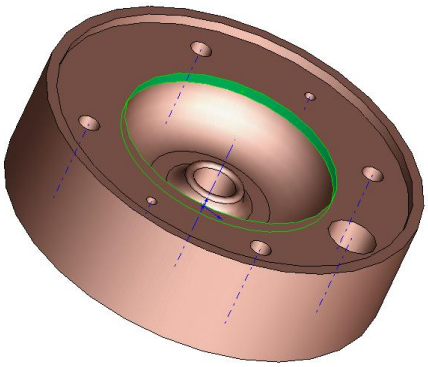

Figure 5-17. Flat part missing in machined segments

Due to the fact that inductance goes lower and capacitor goes higher, the net effect is not as dramatic as one could expect. Simulating with HFSS this new dimension gives a resonant frequency of 5752 MHz, quite closer to the experimental values (see Table 5-1). Looking into another parameter measured in dimensional control: radius Ra of cavity is 19.712 mm when theoretical one should be 19.699 mm (13 um error) which is within tolerances specified. Introducing this in HFSS gives a theoretical resonant frequency of 5749.2 MHz. Some other combination of errors within tolerances and pressure applied could easily give the resonant frequency measured.

Table 5-1. RF properties of test cavity I

	Q Factor	Resonant Frequency (MHz)
HFSS simulation	11000	5752
COPPER PAIR I	10200	5745
COPPER PAIR II	10500	5743

5.1.1.4.2 RF measurements after brazing

After brazing of the copper pair I, the RF parameters have been measured once more: the resonant frequency was higher and Q factor was lower (a 70% of theoretical value). Table 5-2 shows the parameters obtained. This change in the parameters could be explained by the alloy spreading into the inner surface: if so, the inductive part would be lower due to the reduction

in the volume and therefore increasing the resonant frequency. The lower Q factor could be explained by the power loss increase because the inner surface is ruined.

Table 5-2. RF properties of test cavity I after brazing

	Q Factor	Resonant Frequency (MHz)
Simulation	11500	5752
COPPER PAIR I	8000	5753

This was verified when the structure was cut (as it has been explained in 5.1.1.3).

It seems that good RF parameters can be achieved with current design before the process of brazing. However, the brazing has ruined the structure, so this problem must be studied in detail.

5.1.2 Test cavity II

5.1.2.1 The goals and the parameters of the test cavity

With the first test cavity the machining quality of the accelerating cell has been checked out. As well, the first steps into the brazing process have been taken. However, there are some issues that could not be studied. This second test cavity has been proposed in order to study the followings aspects:

- RF parameters measurement of an accelerating cavity with coupling slots and coupling cells.
- Study of the RF properties change after a proper brazing (the process will be performed at CERN).
- Leakage test study.

The test cavity II consists of two half accelerating cells and one coupling cell with coupling slots. The geometry of this structure is similar to the one calculated in section 3.3.2.5 for the preliminary linac segment 2b+3a. Nevertheless, there is a difference which consists of including the beam pipe in order to introduce a view scope so the inner surface after brazing

may be observed. The beam pipe hole could also allow measuring the electric field along the axis.

Figure 5-18 shows the field plots for the three resonant modes TM_{010} –like appearing in the structure. It may be noticed that the resonant frequency for the π/2 mode (Figure 5-18(b)) is not equal to the operation frequency. This is because the beam pipe hole makes the capacitive component to decrease, raising the resonant frequency 1 %.

f_{π} = 5479 MHz Q= 2600

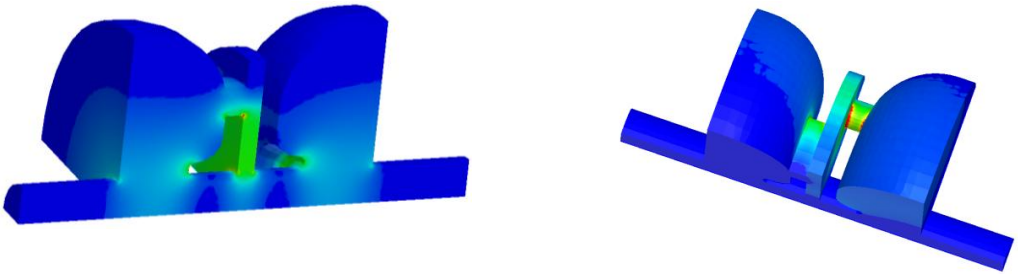

E field H field

(a)

$f_{\pi/2}$ = 5757 MHz (accelerating mode) Q= 6700

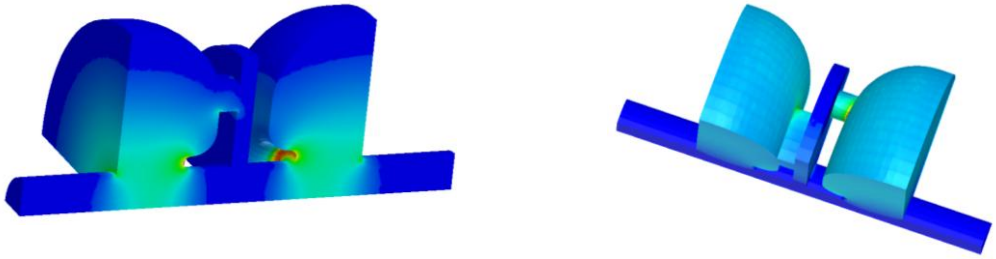

E field H field

(b)

f_0= 6083 MHz Q= 3200

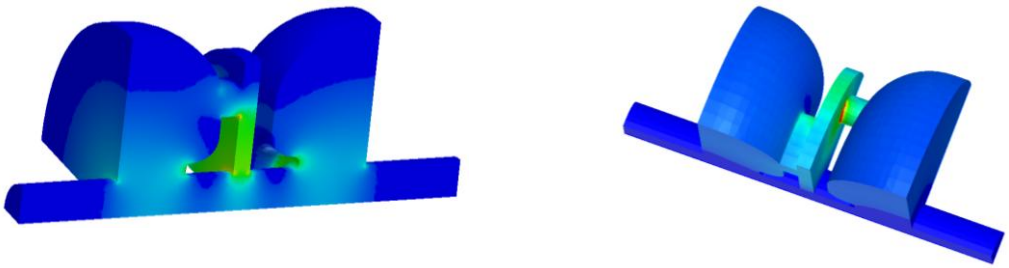

E field H field

(c)

Figure 5-18. E and H field plots for the three resonances in test cavity II

5.1.2.2 *Mechanical design, machining technology and results*

The test cavity II is made of four OFE copper segments. Figure 5-19(a) shows the structure cross section with the coupling cell in the middle and the two half accelerating cells at both sides. In Figure 5-19(b) four VCR Swagelok connectors are shown. They have been included in the design in order to do a leakage test after brazing in each of the four cooling pipes.

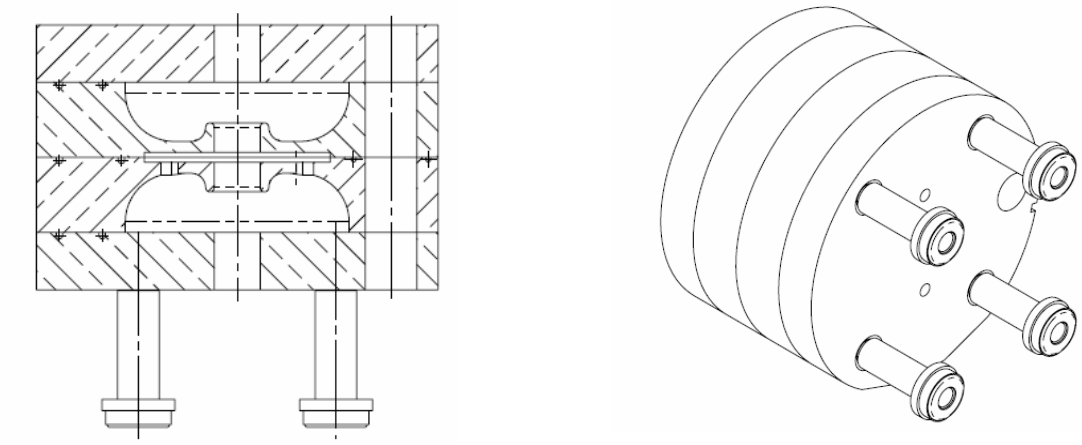

(a) (b)

Figure 5-19. Test cavity II: Cross section (a) and 3D model (b)

The pieces have been made in the company Utillajes Huerta S.L. As performed with test cavity I, before the final machining a rough machining was done. Then, the pieces were introduced in the furnace for 1 hour at 220 ºC to release the internal stresses that the copper could have. During the machining of the inner surface not only the turning machine was used but the milling one too because there is no axial symmetry when the coupling slots are included.

Figure 5-20 shows the segments of the test cavity II after the final machining.

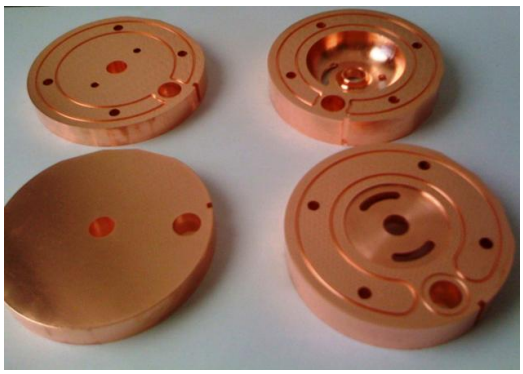

Figure 5-20. Four copper segments machined

Mechanical measurements were performed with the 3D numerical control machine by touching different points on the surface and comparing with the 3D model. An example of this is shown in the following figure. Almost all the important parameters measured were within ± 20 µm.

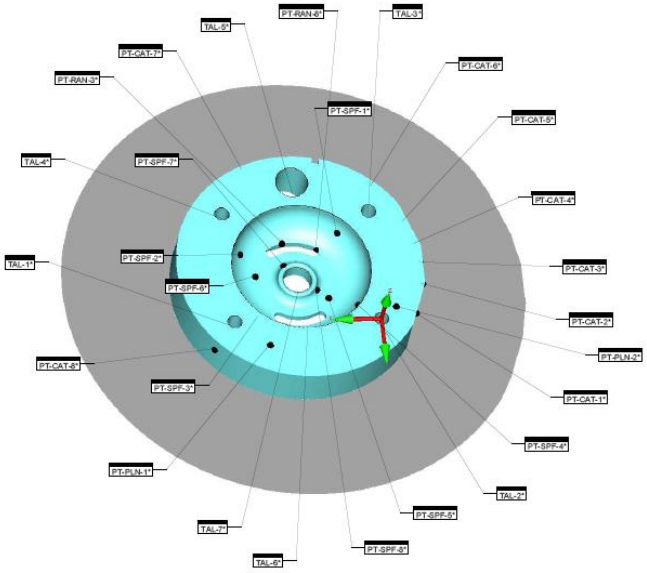

Figure 5-21. 3D numerical control machine

5.1.2.3 Technology and results of brazing

This cavity has been brazed after the RF measurements. The process was carried out at CERN in a vacuum furnace. The main differences from the furnace used in the test cavity I are:

- The furnace has a view port to control when the alloy is melted
- It has metallic heating elements (while the other furnace has graphite heating elements).

The alloy is again the eutectic Cu28 % Ag 72%. Figure 5-22 shows the grooves for the brazing alloy in one of the four segments of the structure. They are placed at 4 mm from the inner surface and surrounding the water cooling holes in order to guarantee the absence of leakages.

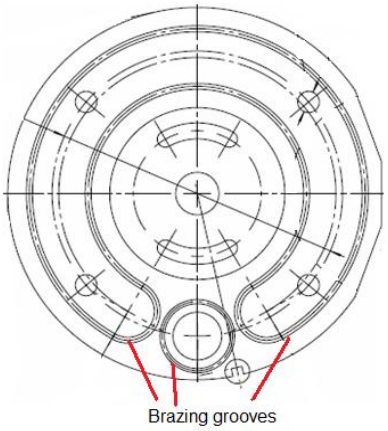

Figure 5-22. Grooves to place alloy in the test cavity II

The pins made in the test cavity I have been removed: now the alignment during brazing is performed by a groove in the outer surface and alumina cylinders and molybdenum wire (Figure 5-23[23]).

Figure 5-23. Alignment by means of alumina tubes and molybdenum wire

Before taking the pieces to CERN they have been cleaned in an ultrasounds bath (Figure 5-24) with a solution of distilled water (60 º C) and 2 % Citranox for 30 minutes. Afterwards the pieces were rinsed with distilled water and they went dry in hot air.

[23] *This picture is not taken from the test cavity II but from a pill-box structure developed at CIEMAT in order to study the brazing.*

Figure 5-24. Ultrasounds bath

The thermal cycle used is shown in Figure 5-25. The time above the melting point (with a maximum of 786ºC) is about 2 minutes.

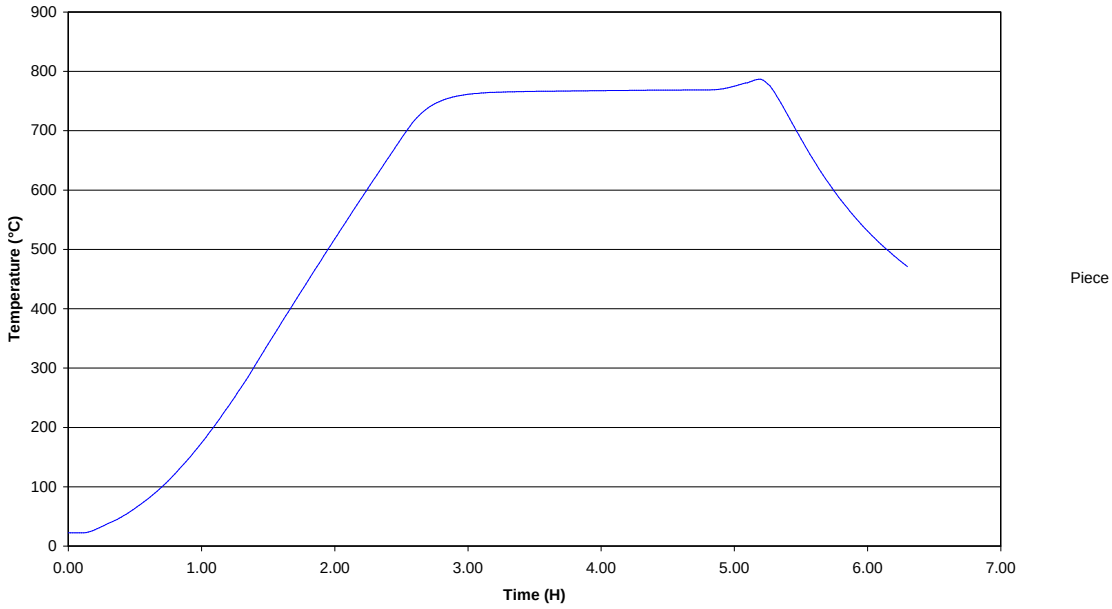

Figure 5-25. Brazing cycle for test cavity II

Figure 5-26(a) shows the cavity after brazing the four segments and the VCR connectors. The dark marks on the top surface are produced by the stainless steel loads that were placed on the segments to guarantee a proper brazing. A picture taken from the inner surface (Figure 5-26(b)) shows no sign of filler alloy spreading.

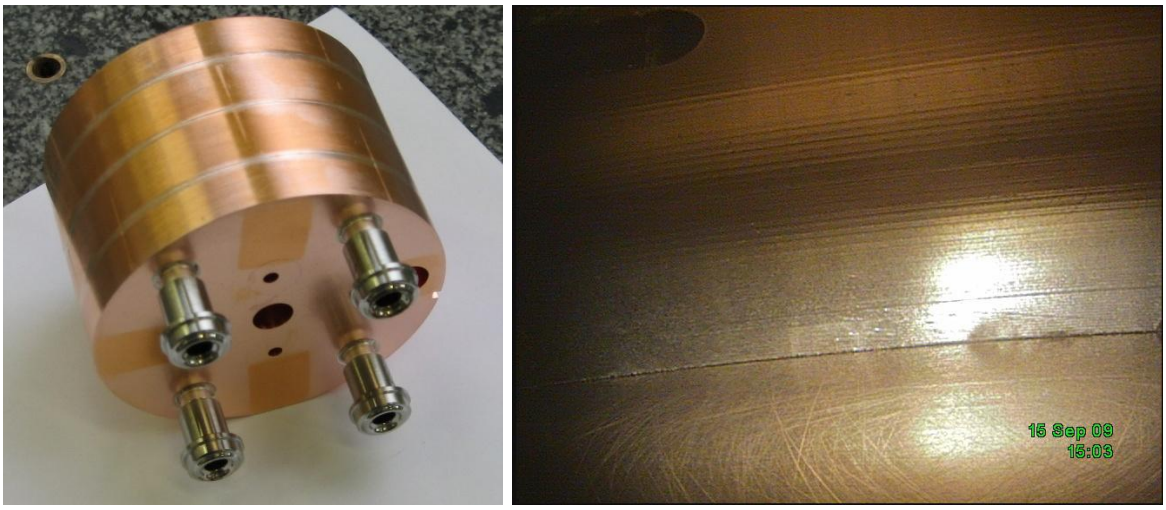

(a) (b)

Figure 5-26. Cavity II brazed (a) and inner surface (b)

In order to find out if there is any leak in the connectors or in any place of the cooling pipes, a test was performed using a leak detector (Figure 5-27) equipped with two pumps (a primary pump and a turbo molecular pump to produce high vacuum) and a probe to detect helium.

Figure 5-27. Leak detector. Leybold. Phoenix L 300

To connect the VCR connectors to the leak detector, an adapter from ¼ VCR to N 16 KF is needed. Vacuum level on each connector is registered, and afterwards a helium gun is applied all over the possible places of leaks (Figure 5-28). If there is any, the probe in the leak detector will detect the helium.

Figure 5-28. Applying He to detect leaks

Detected leak rate is below 10^{-13} $Pa.m^3 s^{-1}$ which is well below specifications.

From this test and from the previous one, many important aspects in order to succeed in the brazing for accelerating structures (at high frequency) have been learned.

- If possible, the vacuum furnace must have a view port to control exactly the moment when the filler is melting.

- The flatness of the pieces to be brazed is really important (<0.02 μm).

- Roughness should be good, but a certain roughness must exist in order to allow a path to the melted filler. A value of 0.8 μm is optimum.

- Thermocouples of the furnace must be properly calibrated, if possible with the melting point of the eutectic alloy.

- In order to braze the copper structure with the VCR connectors (made of stainless steel), a thin layer of Ni must be deposited on the connectors. In this test, the layer has been produced by electro deposition (1 – 5 μm of Ni). Besides, the gap that should remain between connector and copper should be in the range [5-25 μm].

- For our segments, a distance of 4-5 mm between inner surface and the groove to place the filler is desired.

5.1.2.4 Results of RF measurements

In this case, the electric probes will no longer be used to measure RF properties but magnetic (loop) ones are going to be used instead. This is done in order not to perturb the cavity field too much. In the test cavity II the probes are going to be placed in the middle plane of one accelerating cell, so, in order to make the coupling between the TEM mode and the accelerating mode is better to use magnetic probes at a certain distance from axis.

5.1.2.4.1 RF measurements before brazing

As it was done with the test cavity I, the copper segments were placed into the hydraulic press. For this test we did not use any washer and just 0.5 tons were applied. Pressure is applied just to the point in which the resonant frequency begins to stabilise as we do not want to ruin the good flatness obtained in the machining.

Figure 5-29 shows the experimental procedure to measure before brazing.

Figure 5-29. RF measurements before brazing

By measuring the transmission S21 from one probe to the other with the network analyzer, the three resonances appear (Figure 5-30). Special care has been taken in order not to perturb the resonant frequency with the probes (as it has been shown that might happen in 4.1.3).

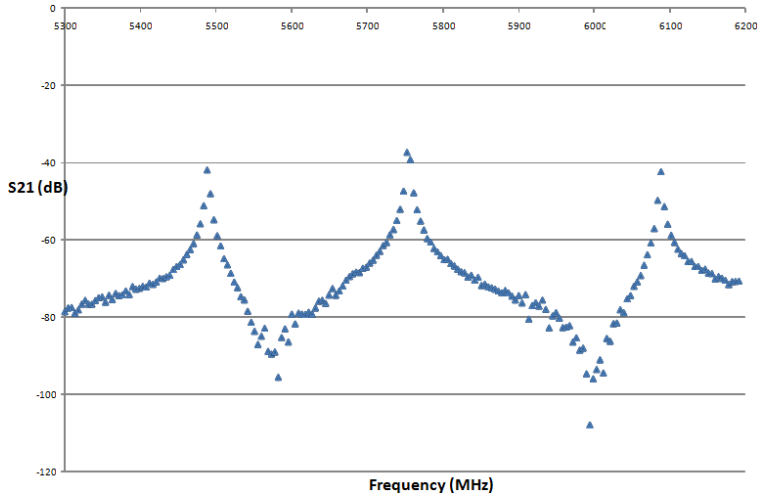

Figure 5-30. Experimental measurements of π, π/2 and 0 modes before brazing

5.1.2.4.2 RF measurements after brazing

The test cavity II is measured again after brazing. The S21 parameter is shown in Figure 5-31.

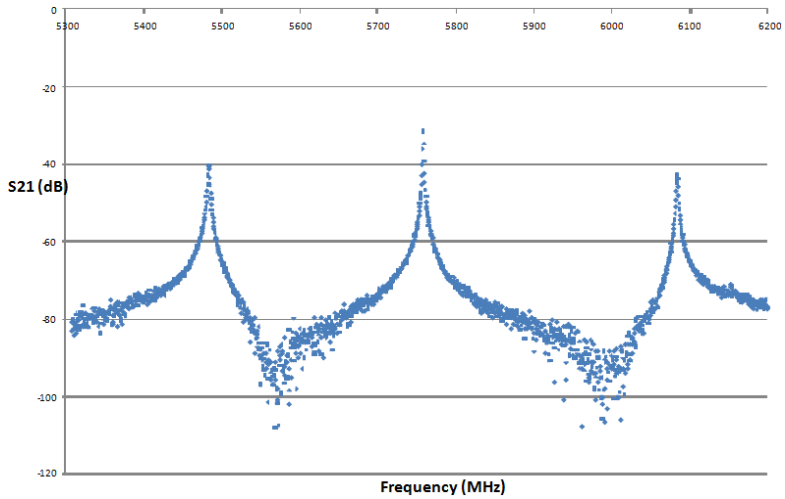

Figure 5-31. Experimental measurements of π, π/2 and 0 modes after brazing

Table 5-3 shows the theoretical resonances and the experimental ones before and after brazing.

Table 5-3. RF properties. Theoretical and experimental before and after brazing

	f_π (MHz)	$f_{\pi/2}$ (MHz)	f_0 (MHz)	Q_π	$Q_{\pi/2}$	Q_0	k (%)
Theoretical	5479	5757	6083	2600	6700	3200	10.6
Before Brazing	5489	5756	6091	1500	1000	2000	10.4
After Brazing	5483	5758	6083	2300	5900	2900	10.4

The π/2 mode frequency is almost the same for theoretical as for experimental measurements. However the other modes are a little displaced which may be explained looking at the coupling factor which looks a bit lower than the theoretical one. So this is likely due to some deviation in the shape of the coupling slots. Low Q factors have been obtained before brazing, which is due to the low pressure applied during measurements. After brazing is clear that the electrical contact is improved, as the Q factor is about 90 % of theoretical one.

After these results it can be concluded that the process followed is good enough to build the real structure.

5.1.3 Aluminium cavity

5.1.3.1 The goals and the parameters of the test cavity

Aluminium models are ordinary used to build the RF cavities before the machining of the final structure. As the aluminium is cheaper and easier to machine than copper, making a prototype it is useful to prevent from discrepancies from computational models and to correct possible errors.

Besides the mentioned reasons, for our RTM linac, the main reason to build the aluminium model has been to verify that the machining of the coupling iris will be possible after brazing and also quite important, if the process used for cleaning after brazing will remove all potential chips that could have remained after this machining. This test will also be used to study the E field on axis.

This structure has been made of segments 4a+3b+3a+2b+ coupler. The simulation model is shown in Figure 5-32(a) and S11 parameter showing resonance of accelerating mode is shown in Figure 5-32(b)

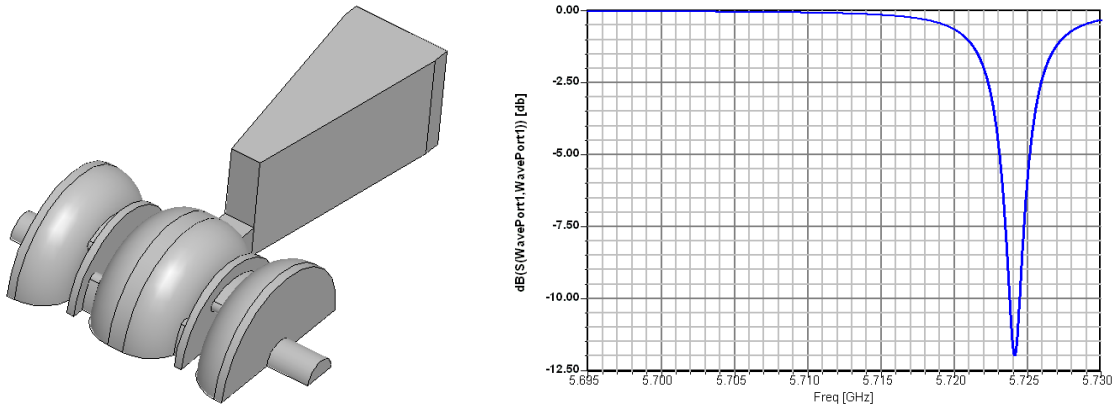

(a) (b)

Figure 5-32. HFSS model (a) and S11 parameter for accelerating mode (b)

The main parameters of the simulation for this structure are summarized in the following table.

Table 5-4. Main parameters of aluminium model

Resonant frequency of accelerating mode	5724 MHz
Q0	4620
QL	1730
Coupling factor β	1.78

It should be noticed that the resonant frequency is higher than in final linac because of the beam hole in the end plates.

5.1.3.2 Mechanical design, machining technology and results

This structure has been made of aluminium AW 2011- T3 by turning and milling machine. A cross section of the cavities is shown in Figure 5-33 (a) and the tapered waveguide in Figure 5-33 (b).

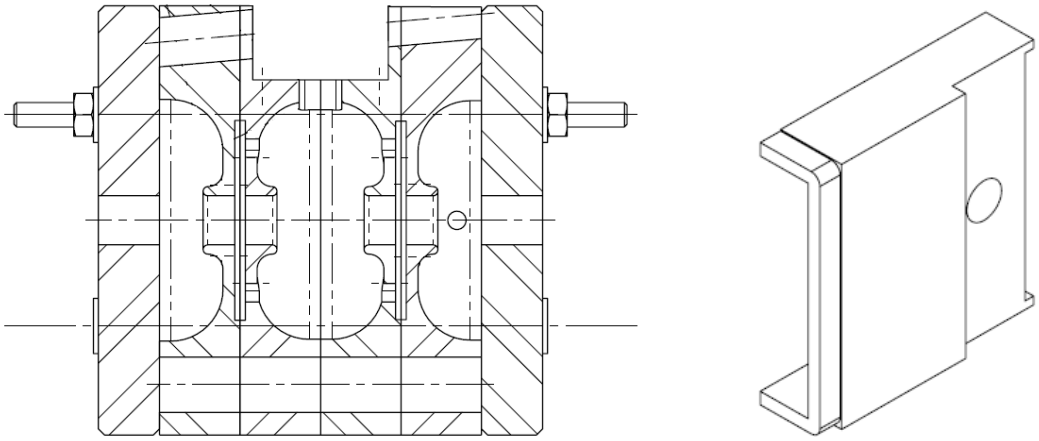

(a) (b)

Figure 5-33. Cross section of aluminium structure (a) and tapered waveguide (b)

The first step was the machining of the segments (Figure 5-34). The mechanical design of these segments is identical to the one for the final linac except for all the grooves required for the brazing because the aluminium structure will not be brazed but clamped instead.

Figure 5-34. Aluminium segments machined

The coupling iris of the structure was machined by the milling machine (Figure 5-35). During iris machining segments were clamped together to simulate the effect of brazing because of in final linac the iris will be machined after brazing.

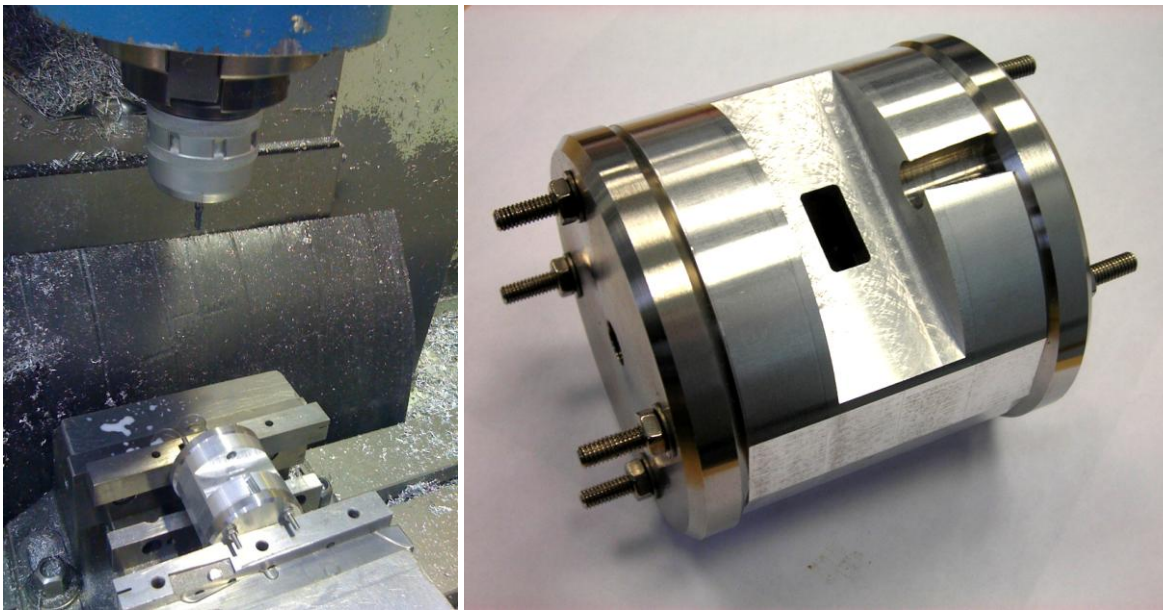

(a) (b)

Figure 5-35. Milling machine performing the iris hole (a) and aluminium structure finished (b)

The most delicate part during the machining of the iris was the removing any potential metal tip that could have remained inside the RF structure (Figure 5-36(a)). Figure 5-36(b) shows a special tool used with the milling machine to remove these tips.

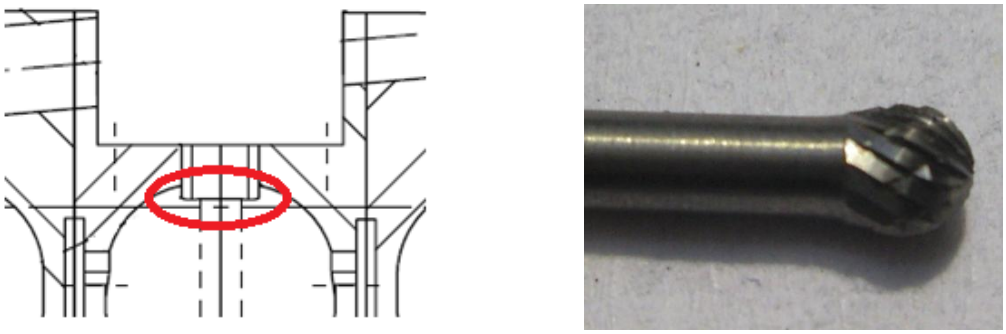

(a) (b)

Figure 5-36. Place for potential metal tips (a) and tool used to remove them (b)

After the machining, without disassembling the segments, the structure was cleaning in the ultrasounds machine with a solution of distilled water (60^{o} C) and 2% Citranox for 20 minutes. During the process, the structure was shaken with care, in order to remove impurities that could have remained inside. Afterwards the pieces where rinsed with distilled water and afterwards introduced in alcohol so the evaporation of liquid was faster. The structure went dry in a furnace preliminary heated at 60^{o} C.

When structure has been disassembled no remains have been found. However, looking at the segment 3 where the iris had been machining it has been observed (Figure 5-37) that not all the inner surface has been touched by the special tool shown before. Therefore, for the iris machining in final linac a different tool with a greater inclination angle should be used.

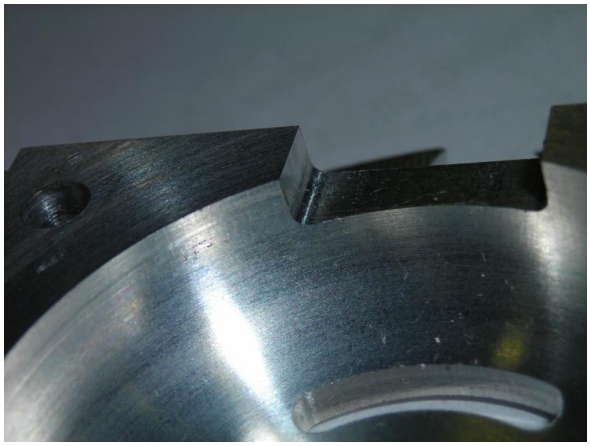

Figure 5-37. Coupling iris in aluminium

5.1.3.3 Results of RF measurements

The aluminium structure (including the tapered waveguide machined in aluminium as well) has been placed into the test bench to measure its RF properties (Figure 5-38).

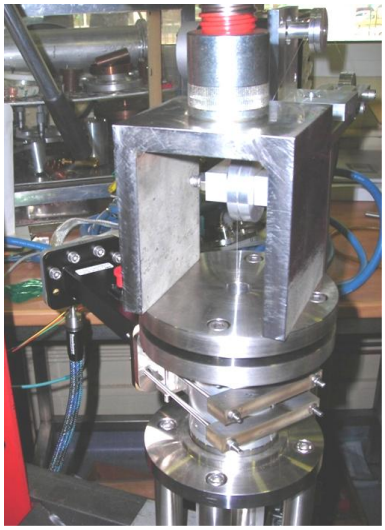

Figure 5-38. Experimental measurement of Al RF structure

The port 1 of VNA was connected through an adapter and a waveguide transition to the coupler in order to feed the structure and the port 2 was connected to a small magnetic loop probe similar to those used in the test cavity II. The probe has been introduced through a 3 mm diameter hole made in the segment 2b. Figure 5-39 shows the reflection S11 (obtained with 6tons -maximum pressure of 30 MPa-).

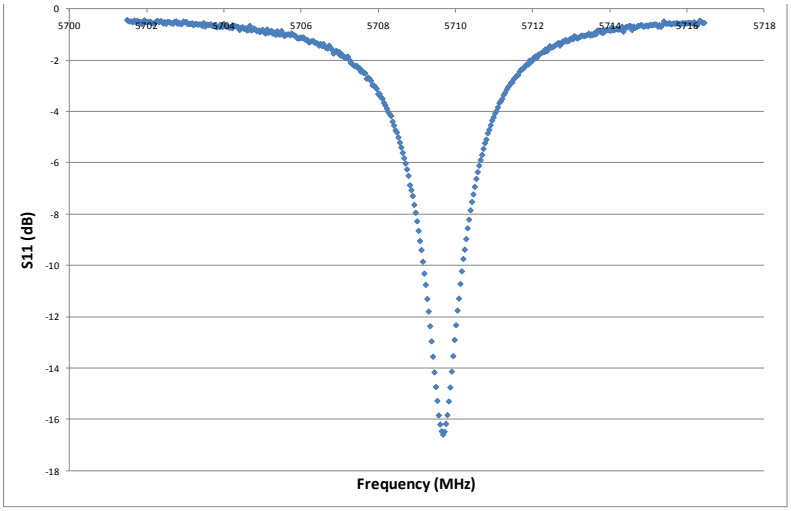

Figure 5-39. S11 parameter showing the accelerating mode

Figure 5-40 shows the transmission S21 where five modes TM_{010}-like are found (the structure has got five cells).

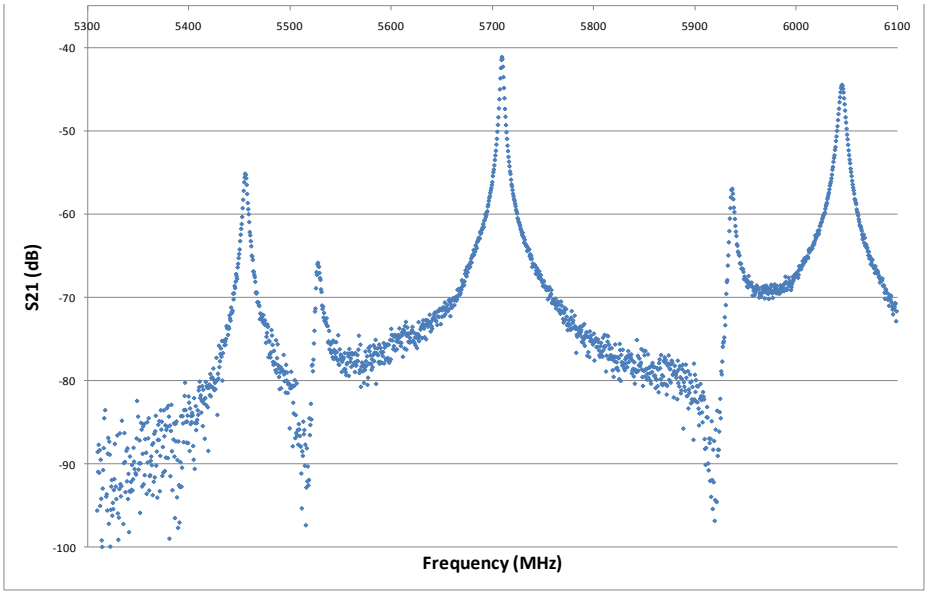

Figure 5-40. Accelerating and adjacent modes in Al structure: S21 parameter

The comparison between theoretical modes and experimental ones is shown in Table 5-5.

Table 5-5. Resonant frequencies comparison. Theoretical and experimental

	f_1 (MHz)	f_2 (MHz)	f_3 (MHz)	f_4 (MHz)	f_5 (MHz)	k (%)
Theoretical	5464	5533	5724.0	5936	6045	10.2
Experimental	5455	5527	5709.7	5936	6044	10.3

And the main properties of the structure are summarized in the following table.

Table 5-6. Main RF parameters for the accelerating mode

	Q_L	Q_0	β	f (MHz)
Experimental	1790	4200	1.35	5709.7
Δvalue/ HFSS value x 100	+3 %	-13%	-24 %	-0.25 %

The most significant change from expected values is the coupling factor β. It has been observed that at first without pressure the structure was under coupled. The more pressure was applied the more coupling was managed as the electrical contact between segments was being improved.

Only with the minimum value of S11 it is not possible to decide if the structure is under coupled or over coupled. One must be careful to observe that origin of Smith Chart is inside the resonant circle to conclude that structure is over coupled (Figure 5-41). This happens for a certain pressure after which β>1.

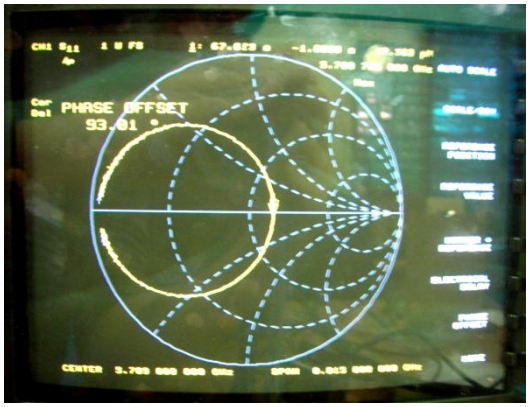

Figure 5-41. Smith chart for linac structure when structure is over coupled

Figure 5-42 shows the behaviour of β with pressure. After 1 tons the structure becomes over coupled and after 6 tons no significant changes in RF properties happen. A maximum pressure[24] of 50 MPa was applied by the hydraulic press .

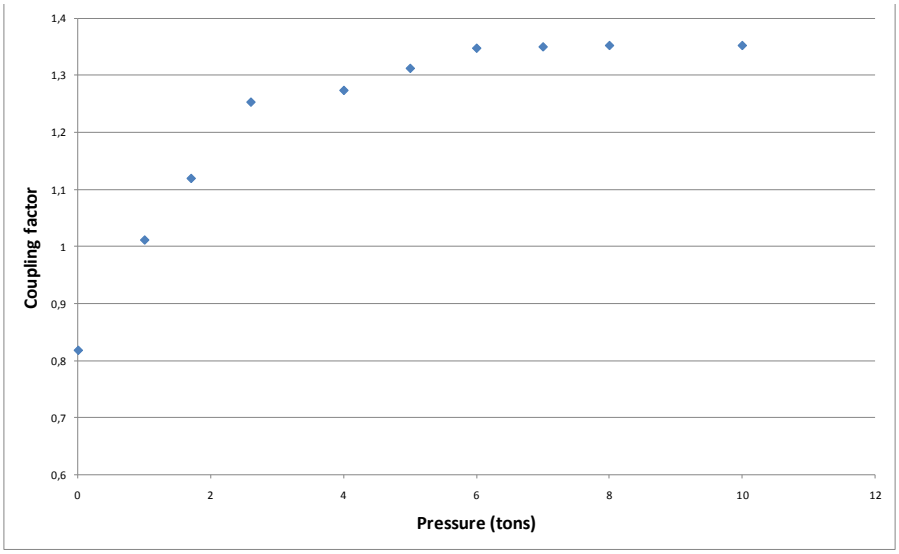

Figure 5-42. Coupling factor vs pressure in aluminium structure

It should be taken into account that in spite of the copper reaches plastic deformation before the aluminium, the elastic deformation in aluminium is greater than the one obtained with copper at the same pressure[25]. Consequently, the electrical contact is produced easily than in copper. Therefore the pressure applied must have been enough to reach the best possible properties but of course the contact will be always worse than with a brazing process.

There may be other reasons for the big discrepancy of β from calculations. Some of the possibilities are the following:

- Conductivity is lower than expected (22 MS/m): Conductivity has been measured giving a value of 20 MS/m. A new set of simulations has been performed concluding that the error in coupling factor[26] may be reduced from 24% to 19%. The error in Q_0 is also reduced from 13% to 9%).
- After the segments are assembled, the machining of the iris has inevitably a certain rounding produced by the tool of the milling machine. For this structure the rounding is 1mm radius so the iris hole is smaller than it is supposed to. This is a deviation from

[24] *Obtained when 10 tons are applied on the middle plane of accelerating cells*
[25] *Young's modulus of aluminium AW 2011- T3 is 70 GPa (at least a 20 % lower than copper used)*
[26] *New value for coupling factor is 1.67*

theoretical model that may reduce coupling factor. When linac will be brazed this may be tuned easily.

- Iris dimensions could be out of tolerances. However, the mechanical measurements have shown that the dimensions obtained for the iris are within tolerances.

Q_L value is quite close to the theoretical value. Q_0 is obtained with Q_L and β. The discrepancy (-13%) obtained in the Q_0 factor value is common for a structure which is not brazed.

The resonant frequency is the most significant disagreement with respect to the theoretical values (14 MHz difference) which can only be explained by small deviations in the geometry machining with respect to the geometry designed. In previous chapter (see 4.1.5.2) according to the tolerances specified for machining, an error up to 6 MHz could be expected for the linac. Calculating this error for the aluminium structure gives up to 4 MHz error. Besides, according to the environmental conditions error (see 4.1.5.5) and as measurements have been taken at 23 ^{o} C a reduction of 1 MHz in resonant frequency has been obtained. None of these effects (5 MHz) may explain the 14 MHz difference so the pieces must have little deviations from tolerances specified to the machining company.

The aluminium pieces have been measured with the 3D numerical control machine by touching different points on the surface and comparing to the 3D model. Some dimensions were out of tolerances but the main deviation was found in some points on the nose cones which were closer to the accelerating cell mid planes (in all segments). So far, it has already been explained a few times the importance of the position of the nose cones and we know that if they come closer to each other the resonant frequency is decreased due to an increase in the capacitive component. So this is likely the cause for the smaller frequency measured. However it should be taken into account that the 3D mechanical measurements are not usually quite accurate when measuring rounding surfaces. Therefore a simple micrometer was used afterwards to check this point showing that indeed cones of segments 2b and 4a were closer than the tolerances permit to their accelerating cells mid planes.

The test bench developed to measure E field on axis (see chapter 4) has been tried on this structure to check its performance. The step motor moves the nylon thread with different types of probes available. As discussed before, in principle, with smaller objects more accuracy could be obtained in representing the electric field in places where it is strongly changed over the short distance, as could be the coupling cells. However, the lower is the change produced in resonant frequency by the perturbation of the object the lower is the Signal/Noise ratio. E. g. when using the 0.56 mm cylinder, the maximum change in frequency is 0.5 MHz and lower

span is used to get more accuracy, however the S21 log mag has a great amount of noise (Figure 5-43) and the sensitivity to measure maximum of S21 for small changes in frequency is poor.

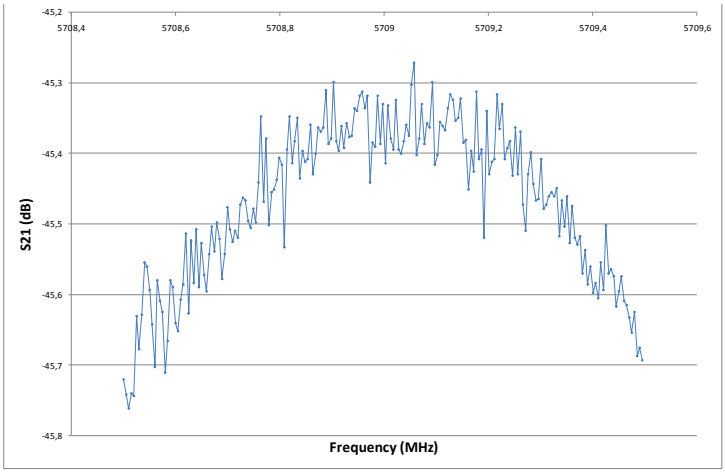

Figure 5-43. S21/noise: 0.56 mm cylinder (small perturbing object)

Therefore, the E field obtained with this kind of signal -using (4.4)- will not be acceptable (Figure 5-44).

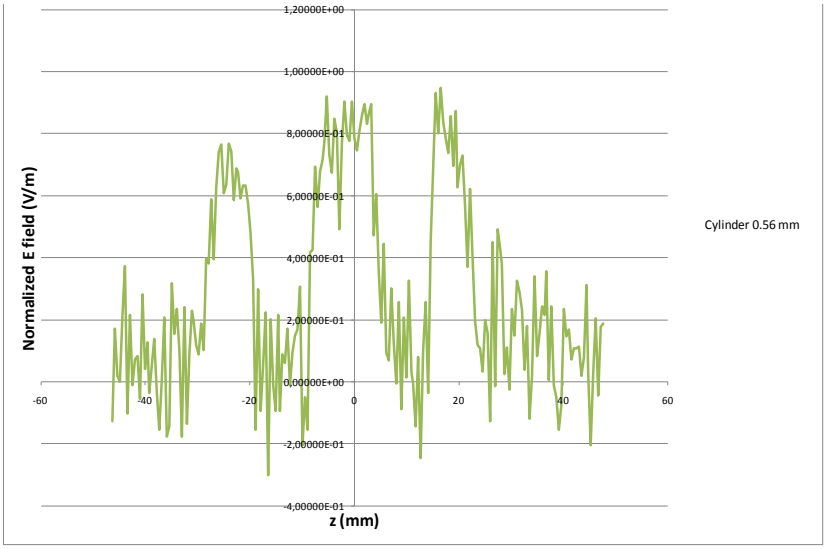

Figure 5-44. Effect of low S/N ratio: E field measured with 0.56mm cylinder

With more perturbing objects the signals must be less noisy but the spatial resolution is worse. Figure 5-45 shows the E field on-axis comparison between theoretical field and the ones obtained with a 4 mm metallic ball and a 2.3 mm cylinder. For the bigger ball, the highest Signal/noise ratio is found and therefore the E field appears to be smoother (the maximum

change in resonant frequency is 36 and 3.5 MHz for metallic ball and cylinder probes respectively).

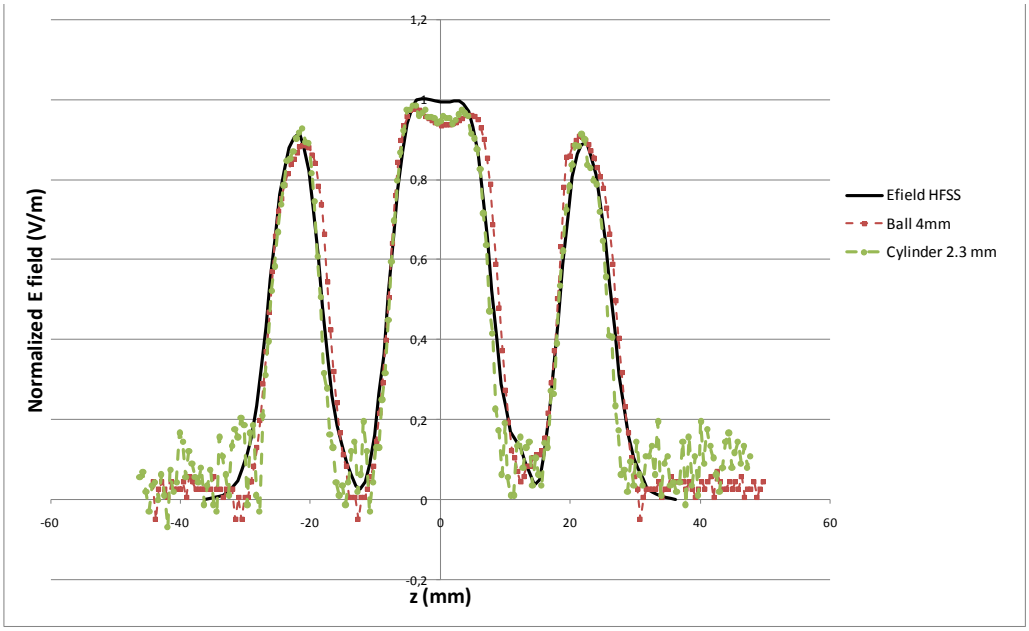

Figure 5-45. E field on-axis. Aluminium structure

In spite of these results are good to picture the E field, for final linac is desirable obtain a more clear inspection of what the E field will be on the coupling cells in order to detect any problem. For that, smaller probes (less perturbing) must be used and therefore, a hardware filtering and smothering must be applied in order to measure E field on final linac.

The following picture shows how the S21 from Figure 5-43 is much less noisy after filtering and smothering. However, the more filter is applied the more time it takes for the acquisition of E field values. This will be taken into account for E field measurements in the final linac.

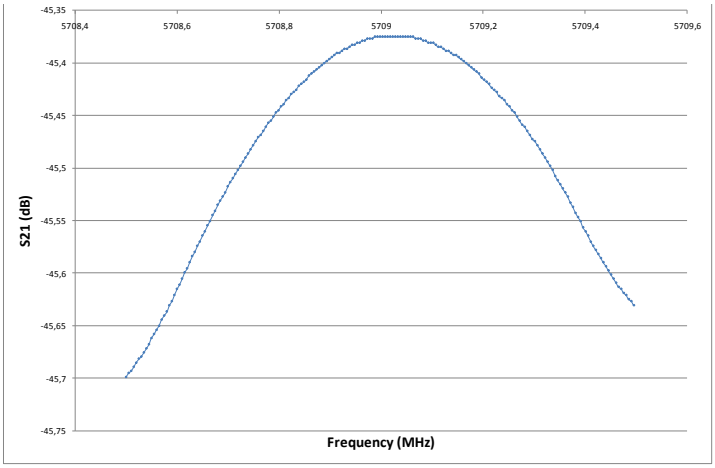

Figure 5-46. S21/noise after hardware filtering and smothering

5.2 Linac

5.2.1 Mechanical design and machining

There are many important things that have been learned from the previous tests and therefore many elements have been incorporated (and many other removed) to the RTM linac design. In this section the final version of the mechanical design is shown (Figure 5-47).

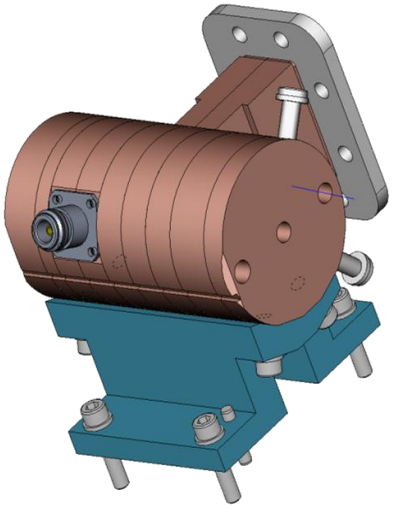

(a)

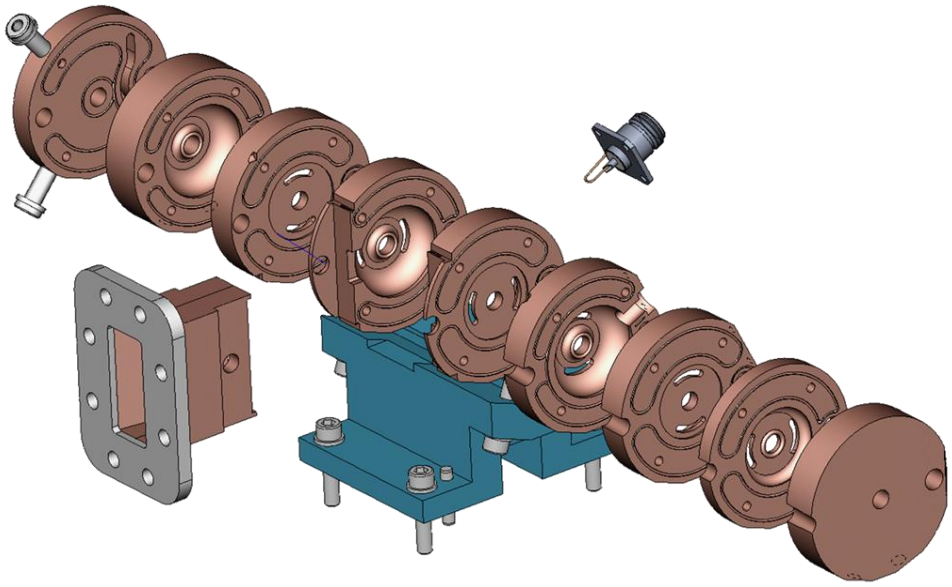

(b)

Figure 5-47. 3D Solid Works model for linac and support (a) and expanded version (b)

The main characteristics of the linac mechanical design are:

- It will be made of 9 OFE copper segments.
- Tapered waveguide will be made of two pieces of OFE copper.
- The RF flange will be made of 316LN stainless steel.
- Dimensions are required to be machined within tolerances. The best tolerance required for the sensitive parts is 20 µm.
- Roughness Ra, of inner surfaces has been asked to the machining company to be 0.3 µm. Ra for contact surfaces between segments has been asked to be 0.8 µm.
- An RF loop probe will be placed in the middle plane of segments 2a+2b.
- There are some holes and cuts to be made in the linac body as Figure 5-48(a) shows. They are made for different orbits of electrons (e.g. 4 MeV orbit and extraction orbit).
- Two stainless steel VCR Swagelok connector (inlet and outlet of water -see Figure 5-48(b)-).
- Alignment of linac with RTM tank will be performed through a support (Figure 5-47) and three reference planes will be machined along the linac.
- Alignment of segments for brazing will be carried out by means of a 3 mm groove (made along all the segments on the outer diameter in which a ceramic will be placed) and molybdenum wires with alumina cylinders (as shown in test cavity II).
- All brazing grooves are 1.1 mm (in order to place a 1mm diameter filler) except for certain places where not having enough space a 0.8 mm grooves have been required (0.5 mm diameter filler will be used in those places). Grooves will be machined on the VCR connectors and afterwards a thin layer of Ni will be applied by electro deposition (1 – 5 µm of Ni).

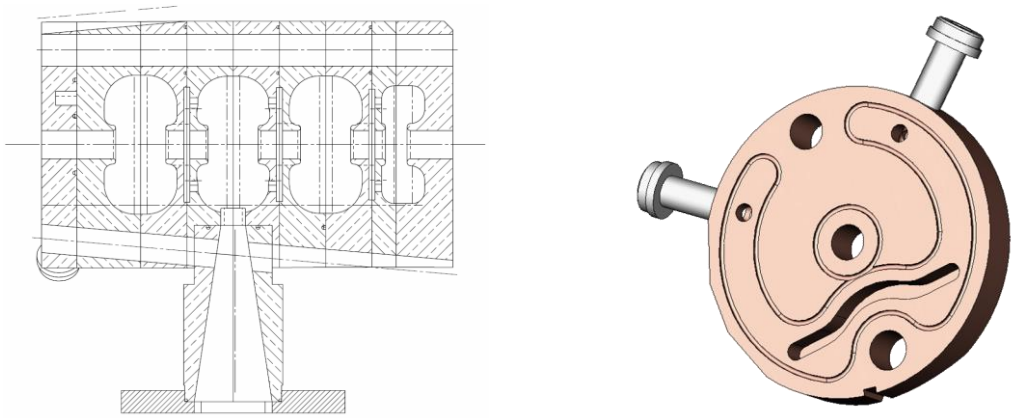

(a) (b)

Figure 5-48. Cross section of linc showing holes for different orbits (a) and segment 4c showing the inlet and outlet for cooling (b)

The high precision copper pieces have been made by turning, drilling and milling operations using CNC machine tools in the company Utillajes Huerta S.L. As performed with tests cavities, before the final machining a rough machining has been prepared. Then, the pieces were introduced in the furnace for 1 hour at 220 ^{o}C to release the internal stresses that the copper might have with the following fine machining to obtain final geometry (Figure 5-49).

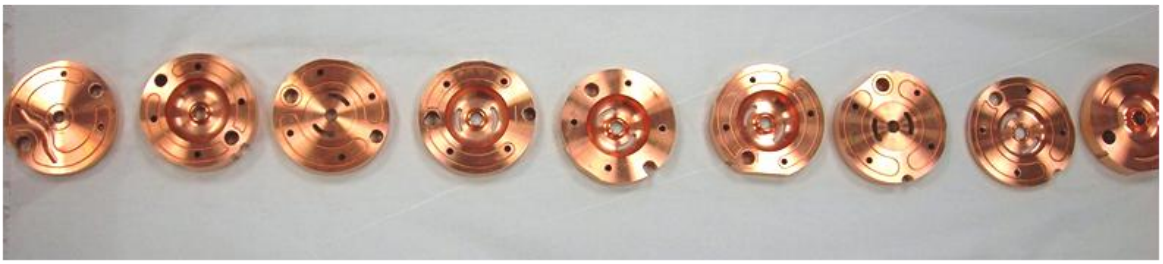

Figure 5-49. Linac copper segments machined

It should be noticed that the brazing process needed for the RTM linac is quite complicated and compels to perform the machining in different steps:

- The machining of the iris will be made after the brazing of the copper segments. The two copper pieces for the tapered waveguide will be fine machining after brazing them.
- After the machining of the iris, the linac will be once more brazed to the tapered waveguide and RF flange. This way, a perfect surface is obtained to braze the waveguide to the copper segments.

5.2.2 Mechanical and RF measurements before brazing

The brazing process and the measurements after brazing will not be included in this thesis dissertation and they will be performed in the near future. As the iris will be machined after brazing, the RF measurements, in principle, were not possible to be performed without thinking of something. The idea has been to do the RF measurements with the help of the coupler made of aluminium. Therefore, there are two issues that should be taken into account:

- The copper segment 3a+3b will not be tested as part of the linac until it is brazed and machined.
- The RF measurements will not be exactly equal to simulations performed as the conductivity of aluminium is a 40% of the copper. This will produce more RF losses causing a reduction of coupling factor.

In order to make an adequate comparison of experimental and theoretical values, linac simulation with the two aluminium segments has been performed. The values are summarized in the following table.

Table 5-7. Theoretical parameters with Al segments 3a+3b

Q_0	7710
Q_L	2856
Coupling factor β	1.70

Figure 5-50 shows the experimental test bench to measure the RF properties of linac (copper segments plus the aluminium coupler).

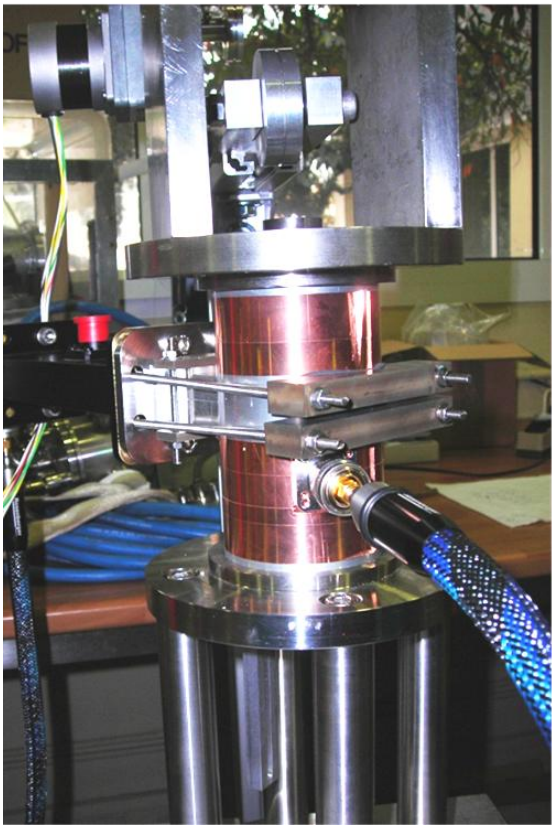

Figure 5-50. Experimental measurement of linac structure

The port 1 of VNA was connected through and adapter and a waveguide transition to the coupler in order to feed the structure and the port 2 was connected to a magnetic loop probe with S21= -20 dB (needed to do frequency pulling when magnetron will fed the linac). The following figure shows this magnetic loop and how it fits[27] into the second accelerating cell.

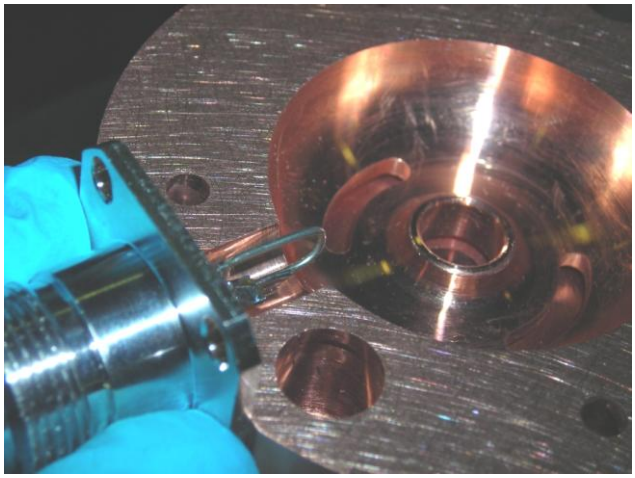

Figure 5-51. Magnetic loop placed in 2nd accelerating cell

Figure 5-39 shows the reflection S11. All measurements (unless it is said differently) are obtained with 5 tons -maximum pressure of 25 MPa- and at 23 º C. It should be taken into account that nylon thread to measure on-axis E field reduces the resonant frequency for 1 MHz (due to dielectric losses) so accurate measures should be performed without it.

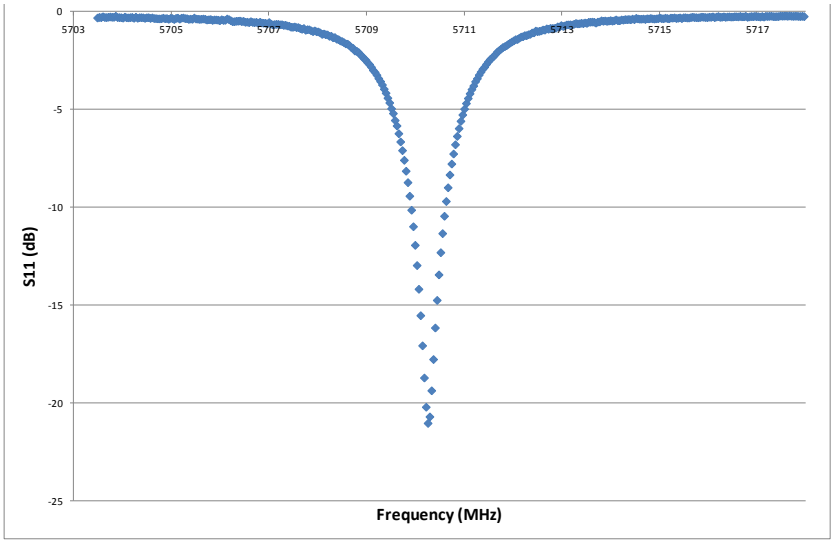

Figure 5-52. S11 parameter showing the accelerating mode

[27] *Probe as shown in picture gave a high coupling. Therefore loop area was reduced and slightly rotated to reduce the coupling in order to obtain S21=-20 dB*

In Figure 5-54 the seven TM_{010}-like modes are shown.

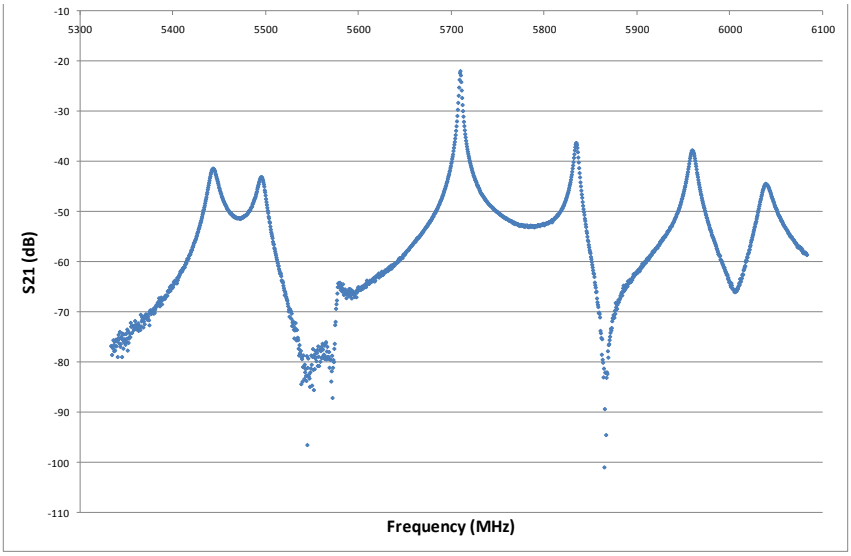

Figure 5-53. Accelerating and adjacent modes in linac: S21 parameter

The comparison between theoretical modes and experimental ones is shown in Table 5-8.

Table 5-8. Resonant frequencies comparison. Theoretical and experimental

	Theoretical	Experimental (5 tons)
f_1 (MHz)	5461.5	5443.9
f_2 (MHz)	5507.3	5496.0
f_3 (MHz)	5594.2	5579.9
f_4 (MHz)	5712.7	5710.6
f_5 (MHz)	5849.5	5835.1
f_6(MHz)	5975,2	5960.4
f_7 (MHz)	6055.3	6040.2
k(%)	10.39	10.45

And the main properties of the structure are summarized in the following table.

Table 5-9. Main RF parameters for the accelerating mode

	Q_L	Q_0	β	f (MHz)
Experimental	2710	6020	1.22	5710.6
Δvalue/ HFSS value x 100	-5.1 %	-22%	-28 %	-0.04 %

Previous results show that measured resonant frequency of the linac is quite close to the one obtained in simulations and, if we consider the environmental conditions, the real frequency will be about 1 MHz higher during operation (5711.6 MHz). However, as we have learned from previous tests, we should not forget that the brazing may change this value when some internal stresses are released during the heating of the pieces.

If we consider all modes obtained in simulation and we compare them to those obtained experimentally we find differences up to 17 MHz (π mode). Nevertheless, a similar result was obtained in test cavity II where, before brazing, the adjacent modes to the π/2 accelerating mode approached to theoretical one as the structure was brazed. This difference is likely caused by elastic deformations produced by the pressure applied. Looking at the data summarize in Table 5-10 for linac measurements without pressure it can be seen that differences to theoretical modes are reduced up to a maximum of 9 MHz. In addition, if we consider the accelerating mode (5712.1 MHz) and we add 1 MHz because of environmental conditions, a difference of only 0.4 MHz is obtained with respect to theoretical value.

Table 5-10. Resonant frequencies comparison. Theoretical and experimental when no pressure is applied

	Experimental (0 tons)	**Diff. to theoretical (MHz)**
f_1 (MHz)	5452.3	-9.2
f_2 (MHz)	5508.8	+1.5
f_3 (MHz)	5585.3	-8.9
f_4 (MHz)	5712.1	-0.6
f_5 (MHz)	5842.7	-6.8
f_6(MHz)	5977.2	+2.0
f_7 (MHz)	6049.4	-5.9
k(%)	10.45	+0.06

The RF measurements show also a quite low coupling factor β (nevertheless over coupled) but, unlike it was said for the aluminium test, it cannot be concluded that pressure has no influence on the coupling. No data were taken above 6 tons applied (maximum pressure of 30 MPa) as copper segments might have been deformed and spoiled (no washers have been used either so the pressure was applied uniformly). In Figure 5-54 the dependence of β with applied pressure shows that more pressure would have been needed to reach the right value of β. Therefore, coupling will be expected to be higher after brazing but may be tuned if necessary.

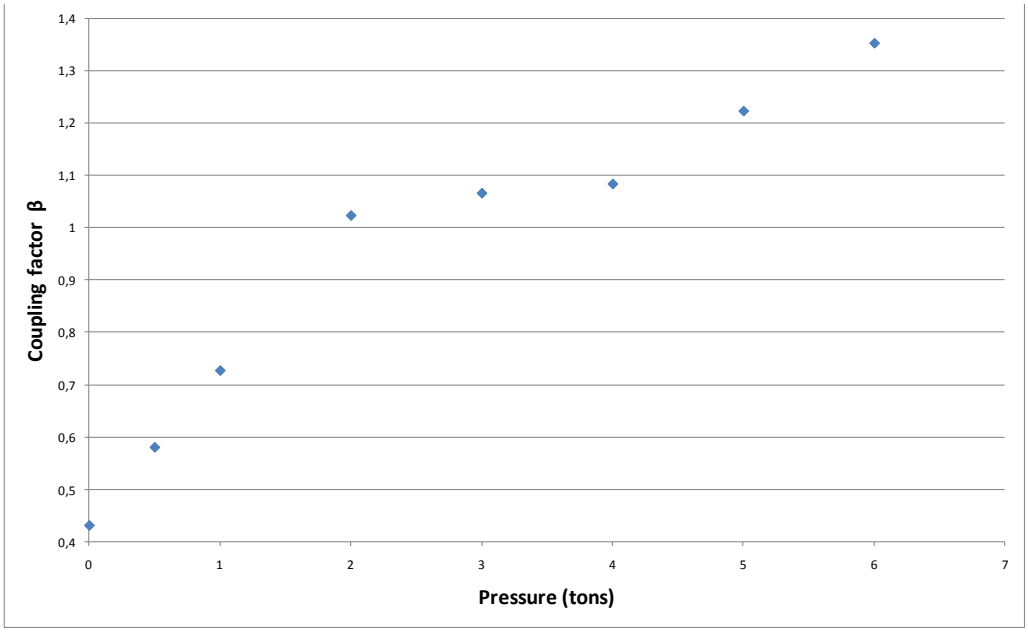

Figure 5-54. Coupling factor vs. pressure

As the copper segments 3a+3b have not been measured (because of the aluminium ones have been used instead) a study of these segments and the effect of the coupling hole in its resonant frequency has to be performed.

By placing the segments 2b+3a+3b+4a (plus two copper end plates) into the hydraulic press and using the electric probe on-axis (as explained in chapter 4) the resonant frequency for aluminium (with iris hole) and copper segments (without iris hole) have been measured. According to a simulation performed with model shown in Figure 5-55 the probe must be placed with at least d>3.5 mm to have an error lower than 1 MHz (and maximum possible d=4.4 mm as the coupling cell must be short-circuited). Therefore special care was taken to place the probe between 3.5mm and 4mm for the experimental measurement.

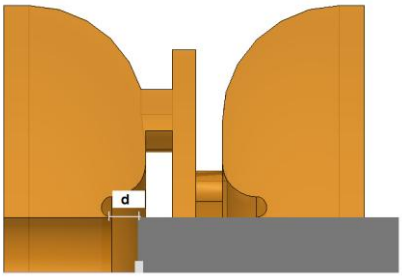

Figure 5-55. On-axis probe model

In the following table the comparison between theoretical an experimental resonant frequencies for these segments is shown. Results are quite close, so, in principle, no problem is expected from the copper segment after the iris will be machined.

Table 5-11. Segment 3a+3b

	With iris hole	**Without iris hole**
f Experimental (MHz)	5712.5	5736.5
f Theoretical (MHz)	5712.3	5737.4

To observe E field on-axis in the accelerating cells the probes simulated in chapter 4 and tested during the aluminium test are good enough (see Figure 5-45). However, in order to get a better accuracy at lower E field (e.g. in coupling cells) smaller probes should be used. On the other hand it has already shown that when low perturbing objects are used the effect of noise spoils the measurements so the ratio of signal/noise had to be improved, but the more sensitivity obtained the more time was required to measure the whole profile of field. For that reason there are some time dependent effects that may lead to inaccurate results (temperature drift, lost of pressure, etc.). In order to improve these measurements, there are a number of parameters that had to be carefully selected every time a different probe was used:

- Frequency span (the lower the span the more number of points are obtained each time the S21 maximum is acquired).

- Hardware filtering and number of points: the more filtering and number of points the better accuracy to get S21 maximum but more time is needed to do the acquisition.

- Smoothing procedure must be applied.

- Number of motor steps after every measurement: The more number of steps after measurement the less time it takes to do the acquisition. However, as the software (at the moment) places the central resonant frequency in previous S21 maximum obtained, a great change in frequency can be found and a higher span has to be used thus reducing the sensitivity.

The small probe with 0.56 mm cylinder has been used to measure the E field after all improvements were applied. In spite of the profile (Figure 5-56) is much better than the one obtained with this probe before (Figure 5-44) the field still has got too much noise. The picture illustrates the effect of frequency drift because of temperature changes (no correction from initial frequency and last frequency have been applied).

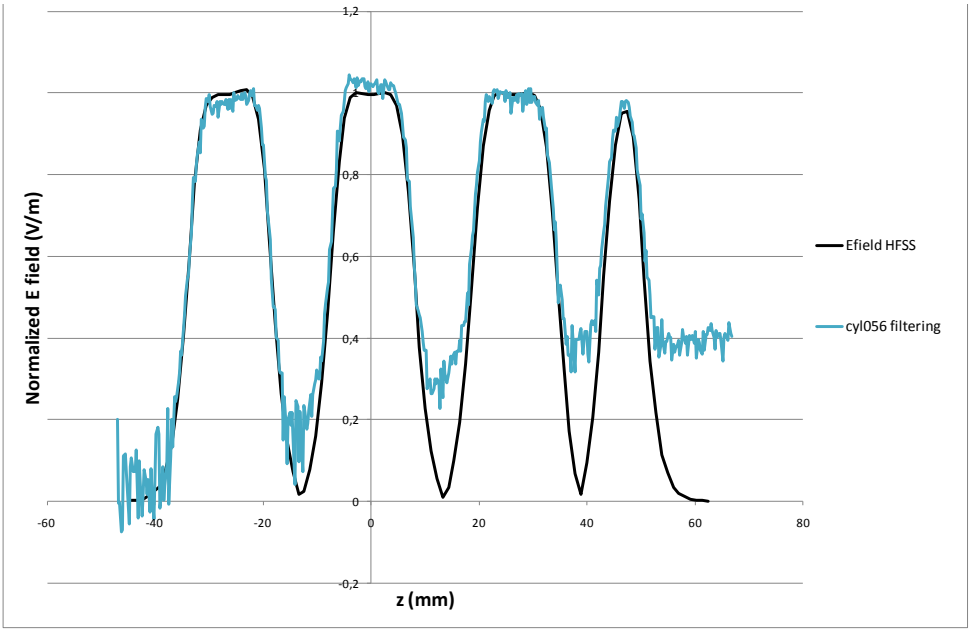

Figure 5-56. On-axis E field obtained with 0.56mm cylinder

The less perturbing is the probe and the more time used for measurements the more important is the frequency drift effect obtained. For this probe, the maximum change in frequency is 0.3 MHz and frequency drift is 0.05 MHz for measurements that took 28 minutes. The conclusion has been that a little more perturbing probe is needed although in order to have sensitivity in coupling cells the object should be smaller than the distance between coupling cell walls (1.75 mm). A small plate of 0.6 mm length (Figure 5-57) has been machined from a cylinder (outer diameter 3.97 mm, inner diameter 0.8mm): with this probe more sensitivity should be obtained along axis but more perturbation is produced as the fields off axis are also included in the measurements.

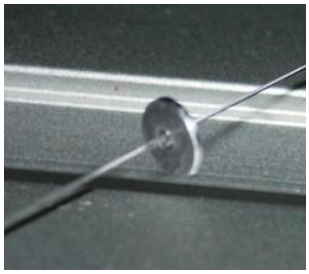

Figure 5-57. Small disc machined to measure on-axis E field

Figure 5-58 shows the E field on-axis obtained with the small disc (and a careful selection[28] of parameters). The room temperature was tried to be kept stable (frequency drift: 0.015 MHz after 29 minutes). Also, it has been checked out that the hydraulic press maintains an almost constant pressure for at least one hour where the RF properties remain unchanged. The maximum perturbation produced by the probe was 2.1 MHz (0.036% operation frequency), which is more than 10 times lower than obtained with the metallic ball, and even though improving dramatically the sensitivity.

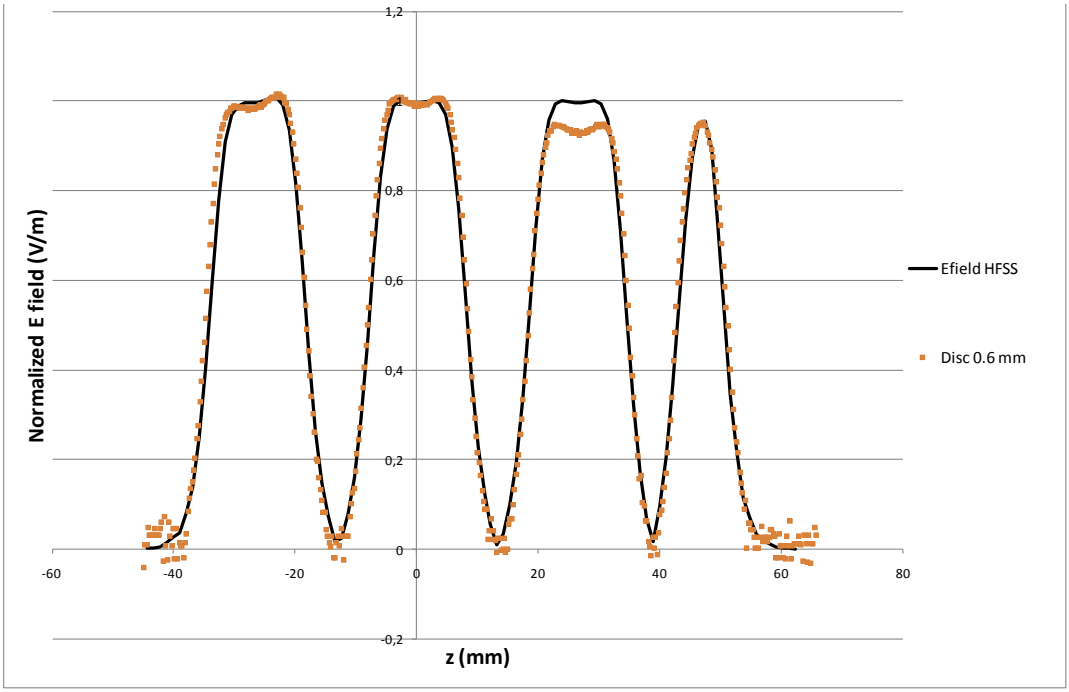

Figure 5-58. On-axis E field obtained with 0.6mm disc

[28] *Acquisition time: 29 min. Measurement every 2.38mm (2 motor steps). Span: 0.5 MHz Filter: IF 100 KHz. Number of points: 101. Smooth applied*

Figure 5-58 shows an E field quite close to theoretical one where no field in the coupling cells is found. However, accelerating cell 2 (segments 2a+2b) shows a lower E field. This is likely caused by a difference in coupling slot shape in segment 2b (coupling slot somewhat bigger), or segment 3a (coupling slot smaller) or segment 2a (coupling slot smaller).

As it follows from beam dynamics simulation observed deviation of the field distribution from theoretical one will not influence essentially on RTM beam dynamics. However after getting final field distribution for the brazed copper structure any observed deviation should be taken into account in the refining calculations of the beam dynamics. The main expected effect is some change of the 1^{st} orbit energy and change of orbits position within few 0.1 mm.

The copper pieces have been measured with the 3D numerical control machine by touching different points on the surface and comparing with the 3D model. The main deviations from tolerances specified are found in the coupling slots dimensions, showing that they are out of tolerances up to 100μm. A combination of these errors has caused the reduction of E field in cell 2a+2b. Nevertheless, as in RF measurements the aluminium segments have been used, a slightly different ratio of maximum E field between accelerating cells will be found.

Conclusions

A summary of the most relevant results obtained during the development of this thesis and the conclusions extracted from them are presented in this section.

As the work performed and the conclusions are based on a set of objectives, which were described in the introduction chapter, they will be summarized here:

- An RF design of a 2 MeV C-Band linac for a RTM had to be carried out and afterwards
- a mechanical design had to be performed so the machining of the structure could be feasible.
- Study of parasitic modes had to be done, especially the TM_{11} - like modes, which could cause transverse BBU.
- Study of multipole fields in the structure had to be carried out to verify their effect on the beam dynamics.
- RF measurements to check out its performance had to be carried out, and for that a measurement test bench had to be designed and built.
- As the final structure is going to be brazed, a study of this process also had to be done.

A significant discussion (see 1.5, 3.1 and 3.2) was carried out about the main parameters chosen and stated below

- Operation frequency (wavelength): 5712 MHz (0.0525 m).
- Energy gain: 2 MeV.
- Injection energy: 25 keV.
- Biperiodic standing wave copper structure with on-axis coupling.

As it was explained, most of the mentioned specifications were chosen because of the tight requirements that the linac had to fulfil mainly because it will be included in the compact RTM for IORT application:

(i) It had to accelerate simultaneously in the same linac the non relativistic beam from the electron gun and several different energy relativistic beams from the orbits.

(ii) It must accelerate beams moving in opposite directions.

(iii) It must have good capture efficiency and beam quality.

(iv) It must have minimal dimensions and weight.

(v) It had to be fed by less than 1 MW of pulsed power.

(vi) It must have sufficiently large beam aperture to decrease beam losses.

The linac optimization was conducted initially with 2D code SUPERFISH in an iterative process including beam dynamics simulation with PARMELA and RTMTRACE. The number of cells, the length of the first cell, accelerating field amplitude in $\beta < 1$ and $\beta = 1$ cells were defined at this step and a first estimation of power was given (521 kW) taking into account effective shunt impedance decrease due to coupling slots. 2D fields of accelerating structure synthesized in this way were used for RTM beam dynamics simulation.

Afterwards, the 3D optimization was carried out in order to calculate all the dimensions that a 2D analysis could not properly accomplish, as may be the coupling slots position and dimensions to provide necessary field distribution with maximum structure efficiency and field stability, tuning of the cells resonance frequency after cutting coupling slots and calculation of coupler geometry providing RF power input with designed value coupling factor. A complete methodology to calculate linac with 3D codes was developed. Since at the beginning it is neither easy nor accurate to optimize the whole cells placed together, the methodology followed for calculating separate parts results in a great help for biperiodic accelerating structures calculations. After this successful step it is concluded that the linac designed, will fulfil specifications in terms of resonant frequency, energy gain, beam losses and power consumption. However, before proceeding to the technical design there were a few more studies to be done in order to check the performance of the linac during operation inside the RTM.

One of these studies was a thorough sensitivity analysis carried out to find out how the accelerating and coupling cell are detuned when their basic dimensions change. The primary objective was to establish the tolerances needed to be asked in technical drawings for the machining, but this analysis has proven to be a really helpful tool in other occasions (thermal deformations, analysis of measurements) as it allows making simple estimations of frequency detuning without doing any computer simulation. The information obtained may be easily

adapted to other biperiodic accelerating structures facilitating their design. The main conclusion extracted from this analysis was that noses geometry (*Rn,R2),* the distance between them and the diameter of coupling and accelerating cells had much greater impact than other dimensions on the resonant frequency.

Due to the axial asymmetry of the linac, caused by the coupler and coupling slots, quadrupole fields have been found and their effect on off-axis particles has been studied. The main results show that the quadrupole fields are much stronger in the coupling cells (coupling slots rotated 90 ^{o}) than in accelerating cells (coupling slots not rotated). The most essential effect of coupling slots on transverse beam dynamics takes place during the first acceleration due to low momentum of accelerated particles. The estimation performed for the focal length indicates that for the RTM the quadrupole effect of coupling slots will not be negligible and must be taken into account for the beam dynamic study.

It has been shown that other modes different from the accelerating one are unwanted but may be excited by the beam itself. A study of a few higher order modes (HOM) has been performed where special attention has been paid to the TM_{110}-like modes. Because of their large transverse shunt impedance they may interact with the beam and at a given threshold current the beam blow-up may happen. The lowest BBU threshold current (1mA) has been found for the TM_{110}-like mode at 9982 MHz. Nevertheless, the estimation performed takes into account a steady state but in the RTM under construction, with a 3 μs pulse and with parasitic mode frequency not being harmonic to the operating one, the real threshold current will be much higher. Nevertheless, these calculations were performed in order to characterize the accelerating structure in all details and in the future, if higher currents are needed, results presented here of the shunt impedance for these modes will be quite useful for beam blow-up simulation with more sophisticated models.

The RF power dissipated in the copper surfaces of the linac (required to produce the high electric field of 43-45 MV/m to accelerate the electrons) and the power that might be deposited by the beam itself, will heat the structure. Therefore, a study of the thermo mechanical behaviour of the linac was carried out to check out the detuning that may be expected during linac operating at high power. It was shown that for the maximum duty factor (0.075%) and 5 mA pulsed current the maximum beam power will be 45 W so, even fully deposited in the walls, the effect is lower than the 400 W average power caused by RF losses. With the cooling pipes designed and specification water flow for the RTM (4 m/s), a maximum water temperature increase of 0.5 K was obtained. The analysis performed with HFSS and

ANSYS showed that minor deformations (0.5 – 1 μm) could be expected up to the moment the steady state is reached. This analysis also showed that frequency changes in coupling and accelerating cells caused by these deformations would be small (<1 MHz) but they must be taken into account in the design of the automatic frequency control system based on the magnetron frequency pulling technique.

In order to characterize the RF linac electrodynamics characteristics a study of the different measurement methods was performed. Designed and built RF (electric on-axis and magnetic loops) probes were described and their effects on the measurements were methodically simulated with HFSS obtaining the optimum positions at which they must be placed so they have as minimal influence as possible on the results. It was found that the electric probes on-axis had a greater impact than the magnetic loop probes on the resonant frequency of a single accelerating cell, being at least 3 mm of free space between noses and the tip of the probe to get a measurement error lower than 1.5 MHz. In addition, a complete analysis of the requirements for performing electric field measurements was carried out. The perturbation technique was described and a collection of metallic perturbing beads was analyzed in a set of simulations to find out the optimum sizes to measure accurately the E field in a single accelerating cell. Cylindrical beads showed a closer value to theoretical shunt impedance calculations than those obtained with metallic balls and the maximum perturbation in the resonant frequency introduced by the beads was found in a range from 0.02% to 1%. Perturbation technique has valid results for all of them as the higher fields were quite accurately represented, though in practice the bigger object will be less sensitive to field changes. However for lower fields, with the less perturbing beads, HFSS did not manage to represent fields correctly. A potential simulation work for the future could be to analyse the upper limit at which the perturbation technique stops being valid and also to use an improved mesh and better computer resources to analyze small perturbing probes.

The causes for potential resonant frequency deviations in final linac were studied in detail (accuracy of simulations, machining error, instrumentation errors, brazing and environmental conditions). From this study it could be concluded that a deviation of few MHz could be obtained being the machining tolerances specified the main cause of potential deviations. It should be noticed that if no better tolerances in the machining were asked (20μm), that was mainly due to the expertise available in Spain to make such complex machining and of course because the price increases dramatically with the required tolerances. In the study, the unpredictable effect in frequency deviations after brazing as a result of internal stresses release in copper was described as well. To reduce this effect the copper pieces were roughly

machined and afterwards heated at 220^{o}C for at least an hour to reduce the stresses to a minimum. The deformations after heating could be reduced in two ways: i) making a rough machining closer to the final one and ii) heating copper at higher temperatures. However at higher temperatures copper becomes softer and machining expertise becomes critical.

In order to perform the RF measurements on the test cavities and linac, a test bench was designed and built. On the one hand the bench was intended to allow the electric contact between pieces before brazing and a set of stainless steel supports were made to guarantee this contact and to allow for measuring with electric and magnetic probes. On the other hand the test bench had to permit field measurements on axis and for that, a mechanical device attached to a hydraulic press was used to make a nylon thread with a metallic bead to pass through the cavities. The bead was moved by a step motor controlled by a LabVIEW program which at the same time controlled the measurements from the VNA. The system was found to work quite well after some modifications oriented to find a compromise solution between reducing the measurement time and at the same time decreasing noise in S21 parameter for low perturbing probes.

Before accomplishing the linac construction a series of tests were performed to check out i) the quality of copper machining and especially difficult machining steps, ii) the quality of brazing –no deformations, no leakage from cooling tubes and no alloy penetration into the RF surfaces- and iii) RF probes and experimental test bench developed.

The test cavity I, consisting of a single accelerating cell made of two copper OFE segments, was designed, machined and measured before and after brazing. The machining technology proved to be valid for obtaining good final surfaces with low RF losses. This was checked with the test bench and the two electric probes when measuring Q factor which was quite close to theoretical one. In spite of a small frequency detuning being found because of some little deviation from tolerances, the main problem found was the brazing of the segments which ruined the structure.

The test cavity II, consisting of two half accelerating cells and one coupling cell with coupling slots was designed, built and measured before and after brazing. The objective was to study the RF properties of accelerating and coupling cells and its change after brazing. The brazing process was successfully carried out at CERN following some important indications: i) Piece flatness was crucial (<0.02 μm). ii) A value of roughness Ra= 0.8 μm on the contact surfaces was optimal. iii) If a piece fitted into each other, the distance between surfaces must allocate some space for the alloy spreading but not too much. A range between 5-25 μm was asked to

the machining company. iv) A 4mm distance from inner RF surface and brazing grooves was desired. v) Thermocouples for measuring piece temperature must be properly calibrated and vi) Structure temperature remained above melting point for less than two minutes. The thermal cycle was immediately interrupted once the alloy began to spread and therefore the vacuum furnace must have a view port. RF measurements showed a good agreement with theoretical value of $\pi/2$ mode frequency and Q factor after brazing was 90% of theoretical. It was concluded that the process followed (RF and mechanical design, machining, brazing and RF measurements) was good for proceeding to accomplish the final structure.

Nevertheless, before constructing the real linac, an aluminium model was made to check out the coupling iris machining that have to be made after all segments were machined and clamped (which in real structure will be performed after brazing). The iris was accurately made and afterwards an ultrasonic cleaning for 20 minutes completely removed the aluminium remains that could have been accumulated on the inner surfaces during machining. Despite no metal tips being produced in the iris, the special machining tool did not touch all the surfaces and therefore for the final linac this should be taken care of. The RF measurements showed a detuning of -14 MHz (compared to values obtained with HFSS) which was explained by out of tolerance geometry especially on the nose cones distance to accelerating cells mid plane. The coupling factor had the most manifest disagreement with respect to theoretical values (-24%) which could be explained by the radius of the iris corners and because of lower aluminium electrical conductivity than expected. The first version of test bench to acquire E field on-axis was tried on this structure and was found to work well (Figure 5-45) for the highest perturbing beads (0.1 -0.4 % of maximum frequency shift) and as mentioned before it was improved to obtain accurate E field values with lower perturbing beads (0.04 %) in final linac.

All important aspects learned in previous tests about e.g. mechanical design, RF measurements, were incorporated into the RTM final linac design and also into the RF measurements test bench. The nine OFE copper segments machined showed a roughness according to specifications (Ra= 0.3 μm for inner surfaces and Ra= 0.8 μm for contact surfaces between segments). Mechanical measurements were all almost within tolerances except for the coupling slots dimensions which were a little bit bigger than specified in technical design. RF measurements before brazing demonstrated that the linac had a resonant frequency deviation from theoretical design lower than 1 MHz (0.017 %) . However, theoretical coupling factor was never obtained because not a sufficient amount of pressure was applied in order not to spoil the segments (i.e. plastic deformation of copper). Nevertheless the dependence of coupling factor with applied pressure showed that a better electrical contact would give a

higher coupling factor value. Therefore, coupling will be expected to be higher after brazing but may be tuned if necessary.

The more accurate E field on-axis (Figure 5-58) was obtained with a small disc and a careful experimental procedure. This bead produced a maximum perturbation of 2.1 MHz (0.036%) and dramatically improved the field sensitivity with respect to other beads tested. The E field obtained was quite close to theoretical except for accelerating cell 2 which showed a lower E field caused by a difference in coupling slots dimensions. As it followed from beam dynamics simulation this deviation of the field distribution from the theoretical one will not essentially influence on RTM beam dynamics. The main expected effect was some change of the 1^{st} orbit energy and change of orbits position within a few 0.1 mm.

Because at some point the dissertation must be brought to an end, it was decided not to wait for brazing of final linac so RF measurements after brazing will be performed in the near future to find out if some changes have taken place.

On the other hand in section 4.1.3 the method for measurements of $\pi/2$ frequency of accelerating and coupling cells was discussed. With this method one could get direct estimations of the stop band. However large beam hole diameter of our structure, chosen to provide beam pass through the linac of different orbits beam, thin webs between cells and short noses did not permit measuring coupling cells frequency as it is shown in Figure 4-10(b) because perturbation introduced by electric probes on-axis was too large. In addition, the presence of the 1^{st} accelerating cell with parameters different from the parameters of the regular cell together with small number of cells prevented from using lumped circuit model (see section 2.7) to extract stop-band value from the measured dispersion curve (Table 5-8). Nevertheless, we can state that for such a short structure (four accelerating cells) with so high (>10%) coupling factor (*k)* influence of the stop band, if such is available at the level of few MHz, can be neglected. Measured on-axis electric field distribution clearly demonstrated that there was no field in coupling cells which together with reasonable accelerating cells field distribution permits us to state that accelerating structure (as it is before brazing) satisfies to specifications applied to RTM linac.

ORIGINAL CONTRIBUTIONS

There are a number of original contributions proposed in this thesis. Some related studies may have been done, but for different applications (e.g. not for RTM), for different wave bands (e.g. S-Band) or for different operating conditions. The most important are summarized in the statements below:

- C-band linac design for a compact RTM - choice of length and number of cells, RF field level in different cells-.
- Method of linac simulation providing tuning of cell parameters to provide accurate field distribution in the whole linac with zero field in the coupling cells.
- 3D analysis of asymmetrical field components, estimations of linac quadrupole focusing properties during first acceleration.
- parasitic modes 3D simulation in biperiodic accelerating structure, estimations of RTM BBU threshold.
- 3D thermal analysis of C-band accelerating structure.
- 3D simulation of RF field distribution measurements technique.
- C-band RTM linac engineering design for specific linac use: placing in vacuum, but with cooling channels.

Some of the contributions proposed by the author in the present dissertation may be found in the following papers:

- Current status of the 12 MeV UPC race-track microtron, Proceedings of PAC 2009. Yu.A. Kubyshin, J. Berenguer, A.Crisol, X.González, G. Montoro, J.P. Rigla, F. Roure, D. Carrillo, L. Garcia-Tabares, F. Toral, J. Lucas, A.V. Aloev, V.I. Shvedunov.

- C-band Linac Optimization for a Race-track Microtron. Proceedings of EPAC 2008. Yu.A. Kubyshin, D. Carrillo, L. Garcia-Tabares, F. Toral, A.V. Poseryaev, V.I. Shvedunov.

- (Publication pending). Electron Gun with Off-axis Beam Injection for a Race-track Microtron. A.V. Aloev, D. Carrillo, Yu.A. Kubyshin, N.I. Pakhomov, V.I. Shvedunov. Nuclear Instruments and Methods.

- (Publication pending). Preliminary Study of High Precision Joints in Particle Accelerator Components Performed by Vacuum Brazing. L Sánchez, D. Carrillo, E. Rodríguez, F. Aragón, J. Sotelo, F. Toral. Journal of Materials Processing Technology.

Bibliography

[1] *Cold Test on C-Band Standing-Wave Accelerator.* **Kim, S.H., et al.** Albuquerque : Particle Accelerator Conference, 2007.

[2] *The C-Band (5712-MHz) Linac for the SPRING-8 Compact SASE Source (SCSS).* **Matsumoto, S., Takeda, S. y Shintake, T.** Gyeongju : LINAC, 2002.

[3] *Status of MUSL-2, The Second Microtron Using a Superconducting Linac.* **Axel, P., cardman, L.S. and Hanson, A.O.** Illinois : IEEE Transactions Nuclear Science, 1977, Vols. NS-24.

[4] *Status Report on the Harmonic Double Sided Microtron of MAMI-C.* **Jankowiak, A.** Edinburgh : European Particle Accelerator Conference, 2006.

[5] *Improved Mobile 70 MeV Race-Track Microtron Design.* **Shvedunov, V.I., et al.** Blacksburg : IEEE Transactions, 1996, Vol. 1996 p810.

[6] *Design of 12 MeV RTM for multiple applications.* **Poseryaev, A.V., et al.** Edinburgh : EPAC, 2006.

[7] *Current Status of the 12 MeV UPC Race-Track Microtron.* **Kubyshin, Yu.A., et al.** Vancouver : Particle Accelerator Conference, 2009.

[8] **Schonberg, R.J.** *Intraoperative Electron Beam Therapy System and Facility. 5.321.271* US, 14 de June de 1994.

[9] **Bardi, G.** *Apparatus for the Linear Acceleration of Electron, particularly for Intraoperative Radiation Therapy. 5.635.721* US, 3 de June de 1997.

[10] **Fantini, M.** *Machine for Intraoperative Radiation Therapy. 20050259786* US, 24 de November de 2005.

[11] Tomsk Polytechnic University. [Online] http://www.tpu.ru/eng/betatrons.htm.

[12] http://sec.edgar-online.com/2004/02/25/0001014897-04-000040/Section2.asp . [En línea]

[13] *C-Band Linac Optimization for a Race-Track Microtron.* **Kubyshin, Yu. A., et al.** Genoa : European Particle Accelerator Conference, 2008.

[14] *The importance of particle accelerators.* **Amaldi, Ugo.** Vienna : European Particle Accelerator Conference, 2000.

[15] **Betghe, K.** 20, s.l. : Nucl. Phys. News, 1999, Vol. 9/1.

[16] **Wangler, Thomas P.** *Principles of RF Linear Accelerators.* s.l. : Wiley & Sons , 1998.

[17] **Bryant, P. J.** A Brief History and Review of Accelerators. *CERN Accelerator School.* Geneva : s.n., 1994.

[18] *Electron and Ion Sources.* **Scrivens, R.** Zakopane : Cern Accelerator School, 2006.

[19] *Beam Diagnostics.* **Raich, Ulrich.** Zakopane : Cern Accelerator School, 2006.

[20] **Tsipenuk, Yuri M.** *The Microtron. Development and Applications.* London : Taylor & Francis, 2002.

[21] **Kapitza, S.P., Bykov, V.P. and Melekhin, V.N.** 997, s.l. : Sov. Phys. JETP , 1960, Vol. 41.

[22] **Babic, H. and Sedlacek, M.** 170-172, s.l. : Nuclear Instrumentation Methods, 1967, Vol. 56.

[23] *Electron Gun with Off-axis Beam Injection for a Race-track Microtron.* **Aloev, A.V., et al.** s.l. : (Submitted to) Nuclear Instruments and Methods in Physics Research,

2010.

[24] *Microtrons and Recirculators.* **Jankowiak, Andreas.** Zeegse : CERN Accelerator School, 2005.

[25] *Racetrack microtron: Principles of design and its applications.* **Shvedunov, V.I.** Barcelona : UPC, 2006.

[26] *Yields of multiparticle photoneutron reactions on the 209Bi isotope.* **Belyshev, S.S., et al.** 3, s.l. : Moscow University Bulletin, 2008, Vol. 63, pp. pp. 208-210.

[27] *Commissioning of the ANKA Storage Ring.* **Einfeld, D., et al.** Vienna : Proceedings of EPAC, 2000.

[28] IBA. [Online] http://www.iba-worldwide.com/.

[29] *Use of a Split Microtron for Instrumental Gamma Activation Analysis.* **Aliev, R., et al.** 10, s.l. : Journal of Analytical Chemistry, 2005, Vol. 60, pp. pp. 951-955.

[30] **Cherry, Simon R., Sorenson, James A. y Phelps, Michael E.** *Physics in Nuclear Medicine.* Philadelphia : Saunders, 2003.

[31] *Atomic Energy.* **Oganesyan, Yu. Ts., Starodub, G. Ya. and Baklamnov, G. V.** 1990, Vol. 68, p. p. 271.

[32] *A New Generation of Accelerators for the Production of Short- lived PET Radioisotopes.* **VanBrocklin, H. F., Leemans, W. P. and Trower, W. P.** Denton, TX : 17th International Conference on the Application of Accelerators in Research and Industry, 2002.

[33] *Multi-Energy Cargo Inspection System Based on an Electron Accelerator.* **Ishkhanov, B., et al.** WO/2008/048246.

[34] **Alvarez, L. W.** *4756866* US Patent.

[35] *The Nitrogen Camera and the Detection of Concealed Explosives.* **Trower, W.P.**

s.l. : Nucl. Instr. & Meth. , Vol. B79 (1993) 589.

[36] *Small Size 3-cm wavelenght Microtron for Defectoscopy.* **Bondus, A.A., Gorbachev, V.P. and Stepanchuk, V.P.** Saint-Petersburgh : XI International Conference on Charged Particle Accelerators Applied in Medicine and Industry, 2005.

[37] **Halbach, K.** *Design of Permanent+iron magnet for RTM.* 1996.

[38] *Medical Applications of C-Band Accelerator Technologies.* **Tanabe, E., et al.** s.l. : Linac, 1998.

[39] *Conceptual Design of the Miniature Electron Accelerator Dedicated to IORT.* **Ishkkhanov, B.S., et al.** Saratov : Russian Particle Accelerator Conference, 2004.

[40] *70 MeV Racetrack Microtron.* **Shvedunov, V.I., et al.** s.l. : Nucl. Instrum. Meth, Vols. A550 (2005) 39-53.

[41] *A Racetrack Microtron with High Brightness Beams.* **Shvedunov, V.I., et al.** s.l. : Nucl. Instrum. Meth., Vols. A531 (2004) 346-366.

[42] **Pozar, David M.** *Microwave Engineering.* s.l. : Wiley, 2004. 978-0471448785.

[43] *Joint Universities Accelerator School.* **Caspers, f. and Pirkl, W.** 2005.

[44] **Knapp, E. A., Knapp, B. C. and Potter, J. M.** s.l. : Sci. Instr., 1968, Vol. 39, p. p. 979.

[45] **Nishikawa, T., Giordano, S. and Carter, D.** s.l. : Sci. Instr., 1966, Vol. 37, p. p. 652.

[46] **Andreev, V. G., et al.** s.l. : Proton Linac Conference, 1972. p. p. 114. LA- 5115.

[47] **Chao, Alexander Wu y Tigner, Maury.** *Handbook of Accelerator Physics and Engineering.* s.l. : World Scientific Pub, 1999.

[48] *Introduction to wakefields and wakepotentials.* **Wilson, P.B.** s.l. : SLAC-PUB 4547, 1989.

[49] *Superconducting Cavities.* **Bisoffi, G.** s.l. : Cern Accelerator School, 2003.

[50] *Introduction to Microwave Linacs.* **Whittum, D.H.** s.l. : SLAC-PUB-8026, 1998.

[51] *Dynamics and acceleration in linear structures.* **Le Duff, J.** s.l. : CERN Acceleration School, 1994.

[52] *Choice of RF frequency.* **Pirkl, W.** s.l. : CERN Accelerator School 2003.

[53] *CTF3.* [Online] http://clic-meeting.web.cern.ch/clic-meeting/clic500-3000.html.

[54] **Rodney, J. and Vaughan, M.** 7, s.l. : IEEE Transactions. Electron Devices, 1988, Vol. 35.

[55] *The 4.9 GHz Accelerating Structure for MAMI C.* **Euteneuer, H., et al.** Vienna : Proceedings of EPAC, 2000. pp. pp. 1954-1956.

[56] **Feynman, Richard P., Leighton, Robert B. y Sands, Matthew.** *The Feynman Lectures on Physics, Vol.2, mainly electromagnetism and matter.* Pasadena : Addison-Wesley Publishing Company, INC, 1964. 978-0201021158.

[57] *Five Parameter Method of Tuning of Biperiodic pi/2 Accelerating Structures.* **Kulinski, S. and Sekutowicz, J.** s.l. : EPAC, 1988.

[58] [Online] http://laacg1.lanl.gov/laacg/services/download_sf.phtml.

[59] *Studies of coupled cavity linac accelerating structures with 3-D codes.* **Spalek, G.** California : XX International Linac Conference.

[60] *Comparison of Standing Wave Accelerators Operating in the 2pi/3 and the pi/2 modes.* **Schriber, S. O.** 3, s.l. : IEEE Transactions of Nuclear Science, 1975, Vols. NS-22.

[61] *Operational experience with room temperature continuous wave accelerator structures.* **Alimov, A.S., et al.** s.l. : Nuclear Instruments and Methods, Vol. A328(1993)385.

[62] *SUPERFISH - A computer Program for Evaluation of RF Cavities with Cylindrical Symmetry.* **Halbach, K. and Holsinger, R.F.** s.l. : Particle Accelerators, Vols. 7(1976)213-222.

[63] *The Cut Disk Accelerating Structure for High Energy Linacs.* **Paramonov, V.V.** s.l. : PAC, 1997. p. 2962.

[64] *PARMELA.* **Crandall, K.R. and Young, L.** s.l. : Compendium of Computer Codes for Particle Accelerator. Design and Analysis.

[65] *Recent Technological Developments in Accelerating Structures.* **Yamakazi, Y.** Japan : KEK Reports. National Laboratory for High Energy Physics, 1992.

[66] *Effect of the Coupling Slots on Beam Dynamics in Accelerator Structure of Moscow CW RTM.* **Shvedunov, V.I., et al.** s.l. : IEEE, 1996, pp. 3361-3363.

[67] *Optimizing Coupling in Biperiodic Accelerating Structures.* **Kostin, D.V., et al.** 3, s.l. : IEEE Transactions on Nuclear Science, 1998, Vol. 45.

[68] *Some Considerations Concerning the Transverse Deflection of Charged Particles in Radio-Frequency Fields.* **Panofsky, W.K.H. and Wenzel, W.A.** 11, s.l. : Review of Scientific Instruments, 1956, Vol. 27.

[69] **Holzer, Bernhard.** *Transverse Beam Dynamics.* Zakopane : Cern Accelerator School, 2006.

[70] *Beam Based HOM Analysis of Accelerating Structures at the TESLA Test Facility LINAC.* **Wendt, M., et al.** s.l. : DIPAC, 2003.

[71] *Microtron Using a Superconducting Electron Linac.* **Axel, P., et al.** 1176, s.l. : IEEE Trans. Nucl. Sci., 1975, Vol. 22.

[72] *Beam Blow-Up in Race Track Microtrons.* **Herminghaus, H. and Euteneuer, H.** s.l. : Nuclear Instruments and Methods, 1979, Vol. 163.

[73] *Beam Blow-Up Calculations for RTM and DSM.* **Shvedunov, V.I., et al.** s.l. : EPAC, 1998.

[74] *Simple contermeasures against the TM110-Beam-Blowup-Mode in Biperiodic Structures.* **Euteneuer, H., Herminghaus, H. and Schöler, H.** s.l. : EPAC, 1984.

[75] **Marhauser, F.** *Finite Element Analyses for RF Photoinjector Gun Cavities .* s.l. : TESLA FEL Report 2006-02.

[76] **Caspers, F.** *Basic Concepts II.* s.l. : CERN Accelerator School, 1992.

[77] **Slater, J.C.** *Microwave Electronics.* s.l. : D. Van Nostrand Company, 1950.

[78] **Sobenin, N.P. and Zverev, B.V.** *Electrodynamic Characteristics of Accelerating Cavities.* s.l. : FISEC - MEPIUP, 1999.

[79] The Brazing Book. [Online] 2009. http://www.handyharmancanada.com/TheBrazingBook/.

[80] **Jensen, Erk.** *Fabrication and Testing of RF Structures.* s.l. : CERN-AB-2003-092 RF, 2003.

[81] **Wilson, I.** *Cavity Construction Techniques.* s.l. : CERN Accelerator School, 1992.